Development of Mn and Si based 3rd Generation Advanced High Strength Steels for Automobile Applications

Doctoral Thesis

by

"Suresh Chand"

(2020MMZ0007)



DEPARTMENT OF METALLURGICAL AND MATERIALS ENGINEERING

INDIAN INSTITUTE OF TECHNOLOGY ROPAR

SEPTEMBER, 2024

Development of Mn and Si based 3rd Generation Advanced High Strength Steels for Automobile Applications

A Thesis Submitted

In Partial Fulfilment of the Requirements for the Degree of

DOCTOR OF PHILOSOPHY

by

"Suresh Chand"

(2020MMZ0007)



DEPARTMENT OF METALLURGICAL AND MATERIALS ENGINEERING

INDIAN INSTITUTE OF TECHNOLOGY ROPAR

SEPTEMBER, 2024

Copyright © "2025" by Indian Institute of Technology Ropar
All Rights Reserved

DEDICATED
TO
MY PARENTS

Mr. Rohan Lal & Mrs. Savitri Devi

A father's goodness is higher than the mountain;

A mother's goodness is deeper than the sea.

- Japanese Proverb

DECLARATION

I declare that this work entitled "Development of Mn and Si based 3rd Generation

Advanced High Strength Steels for Automobile Applications" has not previously been

accepted in substance for any degree and is not being simultaneously submitted in

candidature for any other degree. This thesis is being submitted in partial fulfillment of the

requirements for the degree of PhD in Metallurgical and Materials Engineering. This thesis

is the result of my own independent investigation, except where otherwise stated. I have

acknowledged all the other sources by stating the references explicitly. I declare that any

idea /data /fact /source stated in my thesis has not been fabricated/ falsified/ misrepresented.

All the principles of academic honesty and integrity have been followed. I understand that

any violation of the above will be cause for disciplinary action by the institute and can also

evoke penal action from the sources which have thus not been properly cited or from whom

proper permission has not been taken when needed. I hereby give consent for my thesis, if

accepted, to be available online after 2 years in the Institute's Open Access repository and

for inter-library loan, and for the title and abstract to be made available to outside

organizations.

Suresh Chand

06-02-2025

Signature

Name- Suresh Chand

Entry Number- 2020MMZ0007

Program-PhD

Department of Metallurgical and Materials Engineering

iii

CERTIFICATE

It is certified that the work contained in the thesis titled "Development of Mn and Si based 3rd Generation Advanced High Strength Steels for Automobile Applications" by "Suresh Chand" has been carried out under our supervision and that this work has not been submitted elsewhere for the award of any degree.

Khushboo Rakha 06-02-2025

Signature of the Supervisor 1

Dr. Khushboo Rakha

Ravi Mohan Prasad 06-02-2025

Signature of the Supervisor 2

Dr. Ravi Mohan Prasad

Department of Metallurgical and Materials Engineering

Indian Institute of Technology Ropar

Rupnagar, India, 140001

ACKNOWLEDGMENTS

I would like to express my sincere gratitude to my supervisors, **Dr. Khushboo Rakha and Dr. Ravi Mohan Prasad** (Department of Metallurgical and Materials Engineering, Indian Institute of Technology Ropar) for their expertise, patience, criticism and encouragement in shaping this work and my academic growth. I would like to thank **Dr. Khushboo Rakha** for always being an inspiration and for providing a great deal of support, guidance and encouragement during my thesis work. I would like to thank **Dr. Ravi Mohan Prasad** to support in discussions and valuable suggestions which have contributed greatly to the improvement of the thesis. **Dr. Khushboo Rakha** has always been very kind, helpful, supportive and cordial throughout the entire journey of this dissertation.

I am thankful to our collaborator **Shahriar Reza** who helped me in technical discussion and formal analysis of 3D Atom Probe Tomography which was essential to identify and characterize retained austenite. I am highly grateful to **Prof. Krishanu Biswas** (Professor, Department of Materials Science and Engineering, Indian Institute of Technology Kanpur) for extending support and guidance. Also, I would like to thank Mr. Sarvesh Kumar, Buddhvir and PhD Scholars Abhinav Dixit, Mustaq and Rahul Mitra (IIT Kanpur of MSE-department).

I would like to express my sincere gratitude to the doctoral committee members: **Dr. Neha Sardana**, **Dr. Pratik K. Ray**, **Dr. Prince Kumar Singh**, and **Dr. Samir Roy** for their insightful feedback, constant support and dedication to excellence. I extend my appreciation to **Central Research Facility**, **IIT Ropar**. I would like to thanks to PhD scholar Mr. Abhinesh Verma, Mr. Atul Kumar Pandey and Mr. Mohit for their invaluable support in characterization. I also would like to thank **Dr. Rajiv Kumar** (Assistant Professor, Department of Metallurgical and Materials Engineering, Indian Institute of Technology-Ropar) who supported me in all my personal difficulties during this work.

I would like to express my thanks and gratitude to **Prof. Rajeev Ahuja** (Director, Indian Institute of Technology Ropar) and **Dr. Pratik K Ray** (Head, Department of Metallurgical

and Materials Engineering) for providing, infrastructural, and administrative support in carrying out this work.

I would like to express thanks to Prof. Baldev Setia and Prof. Dheeraj Sanghi (Ex-Directors, Punjab Engineering College- Chandigarh) who supported and helped me to grow and progress in this work. I like to extend thanks to Dr. Uma Batra (Professor, Ex-HOD, Department of Metallurgical and Materials Engineering, Punjab Engineering College-Chandigarh) for kind support in my PhD. I am also obliged to Dr. J. D. Sharma (Department of Metallurgical and Materials Engineering, Punjab Engineering College- Chandigarh) for kind support during this work.

I am highly obliged and wish sincere thanks to the technical staff- Mr. Deepak Kumar, Mr. Abhishek Sharma, Mr. Amit Kumar, Mr. Sarbjeet Singh who helped in all the possible way during experimental work. I would also thank Dr. Tarwinder Singh Handa, Librarian for his constant support. I am indebted to my co-scholars Dr. Saminderpreet Singh, Mr. Abhinesh Verma, Mr. Krishan Kumar, Mr. D. Parmeswaran and Mr. Vishnu Girish for their camaraderie, intellectual exchange and moral support. Thanks are due to Mr. Sanjay Bansal, Mr. Anil Kumar and all my friends who have encouraged me and made this journey more enjoyable and rewarding.

Above all, I owe my deepest gratitude to my family (my wife and 3 sons) for their unconditional love, encouragement and belief in my abilities. Their unwavering support and sacrifices have been a constant source of strength and motivation. I also want to express my gratitude to everyone who has supported me and encouraged me to pursue my goals but I missed his/her name to acknowledge. Lastly, I dedicate this thesis to my parents and my family.

Thank you Almighty for blessing me with this wonderful life!

LAY SUMMARY

The automobile sector is focusing on reducing weight without losing strength to achieve high fuel efficiency and crash resistance. Composite materials and alloys are used, but their high costs limit the utilization. The "ULSAB-AVC" consortium developed "AHSS" steels, which have yield stress and tensile stress greater than 300 and 550 MPa respectively. AHSS's mechanical properties are controlled by factors like phase composition and distribution.

First generation AHSS, also known as conventional AHSS, is a lean steel with ferrite-based, multi-phase microstructures. Its ultimate tensile strength is higher than conventional steels, but limited ductility and formability issues remain the main concern. Second generation austenitic steels, known as "U-AHSS," were developed to address the formability issue of first generation AHSSs. These steels, with a strength-percent elongation product of over 50,000 MPa, offer outstanding strength-formability due to retained austenite in the microstructure. However, they are limited due to high alloying content, delayed cracking, and poor weldability. Third generation AHSS, also known as "X-AHSS" steels, is an extension of first generation AHSS by improving mechanical properties through grain refinement and processing routes. Strategies include enhancing DP steel properties, altering conventional processing of TRIP steels, obtaining ultrafine bainite microstructures, employing new fabrication routes like quenching and partitioning, and developing TRIP steels with medium Mn (3-12 wt.%) content.

In the present investigation, the 3rd generation AHSS have been designed using Thermo-Calc and JMatPro and further developed experimentally with variation of Mn and Si as principle alloying elements. The properties were simulated and based on simulation results five compositions were developed using melting route.

The five AHSS, thus developed were homogenised. After homogenization, the alloys were characterized to identify the phases. Further, the homogenised AHSS were hot rolled to develop steel sheets below 1.6 mm gauge which is currently used sheets in latest car bodies.

Two hot rolling temperatures were used for hot rolling followed by air cooling. The AHSS sheets thus developed were characterized to identify the phases as well as mechanical property evaluation. The results thus obtained are presented in this thesis.

ABSTRACT

Automotive industries require materials with higher strength, plasticity and crashworthiness, aiming for 3rd generation of advanced high strength steels (AHSS) with medium Mn, Si and minor alloying elements. In this investigation, 3rd generation AHSS were developed using a vacuum arc melting furnace with manganese (Mn) and silicon (Si) as major alloying elements as well as minor additions such as Cr, Al, Ni, etc. Time Temperature Transformation (TTT) diagrams were simulated using JMatPro. AHSS homogenized treatment was performed at 1200 °C for 4 hours. Ferrite peaks were identified in homogenized steels. Field emission scanning electron microscope revealed ferrite and pearlite in the homogenized steels. The alloy steels after casting and homogenization were subjected to hot rolling at 900 °C and 1100 °C. The steels thus developed were characterized using FE-SEM, XRD, microhardness tester, universal testing machine (UTM) and 3-dimensional Atom Probe Tomography (APT).

The homogenized AHSS were hot rolled at 900 °C for multiple passes followed by air cooling. The microstructure revealed 1-2% martensite, 20-40% bainite, 10-12% retained austenite, and 46-69% ferrite. The presence of retained austenite was also verified by XRD analysis. The ultimate tensile strengths (UTS) of Alloy 1 (Fe-4Mn-1.5Si), Alloy 2 (Fe-6Mn-1.5Si), and Alloy 3 (Fe-8Mn-1.5Si) hot rolled at 900 °C were found to increase from 1418 MPa to 1625 MPa with elongation of 17% to 15%. The addition of manganese increased UTS and hardness while decreased ductility of alloys. The ultimate tensile strengths (UTS) of Alloy 4 (Fe-6Mn-1Si), Alloy 2 (Fe-6Mn-1.5Si), and Alloy 5 (Fe-6Mn-2Si) were not changed significantly and elongation was observed to decrease from 18% to 12%. Effect of silicon variation from 1 to 2 wt.% keeping Mn constant at 6 wt.% was also analyzed. The addition of silicon increased hardness while decreased the ductility of alloys.

Further, the alloy steels after casting and homogenization were subjected to hot rolling at 1100 °C. The FE-SEM micrographs revealed a complex phase microstructure with martensite, ferrite, bainitic ferrite and retained austenite in the specimens obtained after rolling and air cooling. The microhardness of the developed alloys was found to be in the

range of 395 to 502 VHN in the hot-rolled and air-cooled condition of the specimen. The tensile strength of alloys was measured to be in the range of 1412 to 1614 MPa with elongation of 12% to 19%. The analysis of fracture surfaces after tensile tests for developed alloys revealed that Alloy 1 (Fe-4Mn-1.5Si) had dimples indicating ductile fracture while Alloy 2 (Fe-6Mn-1.5Si) has a mixture of dimples and facets, and Alloy 3 (Fe-8Mn-1.5Si) has lower dimples but larger facets, confirming quasi-ductile fracture with a lower ductility limit of 12%. Atom Probe Tomography was performed to study the complex phase structure at nanoscale through re-distribution of carbon and other alloying elements. 3D APT revealed the presence of very fine retained austenite film of thickness ~4-5 nm and carbon content of 6-8 at.%. This complex phase microstructure obtained after hot rolling and normalizing is made of very fine bainitic ferrite with film type retained austenite also providing TRIP effect, in addition martensite and ferrite resulting in high strength and toughness.

LIST OF PUBLICATIONS

Publications from Thesis

Journal publications

- 1. **Suresh Chand**, S. Reza, K. Biswas, R. M. Prasad, and K. Rakha, "Novel Mn and Si alloyed complex phase steel for automotive applications," *Materials Science and Engineering: A*, vol. 916, p. 147292, 2024. doi: 10.1016/j.msea.2024.147292
- 2. **Suresh Chand,** S. Reza, R. M. Prasad, and K. Rakha, "Effect of Si content on novel medium-Mn complex phase steels," *Transaction of the Indian Institute of Metals*, vol. 77, p. 3799-3808, 2024. doi.org/10.1007/s12666-024-03436-3

Patents (Published)

 Suresh Chand, Khushboo Rakha, Ravi Mohan Prasad, "An advanced high-strength steel (AHSS) for automotive applications and manufacturing method thereof" (2024) IP Patent Application No. 202411001312

Conference participation/Publication

1. Oral presentation on "Thermodynamic study of Fe-Mn-Si novel alloys" at *International Conference on Fundamentals and Industrial Research in Materials (iConFIRM-2023, IIT Ropar, December, 2023)*

Suresh Chand, Ravi Mohan Prasad, Khushboo Rakha, "Thermodynamic study of Fe-Mn-Si novel alloys", Springer Proceeding Phys, vol. 308, p. no. 82–91, Online-ISBN, 2024.

TABLE OF CONTENTS

DECLARATION	iii
CERTIFICATE	iv
ACKNOWLEDGMENTS	v
LAY SUMMARY	vii
ABSTRACT	ix
LIST OF PUBLICATIONS	xi
TABLE OF CONTENTS	xii
LIST OF FIGURES	xviii
LIST OF TABLES	XXV
LIST OF ABBREVIATIONS	xxvii
Chapter 1	1
Introduction	1
1.1 Background	1
1.2 Motivation	3
1.3 Objectives and scope	3
1.4 Thesis structure organization:	4
Chapter 2	6
Literature Review	6
2.1 Introduction	6
2.1.1 The AHSS developed and area of interest for research	7
2.1.2 Various parts made by AHSS in automotive applications	
2.2 Heat Treatment applied to AHSS	9

2.2.1 Austempering	9
2.2.2 Quenching and partitioning (Q & P process)	10
2.2.3 Quenching, partitioning and tempering (Q-P-T process)	10
2.2.4 Thermo-mechanical treatment (TMT)	11
2.2.5 Intercritical annealing	11
2.2.6 Austenite Reverted Transformation (ART) ART	12
2.2.7 Ausforming treatment	13
2.2.8 Deformed and partitioned (D&P process)	13
2.2.9 Dual stabilization heat treatment (DSHT) process	13
2.3 Effect of alloying elements	14
2.3.1 Effect of Carbon (C)	14
2.3.2 Effect of Manganese (Mn)	14
2.3.3 Effect of Silicon (Si)	14
2.3.4 Effect of Chromium (Cr)	14
2.3.5 Effect of Nickel (Ni)	15
2.3.6 Effect of Titanium (Ti)	15
2.3.7 Effect of Aluminum (Al)	15
2.3.8 Effect of Phosphorous (P)	15
2.3.9 Effect of Sulphur (S)	16
2.4 List of developed AHSS	17
2.4.1 Microstructure of medium Mn 3G-AHSS	18
2.4.2 Mechanical properties of medium Mn 3G-AHSS steels	22
2.4.3 Transformation induced plasticity (TRIP) Effect	23
2.5 Nano-scale characterization of medium Mn steels	31
2.6 Present status of research in the field of AHSS.	36
2.7 Research gaps	37
2.8 Objectives	37

Chapter 3	38
Research Methodology	38
3.1 Research design	38
3.2 Materials and methods	39
3.3 Homogenization Heat treatment	40
3.4 Thermomechanical treatments	42
3.5 Characterizations.	43
3.5.1 Optical microscopic examinations	43
3.5.2 Field Emission Scanning Electron Microscopy (FESEM)	44
3.5.3 X-Ray Diffraction (XRD)	44
3.5.4 Microhardness measurements	44
3.5.5 Tensile Testing:	45
3.5.6 Atom probe tomography (APT)	46
3.6 Process flow chart of the research methodology	46
Chapter 4	47
Alloy Design and Development	
4.1 Introduction	
4.2 Alloy design	
4.2.1 Alloy Phase diagrams	
4.2.2 Simulated Continuous cooling curves (CCT) and temperature time transformation (TTT)	
4.2.2.1 TTT and CCT diagrams with variation in Mn	
4.2.2.2 TTT and CCT diagrams with variation in Si	
4.2.2.3 Phase transformation temperatures	
4.2.2.4 Simulated solidification paths of Alloys	
4.3 Alloy development	

4.3.1 Alloy casting	58
4.3.2 Homogenization heat treatment	59
4.4 Characterization	60
4.4.1 Optical Micrographs of homogenised AHSS	60
4.4.2 Field-Emission Scanning Electron Micrographs (FE-SEM)	
4.4.2.1 Effect of manganese (Mn) alloying on micrographs	63
4.4.2.2 Effect of silicon (Si) alloying on micrographs	
4.4.3 X-Ray Diffraction (XRD) Patterns	
4.5 Discussion	6/
4.5.1 Effect of Mn alloying	67
4.5.2 Effect of Si alloying	67
4.6 Conclusions	68
Chapter 5	69
Thermo-mechanical treatment at 900 °C and mechanical properties	69
5.1 Introduction	69
5.2 Methodology	70
5.2.1 Thermo-mechanical treatment	70
5.2.2 Characterization of hot rolled steels	
5.3 Results	
5.3.1 Optical micrographs of hot rolled at 900 °C	
5.3.2 FESEM micrographs of hot rolled at 900 °C	
5.3.2.1 Effect of manganese (Mn) alloying	
5.3.2.2 Effect of silicon (Si) alloying	
5.3.3 X-ray Diffraction of hot-rolled at 900 °C	77
5.3.4 Mechanical Properties of hot-rolled at 900 °C	80
5.3.4.1 Microhardness measurements of hot-rolled at 900 °C	80
5 3 4 2 Stress-Strain curves	82

5.3.5 Fracture Analysis	86
5.3.5.1 Effects of Mn alloying	86
5.3.5.2 Effects of Si alloying	87
5.4 Discussion	88
5.4.1 Structure Property-corelation: Effect of Mn alloying	88
5.4.2 Structure Property-corelation: Effect of Mn alloying	89
5.5 Conclusion	90
Chapter 6	91
Thermo-mechanical treatment at 1100 °C and mechanical properties	91
6.1 Introduction	91
6.2 Methodology	94
6.2.1 Thermo-mechanical treatment	94
6.2.2 Characterization of hot-rolled steels	96
6.2.3 Three-dimensional atom probe tomography	96
6.3 Results and discussion	97
6.3.1 Optical micrographs of hot-rolled at 1100 °C	97
6.3.2 Field-Emission micrographs of hot rolled at 1100 °C	99
6.3.2.1 Effect of manganese (Mn) alloying on micrographs	99
6.3.2.2 Effect of silicon (Si) alloying on micrographs	101
6.3.3 X-ray Diffraction of hot rolled at 1100 °C	103
6.3.4 Mechanical Properties of hot-rolled at 1100 °C	106
6.3.4.1 Microhardness measurements of hot-rolled at 1100 °C	106
6.3.4.2 Effect of Mn on mechanical properties	108
6.3.4.3 Effect of silicon additions on mechanical properties of steel	110
6.3.5 Fracture Analysis	114
6.3.5.1 Effect of Manganese on fracture behavior	114
6.3.5.2 Effect of silicon on fracture behavior	115
6.3.6 Atom probe tomography results	116

6.3.6.1 Nanoscale distribution of elements and its effect on mechanic 120	al properties
6.3.7 Effect of hot rolling temperature on microstructure and Mechanical pro	operties121
6.4 Conclusion	122
Chapter 7	124
Conclusion and Future Scope	124
The main aim of the present work was to achieve following objectives:	124
7.1 Conclusions	124
7.2 Future Scope	126
References	127

LIST OF FIGURES

Figure 2.1 Tensile strength is the total elongation of different steels
Figure 2.2 Application of 3 rd Generation AHSS [27]8
Figure 2.3 Austempering heat treatment for hypoeutectoid steels
Figure 2.4 Quenching and partitioning process for steels
Figure 2.5 Schematic diagram of quenching and partitioning and tempering process for steels
Figure 2.6 Schematic diagram of intercritical annealing process for steels
Figure 2.7 Schematic diagram of austenite reverted (ART) process for steels13
Figure 2.8 The hot rolled steel of composition Fe–9.0Mn–0.05C (wt.%), annealed at 893 K for 600 seconds, (a) EBSD phase maps, (b) TEM images in bright field imaging mode [16]
Figure 2.9 (a) Phase analysis and EBSD map, (b) XRD spectra, intercritical annealing [23]
Figure 2.10 (a) A schematic diagram of DSHT and T-T-T curves (b) SEM micrograph after dual stabilization heat treatment, (c) EBSD map of cross section of rolled specimen [45]
Figure 2.11 Elongation vs. ultimate tensile strength in medium-manganese alloys under different austenite reverted transformation conditions [12]23
Figure 2.12 Dislocation density in mild steel, dual-phase steel, and TRIP steels [53]24
Figure 2.13 Mn steels based on percentage added. UFG = ultrafine-grained, SBIP = shear band induced plasticity, TWIP = twining induced plasticity [53]24
Figure 2.14 SEM micrographs for specimens, (a) Step-I intercritical annealing at 1033 K (b) Step-II intercritical annealing at 993 K (c) Stress-strain curves after heat treatments,
(d) XRD patterns for specimens after heat treatments [54]

Figure 2.15 SEM microstructures alloy at Finish Rolling temperature (FRT), (a) FRT-700
°C, (b) FRT-900 °C (c) X-ray diffraction patterns of the steels at various finish rolling
temperatures, FRT [55]
Figure 2.16 SEM microstructures of alloy, (a) high, 1.5 wt.% Si, (b) medium, 0.7 wt.% Si, (c) low, 0.25 wt.% [56]
Figure 2.17 (a) Stress-strain curves of the hot rolled (HR), Warm Rolled (WR), intercritical annealing (IA), 25 % cold rolled (CR), and partitioned at different temperatures, 623 K, 673 K, 723 K, and 773 K, respectively [37]28
Figure 2.18 (a) The heat treatments applied to steel (b). Stress-strain curves [59]30
Figure 2.19 3D atom probe tomography maps of carbon and manganese in (a) water-quenched (WQ), (b) air-cooled (AC), (c) distribution of C, Mn and Al atoms in ROI 1, (d) 2-dimensional concentration maps of carbon in the ROI, (e) distribution of C, Mn and Al atoms in ROI 2, and (f) 2-dimensional concentration maps of carbon in the ROI 2 [62]
Figure 2.20 (a) EBSD map, (b) TEM image, austenite and martensite with precipitate, (c) atom probe tomography (APT), (d) magnified 3D image of APT, (e) Atomic map isoconcentration surfaces for Mn atoms (blue colour), at 18.0 at.% (yellow colour), and (f) variation of Mn across martensite to austenite phase boundary [63]
Figure 2.21 Atom probe tomography analysis of Fe-7Mn-0.5Si-0.1C (wt.%) steel, tempered at 450 °C, for 6 hours (a-e) and 1 hour (f-g), (a) reconstruction of APT, (b) Proxigram of carbides seen in Figures (a, c, d); (c) Mn atoms are displayed; (d) concentration at the interface. (e) TEM image in bright field mode; (f) Proxigram of the carbides with a similar composition to M23C6. (g) Proxigram of carbides with a lower carbon (C) concentration [64]
Figure 2.22 Tensile strength- total elongation different steels [65]
Figure 3.1 Experimental setup of vacuum arc melting furnace
Figure 3.2 The homogenization heat treatment cycle (Cycle 5)41
Figure 3.3 Lab scale rolling mill and muffle furnace for thermomechanical treatment 42

Figure 3.4 Schematic of tension test specimen machined as per ASTM E8, (substandard specimen)
Figure 3.5 Actual tensile test specimen machined from hot rolled and air-cooled sheet of five compositions using CNC machine
Figure 3.6 Process flow chart with expermental conditions
Figure 4.1 Phase diagrams of alloy systems, (a) Binary phase diagram of Fe-Mn System, (b) Binary phase diagram of Fe-Si System
Figure 4.2 Ternary phase diagram of Fe-Mn-C System at 1000 °C
Figure 4.3 Ternary phase diagram of Fe-Si-C System at 1000 °C50
Figure 4.4 Ternary phase diagram of Fe-Mn-Si System at 1000 °C50
Figure 4.5 Time Temperature Transformation (TTT) and advanced CCT diagrams of novel alloy steels determined by materials Property software: (a1) TTT Diagram, Alloy 1, (b1) TTT Diagram, Alloy 2, and (c1) TTT Diagram, Alloy 3, (a2) advanced CCT, Alloy 1, (b2) advanced CCT, Alloy 2, (c2) advanced CCT, Alloy 3
Figure 4.6 Time Temperature Transformation (TTT) and advanced CCT diagrams of novel alloy steels determined by materials Property software: (a1) TTT Diagram, Alloy 4, (b1) TTT Diagram, Alloy 2, and (c1) TTT Diagram, Alloy 5, (a2) advanced CCT, Alloy 4, (b2) advanced CCT, Alloy 2, (c2) advanced CCT, Alloy 5
Figure 4.7 Effect of (a) Mn, and (b) Si variation on lower critical (A1) and Upper critical (A3) temperatures.
Figure 4.8 Effect of (a) Mn and (b) Si variation on phase transformation temperature of alloy steels
Figure 4.9 Solidification behaviour using Scheil solidification model determined by Thermo-Calc software with variation in Mn
Figure 4.10 Solidification behaviour using Scheil solidification model determined by Thermo-Calc software with variation in Si
Figure 4.11 Finger shaped casting produced by re-melting of button

Figure 4.12 Homogenization heat treatment, at 1200 °C, for 4 hours60
Figure 4.13 Optical micrographs of Fe-xMn-1.5Si steels homogenized at $1200 ^{\circ}\text{C}$, 4 hours. at 200X , (a) Alloy 1, (b) Alloy 2, (c) Alloy 3. (where $x = 4, 6, 8$)
Figure 4.14 Optical micrographs of Fe-6Mn-ySi (y = 1, 1.4, 2.0) steels homogenized at 1200 °C, 4 hours. at 200X, (a) Alloy 4 (Fe-6Mn-1.0Si), (b) Alloy 2 (Fe-6Mn-1.5Si), (c) Alloy 5 (Fe-6Mn-2.0Si).
Figure 4.15 Field Emission Scanning Electron micrographs of AHSS homogenized at 1200 °C, 4 hours, at 1500X (a) Alloy 1 (Fe-4Mn-1.5Si), (b) Alloy 2 (Fe-6Mn-1.5Si), (c) Alloy 3 (Fe-8Mn-1.5Si).
Figure 4.16 Field Emission Scanning Electron micrographs of AHSS homogenized at 1200 °C, 4 hours, at 2000X (a) Alloy 4 (Fe-6Mn-1.0Si), (b) Alloy 2 (Fe-6Mn-1.5Si), (c) Alloy 5 (Fe-6Mn-2.0Si).
Figure 4.17 XRD-spectra of AHSS homogenized at 1200 °C, 4 hours, (a) alloy 1 (Fe-4Mn-1.5Si), (b) alloy 2 (Fe-6Mn-1.5Si), (c) alloy 3 (Fe-8Mn-1.5Si)
Figure 4.18 XRD-spectra of AHSS homogenized at 1200 °C, 4 hours, (a) alloy 4 (Fe-6Mn-1.0Si), (b) alloy 2 (Fe-6Mn-1.5Si), (c) alloy 5 (Fe-6Mn-2.0Si)
Figure 5.1 The schematic of the process flow chart70
Figure 5.2 The finger-shaped sample, hot rolled to manufacture a sheet of (150 mm long, 15 mm width, 1.6 mm thickness) dimensions
Figure 5.3 Optical micrographs of alloy steels hot rolled at 900 °C (a) Alloy 1 (Fe-4Mn-1.5Si), (b) Alloy 2 (Fe-6Mn-1.5Si), and (c) Alloy 3 (Fe-8Mn-1.5Si)
Figure 5.4 Optical micrographs of Fe-6Mn-ySi steels hot rolled at 900 °C, 20 min., (a) Alloy 4 (Fe-6Mn-1.0Si), (b) Alloy 2 (Fe-6Mn-1.5Si), (c) Alloy 5 (Fe-6Mn-2.0Si)73
Figure 5.5 Field emission scanning electron micrographs of steels hot rolled at 900 °C, 20 min., (a1, a2) Alloy 1 (Fe-4Mn-1.5Si), (b1, b2) Alloy 2 (Fe-6Mn-1.5Si), (c1, c2) Alloy 3 (Fe-8Mn-1.5Si).
(1 0 01:111 1:0 01):

Figure 5.6 Field emission scanning electron micrographs of steels hot rolled at 900 °C, 20
min., at 2500X, (a1, a2) Alloy 4 (Fe-6Mn-1.0Si), (b1, b2) Alloy 2 (Fe-6Mn-1.5Si), (c1,
c2) Alloy 5 (Fe-6Mn-2.0Si)76
Figure 5.7 XRD spectra of AHSS hot-rolled at 900 °C, Alloy 1 (Fe-4Mn-1.5Si), Alloy 2
(Fe-6Mn-1.5Si), and Alloy 3 (Fe-8Mn-1.5Si)
Figure 5.8 XRD spectra of AHSS hot-rolled at 900 °C, Alloy 4 (Fe-6Mn-1.0Si), Alloy 2
(Fe-6Mn-1.5Si), and Alloy 5 (Fe-6Mn-2.0Si)79
Figure 5.9 Microhardness of novel AHSS hot-rolled at 900 °C, Alloy 1 (Fe-4Mn-1.5Si),
Alloy 2 (Fe-6Mn-1.5Si), and Alloy 3 (Fe-8Mn-1.5Si)80
Figure 5.10 Microhardness of novel AHSS hot-rolled at 900 °C, Alloy 4 (Fe-6Mn-1.0Si),
Alloy 2 (Fe-6Mn-1.5Si), and Alloy 5 (Fe-6Mn-2.0Si)
Figure 5.11 Stress-strain curves of novel AHSS hot-rolled at 900 °C, Alloy 1 (Fe-4Mn-
1.5Si), Alloy 2 (Fe-6Mn-1.5Si), and Alloy 3 (Fe-8Mn-1.5Si)
Figure 5.12 Stress-strain curves of novel AHSS hot-rolled at 900 °C, Alloy 4 (Fe-6Mn-
1.0Si), Alloy 2 (Fe-6Mn-1.5Si), and Alloy 5 (Fe-6Mn-2.0Si)
Figure 5.13 Effect of manganese (Mn) alloying in the novel AHSS hot-rolled at 900 °C,
Alloy 1 (Fe-4Mn-1.5Si), Alloy 2 (Fe-6Mn-1.5Si), and Alloy 3 (Fe-8Mn-1.5Si)84
Figure 5.14 Effect of silicon (Si) alloying in the novel AHSS hot-rolled at 900 °C, Alloy
4 (Fe-6Mn-1.0Si), Alloy 2 (Fe-6Mn-1.5Si), and Alloy 5 (Fe-6Mn-2.0Si)85
Figure 5.15 Fractographs of novel AHSS hot rolled at 900 °C at 4000X: (a) Alloy 1 (Fe-
4Mn-1.5Si), (b) Alloy 2 (Fe-6Mn-1.5Si), and (c) Alloy 3 (Fe-8Mn-1.5Si)86
Figure 5.16 Fractographs of novel AHSS hot rolled at 900 °C, at 5000X (a) Alloy 4 (Fe-
6Mn-1.0Si), (b) Alloy 2 (Fe-6Mn-1.5Si), and (c) Alloy 5 (Fe-6Mn-2.0Si)87
Figure 6.1 The process flow chart for manufacturing advanced high strength steels94
Figure 6.2 The finger-shaped sample is hot rolled to manufacture a sheet, 15 mm wide,
and 1.6 mm thick

Figure 6.3 Optical micrographs of AHSS steels hot rolled at 1100 °C, (a) Alloy 1 (Fe-
4Mn-1.5Si), (b) Alloy 2 (Fe-6Mn-1.5Si), and (c) Alloy 3 (Fe-8Mn-1.5Si)97
Figure 6.4 Optical micrographs of steels hot rolled at 1100 °C, (a) Alloy 4 (Fe-6Mn-1.0Si), (b) Alloy 2 (Fe-6Mn-1.5Si), and (c) Alloy 5 (Fe-6Mn-2.0Si)98
Figure 6.5 Field Emission Scanning Electron micrographs of steels hot rolled at 1100 °C, (a1, a2) Alloy 1 (Fe-4Mn-1.5Si), (b1, b2) Alloy 2 (Fe-6Mn-1.5Si), (c1, c2) Alloy 3 (Fe-8Mn-1.5Si).
Figure 6.6 Field Emission Scanning Electron micrographs of steels hot rolled at 1100 °C, at 2500X, (a1, a2) Alloy 4 (Fe-6Mn-1.0Si), (b1, b2) Alloy 2 (Fe-6Mn-1.5Si), (c1, c2) Alloy 5 (Fe-6Mn-2.0Si).
Figure 6.7 XRD-spectra of AHSS hot rolled at 1100 °C, Alloy 1 (Fe-4Mn-1.5Si), Alloy 2 (Fe-6Mn-1.5Si), and Alloy 3 (Fe-8Mn-1.5Si).
Figure 6.8 XRD-spectra of AHSS hot rolled at 1100 °C, Alloy 4 (Fe-6Mn-1.0Si), Alloy 2 (Fe-6Mn-1.5Si), and Alloy 5 (Fe-6Mn-2.0Si).
Figure 6.9 Microhardness of novel AHSS hot-rolled at 1100 °C, Alloy 1 (Fe-4Mn-1.5Si), Alloy 2 (Fe-6Mn-1.5Si), and Alloy 3 (Fe-8Mn-1.5Si).
Figure 6.10 Microhardness of novel AHSS hot rolled at 1100 °C, Alloy 4 (Fe-6Mn-1.0Si), Alloy 2 (Fe-6Mn-1.5Si), and Alloy 5 (Fe-6Mn-2.0Si)
Figure 6.11 (a) Engineering stress-strain plots, (b) True stress-true strain plots, for AHSS hot rolled at 1100 °C and soaked for 20 min for Alloy 1 (Fe-4Mn-1.5Si), Alloy 2 (Fe-6Mn-1.5Si), and Alloy 3 (Fe-8Mn-1.5Si).
Figure 6.12 Effect of manganese (Mn) alloying in the novel AHSS hot rolled at 1100 °C, Alloy 1 (Fe-4Mn-1.5Si), Alloy 2 (Fe-6Mn-1.5Si), and Alloy 3 (Fe-8Mn-1.5Si)110
Figure 6.13 (a) Stress-strain curves of novel AHSS, (b) True stress-strain curve, hot rolled at 1100 °C, Alloy 4 (Fe-6Mn-1.0Si), Alloy 2 (Fe-6Mn-1.5Si), and Alloy 5 (Fe-6Mn-2.0Si).
Figure 6.14 Effect of silicon (Si) alloying in the novel AHSS hot rolled at 1100 °C, Alloy 4 (Fe-6Mn-1.0Si). Alloy 2 (Fe-6Mn-1.5Si), and Alloy 5 (Fe-6Mn-2.0Si).

Figure 6.15 Fractographs of novel AHSS hot rolled at 1100 °C, 20 min., at 2000X, (a)
Alloy 1 (Fe-4Mn-1.5Si), (b) Alloy 2 (Fe-6Mn-1.5Si), (c) Alloy 3 (Fe-8Mn-1.5Si)114
Figure 6.16 Fractographs of novel AHSS hot rolled at 1100 °C, at 2500X (a) Alloy 4 (Fe-
6Mn-1.0Si), (b) Alloy 2 (Fe-6Mn-1.5Si), and (c) Alloy 5 (Fe-6Mn-2.0Si)115
Figure 6.17 Three-dimensional Atom probe tomography of AHSS: (a) All elements, (b)
Carbon (c) Manganese, (d) Silicon, (e) Chromium, (f) Titanium, and (g) Nickel116
Figure 6.18 Three-dimensional Atom probe tomography of AHSS: (a) Carbon atoms, (b)
Mn, Si, and C atoms (c) Proxigram developed from the data of iso surfaces displayed in,
(d) Proxigram developed from the data of iso surfaces displayed in for Mn, Si, and C
atoms
Figure 6.19 Three-dimensional Atom probe tomography of AHSS: (a1-a6) Carbon atoms,
(b1-6) Mn atoms (c1-c6) Si atom
Figure 6.20 Three-dimensional Atom probe tomography of AHSS:(a) retained Austenite
film (b) Proxigram developed from the data of iso-surfaces displayed in (a) at 3.5 at.%

LIST OF TABLES

Table 2.1 Properties and limitations of AHSS [24], [25], [26]7
Table 2.2 Compositions of AHSS studied listed from literature
Table 2.3. Chemical composition of steels studied (wt.%) [56]
Table 2.4 Solid solution strengthening components in bainite and alloy composition [58].
Table 3.1 Parameter of homogenization heat treatment cycles applied for homogenization of bulk
Table 3.2 Parameter of rolling operation to manufacture alloy steel sheets42
Table 3.3 Temperature variations during the rolling process
Table 3.4 Etching parameter for newly developed AHSS
Table 4.1 Simulated phase start transformation temperatures (°C) of novel AHSS determined by JMatPro software
Table 4.2 The compositions of novel third-generation advanced high-strength alloys (Spectrometer analysis of novel alloys)
Table 4.3 Peak positions of alloy 1, alloy 2 and alloy 3 homogenized at 1200 °C, 4 hours soaking. (with increase in Mn contents).
Table 4.4 Peak positions of alloy 4, alloy 2 and alloy 5 homogenized at 1200 °C, 4 hours. soaking. (with increase in Si contents)
Table 5.1 Strain applied in the rolling operations for Alloy 1, Alloy 2, Alloy 3, Alloy 4, and Alloy 5
Table 5.2 Phase estimation of developed alloys with variation in Mn hot rolled at 900 °C.
Table 5.3 Phase estimation of Alloys with variation in Si hot rolled at 900 °C77

Table 5.4 Peak positions of Alloy 1, Alloy 2, and Alloy 3 hot-rolled at 900 °C, (retained
austenite, γ_A) with an increase in Mn contents
Table 5.5 Peak positions of alloy 4, alloy 2, and alloy 5 homogenized at 1200 °C for 5
hours of soaking. (retained austenite, γ_A) with an increase in Si contents79
Table 5.6 Microhardness values of alloys hot-rolled at 900 °C80
Table 5.7: Mechanical properties of novel AHSS hot-rolled at 900 °C85
Table 6.1 Strain applied in the rolling operations for the Alloy 1, Alloy 2, Alloy 3, Alloy
4 and alloy 595
Table 6.2: Phase estimation of Alloy 1 (Fe-4Mn-1.5Si), Alloy 2 (Fe-6Mn-1.5Si), and
Alloy 3 (Fe-8Mn-1.5Si) hot rolled at 1100 °C
Table 6.3 Phase estimation of Alloy 4 (Fe-6Mn-1.0Si), Alloy 2 (Fe-6Mn-1.5Si), and
Alloy 5 (Fe-6Mn-2.0Si) hot rolled at 1100 °C
Table 6.4. Peak positions of Alloy 1, Alloy 2 and Alloy 3 hot rolled at 1100 °C, (retained
austenite, γ_A) with an increase in Mn contents
Table 6.5 Peak positions of alloy 4, alloy 2 and alloy 5 homogenized at 1200 °C, for 4
hrs. soaking. (retained austenite, γ_A) with an increase in Si contents105
Table 6.6 Microhardness values of AHSS hot-rolled at 1100 °C106
Table 6.7 Mechanical properties of Alloy 1, Alloy 2 and Alloy 3, hot rolled AHSS
determined from tension tests
Table 6.8 Mechanical properties of novel AHSS hot-rolled at 1100 °C112

LIST OF ABBREVIATIONS

Abbreviations	Description	
AHSS	Advanced High Strength Steel	
Al	Aluminum	
APT	Atom Probe Tomography	
ASTM	American Society for Testing and Materials	
В	Bainite	
C	Carbon	
Cr	Chromium	
F	Ferrite	
Fe	Irom	
FESEM	Field Emission Scanning Electron Microscopy	
HV	Vickers Hardness	
M	Martensite	
Mn	Manganese metal	
OM	Optical Micrograph	
P	Phosphorous	
RA	Retained Austenite	
S	Sulphur	
SEM	Scanning Electron Microscopy	
Si	Silicon	
TEM	Transmission Electron Microscope	
Ti	Titanium	
TWIP	Twining induced plasticity	
ULSAB-AVC	Ultra Light Steel Auto Body-Advanced Vehicle Concepts	
UTM	Universal Testing Machine	
DSHT	Dual stabilization Heat Treatment	
CCT	Continuous Cooling curve	
TTT	Time-Temperature- Transformation curves	
XRD	X-ray Diffraction	

Chapter 1 Introduction

1.1 Background

Global automotive industries have been desperately striving to solve the challenge of weight reduction in automobiles in order to decrease the carbon footprint and lower the fuel consumption. Since the sheet steels remain as the major structural material for use in automobiles, development of stronger steels is the primary approach adopted by material scientists to fulfill the demands from the automotive industries. Alternative avenues to decrease the density of steels or increase the Young's modulus to counter the stiffness loss due to excessive lower-gauging of steel parts are also being investigated [1], [2], [3]. The current trends in the automotive industry are mainly focused on increasing the crashworthiness properties of automobiles and at the same time reducing the fuel consumption and CO₂ emissions.

AHSS is classified as first generation AHSS (1G-AHSS), second generation AHSS (2G-AHSS) and third generation AHSS (3G-AHSS). The 1G-AHSS, which includes dual phase, complex phase and transformation induced plasticity (TRIP) steels, shows high strength of more than 600 MPa but has a relatively low ductility of less than 20% [4], [5], [6]. Low ductility restricts the application of the 1G-AHSS to automobile parts with complex shapes.

Speer and coworkers reported a quench and partition (Q&P) process to produce AHSS with a large quantity of carbon-enriched retained austenite in low-carbon alloys. It was suggested that this could be achieved through austenite stabilization by carbon uptake following carbon rejection from supersaturated martensite under paraequilibrium conditions [7], [8]. More than 30 vol. % retained austenite can be achieved in relatively lean AHSS alloy steels subjected to dual stabilization heat treatment (DSHTs), which results in strength and ductility combinations which can satisfy the demand of third generation AHSS. The mechanical testing results suggested that a three-phase structure with refined

austenite grains will provide the highest strength and ductility. In the alloy composition (0.3C-4.0Mn-2.1Si-1.5Al-0.5Cr), tensile strengths up to 1650 MPa and total elongation of around 20 % were obtained [9]. The tensile strength and elongation values reported for all the different medium Mn steel chemistries, have been superimposed on the well-known strength–elongation diagram for automotive steels. The UTS decreased by ~140MPa when the temperature increases from room temperature to 100°C, which is quite possible due to adiabatic and frictional heating during cold press forming. In this case, the steel was tested with a strain rate of 0.2 s⁻¹ at various subcritical and supercritical temperatures in 'isothermal baths' minimizing the adiabatic heating in order to obtain temperature effects. On the other hand, it is also observed that the steel is sensitive to high strain rate deformation, which is relevant for crash behavior, and exhibits a negative average strain rate sensitivity of stress within the tested range [10]. Medium manganese steels containing 3 to 12 wt% Mn are promising candidates as third-generation AHSS due to the better combination of strength and ductility [11]. To obtain austenite, an intercritical annealing, the austenite reverted transformation (ART), can be performed. During annealing, the segregation of Mn and C to grain boundaries promotes nano-laminate austenite to nucleate at martensite lath boundaries. In fact, the austenite is stabilized at room temperature through the partitioning of carbon and manganese to the austenite grains, while the martensite is being reverted to austenite [12]. In these alloys, the austenite plays a crucial role in controlling the mechanical properties and the enhancement of ductility and work hardening. Cr was added to further increase the hardenability of the steel. Si was also considered to reduce the carbon activity and hinder the carbide formation. The addition of copper was also elaborated to promote the matrix strengthening through fine copper-rich Fe-Cu precipitates.

The 2G-AHSS, which includes high Mn TRIP and twinning induced plasticity steels, shows a remarkable combination of high strength of more than 700 MPa and large uniform ductility exceeding 50% [13], [14], [15]. The higher tensile properties of the 2G-AHSS result from the high strain hardening rate, which is due to the formation of strain induced martensite or mechanical twins in the austenite phase during plastic deformation. However, the 2G AHSS has difficulties in mass production due to material cost and weldability. These difficulties are arised primarily by a high amount of alloying elements, greater than

approximately 17 wt%. Therefore, nowadays, the 3G-AHSS, which includes lightweight steel, quenching and partitioning processed steel and medium Mn steel has become attractive because steels in this category have a good trade-off between material cost and mechanical properties of the 3G-AHSS steels [16], [17].

In the present investigation, novel medium manganese steels with silicon additions are explored and investigated for automotive application that provide tensile strength of more than 1 GPa with an elongation of 15 to 20 %. The nanoscale characterization using Atom Probe Tomography (APT) has been performed to understand the nano-scale elemental distribution and its effect on the mechanical response of developed steels. It also involves establishing a simpler process to manufacture advanced high-strength steels for the automotive industries. The novelty of present investigation is formation of bainite in hot-rolled air-cooled specimen and formation of complex-phase structure reaching a strength more than 1 GPa.

1.2 Motivation

Currently, automotive industries are striving for new materials that can be used as candidate materials to replace existing materials. The automotive industry is focusing on reducing the weight of automotive vehicles, increasing fuel efficiency, and reducing CO and CO₂ emissions. To meet the present requirements of the automotive industry, 3rd generation advanced high-strength steels (AHSS) can be important materials. 3rd generation steels are under development and alloyed with manganese (3–12 wt.%). These steels possess high strength (more than 1 GPa) and good ductility (20%). The 1st and 2nd generation steels exhibit issues of poor weldability and high manufacturing costs, respectively. Hence, the present work presents the development of 3rd generation AHSS steels for automotive industries [18], [19], [20], [21].

1.3 Objectives and scope

The main emphasis of this work is to develop 3rd generation medium manganese steel for automotive applications. The current work has the following objectives:

- 1. To study the effect of Mn concentration (4-8 wt.%) and Si (1-2 wt.%) on the microstructure and mechanical properties of thus formed steel,
- 2. To study the effect of thermo-mechanical treatment at 900 °C and 1100 °C on microstructure and mechanical properties,
- 3. Nano-scale characterization to study the carbon redistribution in the complex phase microstructure developed.

1.4 Thesis structure organization:

This thesis is organized as follows:

Chapter 1. Introduction: This chapter presents a brief introduction to the development medium Mn and Si alloyed 3rd generation advanced high-strength steels and objectives of this thesis work.

Chapter 2. Literature Review: This chapter presents an overview of the development of advanced high-strength steel for automotive applications, methods to improve tensile strength and elongation, different types of heat treatment and thermo-mechanical methods and current state of the art.

Chapter 3. Research Methodology: This chapter discusses experimental procedures used for the development of advanced high-strength steels, mechanical testing and characterization techniques used.

Chapter 4. Alloy Design and Development: This chapter investigates and presents alloy design using Thermo-Calc and JMatPro softwares. Structural characterization of homogenized alloys at 1200 °C for 4 hours is discussed.

Chapter 5. Thermo-mechanical treatment at 900 °C and mechanical properties: The AHSS developed were hot rolled at 900 °C in pilot scale rolling followed by air cooling to develop complex phase steels. The AHSS thus developed were mechanically tested and characterized to develop a structure property correlation.

Chapter 6. Thermomechanical treatment at 1100 °C and mechanical properties: The AHSS developed were hot rolled at 1100 °C in pilot scale rolling followed by air cooling to develop complex phase steels. The AHSS thus developed were mechanically tested and characterized to develop a structure-property correlation. Atom Probe Tomography is performed to understand nanoscale segregation and clustering which influences the mechanical properties of AHSS.

Chapter 7. Conclusions and Future Scope: This chapter summarizes the present thesis work and underlines its prospective future by evaluating the obtained results. A brief discussion about the possible future vision is presented.

Chapter 2 Literature Review

2.1 Introduction

Advanced high-strength steels (AHSS) are used in automotive applications due to their superior mechanical properties. There are three classes: 1st generation, 2nd generation, and 3rd generation. 1st generation AHSS is ferrite-based, offering higher strength but poor ductility and formability. 2nd generation AHSS, with high manganese content and alloying additions, offers a good combination of strength and formality but is costly. 3rd generation AHSS is under development, extending the 1st generation by grain refinement and lowering manufacturing costs [22]. The brief description of 1st, 2nd, and 3rd generation steels are given in Table 2.1. Low manganese AHSS exhibit less than 3 wt.% Mn and High Mn AHSS alloyed more than 12 wt.% Mn. While, Medium manganese steels with 3 to 12 wt.% Mn are promising for third-generation AHSS due to their superior strength and ductility [11]. Austenite reverted transformation (ART) is an intercritical annealing process that promotes nano-laminate austenite nucleation at martensite lath boundaries, stabilizes at room temperature, and reverts martensite to austenite [12]. Austenite controls mechanical properties and enhances ductility and work hardening in alloys. Cr, Si, and Cu are added for increased hardenability and matrix strengthening. AHSS is classified into first, second, and third generations [4], [5], [6]. Hann et al. [16] and Lee et al. [17]. studied medium Mn alloys with Fe, revealing EBSD maps and XRD-spectra revealing austenite, ferrite, and martensite peaksv.3G-AHSS steel, including lightweight, quenching, partitioning, and medium Mn steel, offers a good trade-off between material cost and mechanical properties [16], [17]. H. Aydin et al. examined medium Mn alloyed steel, revealing EBSD maps and XRD-spectra revealing austenite, ferrite, and martensite peaks [23].

Table 2.1 Properties and limitations of AHSS [24], [25], [26].

AHSS Category	Properties	Limitations
1 st Gen AHSS	Ferrite-based AHSS. Higher strength than conventional HSS	Limited ductility and formability is the main concern
2 nd Gen AHSS	AHSS with austenite phase stabilized in the microstructure. Contain high Mn content and other alloy additions. Offer excellent combination of strength and formability	High cost due to high alloy additions. Tendency for delayed cracking and poor weldability
3 rd Gen AHSS	Extension of first generation by grain refinement, different processing routes etc. at lower cost. Lean alloy steel compositions are used for their development. Intended to act in between 1 st and 2 nd generation AHSS. Multi-Phase microstructures	Currently under development, require special processing routes including controlled cooling at high cooling rates. In some cases require severe thermomechanical deformation

2.1.1 The AHSS developed and area of interest for research.

The total elongation vs tensile strength of various types of steel are shown in Figure 2.1. Figure 2.1 shows a wide range of strength and ductility of 3rd generation steels. The area of interest is highlighted in red colour.

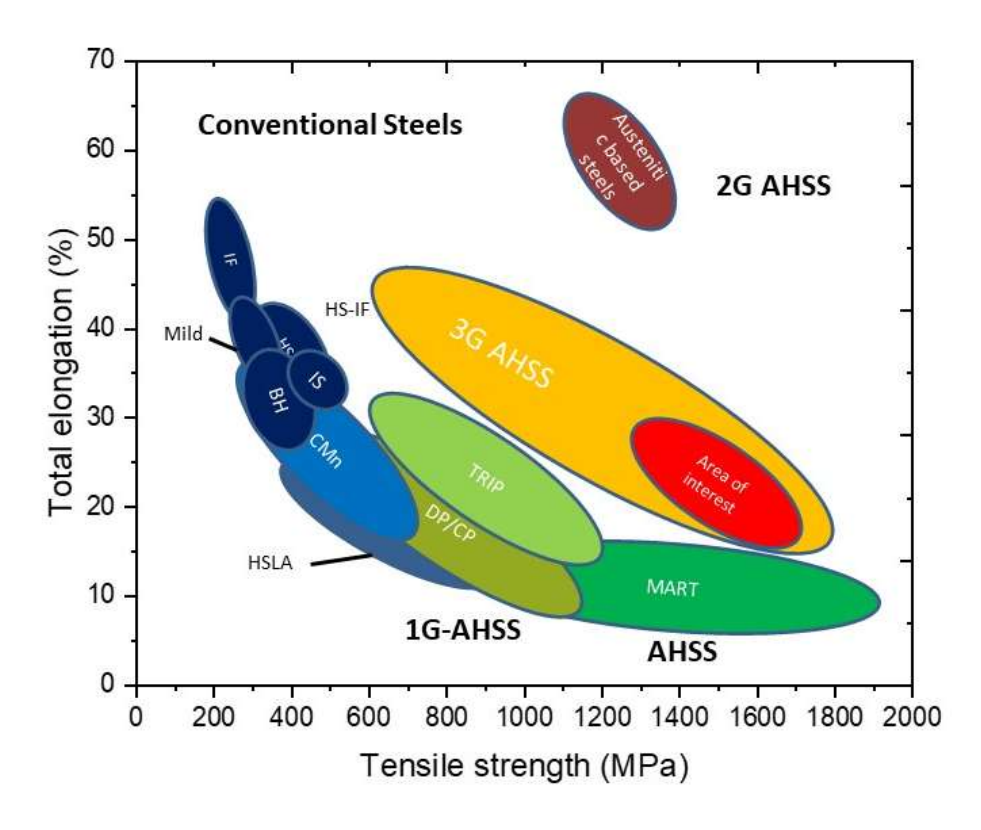


Figure 2.1 Tensile strength is the total elongation of different steels.

2.1.2 Various parts made by AHSS in automotive applications

The engine cradle, brake pedal, suspension arm, Rocker arms and bumpers are manufactured using AHSS which are shown in Figure 2.2. The A, B, C, D-pillers of car bodies are also made AHSS

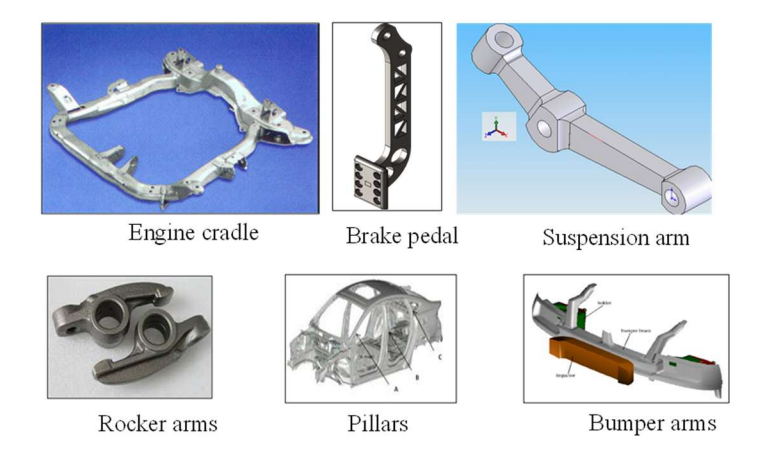


Figure 2.2 Application of 3rd Generation AHSS [27].

2.2 Heat Treatment applied to AHSS

The most common heat treatments employed in the development of AHSS are as follows:

2.2.1 Austempering

Austempering is a heat treatment process used primarily on ferrous alloys, to enhance their mechanical properties. The process involves heating the material to a temperature above its upper critical temperature (A3), followed by quenching it in a medium of molten salt or crude oil to a temperature is generally between 300 °C and 400 °C resulting fine grains in the microstructure. Austempering process is shown in Figure 2.3 with blue colour curve. Austempering improves the toughness of the material, making it more resistant to fracture. Compared to traditional quenching methods, austempering results in less distortion of the material [28], [29], [30].

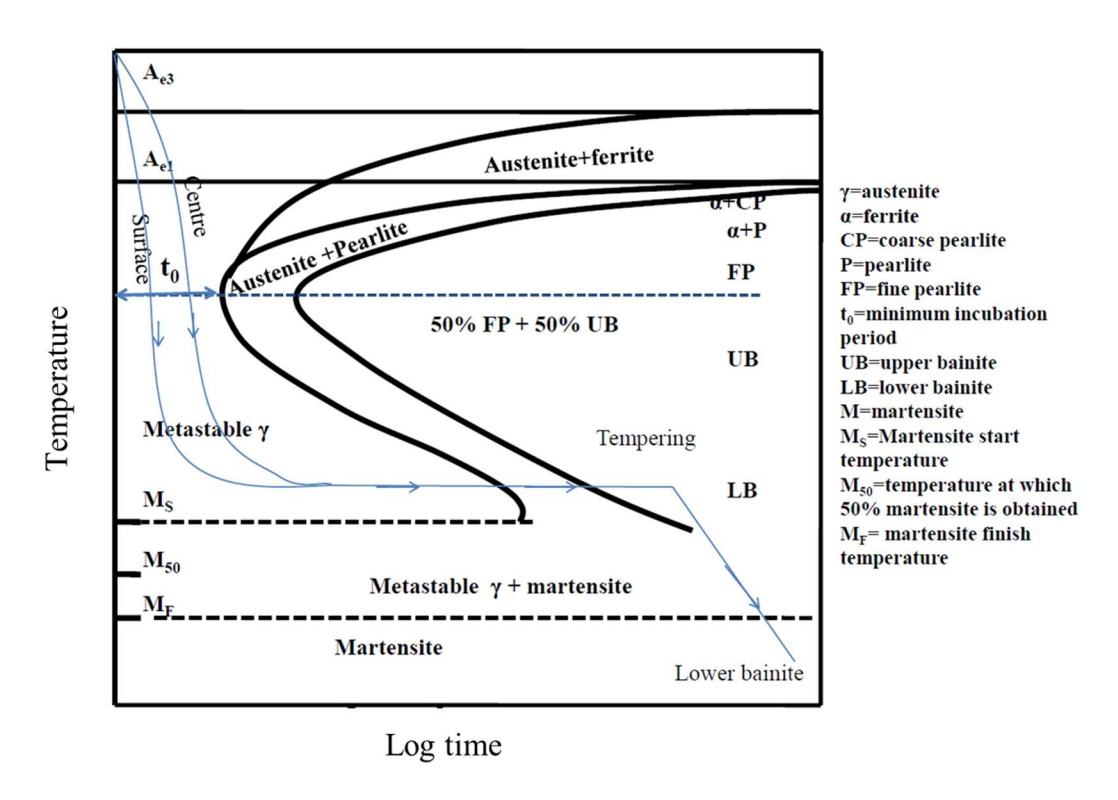


Figure 2.3 Austempering heat treatment for hypoeutectoid steels.

2.2.2 Quenching and partitioning (Q & P process)

The steels are quenched from austenitic temperature to room temperature and again held at slightly higher temperature to diffuse out carbon from martensitic which will stabilize the retained austenite phase followed by air cooling. The microstructure consists of ferrite, martensite and retained austenite. The quenching and partitioning process is shown in Figure 2.4. Speer et al. first proposed this process [31]. The steel with a composition of 0.2% C, 1–1.5% Al, and 1–1.5% Mn, was quenched and partitioned which produced carbon depleted carbide free martensite and carbon enriched retained austenite, these results showed an UTS in the range of 1000 to 1400 MPa with ductility of 10–20% [7] [32], [33], [34].

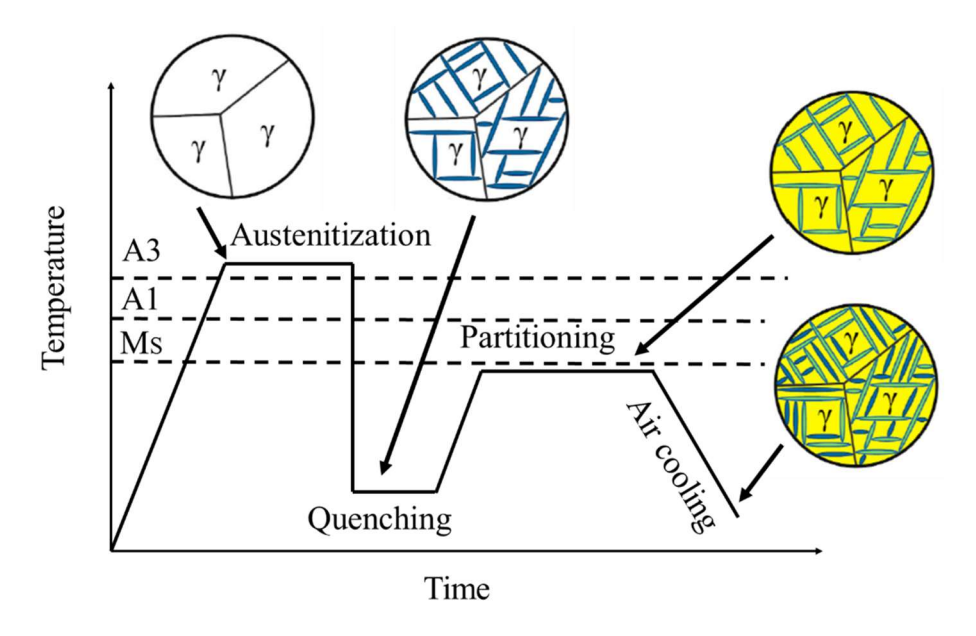


Figure 2.4 Quenching and partitioning process for steels.

2.2.3 Quenching, partitioning and tempering (Q-P-T process)

The Q & P process is modified by adding tempering in the process. The composition Fe–0.2C–1.5Mn–1.5Si–0.05Nb–0.13Mo steel was processed using quenching, partitioning, tempering (Q-P-T) which exhibits UTS of 1500 MPa with elongation 15% [35]. The quenching, partitioning and tempering (Q-P-T) heat treatment cycle is presented in Figure 2.5.

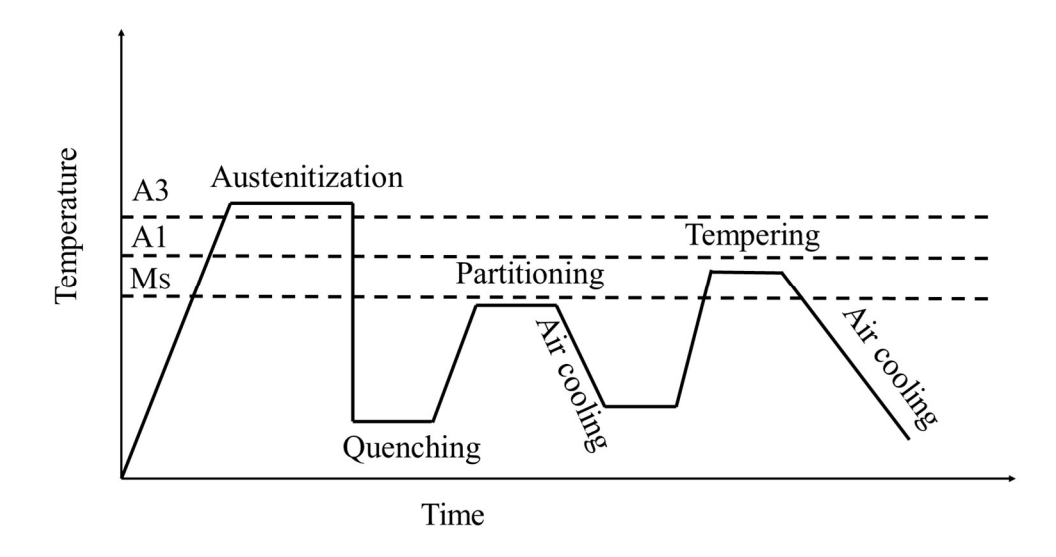


Figure 2.5 Schematic diagram of quenching and partitioning and tempering process for steels.

2.2.4 Thermo-mechanical treatment (TMT)

Thermo-mechanical treatment (TMT) is a process that combines thermal and mechanical processes to enhance the properties of metals and alloys. The material is heated to a specific temperature to alter its microstructure, usually through processes like annealing or quenching. The heating helps to dissolve alloying elements and refine grain structures. After heating, the material undergoes mechanical deformation, such as rolling, forging, or extrusion. This step enhances strength and toughness by refining the grain size and aligning the microstructure. The material is then cooled, often at controlled rates, to achieve the desired microstructure. The advantages of TMT include improved strength, ductility, toughness.

2.2.5 Intercritical annealing

Intercritical annealing is a heat treatment process used primarily for steels, particularly those that exhibit a dual-phase microstructure, such as ferrite and austenite. This process involves heating the steel to a temperature between the upper and lower critical temperatures. Intercritical annealing is used to achieve a desired microstructure that enhances mechanical properties, such as strength, ductility, and toughness. The resulting

microstructure can be tailored for specific applications. This process can refine grain size and improve mechanical properties of the steel.

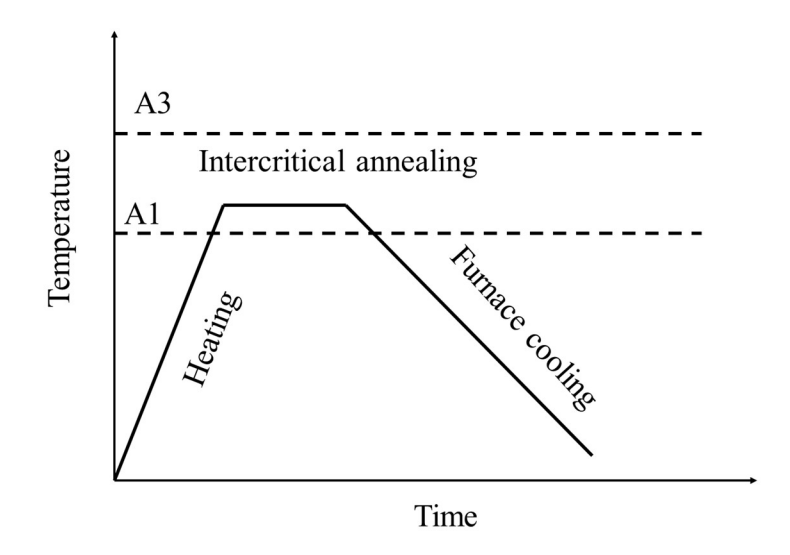


Figure 2.6 Schematic diagram of intercritical annealing process for steels.

2.2.6 Austenite Reverted Transformation (ART) ART

The austenite reverted transformation specifically involves the transformation of martensite back to austenite upon heating. When steel is quenching, it transforms from austenite (a face-centered cubic structure) to martensite (a body-centered tetragonal structure). This results in a hard but brittle microstructure. Upon heating martensitic steel above lower critical temperature, the martensite transforms to austenite through a process called "reversion." Which results increase in ductility. Austenite revert transformation is the process in which martensite transforms into austenite when steel specimen held at austenitic transformation temperature. The phenomena of ART create more TRIP effect in AHSS [36].

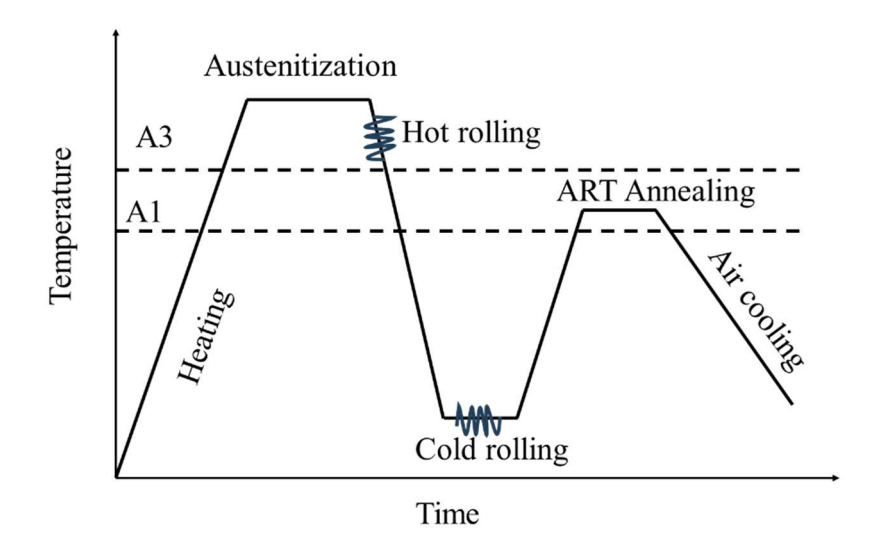


Figure 2.7 Schematic diagram of austenite reverted (ART) process for steels.

2.2.7 Ausforming treatment

Ausforming is a heat treatment process applied to steel, particularly in the production of high-strength components. It involves austenitizing the steel (heating it to above upper critical temperature where it becomes austenite and then deformed it while it is still in the austenitic phase). After deformation, the steel is typically quenched to transform the austenite into martensite, which significantly increases the strength and hardness of the material. This process is often used in manufacturing components like gears, crankshafts, and other critical parts that require a combination of strength and toughness.

2.2.8 Deformed and partitioned (D&P process)

The specimen are subjected to hot deformation and intercritical annealing, cold deformation followed by partitioning treatment [37].

2.2.9 Dual stabilization heat treatment (DSHT) process

This process is derived from quenching and partitioning process. Dual stabilization heat treatment (DSHT) consists of 5 precisely controlled cooling steps [9].

2.3 Effect of alloying elements

2.3.1 Effect of Carbon (C)

Surface quality deteriorates of rimmed steels with increase in carbon concentration. The surface quality of killed steels with a carbon percentage of 0.15 to 0.30 wt.% may be lower, and extra processing may be necessary to achieve surface quality. The tendency of carbon to segregate is moderate, and the segregation of carbon is frequently more important than that of other elements. The main hardening component in all steels is carbon. The tensile strength increases with increasing carbon content in the as-rolled condition up to 0.85% C approximately. The ductility and weldability decrease with increase in carbon concentrations. Carbon stabilizes the retained austenite.

2.3.2 Effect of Manganese (Mn)

Manganese (Mn) has less tendency of macro segregation. Mn is beneficial for surface quality in all carbon ranges, especially in resulfurized steels. It contributes to strength and hardness, but to a lesser extent than carbon. Increased manganese content decreases ductility and weldability, but has a strong effect on steel hardenability. Mn acts as austenite stabilizer.

2.3.3 Effect of Silicon (Si)

Silicon acts as deoxidizer in steels. The rimmed and capped steels having no silicon content present in it., semi-killed steels having moderate amounts, and killed carbon steels may contain up to 0.6 wt.% Si. Silicon acts as ferrite stabilizer.

2.3.4 Effect of Chromium (Cr)

Chromium is typically added to steel to increase resistance to corrosion and oxidation, to increase hardenability, to improve high-temperature strength, or to improve abrasion resistance in high-carbon compositions. Chromium is a strong carbide former. Complex chromium-iron carbides go into solution in austenite slowly; therefore, a sufficient heating time before quenching is necessary. Chromium can be used as a hardening element, and is

frequently used with a toughening. It increases high temperature strength when used in conjunction with molybdenum. Cr acts as ferrite stabilizer.

2.3.5 Effect of Nickel (Ni)

Hardenability, impact strength and fatigue resistance increase when used in combination with chromium in carbon steels. Nickel is used as an alloying element in constructional steels, is a ferrite strengthener. Because nickel does not form any carbide compounds in steel, it remains in solution in the ferrite, thus strengthening and toughening the ferrite phase. Nickel steels are easily heat treated because nickel decreases the critical cooling rate. Ni stabilizes the phase field of austenite.

2.3.6 Effect of Titanium (Ti)

Titanium acts as grain refiner in the microstructure. Tensile strength, yield strength and notch strengths are increased with addition of titanium. It can induce secondary hardening during the tempering of quenched steels and enhances. This is added to constructional steels in the normally in the range of 0.10 to 1.00%. When Ti is in solid solution in austenite prior to quenching, the reaction rates for transformation become considerably slower as compared with carbon steel. Creep strength and temper embrittlement reduce with addition of Ti. Titanium also increases stability of ferrite.

2.3.7 Effect of Aluminum (Al)

Aluminum is widely used as a deoxidizer and to control of grain size. Aluminum is the most effective in controlling grain growth before to quenching. Titanium, zirconium, and vanadium are also effective grain growth inhibitors, however, for structural grades when quenched and tempered. these three elements may have adverse effects on hardenability because their carbides are quite stable and difficult to dissolve in austenite prior to quenching. Aluminum also increases stability of ferrite.

2.3.8 Effect of Phosphorous (P)

Higher phosphorus increases machinability of steels to improve. Phosphorus has less tendency to segregates than carbon and sulfur. Increasing phosphorus increases strength and hardness and decreases ductility and notch impact toughness in the as-rolled condition.

The decreases in ductility and toughness are greater in quenched and tempered highercarbon steels.

2.3.9 Effect of Sulphur (S)

Sulphur element is very detrimental to surface quality, particularly in the lower-carbon and lower-manganese steels. This element is added to improve machinability. Increased sulphur content lowers transverse ductility and notch impact toughness but has only a slight effect on longitudinal mechanical properties. Weldability decreases with increasing sulphur content. Sulphur has a greater segregation tendency than any of the other common elements. Sulphur occurs in steel principally in the form of sulphide inclusions. Obviously, a greater frequency of such inclusions can be expected in the resulphurized grades.

The effect of alloying elements reported in various works is mentioned as under:

It is intended to add key alloying elements like Mn and Si to alloys in order to develop 3G-AHSS. To enhance mechanical qualities, a few alloying elements including Cr, Cu, Al, Ni, Ti, V, Nb, and Mo could be added. By preventing the precipitation of carbide, the addition of certain alloying elements, such as silicon, has been crucial in stabilizing ferrite [38], [39]. The literature reports that the retained austenite stability is lowered with silicon addition [40]. The austenite transition temperature increases and the austenite two phase zone expands with the addition of Si [11]. At room temperature, the fraction of retained austenite (RA) can be effectively increased by adding manganese (Mn). Nevertheless, because of the decreased C concentration that was partitioned into austenite during intercritical annealing treatments, the mechanical stability of RA was decreased. Higher Mn content steels are shown to have improved mechanical characteristics [41]. I. Majia et al. reported that adding Ti results in higher peak stress levels, which are connected to precipitation strengthening and solid solution. Additions of titanium also improve hot ductility [42]. Retained austenite (RA) volume fraction rises with increasing carbon levels up to 0.3 weight percent before decreasing as a result of cementite production. Si addition improves hardenability and boosts strength and elongation [43]. Aluminum raises the equilibrium start (Ae1) and finish (Ae3) temperatures in medium-grade steels, hence decreasing the annealing time and raising the intercritical temperature [32]. Copper, lead, chromium, molybdenum, niobium, aluminum, and other elements enhance atmospheric

corrosion resistance, machinability, hardening, creep resistance, yield strength, grain refinement, and control austenite grain growth in reheated steels [44]

2.4 List of developed AHSS

The compositions of medium-Mn steel studied in the literature are listed in Table 2.2.

Table 2.2 Compositions of AHSS studied listed from literature.

Sr. No.	Composition	Reference
1	Fe-0.2C-3.5Mn	[111]
2	Fe-0.22C-7.15Mn-3.15Si-3.11Al-0.05Mo	[23]
3	Fe-0.3C-4Mn-2.1Si-1.5Al-0.5Cr	[112]
4	Fe-(0.15, 0.3)C-6Mn-1.5Si-3Al	[41]
5	Fe-9Mn-0.05C	[89]
6	Fe-6.15Mn-1.5Si-0.05C	[46]
	Fe-0.08C-6Mn-1.5Si-0.08V	
7	Fe-0.3C-10Mn-2Si-3Al	[47]
8	Fe-0.3C-12Mn-(2, 3)Al	[113]
9	Fe-0.2C-6Mn-1.7Si-0.4Al-0.5Cr	[53]
10	Fe-0.43C-2.27Mn-3.26Si	[35]
11	Fe-0.21C-2Mn-0.77Si-0.76Al-0.08Nb-1.05Cu-1.02Ni-0.26Mo	[54]
12	Fe-0.43C-(0.59-1.17)Mn-(2.03-2.6)Si-0.008Al-0.03Nb-	[80]
	1.33Cr-0.07Ni-0.03Mo-0.01P-0.07Cu-0.004S	
13	Fe-0.19C-0.084Si -4.92Mn- 0.005S-0.0058P-	[55]
	0.73(Mo+V)+0.0032N	
14	Fe-0.4C-1.5Si-2Mn-0.025Al-0.99Cr-0.49Ni	[56]
	Fe-0.4C-0.7Si-2Mn-0.025Al-0.99Cr-0.49Ni	
	Fe-0.4C-0.25Si-2Mn-0.025Al-0.99Cr-0.49Ni	
15	Fe-10.13Mn-0.39C-2.05Al-0.26V	[37]
16	Fe-0.15C-6Mn-1.5Al-1Si	[97]
17	Fe-5.95Mn- 1.55Si- 1.03 Al-0.055C	[114]
18	Fe-12.4Mn-0.57C-1.5Al-0.4Si-0.02Cr-0.03P	[115]
19	Fe-10Mn-2Cr-2Si-2Cu-0.1C	[61]
	Fe-10Mn-2Cr-2Si-2Cu-0.1B	
	Fe-10Mn-2Cr-2Si-2Cu-0.1C-0.1B	
20	Fe-4Mn-0.1C	[99]
21	Fe-3.89Mn-0.101C	[116]
22	Fe-7Mn-0.1C-0.5Si	[62]
23	Fe-11.7Mn-2.9Al-0.064C	[64]
24	Fe-0.18C-11Mn-3.8A1	[34]

2.4.1 Microstructure of medium Mn 3G-AHSS

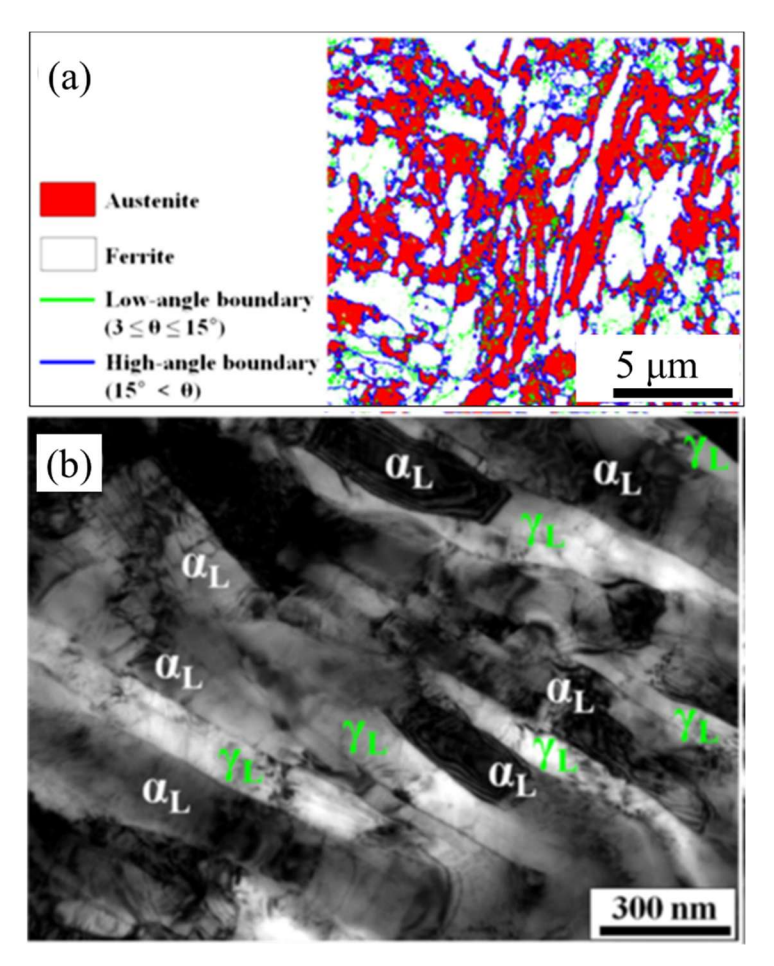


Figure 2.8 The hot rolled steel of composition Fe–9.0Mn–0.05C (wt.%), annealed at 893 K for 600 seconds, (a) EBSD phase maps, (b) TEM images in bright field imaging mode [16].

The research reveals the microstructure of Fe-9Mn-0.05C steels, transforming lath retained austenite into lath ferrite. EBSD and TEM images reveal low and high-angle boundaries, with ferrite and austenite forming distinct shapes. Various shapes of ferrite and lath retained austenite were observed in the microstructure. Retained austenite grains have low density of dislocation as shown in Figure 2.8. The yield strength, UTS and elongation of hot rolled steel were measured 830 MPa, 1034 MPa and 27 % elongation [16].

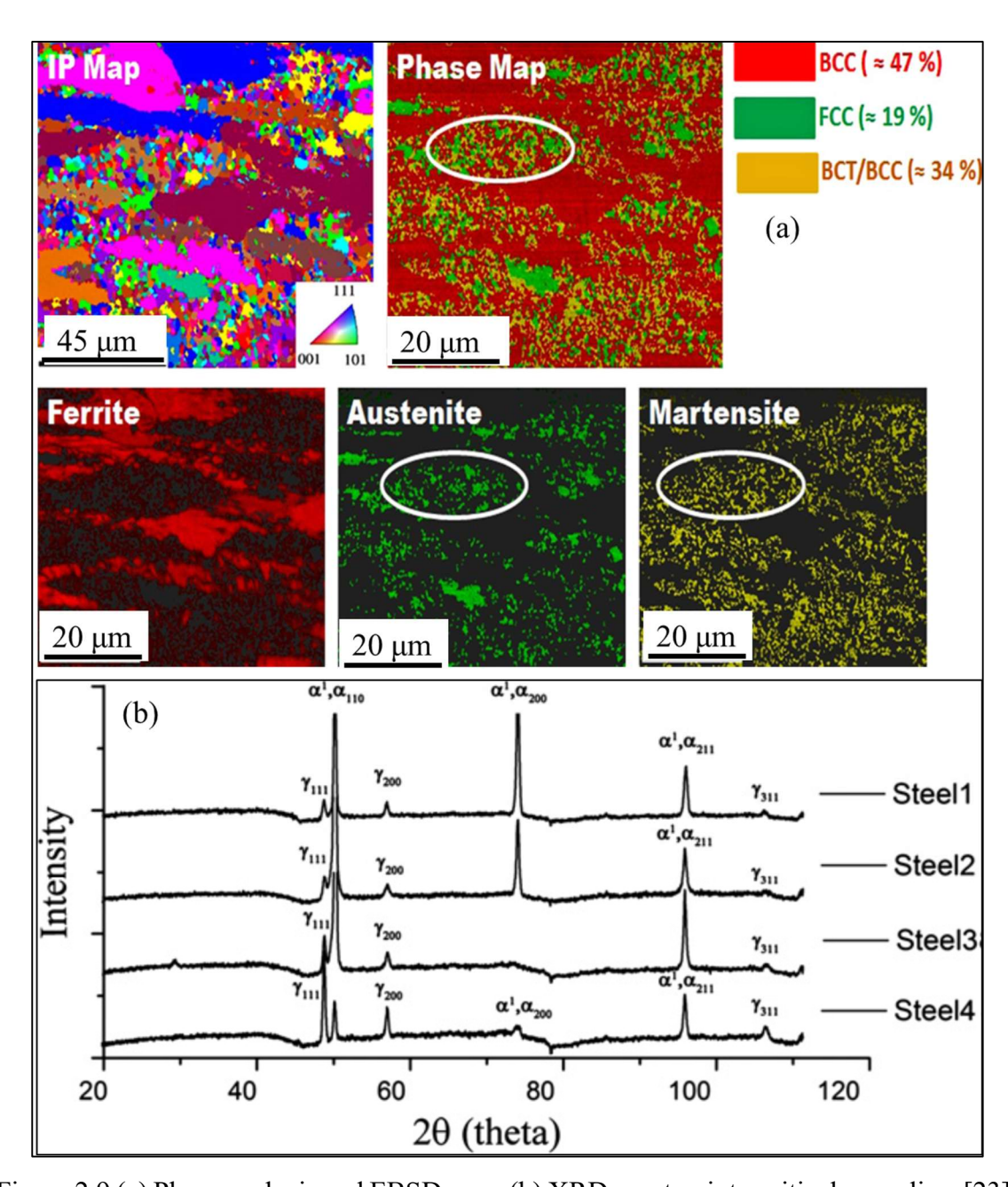


Figure 2.9 (a) Phase analysis and EBSD map, (b) XRD spectra, intercritical annealing [23].

Aydin et al. [23] developed of third-generation Advanced High Strength Steels (AHSS) with medium manganese content, focusing on optimizing heat treatment processes to control the deformation behavior of retained austenite. They examined the relationship between alloy composition, stacking fault energy, and deformation mechanisms, emphasizing the role of manganese and carbon in stabilizing austenite. The study includes

thermodynamic modeling, microstructural characterization, and mechanical testing, revealing that higher manganese levels enhance retained austenite and ductility. The study produces four types of microstructures (ferrite matrix with martensite in austenite islands, resembling TRIP steels) (dual-phase ferrite and retained austenite) with variation in Mn. It finds that carbon enrichment alone is insufficient to stabilize retained austenite in low-Mn steels, and deformation induces austenite transformation. The research highlights the importance of optimizing heat treatment to maximize retained austenite, particularly in high Mn content steels, resulting in a microstructure of ferrite, austenite, and martensite. The study concludes that higher Mn levels lead to increased retained austenite, especially in the highest Mn which has a duplex microstructure with minimal martensite. Figure 2.9 (a) shows EBSD map revealing ferrite, austenite and martensite. The XRD pattern shows retained austenite peak, ferrite and martensite peaks were found overlapped as shown in Figure 2.9 (b).

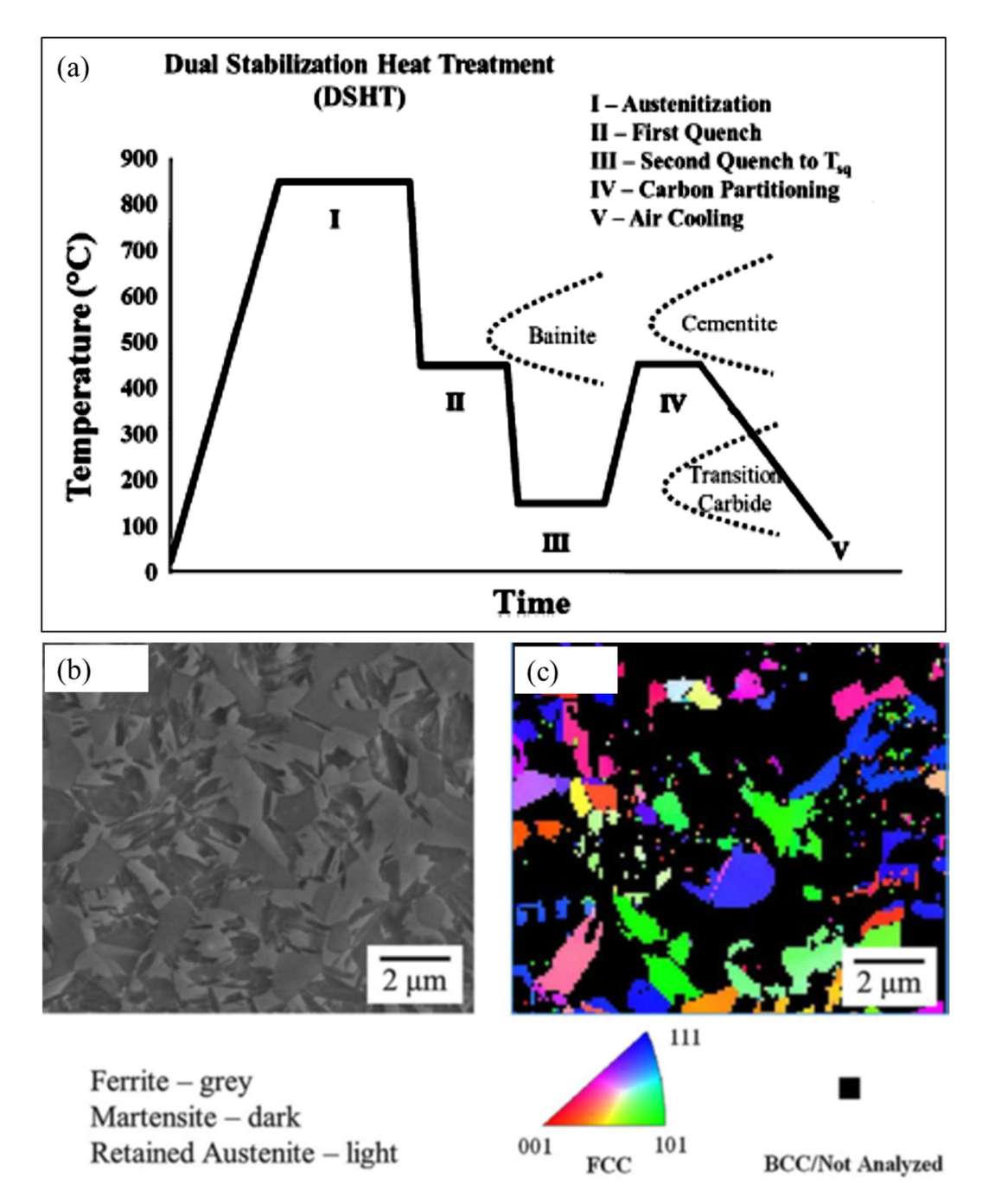


Figure 2.10 (a) A schematic diagram of DSHT and T-T-T curves (b) SEM micrograph after dual stabilization heat treatment, (c) EBSD map of cross section of rolled specimen [45].

Qu et al. [45] produced a third-generation advanced high-strength steel using dual stabilization heat treatment which goes through five-stage thermal processing schedule (involves Austenitization, first quenching, second quenching, carbon partitioning followed by air cooling), with weight percentages of 0.3 wt.% C, 4.0 wt.% Mn, 1.5 wt.% Al, 2.1

wt.% Si, and 0.5 wt.% Cr balance is Fe. They reported tensile strength 1410 MPa to 1650 MPa and elongation 16 % to 22 %. The DSHT cycle is shown in Figure 2.10 (a), Grey region, dark regions and light regions were identified ferrite, martensite and retained austenite respectively as shown in Figure 2.10 (b). The EBSD map for FCC phase was analyzed and shown in Figure 2.10 (c) [45].

2.4.2 Mechanical properties of medium Mn 3G-AHSS steels

The best strength and ductility will be obtained from a three-phases microstructure with refined austenite grains, according to the findings of the mechanical testing. The alloy composition of 0.3C-4.0Mn-2.1Si-1.5Al-0.5Cr, using DSHT method, yielded tensile strengths of up to 1650.0 MPa and overall elongation of about 20 percent [9]. The ultimate tensile strength of Fe-6.15Mn-0.05C-1.5Si (wt.%) steel cold-rolled and annealed at 640°C for three minutes and Fe-6Mn-0.08C-1.5Si-2.0Al-0.08V (wt.%) steel cold-rolled annealed at 740 °C were reported 1100 MPa and 1200 MPa, respectively [46]. Lee et al. reported an ultimate tensile strength of 1144 MPa with an elongation of 65 percent in Fe-10Mn-0.3C-3Al-2Si (wt-%) steel [47]. Medium-Mn steels, with higher yield to tensile strength ratio, are crucial for anti-intrusion automotive part applications due to their higher tensile strength and elongation from 800 MPa -1600 MPa and 10-65% respectively [48], [49], [50]. The critical stress for martensite transformation in medium-manganese Fe-12Mn-0.3C-(2, 3)Al multiphase steel is 887 MPa. The ultimate tensile strength and total elongation of various investigated steels are shown in Figure 2.11.

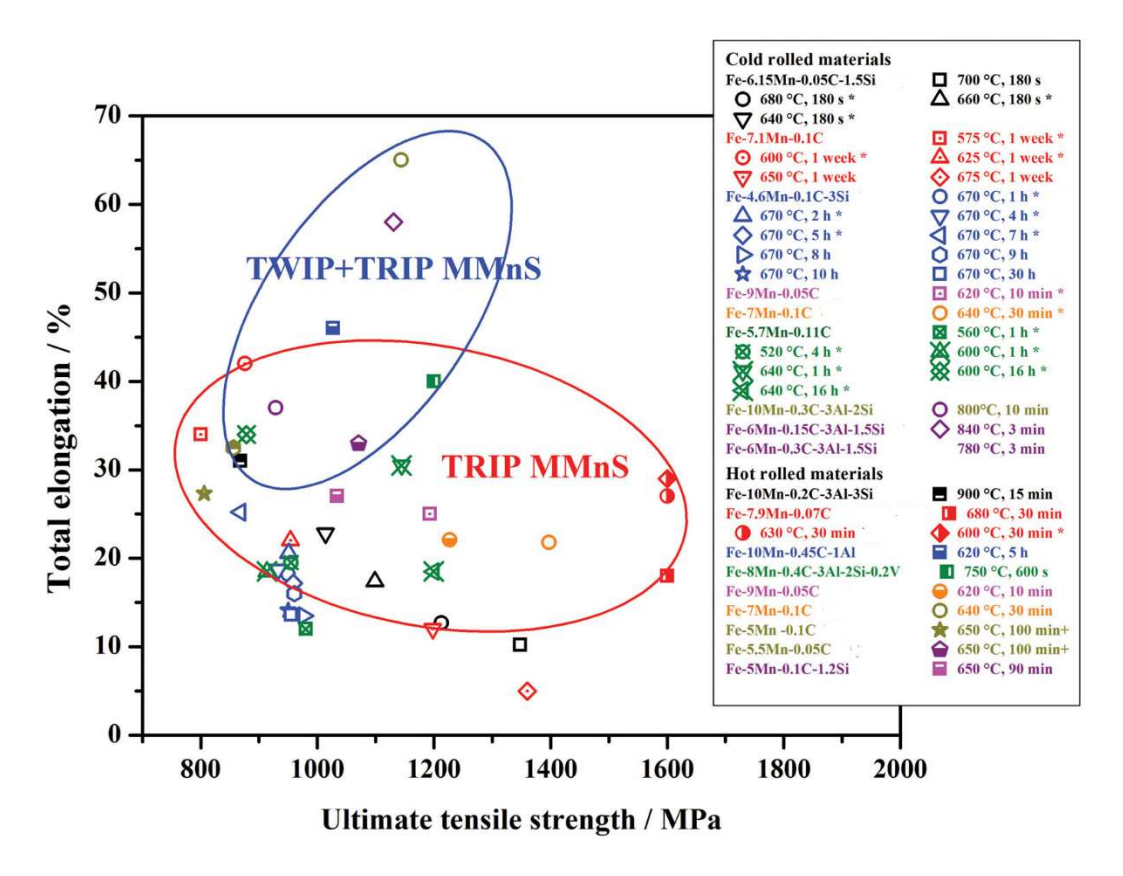


Figure 2.11 Elongation vs. ultimate tensile strength in medium-manganese alloys under different austenite reverted transformation conditions [12].

2.4.3 Transformation induced plasticity (TRIP) Effect

The TRIP effect, or Transformation Induced Plasticity, refers to a mechanism in certain types of steel that enhances their mechanical properties, particularly strength and ductility. This phenomenon occurs in steels that have a microstructure containing retained austenite, which is a phase that can transform into martensite when subjected to stress or strain. TRIP steels typically consist of a mix of phases, including ferrite, bainite, and retained austenite. The retained austenite can stabilize the material's performance under deformation. The TRIP effect leads to improved yield strength and ultimate tensile strength without a significant loss in ductility, making these steels particularly useful in automotive and structural applications [51]. This process requires careful management of retained austenite, enhanced by solute C and fine-tuned to prevent martensite formation during cooling as

shown in Figure 2.12. The formation of grains, shear bands and induced plasticity is shown in Figure 2.13 with variation of manganese [52].

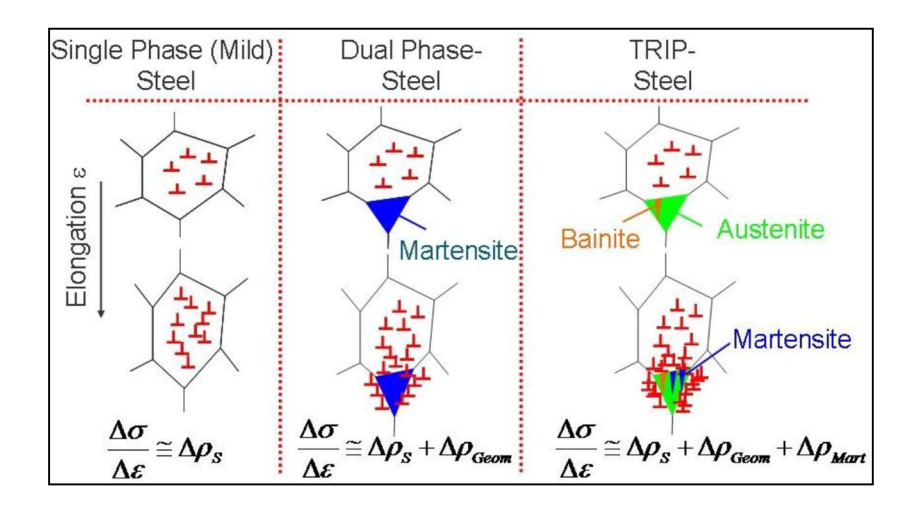


Figure 2.12 Dislocation density in mild steel, dual-phase steel, and TRIP steels [53].

	High	h Mn Mediun		m Mn		
%Mn	>25	22 - 15	12 - 6		7 - 4	
Processing	Conventiona	al annealing	Intercritical annealing Q		Q&P	
Cold rolled	Shear bands	Deformed austenite	Deformed martensite		ite	
Microstructure after annealing	γ		$\gamma + \alpha$			
Plasticity	SBIP	TWIP	TWIP+TRIP	TI	RIP	
γ-ISFE (mJ/m²)	>75	>20	>20	<	10	
γ-stability	γ-composition		γ-composition and size		size	
Role of Mn	γ-stability / SFE		γ-stability / SFE / Hardenability		nability	

Figure 2.13 Mn steels based on percentage added. UFG = ultrafine-grained, SBIP = shear band induced plasticity, TWIP = twining induced plasticity [53].

Kazi M. H. Bhadhon et al. examined the composition of medium-Mn TRIP steel, finding that adding manganese and silicon improves its transformation-induced plasticity resulted in improved mechanical properties. The medium-Mn TRIP steel contains retained austenite, which transforms into martensite during deformation, preventing necking and enhancing work-hardening rates. It is a potential candidate for 3rd-generation AHSS. The

starting microstructure of the steel affects its microstructural evolution during intercritical annealing. The cold rolled (CR) microstructure requires higher temperatures and longer annealing times, while the martensitic (M) microstructure achieves more than 30 % austenite in 3rd generation steel.

Z.J. Xie et al worked with alloy steel of composition Fe-0.26C-2Mn-0.77Si-0.76Al-0.08Nb-1.05Cu-1.02Ni-0.26Mo. The primary findings of the study indicate that low carbon low alloy steel was subjected to a 2-step intercritical heat treatment to produce a multi-phase microstructure containing ferrite, martensite, and residual austenite. (as shown in Figure 2.14 (a, b). The tensile strengths are shown in Figure 2.14 (c). With a uniform elongation of 16.40%, a low yield ratio of 0.32, and a high tensile strength of 1200 MPa, the steel demonstrated outstanding formability and work hardening. These properties are attributed to deformation-induced twin-martensite, with XRD peaks of ferrite and austenite detected in different heat-treated conditions, as shown in Figure 2.14 (d) [54].

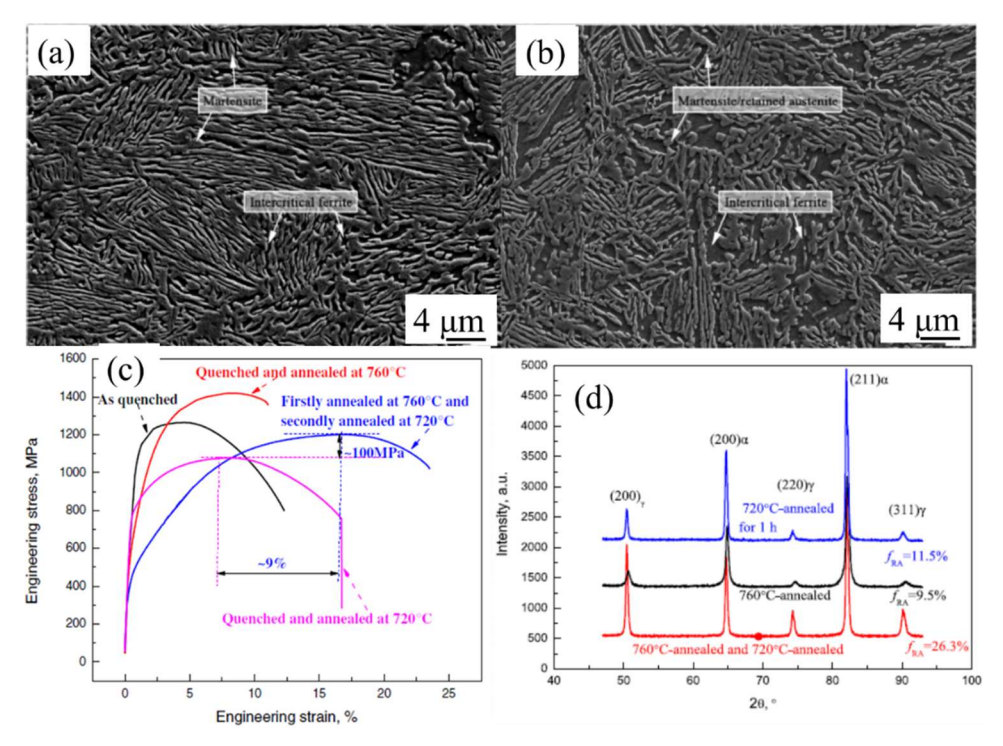


Figure 2.14 SEM micrographs for specimens, (a) Step-I intercritical annealing at 1033 K (b) Step-II intercritical annealing at 993 K (c) Stress-strain curves after heat treatments, (d) XRD patterns for specimens after heat treatments [54].

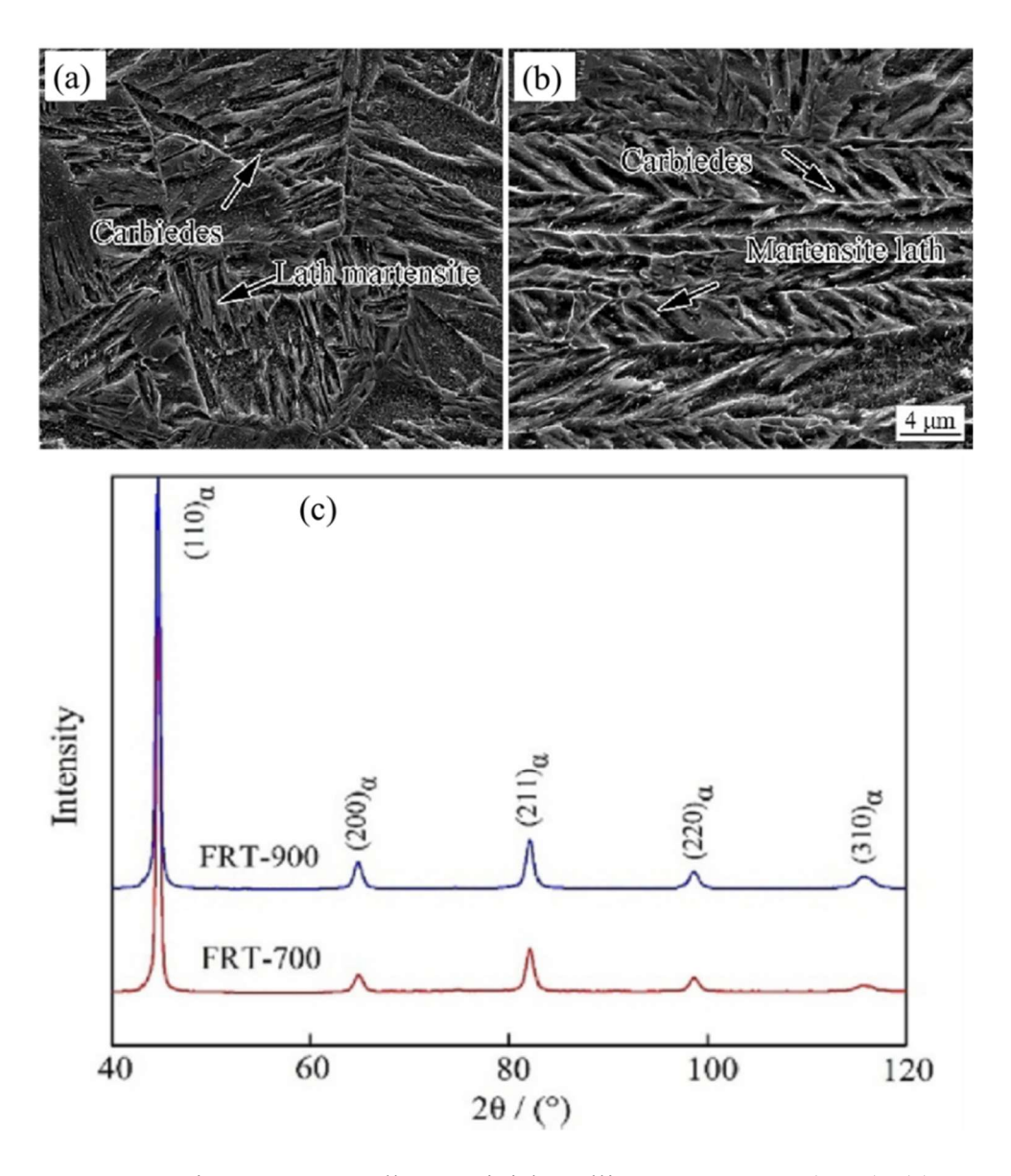


Figure 2.15 SEM microstructures alloy at Finish Rolling temperature (FRT), (a) FRT-700 °C, (b) FRT-900 °C (c) X-ray diffraction patterns of the steels at various finish rolling temperatures, FRT [55].

Ruyang Han et al. [55] examined the application of low-temperature hot rolling on air-cooled medium manganese martensitic steel with composition Fe-0.19C-0.084Si-4.92Mn-0.005S-0.0058P-0.73(Mo + V)-0.0032N, resulting in the refinement of the martensite structure and enhanced dislocation density, V(C, N) precipitation, and more fine Fe₂C carbides as shown in Figure 2.15 (a,b). For steel with a finish rolling temperature (FRT) of

700 °C, the values for the hardness, yield strength, and tensile strength are 482 HB, 1174 MPa, and 1701 MPa, respectively. The yield strength, tensile strength, and Brinell hardness of the FRT700 sample are higher than those of the FRT900 sample; they increase from 973.0 MPa, 1526.0 MPa, and 454.0 HB to 1174.0 MPa, 1701.0 MPa, and 482.0 HB, respectively. The improved microstructure causes the impact energy to rise from 28 to 38 Joules. Ferrite peaks may be seen in the XRD spectra of the FRT900 and FRT700 specimens. The XRD spectra are shown in Figure 2.15 (c) [55].

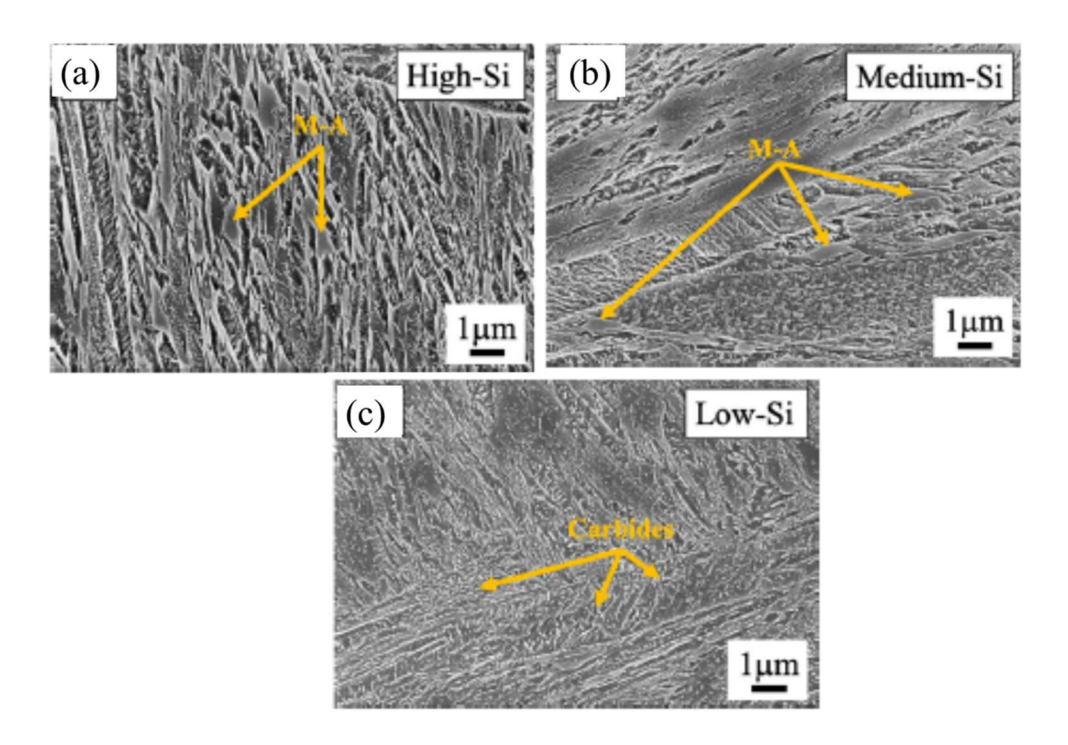


Figure 2.16 SEM microstructures of alloy, (a) high, 1.5 wt.% Si, (b) medium, 0.7 wt.% Si, (c) low, 0.25 wt.% [56].

Sumit Ghosh et al examined, the carbon redistribution, and carbide precipitation of medium C steels alloyed with three levels of silicon using TEM and APT. Characterizations of various carbide forms were obtained from tempering martensite and partial dissolution of C-enriched austenite. The study reveals that High-Si steel forms stable transition carbides, η (Fe₂C), even at high partitioning temperatures as shown in Figure 2.16 (a). Medium (M)-Si steel has partially stable η carbides, while Low -Si steel has coarser cementite precipitates which is shown in Figure 2.16 (b, c). The study also shows C cluster

segregation in martensite lath borders using atom probe tomography (APT). The chemical composition of the steels studied are given in Table 2.3.

Table 2.3. Chemical composition of steels studied (wt.%) [56].

Alloy steel	C	Si	Mn	Al	Cr	Ni
High-Si	0.40	1.50	2	0.025	0.99	0.49
Medium-Si	0.4	0.7	2	0.025	0.99	0.49
Low-Si	0.4	0.25	2	0.025	0.99	0.49

Chengpeng Huang et al. [37] investigated a medium Mn steel with a composition of Fe-10.13Mn-0.39 C-2.05Al-0.26V. The steel was hot-forged into billets after being cast in a vacuum induction melting furnace. The steel was homogenized, and then hot-rolled 2 mm. The warm rolling (WR) strips underwent intercritical annealing at 620°C for five hours. The equilibrium phase fraction of steel was determined using Thermo-Calc software. The upper critical temperature was 730°C, with ferrite and austenite fractions equal at 620°C.

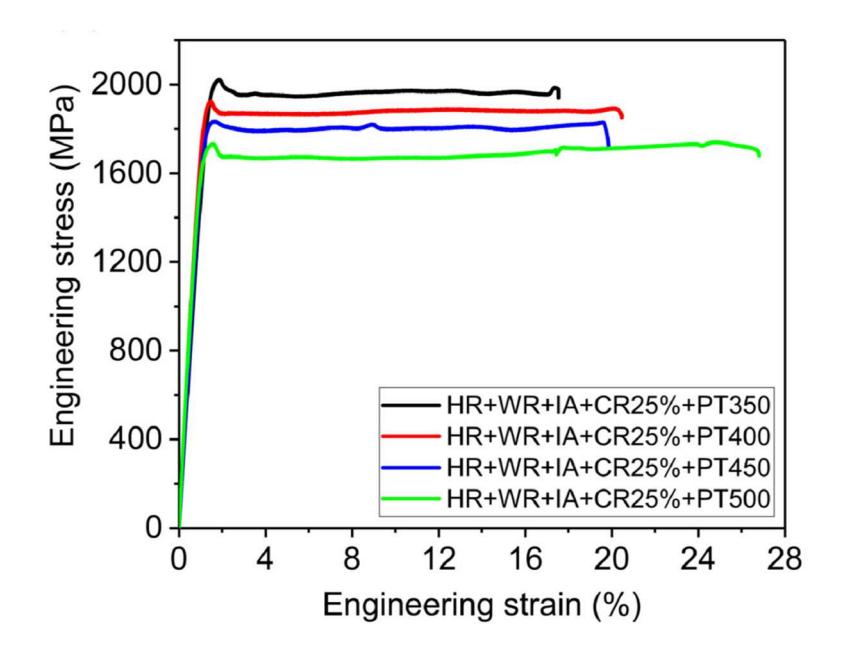


Figure 2.17 (a) Stress-strain curves of the hot rolled (HR), Warm Rolled (WR), intercritical annealing (IA), 25 % cold rolled (CR), and partitioned at different temperatures, 623 K, 673 K, 723 K, and 773 K, respectively [37].

The yield strength decreases from 2020 MPa to 1730 MPa, while total elongation improves from 17.5% to 26.8% when the partitioning temperature is raised from 350°C to 500°C. the tensile strengths are shown in Figure 2.17 [37].

Minal Shah et al. produced lab-produced bainitic steel without carbides using air cooling, optimizing alloying elements through thermodynamic and kinetic calculations, and achieving an ultrafine microstructure with austenite and martensite [57]. Carbon moved to retained austenite after being partitioned during phase change. Compared to the retained austenite of alloy B, the retained austenite of alloy A had less carbon. As a result, austenite was less stable for the alloy A. Alloy A possessed more strength and hardness than alloy B due to its inclusion of fine-scale bainitic lath. The UTS were measured 1348 MPa and 1160 MPa and elongations 15 % and 22 % for alloy A and Alloy B respectively. The solid solution strengthening components in bainite and alloy composition is provided in Table 2.4.

Table 2.4 Solid solution strengthening components in bainite and alloy composition [58].

Elements	Strength contribution (MPa) Elements in (wt.%)	A, wt.%	B, wt.%
С	$(C)^{1/2} \times 1722.5$	0.15	0.15
V	$V \times 9$		
Mn	$Mn \times 32$	0.54	1.6
Si	Si × 85	1.5	2.0
В		0.004	0.004
Cr	$Cr \times -30$	3	0.6
Mo	$Mo \times 30$	0.3	0.25
P		0.020	0.014
S		0.025	0.016
N		0.02	0.02

M. Emami et al. studied the impact of austenite revert transformation and hot rolling at 1100 °C on the mechanical properties of manganese steels with low carbon and/or boron

content. They found martensite, retained austenite, bainite, and precipitates in the microstructures, with Fe(B) and Fe(C) alloys show low stacking fault energy (SFE) leading to increase in strength and ductility. The strength of these alloys is attributed to their high martensitic phase fraction, resulting in 760 and 1100 MPa, respectively, and increased austenite content. The process map and ultimate tensile strengths are shown in Figure 2.18 [59].

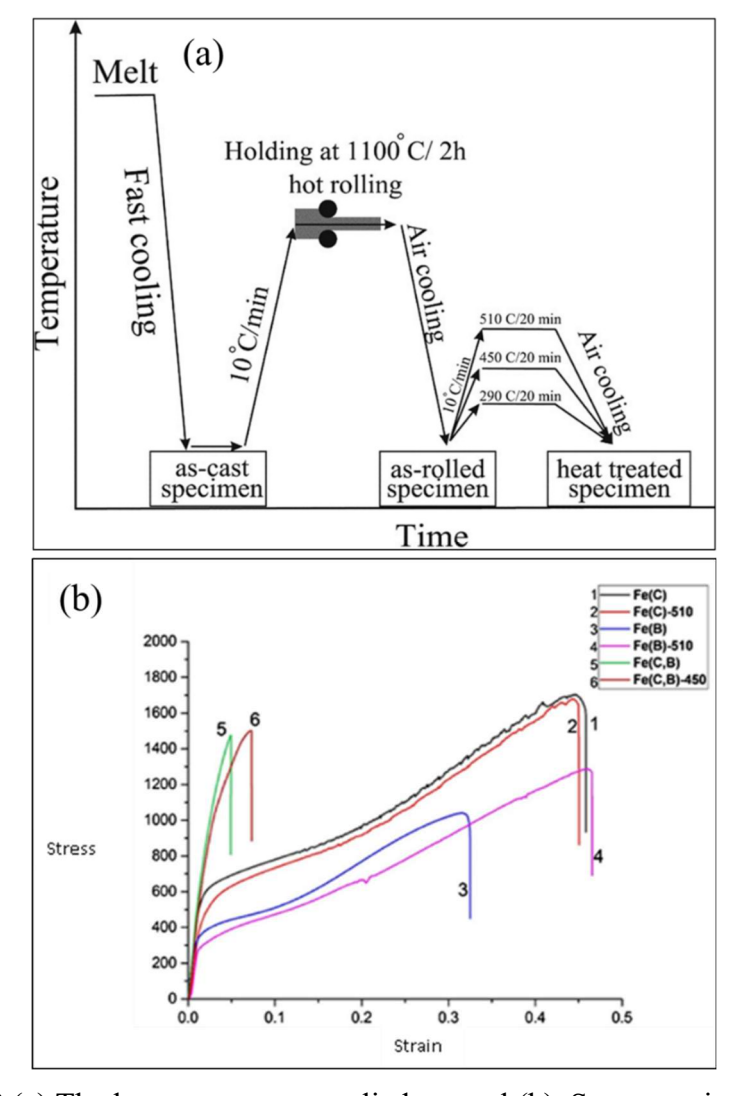


Figure 2.18 (a) The heat treatments applied to steel (b). Stress-strain curves [59].

In Figure 2.18, The diffusional transformations of Fe-4Mn-0.1C steel exhibit a parabolic curve above 342 °C, with rapid transformation below 450 °C bainitic transformation below 450 °C, and ferrite transformation above 480 °C [60]. The phase diagram of Fe-4Mn-0.1

C calculated using Thermo-Calc software was compared with the equilibrium phase diagram of plain carbon steels, austenite single phase region expands. Hot-rolled steel exhibits high strength and ductility, with no retained austenite detected [61].

2.5 Nano-scale characterization of medium Mn steels

Atom probe tomography (APT) is a high-resolution analytical technique used to investigate the three-dimensional composition of materials at the atomic level. APT samples are typically prepared as sharp tips (often less than 100 nm in diameter) using techniques like focused ion beam milling. Field Evaporation is performed in the APT apparatus, a high electric field is applied to the tip, causing individual atoms to be evaporated from the surface of the sample. These atoms are ionized as they leave the tip. The evaporated ions are accelerated towards a detector, where they are counted and analysed. The time of flight (TOF) of the ions provides information about their mass-to-charge ratio, allowing for compositional analysis. The data collected allows for the reconstruction of a three-dimensional atomic map of the sample, revealing information about its composition. Its high spatial resolution makes it a powerful technique for understanding materials' properties and behaviors.

Yan Ma et al. [12] examined medium-Mn low-carbon steel with a chemical composition of Fe-11.7Mn-2.9Al-0.064C (wt. percent). The study showed that carbon segregation at ferrite-austenite phase boundaries was significantly influenced by cooling conditions, with water-quenched (WQ) samples showing no carbon segregation, while air cooling (AC) caused a significant carbon spike, while other microstructural features remained unchanged. The two regions of interest (ROI) are chosen for analysis in two different conditions of water quenching and air cooling which are shown in Figure 2.19 (c-f). Three-dimensional atom probe maps for carbon and manganese are shown in Figure 2.19 (a, b). Figure 2.19 (c, e) shows the distribution of carbon, manganese, and aluminum in the vicinity of the ferrite-austenite phase boundary. The two-dimensional concentration map is presented in Figure 2.19 (d. f). The phase boundary is marked by an 11.0 at.% manganese iso-concentration surface. Atom probe tomography (APT) was used to characterize the elemental distribution across phase barriers at nearly atomic scales. An 11 atom percent

Mn iso-concentration surface served as the phase boundary, and the proximity histogram method was used to display the carbon concentration profile as shown in Figure 2.19 [62]. The properties of complex steels depend on the partitioning that occurs at their phase boundaries.

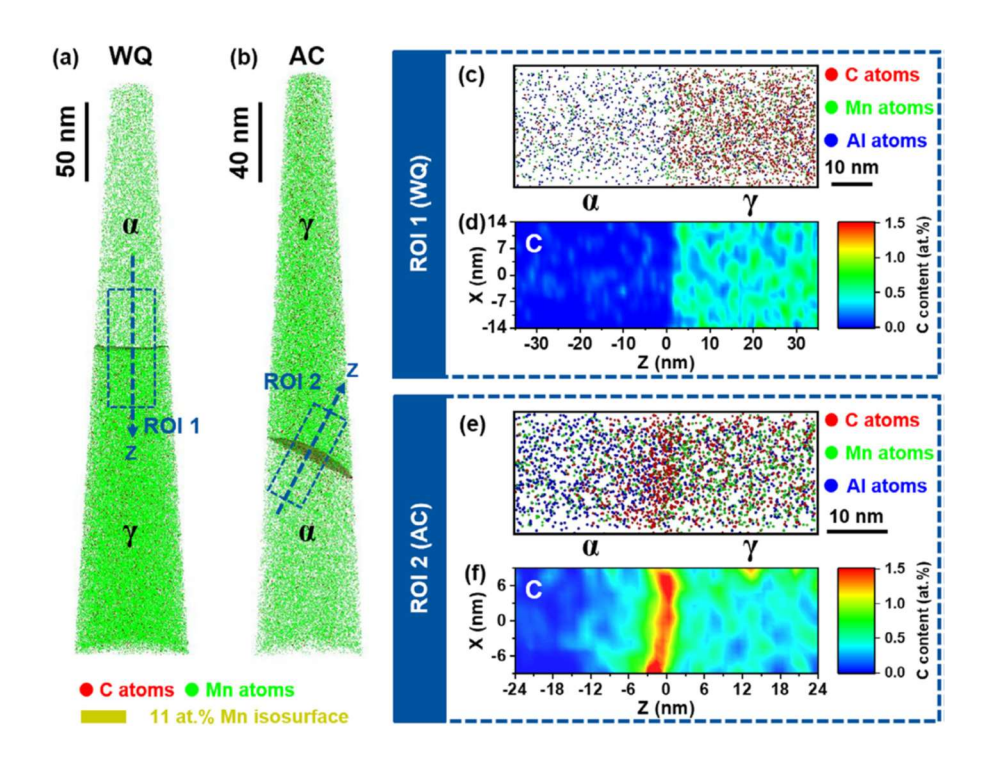


Figure 2.19 3D atom probe tomography maps of carbon and manganese in (a) water-quenched (WQ), (b) air-cooled (AC), (c) distribution of C, Mn and Al atoms in ROI 1, (d) 2-dimensional concentration maps of carbon in the ROI, (e) distribution of C, Mn and Al atoms in ROI 2, and (f) 2-dimensional concentration maps of carbon in the ROI 2 [62].

Dmitrieva O. et al. presented atom probe tomography results in precipitation-hardened maraging-TRIP steel 12.2Mn-1.9Ni-0.6Mo-1.2Ti-0.3Al (at.%) across the martensite/austenite interfaces. At phase boundaries, compositional changes are revealed by the system. The retained austenite, which was already present in the as-quenched condition before aging, is plotted in red in Figure 2.20 (a), which is an EBSD image. The cubic martensite is plotted in green. Figure 2.20 (b) displays a TEM micrograph of austenite that is precipitate-free and martensite that contains precipitates. -An APT replica

with both austenitic and martensitic zones may be seen in Figure 2.20 (c). Mn atoms are displayed in blue, while Ni atoms are in cyan. The iso-surfaces in yellow show 18 at.% Mn. The magnified image of atom probe tomography is shown in Figure 2.20 (d), which represents martensite and austenite. The atomic map of iso-concentration surfaces for manganese atoms (blue color) at 18.0 at.% (yellow colour) can be seen in Figure 2.20 (e). Figure 2.20 (f) displays the segregation of Mn in layers 1 and 2 [63].

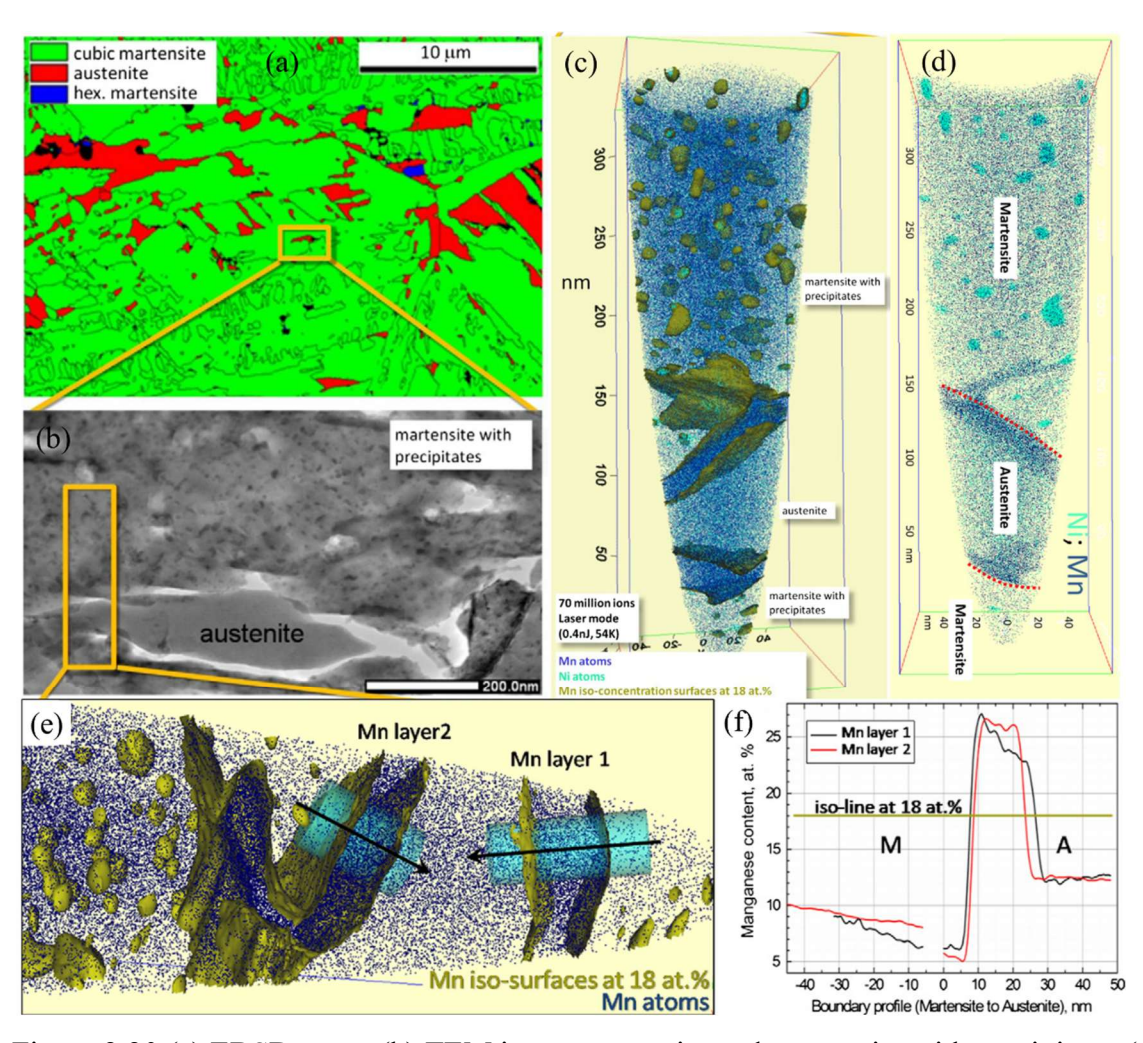


Figure 2.20 (a) EBSD map, (b) TEM image, austenite and martensite with precipitate, (c) atom probe tomography (APT), (d) magnified 3D image of APT, (e) Atomic map isoconcentration surfaces for Mn atoms (blue colour), at 18.0 at.% (yellow colour), and (f) variation of Mn across martensite to austenite phase boundary [63].

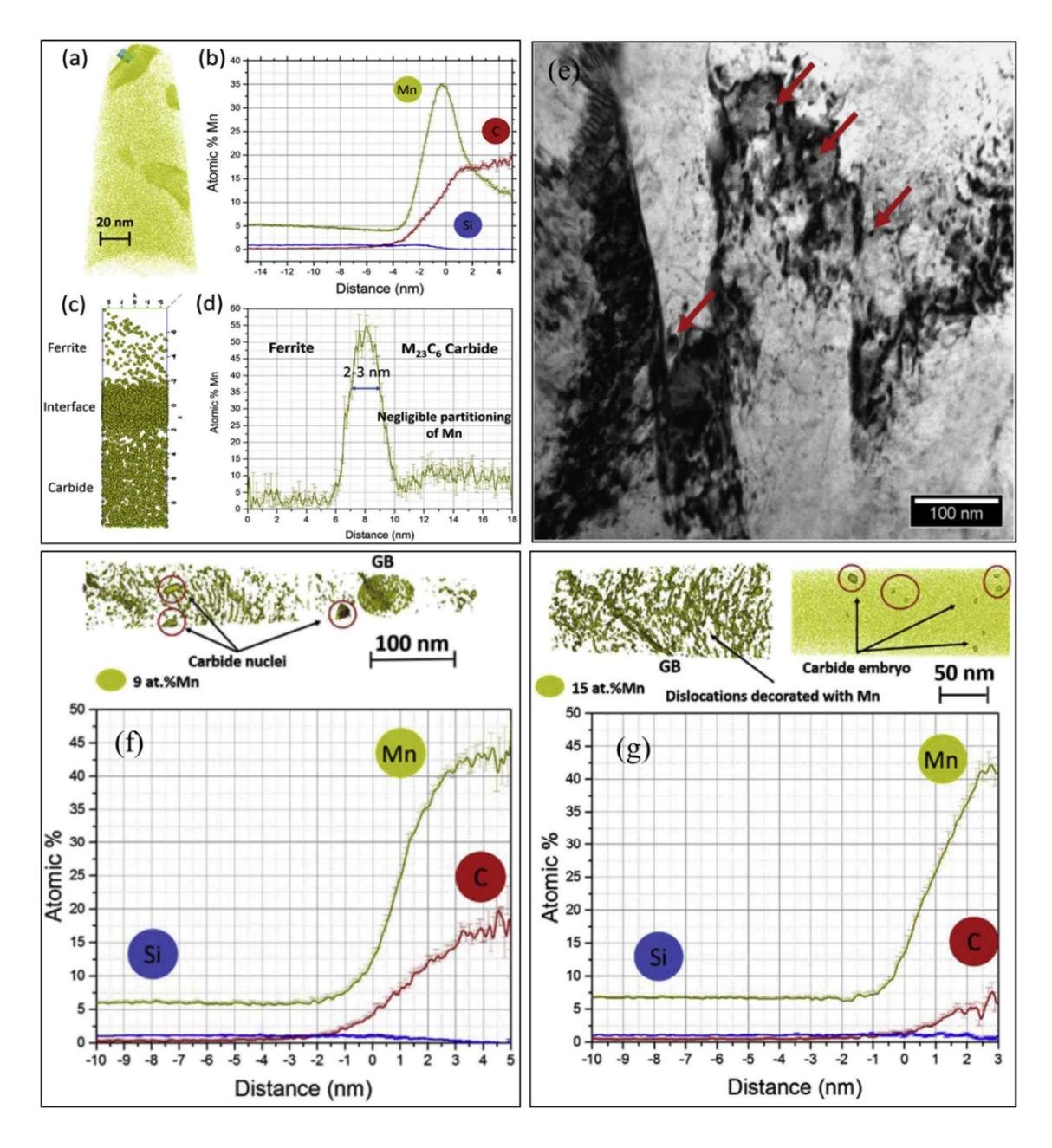


Figure 2.21 Atom probe tomography analysis of Fe-7Mn-0.5Si-0.1C (wt.%) steel, tempered at 450 °C, for 6 hours (a-e) and 1 hour (f-g), (a) reconstruction of APT, (b) Proxigram of carbides seen in Figures (a, c, d); (c) Mn atoms are displayed; (d) concentration at the interface. (e) TEM image in bright field mode; (f) Proxigram of the carbides with a similar composition to M23C6. (g) Proxigram of carbides with a lower carbon (C) concentration [64].

A. Kwiatkowski da Silva et al. investigated a 30 kg ingot of medium manganese Fe-7Mn-0.1C-0.5Si steel casting, homogenized for 12 hours at 1150 °C, and hot-rolled to a 5.5-mm-thick plate. The material showed a martensitic microstructure without retained austenite. The hot-rolled plate was cold-rolled to 2.0-mm-thick sheets and annealed to follow carbide precipitation and austenite reversion kinetics.

The cold deformation was given up to 55%. The tempering was performed at 450 °C for 1 hour and 6 hours. Figure 2.21 (a) shows the reconstruction of APT data. The proxigram (concentration profile) of carbides is observed in Figure 2.21 (b, c, d). The Mn atoms are displayed in Figure 2.21 (c). The concentration profile is observed in Figure 2.21 (d), which represents negligible partitioning of Mn inside the carbide. The arrows indicate precipitation on dislocation and grain boundaries in the transmission electron micrograph (TEM) in bright field imaging mode. The proxigrams of the carbides with a similar composition to M₂₃C₆ and carbides with lower carbon (C) concentrations are shown in Figure 2.21 (f, g). The material's microstructure is typical of martensitic steel that has been cold-rolled. We observe that around grain boundaries and dislocations, very tiny precipitates (<20 nm) are formed. The precipitation areas correspond with those noted by APT. These precipitates were so tiny that crystallographic information could not be obtained from them. This has already seen the segregation of C and Mn at grain boundaries and dislocations at this stage of tempering. The 9 at.% Mn yellow iso-composition surfaces in Figures 2.21 (f) and (g) highlight the Mn segregation. The material's microstructure is typical of martensitic steel that has been cold-rolled. We observe that around grain boundaries and dislocations, very tiny precipitates (<20 nm) are formed. The precipitation areas correspond with those noted by APT. These precipitates were so tiny that crystallographic information could not be obtained from them [64].

2.6 Present status of research in the field of AHSS.

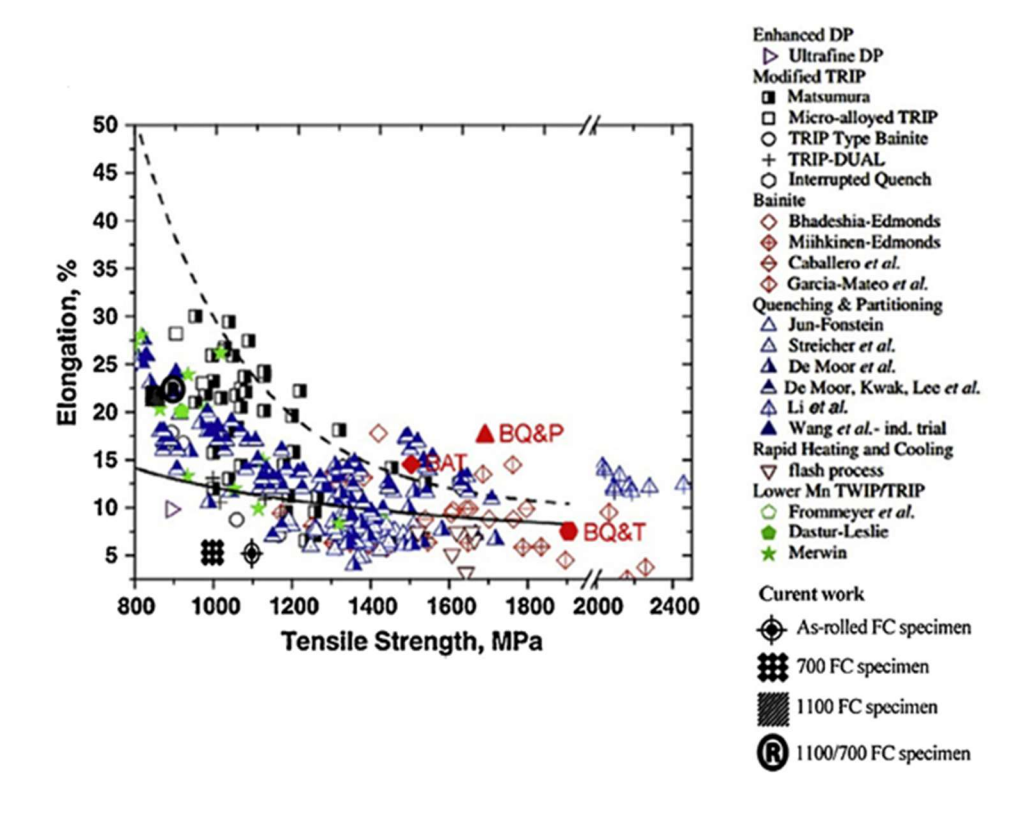


Figure 2.22 Tensile strength- total elongation different steels [65].

The present status of research by various researcher is shown in Figure 2.22. The tensile strengths and elongations are presented in Figure 2.22.

2.7 Research gaps

Based on the literature survey mentioned above, we have identified following research gaps:

- Medium manganese (3-12%) and silicon steels are not yet commercialized and these steels are under development,
- Austempering and ausforming of medium Mn steels is very little investigated,
- Inter-critical annealing of 3rd generation AHSS is less reported,
- Multi-step austempering and inter-critical annealing is reported very less,
- Nanoscale characterization is very rarely reported,
- High strain rate tests for the evaluation of mechanical properties are area of future research almost not been reported.

2.8 Objectives

Based on the literature, the following objectives are defined:

- (i) To study the effect of Mn concentration (4-8 wt.%) and Si (1-2 wt.%) on the microstructure and mechanical properties of thus formed steel,
- (ii) To study the effect of thermo-mechanical treatment at 900 °C and 1100 °C on microstructure and mechanical properties,
- (iii) Nano-scale characterization to study the carbon redistribution in the complex phase microstructure developed.

Chapter 3 Research Methodology

3.1 Research design

The property simulation (JMatPro) software of version 9.0 was used to explore the new steel alloys. The hypothetical compositions were used in the software and the respective continuous cooling transformation (CCT) and time-temperature-transformation (TTT) curves were developed. The stress-strain curves were also developed with the help of the software. The tensile strength and the total elongation were predicted by using properties simulation software. After exploring many alloys with the addition of manganese and silicon we identified a few theoretical steels that possess the mechanical properties which are required for automotive industries. Once the ductility, tensile strength and hardness are matched to the current requirements of the automotive industries and Based on optimized compositions, it was planned to develop the 5 steels alloyed with manganese and silicon which are expected to be among the 3rd Generation advanced high-strength steels. Before developing the actual designed steels, the viability study to develop manganese and highsilicon steel was performed. Based on some preliminary experimental microstructural characterization, it was observed that cracks and segregation increase by the addition of silicon excess of 2 wt.%. Hence, we limited Si additions up to 2 wt.%. It was found in the literature that automotive industries are striving for medium-manganese (3-12 wt.%) steels with high strength and optimum ductility (12-18 % in the present work). The theoretical steels are thought to be added with silicon and manganese as principal alloying elements. Five steels were developed experimentally. Out of five steels, three steels were developed in variation of Mn (4-8 wt.%) and another three steels were developed in variation of Si (1-2 wt.%). It is to note that Alloy 2 was common in both of sets of Mn and Si varying steels. The thermodynamic study of these steels was performed to determine phase diagrams and path of solidification which are described in Chapter 4 with the help of the Thermo-Calc software (version 2023b).

3.2 Materials and methods

Alloying elements (99.99%) were procured from the local supplier. Silicon was in the powder form and other alloying additions (Mn, Fe, C, Cr, Ti, Al, S, P) were in the granule form. Silicon and Manganese, Iron, Chromium Nickel and other alloying additions are weighed in certain proportions as given in the composition table (Table 4.2). The silicon specimens were compacted with hydraulic press. The weight of each sample was 20 grams. After weighing the elements, all these elements were charged into the vacuum arc furnace for melting purposes. The vacuum arc furnace consists of a diffusion pump and a rotary pump. Rotary pump can maintain a vacuum level in the order of 10⁻³ millibar in the melting chamber. And the other pump can maintain the vacuum in the order of 10⁻⁶ mbar in the melting chamber. After charging all the elements in the hemispherical slot of 15 mm diameter and 10 mm depth of the heart of the vacuum chamber of the furnace, the melting chamber was maintained at a vacuum level of 10⁻⁶ mbar. After achieving vacuum, the vacuum was relieved by purging argon gas (99.99%) into the chamber and the pressure level of -0.5 mbar was maintained for melting. The plasma arc was generated and the initial current of 40-50 amperes was used for melting of charged elements while the terminal melting was carried out at 170-180 amperes of current. The melting of the alloy specimens was repeated five times to ensure the homogeneity in the bulk of the samples. The vacuum melting furnace is shown in Figure 3.1.

Two types of samples were cast in the copper heart, one type was the button sample, and the other type was in the form of the finger. The five compositions of the novel alloys are developed in a vacuum arc furnace. After casting the spectrometer was used for analysis of all newly developed alloys was carried out to know the composition.



Figure 3.1 Experimental setup of vacuum arc melting furnace.

3.3 Homogenization Heat treatment

Heat treatments were performed for the homogenization of the proposed alloys (as shown in Table 4.2) followed by the furnace cooling treatment. A tubular furnace with argon rich environment was used for the homogenization of alloys at different temperatures and different times as shown in Table 3.1. The homogenization treatment performed at 1200 °C and holding for 4 hours produced optimal results.

Table 3.1 Parameter of homogenization heat treatment cycles applied for homogenization of bulk.

Heating Cycles	Temperature (°C)	Heating Time for target temperature (hrs)	Holding Time (hrs)	Cooling Time (hrs)	Results
Cycle 1	1100	3	2	12-15	×
Cycle 2	1200	3	1	12-15	×

Cycle 3	1200	3	3	12-15	×
Cycle 4	1100	3	2	12-15	×
Cycle 1	1200	3	5		
Cycle 5	1200	3	4	12-15	$\sqrt{}$

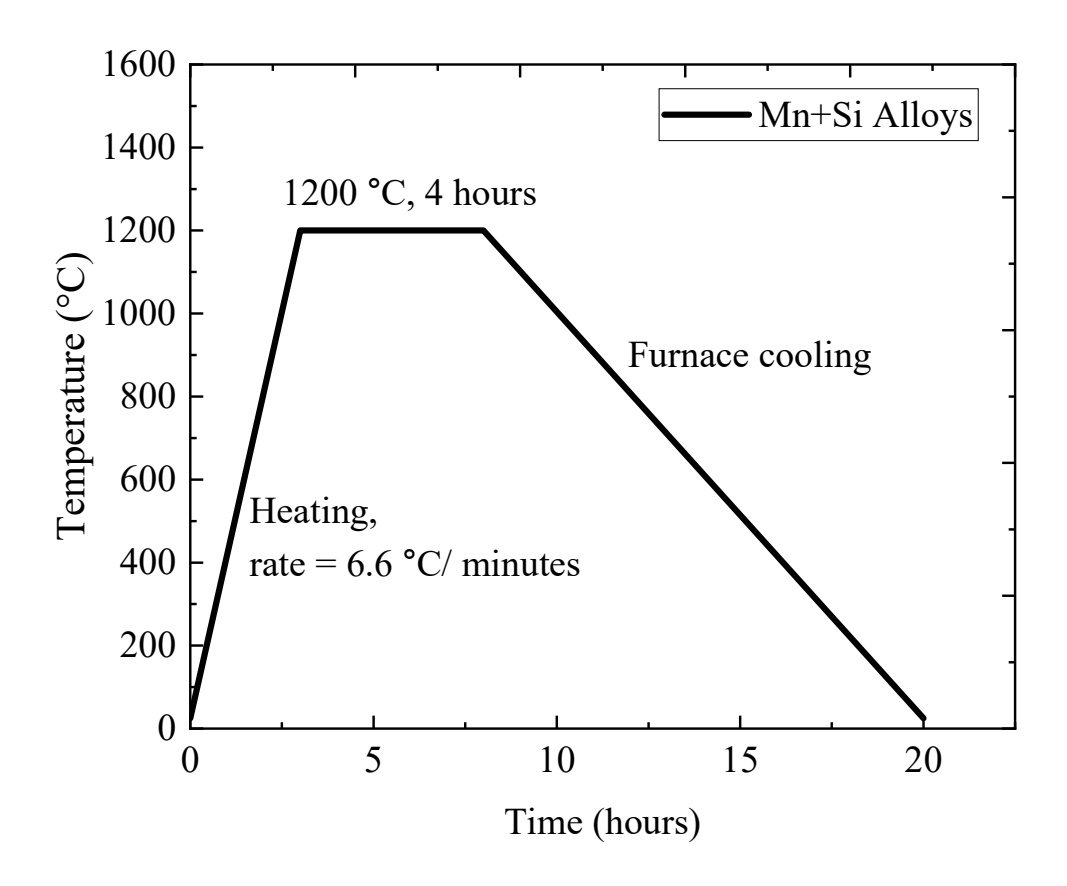


Figure 3.2 The homogenization heat treatment cycle (Cycle 5)

The five homogenization heat treatment cycles were applied to optimize homogenization of the developed novel alloys are shown in Table 3.1. The heat treatment cycle 5 has given good results so we have chosen heat treatment cycle 5 for homogenization of the novel advanced high-strength steels as shown in Figure 3.2. The alloy specimens were heated at 1200 °C and held for 4 hours followed by furnace cooling for 15 hours.

3.4 Thermomechanical treatments

The homogenized alloy steels were subjected to hot rolling in a laboratory-scale rolling mill (shown in Figure 3.3) at different coiling temperatures. One objective of the rolling was to reduce the initial ingot thickness to near net thickness of the sheet used in manufacturing automotive in vehicles in automotive industries. The other objectives of rolling were to refine the microstructure and to develop appropriate complex phases in the steels. The rolling operations were performed using the parameter given in Table 3.2. The temperatures of specimens were measured before and after roll bite with the help of Metravi PRO 65 Max+ Non-contact Infrared Thermometer/Pyrometer.

Table 3.2 Parameter of rolling operation to manufacture alloy steel sheets.

Rolling	Temperature (°C)	Holding Time (min.)	Initial width (mm)	Final width (mm)	Reduction (%)	No. of passes	Rolling Speed (RPM)
Stage-I	1100	20	10.6	2.27	78	8	13
Stage- II	1100	20	2.27	1.68	26	5	13
Stage-I	900	20	10.6	2.27	78	8	13
Stage- II	900	20	2.27	1.68	26	5	13





Figure 3.3 Lab scale rolling mill and muffle furnace for thermomechanical treatment

The temperatures of specimen were measured at the time of entry and exit of rolling mill. The variation of temperature during hot rolling of developed alloy steels in open atmosphere are shown in Table 3.3.

Table 3.3 Temperature variations during the rolling process.

	Rolling temperature (°C)						
Pass	Furnace	Temp. Before	Temp. after one	Temp. drop in			
No	temperature	rolling	pass	pass			
1	1100	1000	800	200			
2	1100	982	790	192			
3	1100	906	685	221			
4	1100	852	650	202			
5	1100	950	780	170			
6	1100	942	746	196			
7	1100	846	682	164			
8	1100	882	672	210			
9	1100	945	741	204			
	Avg	923	727	195			

3.5 Characterizations

Structural characterization was performed using scanning electron microscope (SEM), field emission scanning electron microscope (FE-SEM), X-Ray diffraction (XRD) and optical microscope. Nano-scale characterization was performed using atom probe tomography (APT). The mechanical properties were determine using a universal testing machine and microhardness tester. The details of equipment and operating parameter are described below.

3.5.1 Optical microscopic examinations

The specimens were machined in $10 \text{ mm} \times 10 \text{ mm}$ dimensions. Thereafter the specimens were polished with successive emery papers from 200 to 2000 grits followed by cloth polishing with alumina suspension (0.3 μ m). After polishing the specimens were etched with 2 % Nital. The etching time is shown in Table 3.4. The etching time increases from 15 seconds to 40 seconds with increase in Mn content from 4 to 8 wt.%. The etching was

delayed for Alloy 4 and Alloy 5 also due to higher Si contents. The optical micrographs were analyzed under the Leica microscope in bright field imaging mode.

Table 3.4 Etching parameter for newly developed AHSS.

Elements/ samples	Etching time (seconds)	Etchant
Alloy 1_Fe4Mn1.5Si	15	
Alloy 2_Fe6Mn1.5Si	30	2% Nital
Alloy 3_Fe8Mn1.5Si	40	(2% Nitric Acid+ ethyl alcohol)
Alloy 4_Fe6Mn1Si	50	(270 Titale Field) ethyl diconoly
Alloy 5_Fe6Mn2Si	60	

3.5.2 Field Emission Scanning Electron Microscopy (FESEM)

A carl Zeiss JSM 7610F PLUS, FE-SEM coupled with an energy dispersive spectrometer was used for microstructural observations and composition analysis. The volume fractions of different phases in the microstructure were evaluated from SEM images using ASTM E 562-point count method.

3.5.3 X-Ray Diffraction (XRD)

A phase analysis of advanced high strength steel (AHSS) was done using X-ray diffractogram analysis. XRD measurements were carried out in a Brukers D8 Focus X-ray diffractometer operated at 40 KV with Cu K_{α} (λ = 1.54056 Å). The alloy samples were scanned from 20° to 100° with scan rate 0.5 deg/min. The XRD peaks were identified using PCPDF Win database and x-pert high score software.

3.5.4 Microhardness measurements

The microhardness values were measured for all newly developed alloys. The measurements were taken in homogenized and hot rolled and air-cooled conditions. The specimens prepared for metallography observations are used for microhardness measurements. The tests were performed as per ASTM E 384-17 standard. The microhardness tester of Zwick/Roell of model ZHV μ (load: 300 gf, dwell time: 10 seconds) was used for all measurements of hardness values in various conditions.

3.5.5 Tensile Testing:

The rolled sheet samples of Alloys 1, Alloys 2, Alloys 3, Alloys 4 and Alloys 5 (Table 4.2) were machined to obtain substandard tensile samples according to ASTM E8, ISO 6892-I with gauge length of 20 mm for tensile testing. The strain rate was used 1×10^{-2} s⁻¹. The schematic diagram of substandard samples used for tensile testing are shown in Figure 3.4. The actual machined substandard samples of alloys are shown in Figure 3.5. The uniaxial tensile tests were carried out using universal testing machines (Zwick/Roell, UTM Z010).

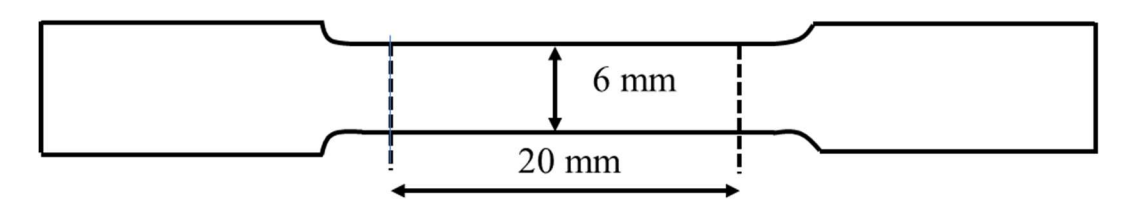


Figure 3.4 Schematic of tension test specimen machined as per ASTM E8, (substandard specimen)



Figure 3.5 Actual tensile test specimen machined from hot rolled and air-cooled sheet of five compositions using CNC machine.

3.5.6 Atom probe tomography (APT)

Atom probe tomography (APT) was used to characterize the elemental distribution across phase barriers at nearly atomic scales. A Local Electrode Atom Probe (LEAP-5000 XR, Cameca Inc.) apparatus with an ultraviolet laser (wavelength 355 nm) operating in laser-pulsing mode was used for the measurements. The analyzing chamber's base temperature was maintained steady at 60 K. The pulse frequency and energy of the laser were 200 kHz and 30 pJ, respectively. The dual-beam Helios G4 UX with focused ion beam was utilized to prepare the APT samples. The software AP-suite (IVAS 6.3) was used for the analysis of the APT data [63], [64], [66].

3.6 Process flow chart of the research methodology

The process flow chart of development, synthesis and characterization techniques utilized are as follows:

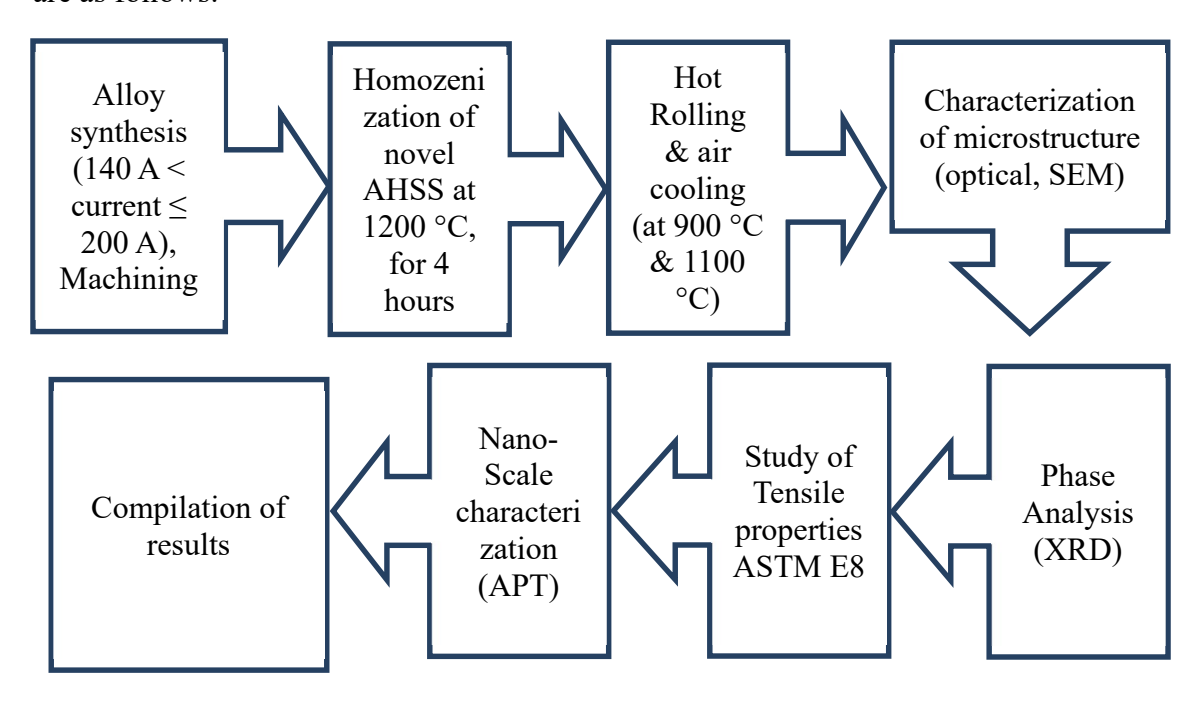


Figure 3.6: Process flow chart with experimental conditions.

Chapter 4

Alloy Design and Development

4.1 Introduction

The alloys are designed using simulation softwares. The phases formed in a particular composition can be predicted using Thermo-Calc software which works based on thermodynamic data. The properties of various compositions can be simulated using property simulation software and CCT and TTT diagrams can be developed. The simulation data can be used to develop alloys experimentally.

In the present chapter, novel advanced high-strength steels have been designed using materials properties simulated data which is generated by materials property simulation software (JMatPro). This software works on thermodynamic data and avoids regression problems. Its calculations are based on physical principles instead of purely statistical methods. This is also viable to relate the material models that have been created for the prediction of microstructure using microstructurally sensitive variables.

Unlike other software, it calculates wide range of materials properties for alloys and is particularly aimed multi component alloys used for industrial practices. Mechanical properties, solidification behavior, phase transformations and chemical properties can be calculated using materials properties simulation software. It includes Java-based user interface with calculation modules and will under any windows operating system. Various compositions were explored and based on simulation results and predicted phase transformations and mechanical properties, some compositions were selected to be developed experimentally. Hence, five compositions are developed using vacuum arc melting furnace with variations in manganese and silicon while the Mn was kept in medium Mn range (3-12 wt.%). The alloys thus developed are characterized, and the results are presented in this chapter. The observations are in good agreement with predictions made by materials properties simulation software. The phase diagrams were developed using Thermo-Calc software. Solidification paths were predicted using scheil model in Thermo-Calc software.

The automotive industries are striving for materials which can replace the existing materials used in automotive industries. Various computer softwares are used to model and simulate the properties materials based on thermodynamics and physical properties [67]. Researchers have applied the characteristics of the individual constituents and related the microstructure to the mechanical properties of the alloys employing the software to estimate the ultimate properties of the alloys [68], [69].

4.2 Alloy design

4.2.1 Alloy Phase diagrams

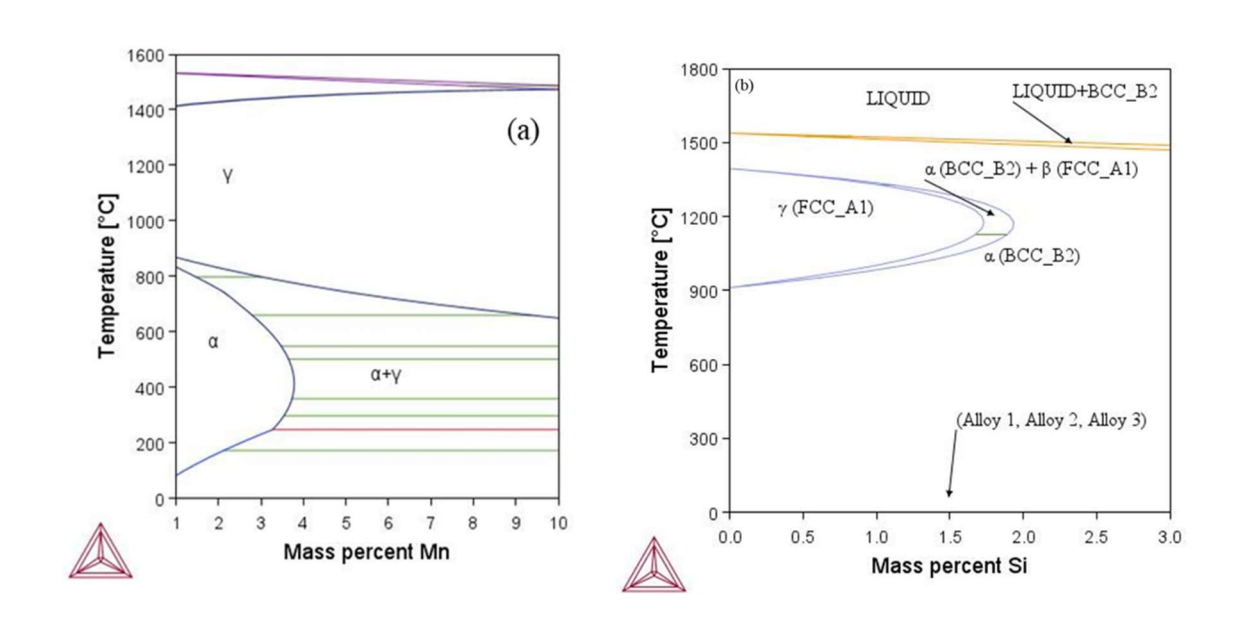


Figure 4.1 Phase diagrams of alloy systems, (a) Binary phase diagram of Fe-Mn System, (b) Binary phase diagram of Fe-Si System.

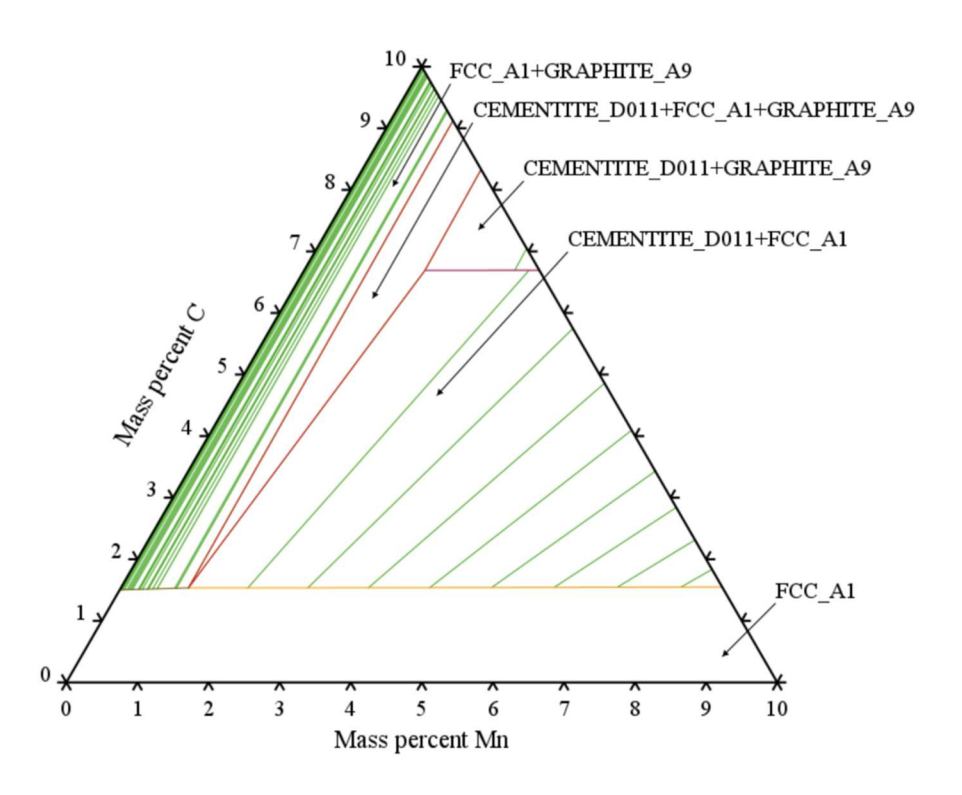


Figure 4.2 Ternary phase diagram of Fe-Mn-C System at 1000 °C.

Figure 4.1. (a) shows a phase diagram of the Fe-Mn binary system that represents the variation of manganese up to 10 wt.%. And Figure 4.1. (b) represents the Fe-Si binary phase diagram in that the silicon axis is limited to 3 wt.%. The ternary phase diagram (Fe-Mn-C) at 1000 °C is shown in Figure 4.2. The ternary phase diagram shows the austenite phase at this temperature. At higher composition of carbon, the combination of austenite, cementite and graphite phase will appear in the microstructure that is labelled in Figure 4.2. The ternary phase diagrams of Fe-Si-C and Fe-Mn-Si are shown in Figure 4.3 and Figure 4.4 respectively.

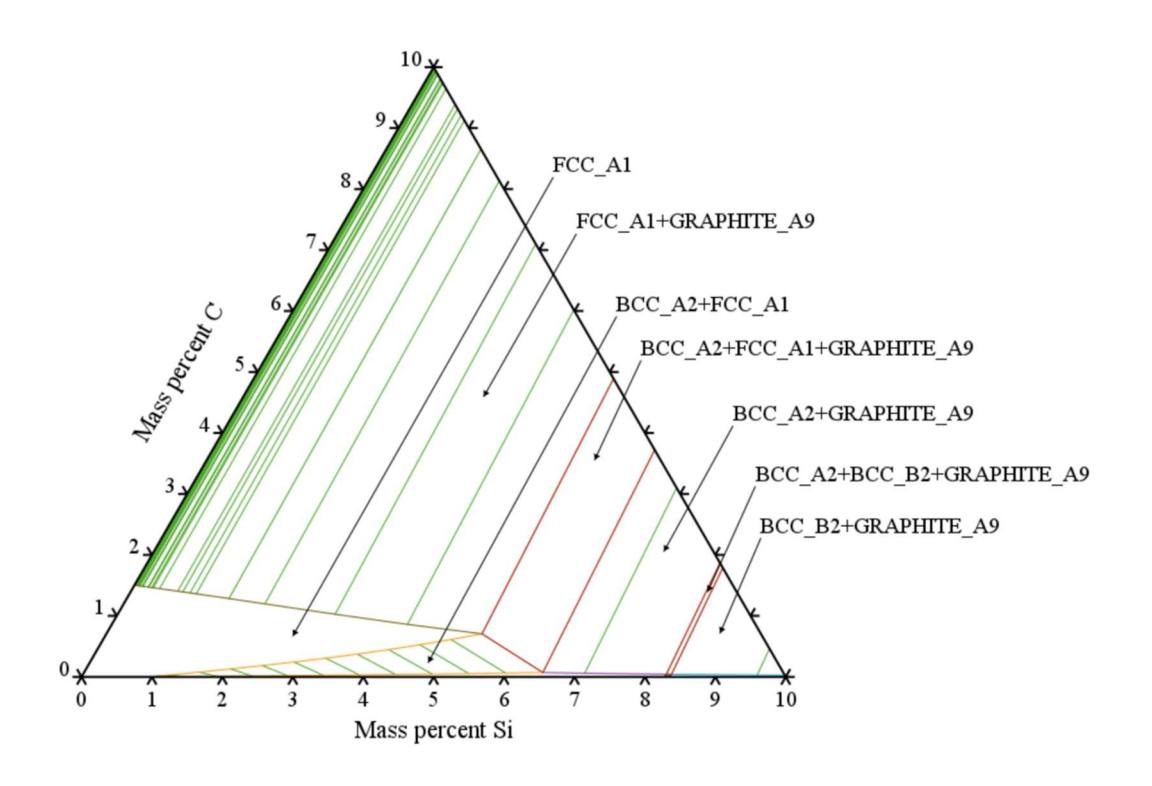


Figure 4.3 Ternary phase diagram of Fe-Si-C System at 1000 °C.

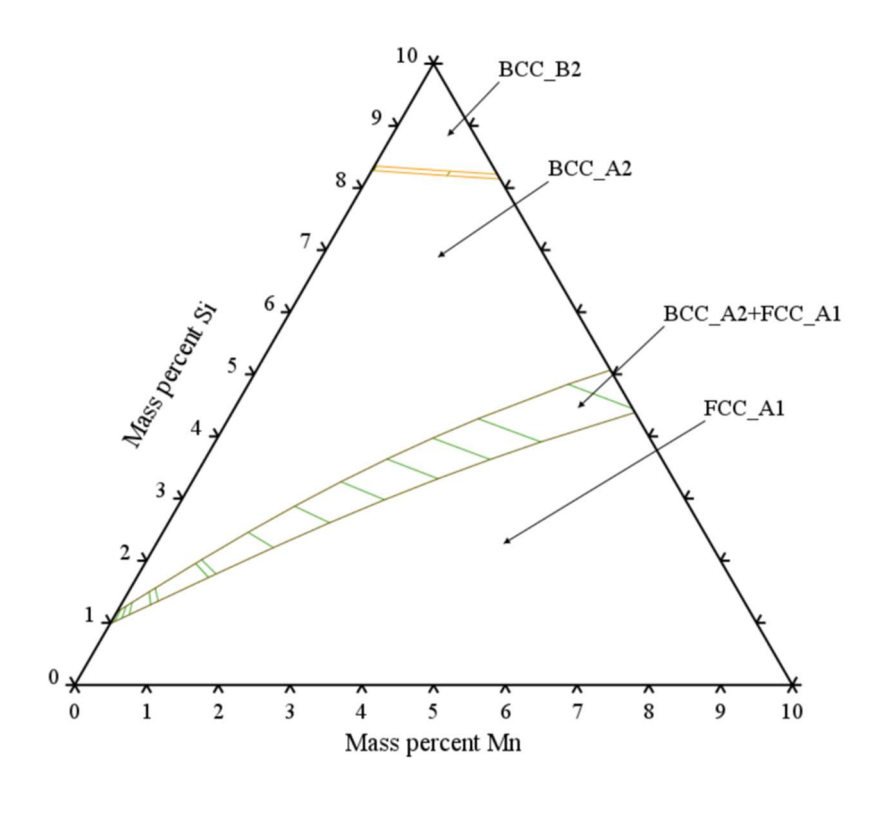


Figure 4.4 Ternary phase diagram of Fe-Mn-Si System at 1000 °C.

The ternary phase diagrams of Fe-Si-C and Fe-Mn-Si are shown in Figure 4.3 and Figure 4.4 respectively. The ternary phase diagrams of Fe-Si-C shows that single phase FCC structure at 1000 °C temperature in the range of Si from 1 to 2 wt.% with a constant 0.2 wt.% carbon. The ternary phase diagram of Fe-Mn-Si alloy system shows two phases (FCC and BCC) in the composition range of silicon 1 to 2 wt.% while FCC single phase will form at 1000 °C temperature as shown in Figure 4.4.

4.2.2 Simulated Continuous cooling curves (CCT) and temperature time transformation (TTT)

JMatPro software was used to determine the CCT and TTT curves of novel third-generation advanced high strength (AHSS) alloys. The phase transformation temperatures were determined by JMatPro software. The time-temperature-transformation (TTT) diagrams as shown in Figure 4.5 (a1, b1, c1) of Alloy 1, Alloy 2, and Alloy 3 show the delayed transformation by increasing the contents of manganese keeping silicon (Si) contents constant. Figure 4.5 (a1, b1, c1) also represents that bainitic transformation may start in the temperature range from 400 °C to 500 °C for Alloy 1 while bainite transformation may start below 400 °C and 325 °C for Alloy 2 and Alloy 3 respectively. The advanced continuous cooling transformation (CCT) curves are presented in Figure 4.5 (a2, b2, c2). These curves represent transformation with varying cooling rates. The time-temperature-transformation (TTT) diagrams for Alloy 4, Alloy 2, and Alloy 5 are shown in Figure 4.6 (a1, b1, c1) which show that the transformation is delayed by increasing contents of silicon (Si) additions keeping manganese content constant. The advanced continuous cooling transformation (CCT) curves are presented in Figure 4.6 (a2, b2, c2). These curves also represent transformation with varying cooling rates.

4.2.2.1 TTT and CCT diagrams with variation in Mn

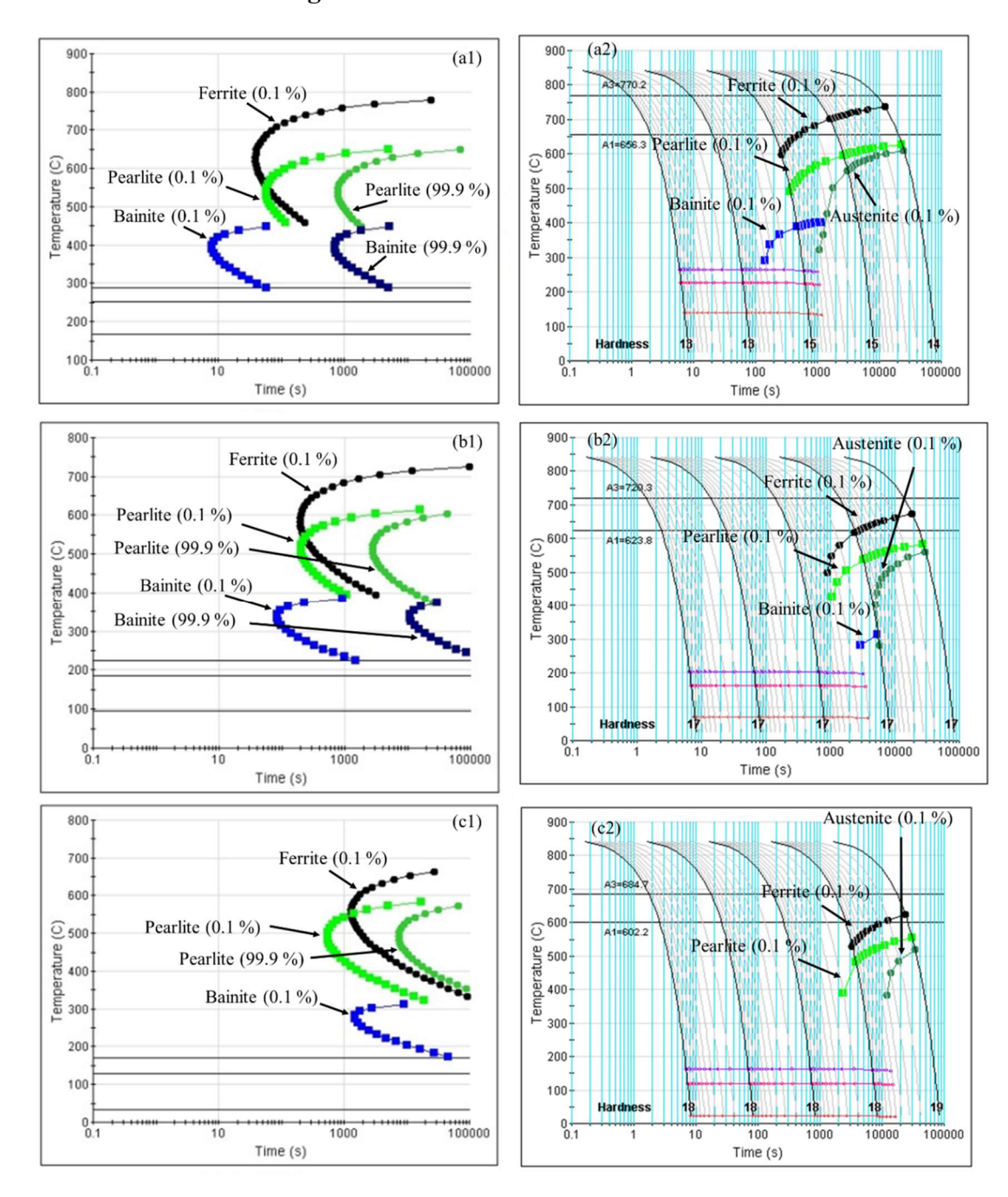


Figure 4.5 Time Temperature Transformation (TTT) and advanced CCT diagrams of novel alloy steels determined by materials Property software: (a1) TTT Diagram, Alloy 1, (b1) TTT Diagram, Alloy 2, and (c1) TTT Diagram, Alloy 3, (a2) advanced CCT, Alloy 1, (b2) advanced CCT, Alloy 2, (c2) advanced CCT, Alloy 3.

4.2.2.2 TTT and CCT diagrams with variation in Si

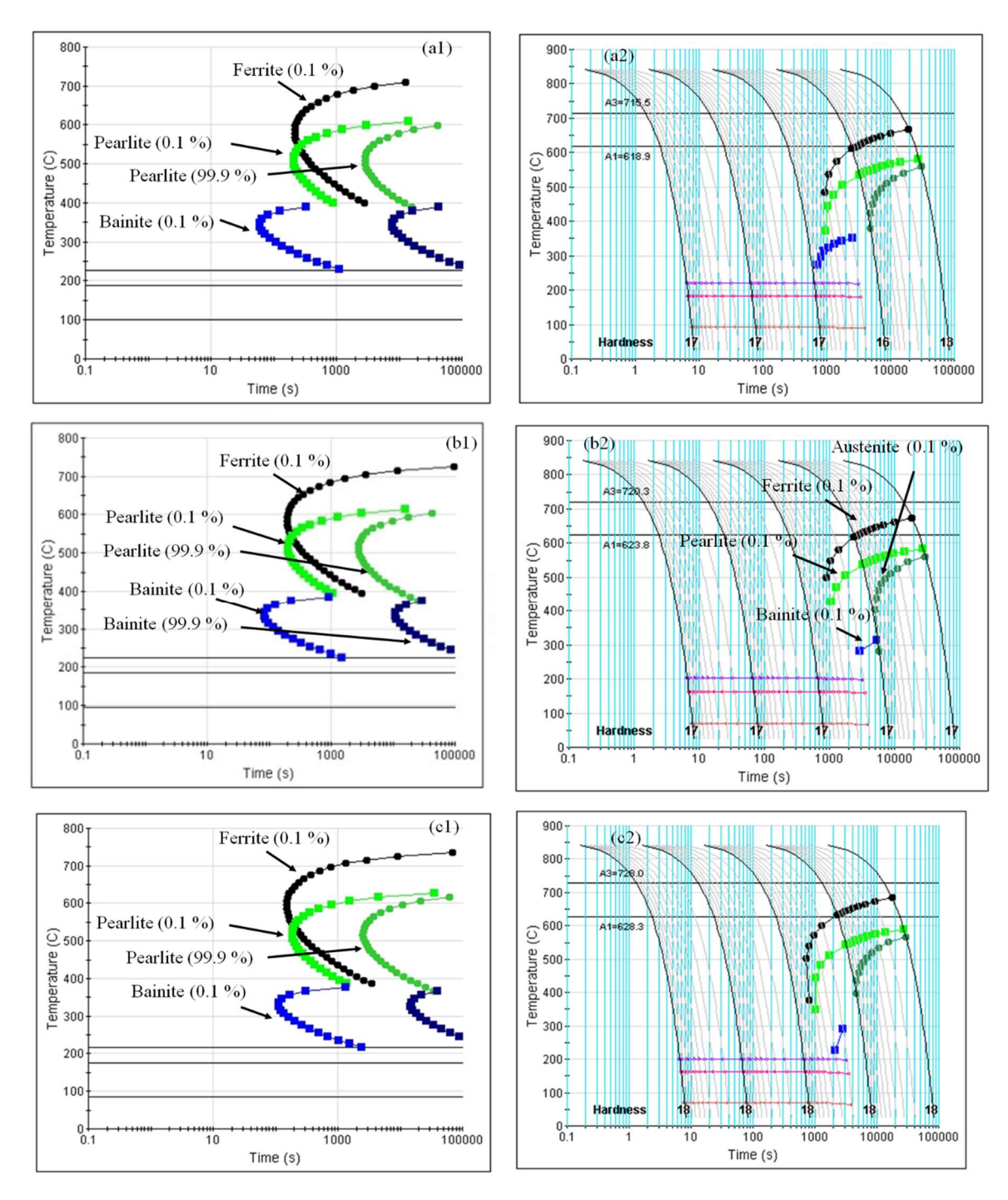


Figure 4.6 Time Temperature Transformation (TTT) and advanced CCT diagrams of novel alloy steels determined by materials Property software: (a1) TTT Diagram, Alloy 4, (b1) TTT Diagram, Alloy 2, and (c1) TTT Diagram, Alloy 5, (a2) advanced CCT, Alloy 4, (b2) advanced CCT, Alloy 2, (c2) advanced CCT, Alloy 5.

4.2.2.3 Phase transformation temperatures

The phase transformation temperatures of proposed alloys were determined using JMatPro property simulation software which are provided in Table 4.1.

Table 4.1 Simulated phase start transformation temperatures (°C) of novel AHSS determined by JMatPro software.

Alloys	A1	A3	Ferrite	Pearlite	Bainite	Martensite
Alloy 1	661	840	780	661	460	288
Alloy 2	626	784	734	626	391	224
Alloy 3	598	738	689	598	321	170
Alloy 4	622	779	729	622	400	228
Alloy 5	634	796	747	634	383	216

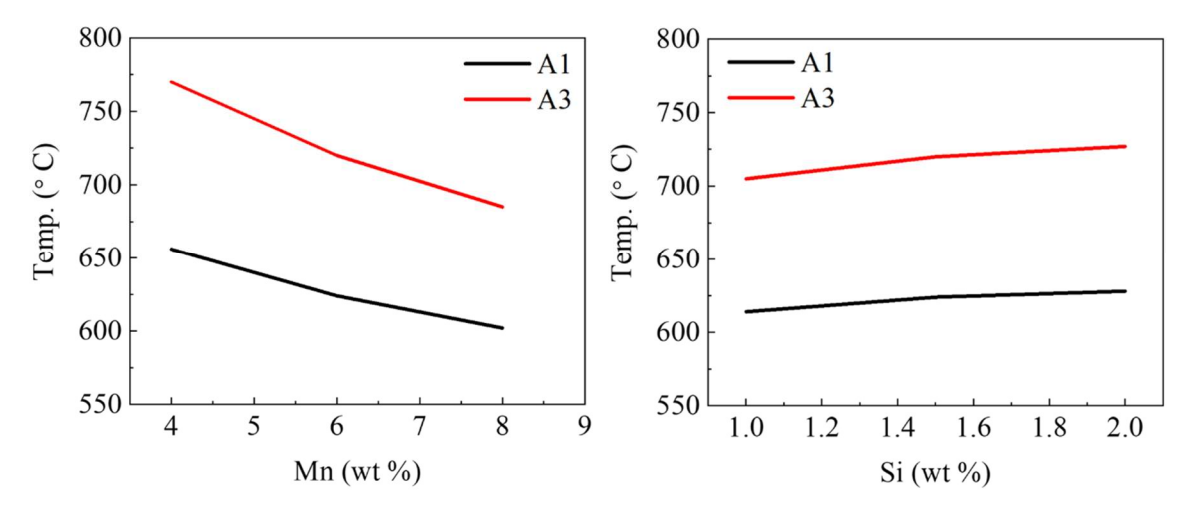


Figure 4.7 Effect of (a) Mn, and (b) Si variation on lower critical (A1) and Upper critical (A3) temperatures.

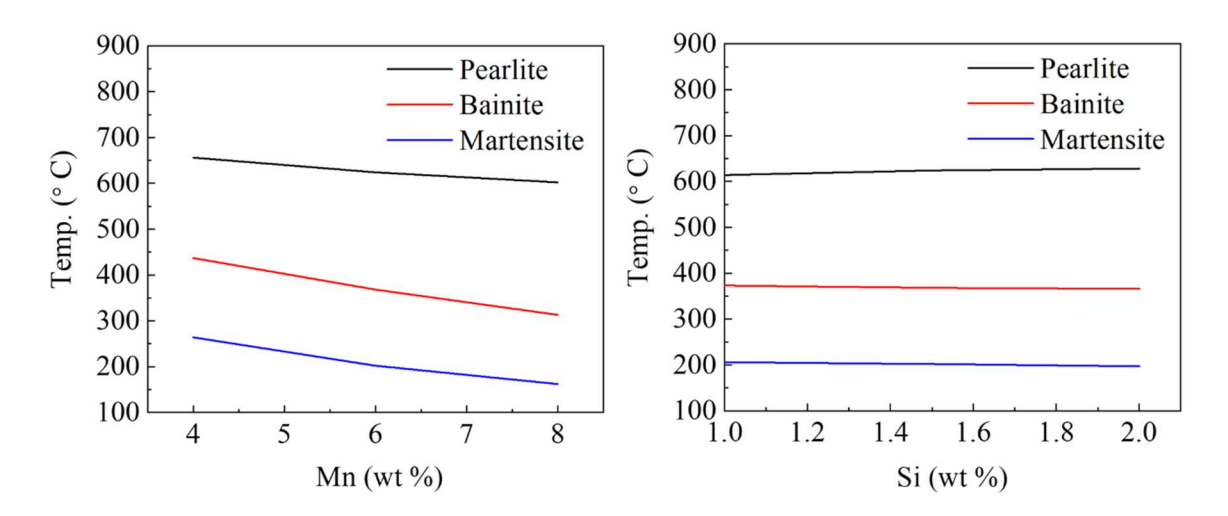


Figure 4.8 Effect of (a) Mn and (b) Si variation on phase transformation temperature of alloy steels.

The upper critical temperature (A1) and lower critical temperatures are lowered by increasing the amount of manganese additions as shown in Figure 4.7 (a) while additions of silicon have the reverse effect on the A1 and A3 temperatures as compared to manganese additions that is shown in Figure 4.7 (b). Figure 4.8 (a) shows that transformation temperatures of bainite, pearlite and martensite are lowered by additions of manganese content. The transformation temperature of bainite falls more rapidly as compared to pearlite and martensite. The additions of silicon in alloy 1, alloy 2 and alloy 3 have no significant effect on phase transformation temperatures as shown in Figure 4.8 (b). The solidification path was predicted.

4.2.2.4 Simulated solidification paths of Alloys

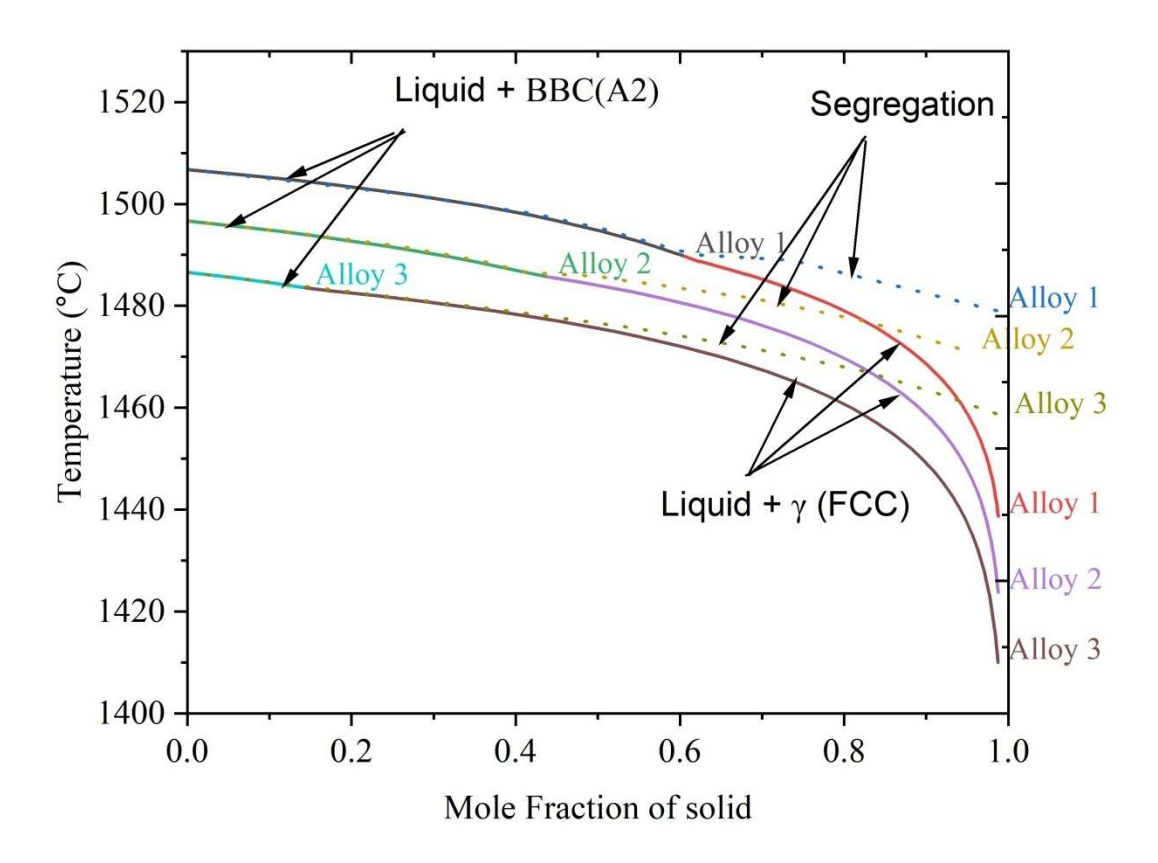


Figure 4.9 Solidification behaviour using Scheil solidification model determined by Thermo-Calc software with variation in Mn.

Using the Scheil model that is shown in Figure 4.9 for Alloy 1, Alloy 2 and Alloy 3. The initial curve at high temperature of Figure 4.9 represents the molten state of alloys while as the temperature falls delta ferrite phase separates. The point of contact of colour change on each plot indicates the start of the formation of austenite during solidification in the alloys. The progression of curves in Figure 4.9 represents the progress of solidification by the drop in temperature. The complete curve for each alloy predicts the path of solidification. The dotted lines shown in Figure 4.9 indicate paths of segregation in the alloys (developed using Thermo-Calc software). It is observed that dotted curves becoming close to the path of the solidification curves with increase in Mn contents. It can be concluded that the level of segregations will be reduced by increasing manganese contents in alloys. The dotted curve of alloy 3 shows the lowest level of segregation among all three

alloys. The solidification paths for Alloy 4, Alloy 2 and Alloy 5 are similar to Alloy 1, Alloy 2 and Alloy 3.

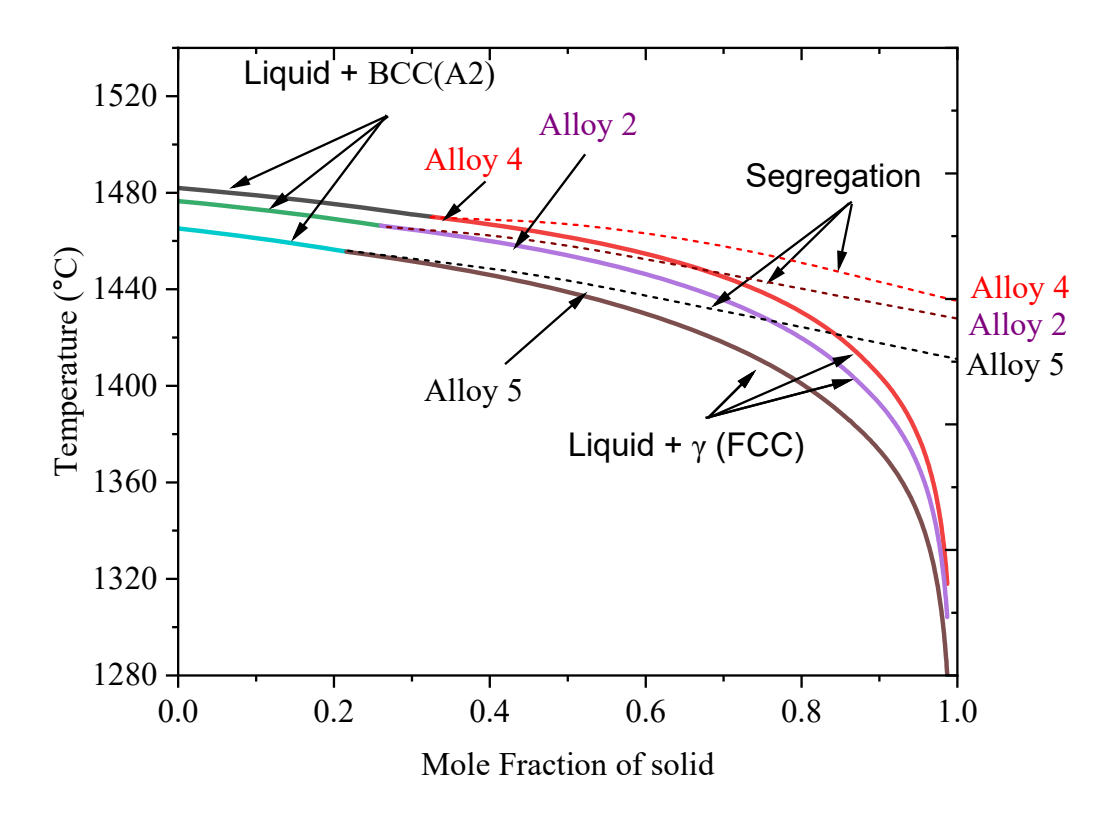


Figure 4.10 Solidification behaviour using Scheil solidification model determined by Thermo-Calc software with variation in Si.

Solidification behaviours were predicted by Thermo-Calc software using the Scheil model that are shown in Figure 4.10 for Alloy 4, Alloy 2 and Alloy 5. The initial curve at high temperature of Figure 4.10 represents the molten state of alloys while as the temperature falls delta ferrite phase separates. The point of contact of colour change on each plot indicates the start of the formation of austenite during solidification in the alloys. The progression of curves in Figure 4.10 represents the progress of solidification with the drop in temperature. The complete curve for each alloy predicts the path of solidification. The dotted lines shown in Figure 4.10 indicate paths of segregation in the alloys. This is observed that dotted curves becoming farther to the path of the solidification curves with increase in Si contents. It can be concluded that the level of segregations will increase with increasing silicon contents in alloys as silicon is ferrite stabilizer. The dotted curve of Alloy 5 shows the highest level of segregation among all three alloys in which silicon is varied.

4.3 Alloy development

4.3.1 Alloy casting

As heat treatment cycles are key for achieving a good combination of strength and ductility, Material property simulation software (JMatPro) was used to develop time temperature transformation curves. Thermo-Calc was also used to develop phase diagrams and to predict solidification behavior. Based on the simulation results, specific compositions were chosen to develop the alloys.

Alloying elements (high purity of 99.99%) were procured from reliable sources (Alfa Aeser). Alloying elements were weighed and mixed in the required ratio and the weight of each sample used for melting was 20 grams. Samples were charged into a vacuum arc furnace. The melting of the alloy samples was repeated at least five times to ensure homogeneity in the bulk of the samples. Two types of samples were cast in the copper hearth as a button and finger shapes. The detailed melting process is mentioned in section 3.2. The chemical compositions of three novel alloys were measured using Spectrolab instrument (Model M-12, Germany) and are provided in Table 4.2. The measured compositions are found to be very close to the compositions analyzed by the spectrometer. The alloy was cast in the form of a button and the buttons were re-melted in the form of finger samples as shown in Figure 4.11.

Table 4.2 The compositions of novel third-generation advanced high-strength alloys (Spectrometer analysis of novel alloys).

Alloy/Ele ments, (wt.%)	C	Si	Mn	Ni	Cr	Ti	Al	S	P	Fe
Alloy 1 (4Mn1.5Si)	0.138	1.41	4.03	0.028	0.043	0.005	0.0025	≤0.008	≤0.004	bal.
Alloy 2 (6Mn1.5Si)	0.14	1.37	6.07	0.028	0.043	0.005	0.0025	≤0.008	≤0.004	bal.
Alloy 3 (8Mn1.5Si)	0.138	1.38	8.04	0.028	0.043	0.005	0.0025	≤0.008	≤0.004	bal.
Alloy 4 (6Mn1Si)	0.14	1.04	5.98	0.028	0.043	0.005	0.0025	≤0.008	≤0.004	bal.
Alloy 5 (6Mn2Si)	0.14	2.05	6.1	0.028	0.043		0.0025	≤0.008	≤0.004	bal.

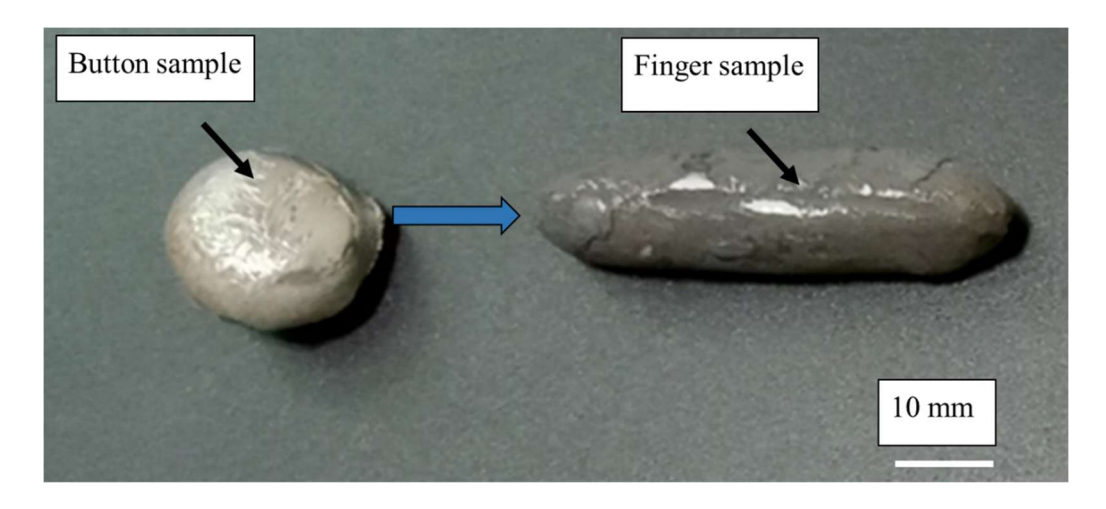


Figure 4.11 Finger shaped casting produced by re-melting of button.

4.3.2 Homogenization heat treatment

The alloy castings were homogenized in an inert atmosphere in a tubular furnace at 1200 °C for 4 hours. The homogenization treatment was performed in a tubular furnace with variation in temperature and time. In homogenization treatment, the sample was heated with a heating rate of 6.6 °C/sec and held for 4 hours followed by furnace cooling in 14 hours. The homogenization heat treatment cycle is shown in Figure 4.12. Specimens thus homogenized are used for further processing and characterization. After homogenization, the samples were machined in the dimensions of 10 mm ×10 mm×5 mm for further analysis. The microstructural characterization was carried out using a Leica microscope scanning electron microscope (SEM) and Field-emission scanning electron microscope (FE-SEM). X-ray diffraction was performed to identify the phases present in the microstructure.

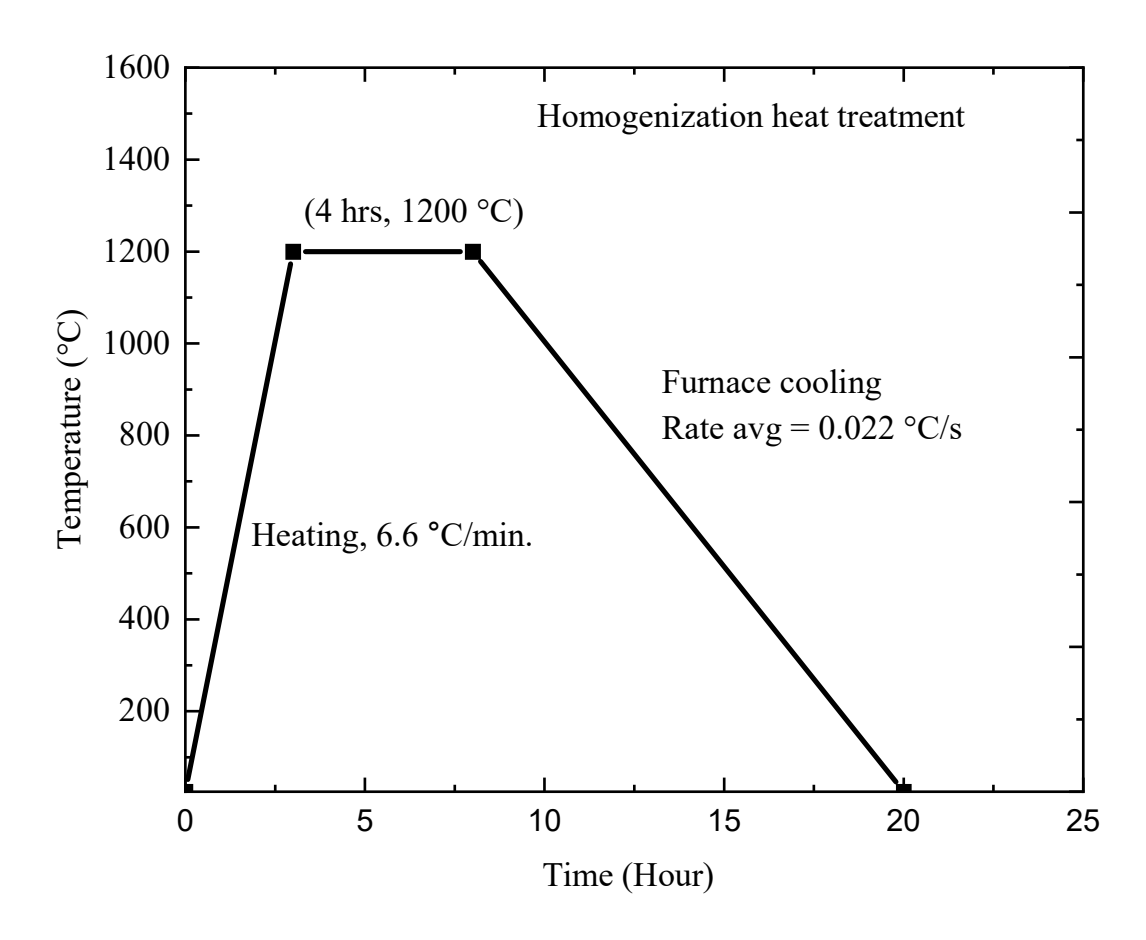


Figure 4.12 Homogenization heat treatment, at 1200 °C, for 4 hours

4.4 Characterization

4.4.1 Optical Micrographs of homogenised AHSS

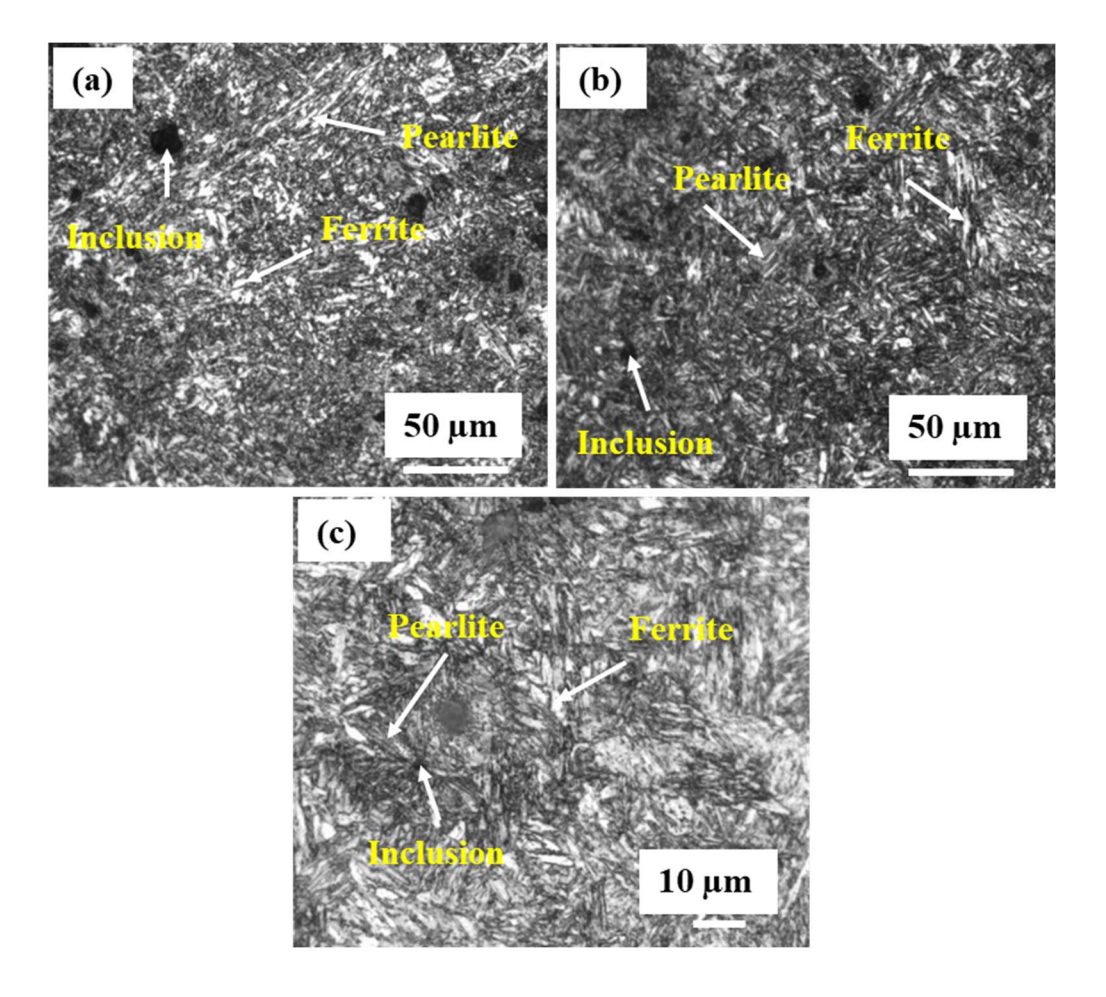


Figure 4.13 Optical micrographs of Fe-xMn-1.5Si steels homogenized at $1200 \,^{\circ}$ C, 4 hours. at 200X, (a) Alloy 1, (b) Alloy 2, (c) Alloy 3. (where x = 4, 6, 8)

The alloy samples were polished for microstructural analysis and etched with 2 % Nital up to 1 minute. The homogenised optical micrographs for Alloy 1, Alloy 2, and Alloy 3, are shown in Figure 4.13 (a, b, c). The microstructure revealed ferrite (bright) and pearlite (lamellar). The similar phases are observed in Alloy 4, Alloy 2 and Alloy 5 in which Si was varied from 1.0 to 2 wt.%. The optical micrographs with Si variation are shown in Figure 4.14 (a, b, c).

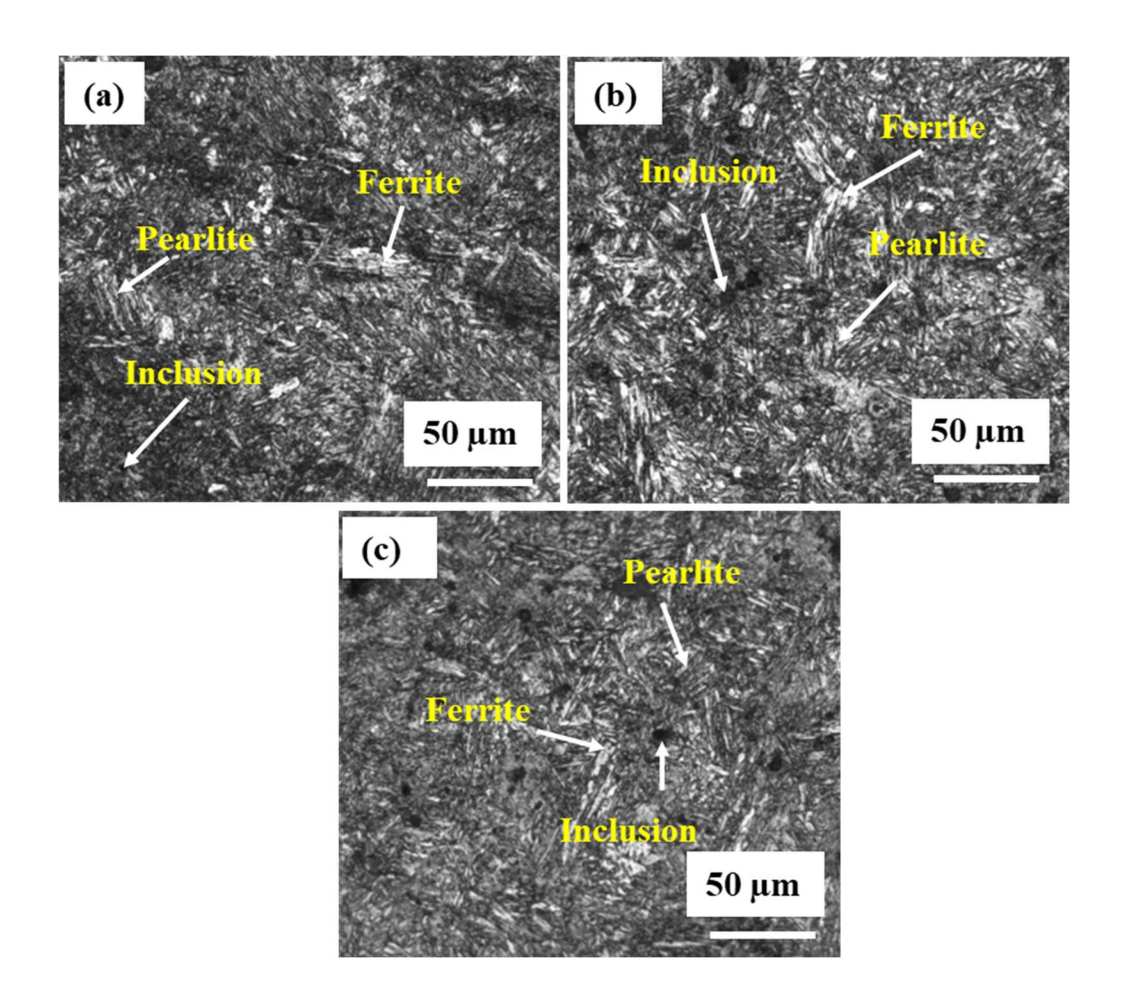


Figure 4.14 Optical micrographs of Fe-6Mn-ySi (y = 1, 1.4, 2.0) steels homogenized at 1200 °C, 4 hours. at 200X, (a) Alloy 4 (Fe-6Mn-1.0Si), (b) Alloy 2 (Fe-6Mn-1.5Si), (c) Alloy 5 (Fe-6Mn-2.0Si).

4.4.2 Field-Emission Scanning Electron Micrographs (FE-SEM)

4.4.2.1 Effect of manganese (Mn) alloying on micrographs

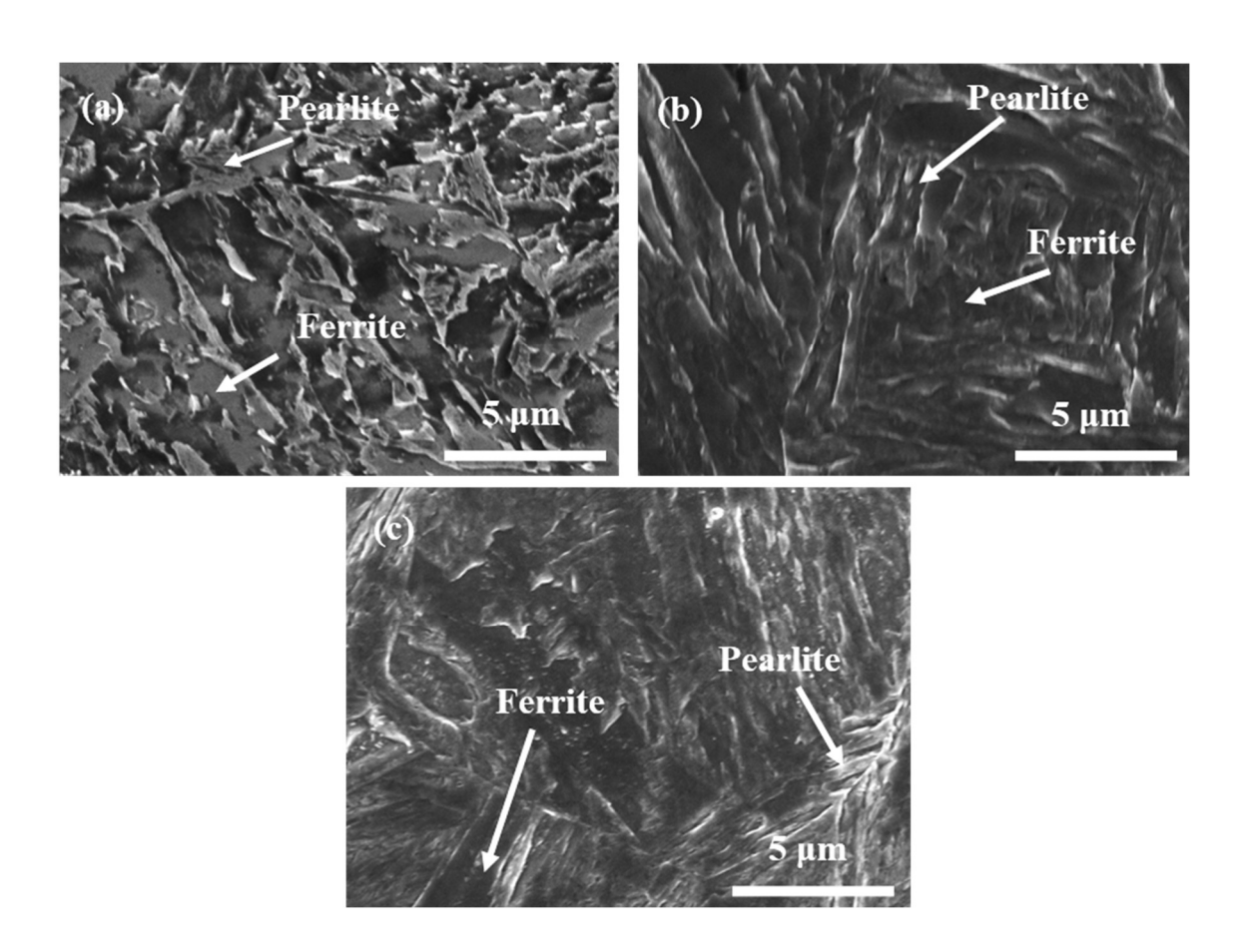


Figure 4.15 Field Emission Scanning Electron micrographs of AHSS homogenized at 1200 °C, 4 hours, at 1500X (a) Alloy 1 (Fe-4Mn-1.5Si), (b) Alloy 2 (Fe-6Mn-1.5Si), (c) Alloy 3 (Fe-8Mn-1.5Si).

4.4.2.2 Effect of silicon (Si) alloying on micrographs.

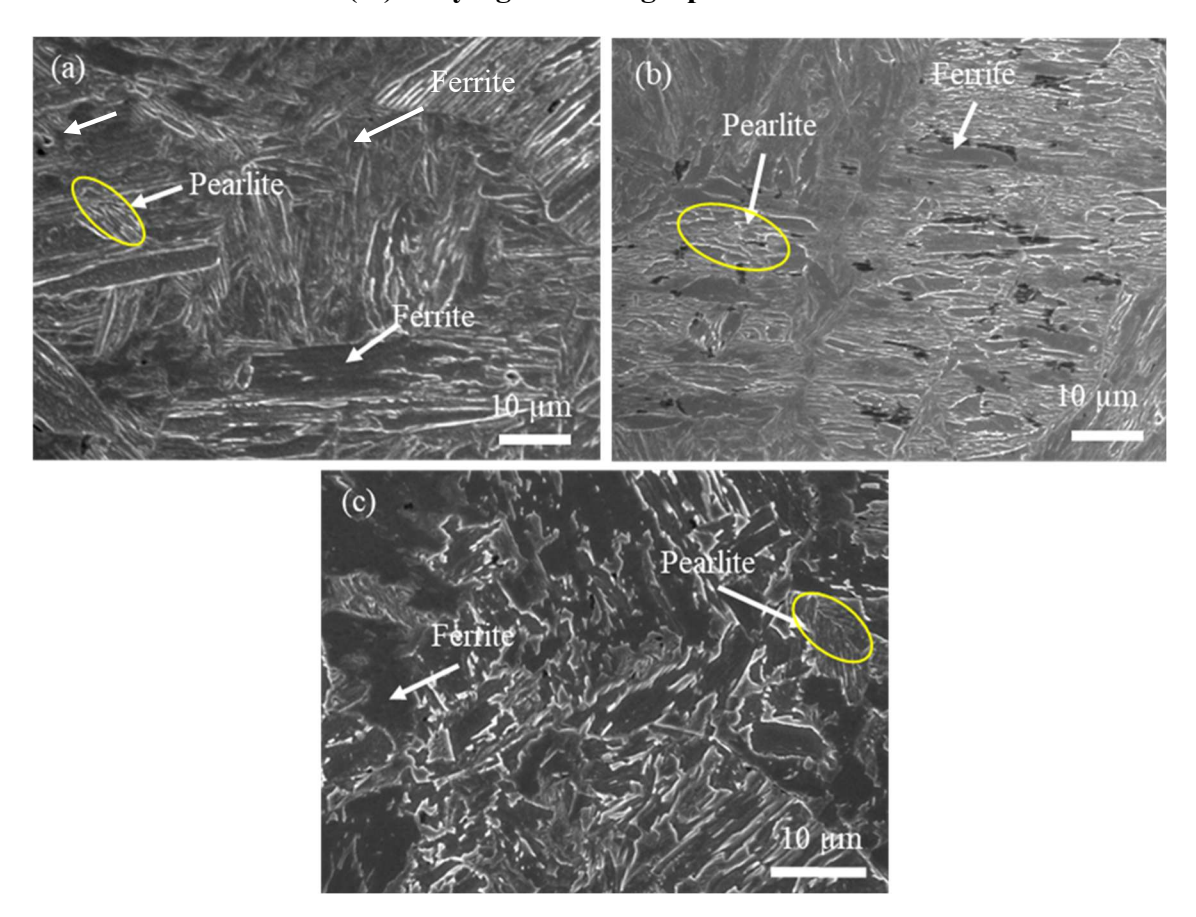


Figure 4.16 Field Emission Scanning Electron micrographs of AHSS homogenized at 1200 °C, 4 hours, at 2000X (a) Alloy 4 (Fe-6Mn-1.0Si), (b) Alloy 2 (Fe-6Mn-1.5Si), (c) Alloy 5 (Fe-6Mn-2.0Si).

The micrographs after homogenization at 1200 °C for 4 hours followed by furnace cooling were obtained from a field emission scanning electron microscope that are shown in Figure 4.15 and Figure 4.16. The phases revealed are presented in 4.15 (a, b, c) for Alloy 1, Alloy 2, and Alloy 3. Similar distribution and phase are observed in Alloy 4, Alloy 2, and Alloy 5 as shown in Figure 4.16. These micrographs represent complex phases in which ferrite and pearlite are revealed. Figure 4.15 also represents lower ferrite by increasing manganese contents from 4 to 8 wt.%. The influence of silicon addition on micrographs is presented in Figure 4.16 for Alloy 4, Alloy 2, and Alloy 5 respectively. These micrographs represent complex phases in which ferrite and pearlite are observed. Calculated volume percentages of ferrite are 85.2 vol. %, 89.7 and 91.9 vol.% for Alloy 4, Alloy 2 and Alloy 5 respectively.

Figure 4.16 also indicates the increase of ferrite by increasing silicon contents from 1.0 wt.% to 2.0 wt.%. This is due to silicon stabilizes ferrite.

4.4.3 X-Ray Diffraction (XRD) Patterns

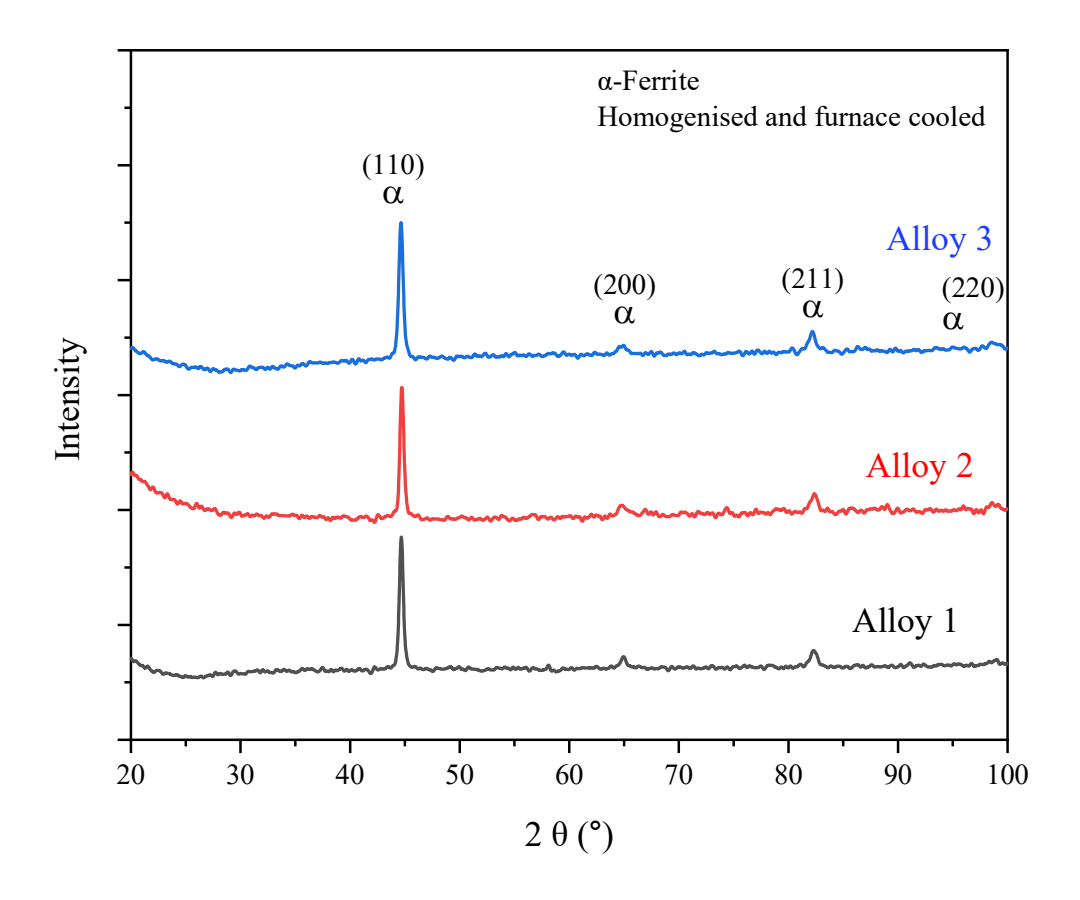


Figure 4.17 XRD-spectra of AHSS homogenized at 1200 °C, 4 hours, (a) alloy 1 (Fe-4Mn-1.5Si), (b) alloy 2 (Fe-6Mn-1.5Si), (c) alloy 3 (Fe-8Mn-1.5Si).

Table 4.3 Peak positions of alloy 1, alloy 2 and alloy 3 homogenized at 1200 °C, 4 hours soaking. (with increase in Mn contents).

Alloy/	α-ferrite,	α-ferrite,	α-ferrite,	α-ferrite,
(hkl)	(110)	(200)	(211)	(220)
Alloy 1	44.68	64.95	82.46	98.97
Alloy 2	44.72	64.78	82.37	98.58
Alloy 3	44.65	64.57	82.19	98.53

Figure 4.17 shows the x-ray diffraction (XRD) pattern of homogenized at 1200 °C for 4 hours Alloy 1, Alloy 2 and Alloy 3. All three alloys exhibit the same number of peaks. The major peak is found at 44.68 ° from the (111) crystallographic plane that corresponds to alpha-ferrite. Three minor peaks of α -ferrite are found at 64.95 °, 82.46 ° and 98.97 ° from (200), (211) and (220) planes. Figure 4.18 depicts the same number of XRD peaks of α -ferrite compared to the XRD pattern of Figure 4.17. Similar peaks were observed [23].

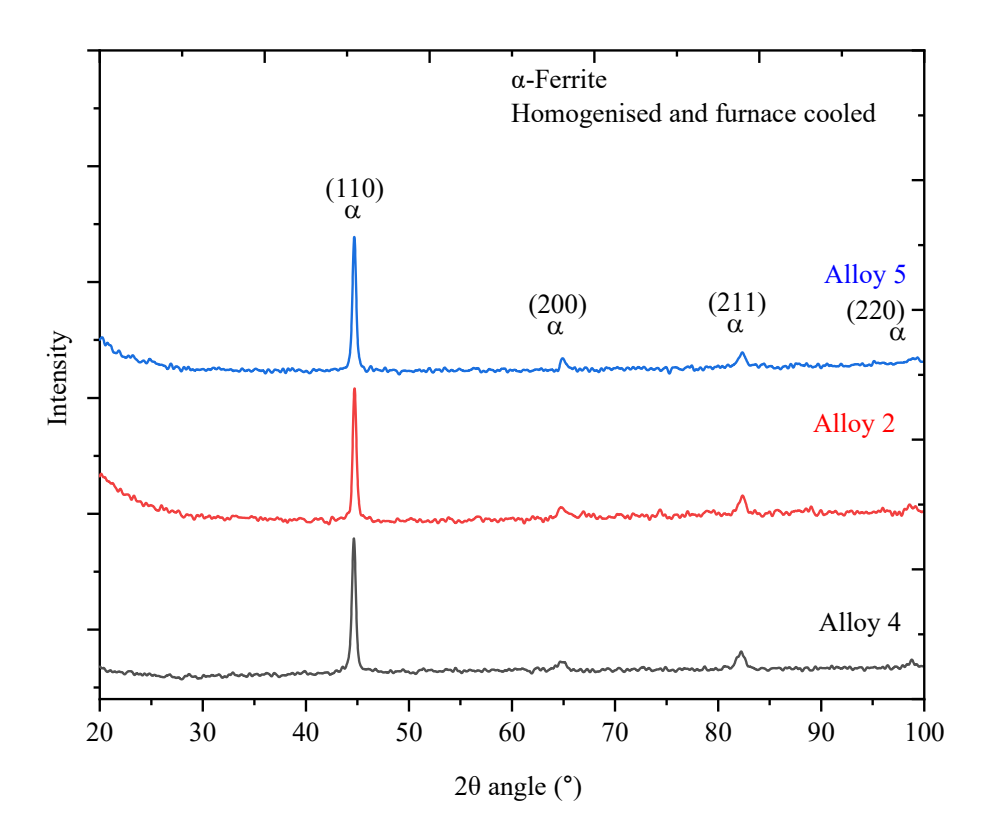


Figure 4.18 XRD-spectra of AHSS homogenized at 1200 °C, 4 hours, (a) alloy 4 (Fe-6Mn-1.0Si), (b) alloy 2 (Fe-6Mn-1.5Si), (c) alloy 5 (Fe-6Mn-2.0Si).

Table 4.4 Peak positions of alloy 4, alloy 2 and alloy 5 homogenized at 1200 °C, 4 hours. soaking. (with increase in Si contents).

Alloy/	α-ferrite,	α-ferrite,	α-ferrite,	α-ferrite,
(hkl)	(110)	(200)	(211)	(220)
Alloy 4	44.65	64.69	82.23	98.79
Alloy 2	44.72	64.78	82.37	98.58
Alloy 5	44.70	64.91	82.35	98.91

4.5 Discussion

4.5.1 Effect of Mn alloying

The addition of Mn in the alloys stabilizes austenite. Hence the increase of Mn reduces volume fraction of pearlite. The addition of Mn formed solid solution alloy at 1000 °C as shown in ternary phase diagram in Figure 4.2. The pearlitic start transformation temperature decreases from 661 °C to 598 °C with increase in Mn from 4 to 8 wt.%. The ferrite start transformation temperature decreases from 780 °C to 689 °C with increase in Mn from 4 to 8 wt.%. A3 temperature drops 102 °C with increase of 4 wt.% Mn while A1 temperature drops 63 °C with increase in Mn up to 8 wt.%, it indicates that A3 temperature lowers double of A1 temperature with increase in 4 wt.% of manganese. The segregation in the alloys were predicted using Scheil model in thermo-Calc software, The dotted lines in Figure 4.9 represents segregation. It was understood the segregation lower with increase in Mn. The separate peaks of cementite were not detected in XRD diffraction pattern shown in Figure 4.17. The XRD pattern shows one major and three minor peaks of ferrite.

4.5.2 Effect of Si alloying

Silicon is added to restrict formation of carbide. The carbide free bainite can be formed with addition of Si. The matrix was strengthened by Si alloying. The addition of Si formed solid solution alloy at 1000 °C as shown in ternary phase diagram in Figure 4.3. The pearlite transformation temperature was not changed significantly with increase in Si from 1 to 2.05 wt.% due to Si restricts formation of carbides. The ferrite start transformation temperature increases from 729 °C to 747 °C with increase in Si from 1 to 2.05 wt.%. A3 temperature does not change significantly with increase in Si up to 2.05 wt.%. The segregation in the alloys were predicted using scheil model in thermos-Calc software, The dotted lines in Figure 4.10 represent segregation. It was found that the segregation increases with increase in Si contents in the alloys. XRD diffraction pattern shows ferrite peaks as shown in Figure 4.18. The separate peaks of cementite were also not detected in XRD pattern.

4.6 Conclusions

- 1 The CCT and TTT curves were simulated using materials property software represent that bainite can be formed in air cooling.
- 2 The phase present in the explored compositions were predicted using thermos-calc software which works on thermodynamic data.
- 3 Solidification paths were found similar for all alloys with silicon and Mn variation.
- 4 Segregation decreases with increase in Mn contents while it decreases with increase in silicon contents
- The advanced high strength steel is developed successfully in vacuum arc melting furnace using high-purity metals. The Time Temperature Transformation was developed using materials property software and the results obtained are in good agreement with phase predicted by phase diagrams and solidification curves.
- 6 The complex phase microstructure was observed under field emission scanning electron microscope (FE-SEM). The microstructure revealed ferrite and pearlite in homogenized alloys.
- 7 The X-ray diffraction was performed for all five advanced high-strength steels. The four ferrite peaks are identified in all XRD spectra.

Chapter 5

Thermo-mechanical treatment at 900 °C and mechanical properties

5.1 Introduction

Thermomechanical treatment (TMT) is a process that uses thermal and mechanical processes to improve the mechanical properties of materials, particularly metals and alloys. It involves heating, deformation, and cooling to achieve desired microstructural changes, leading to improved strength, ductility, and toughness. LTMT is operated at low temperature and HTMT at high temperatures. TMT refines grain size, improves fatigue resistance and accelerates phase transformations. It's widely used in automotive steels to achieve high strength and toughness. The thermo-mechanical treatment was designed on the basis of alloy design presented in Chapter 4 (Figure 4.5 and Figure 4.6).

In the present chapter, medium manganese and silicon-based alloy steels were hot-rolled at 900 °C. Multi-pass hot rolling was performed in two stages at different strain rates to prepare a metal sheet of 1.68 mm. The microstructures of hot rolled and air-cooled sheet specimens are analysed using Optical Microscope and Field Emission Electron Microscope (FE-SEM). X-Ray diffraction was performed in each condition of alloys to detect the phases present in the alloys. To evaluate the mechanical properties, microhardness and tensile tests were performed and the reproducibility of results was confirmed by repeating tests three times. Earlier, Lee et al. had reported an ultimate tensile strength of 1144 MPa with an elongation of 65% in Fe–10Mn–0.3C–3Al–2Si steel [47]. The ultimate tensile strength and the total elongation are reported from 800–1600 MPa and 10–65%, respectively. However, the medium-Mn steels displays high yield/tensile ratio, showing a very high importance for anti-intrusion automotive part applications [48], [49], [50].

5.2 Methodology

5.2.1 Thermo-mechanical treatment

Finger-shaped homogenized steel samples were hot rolled in a laboratory-scale rolling mill as described in Section 3.4. The rolling was performed at 900 °C. To perform rolling, the furnace was heated to the predefined temperature of 900 °C with a heating rate of 6.6 °C per minute. When the furnace reached the target temperature of 900 °C, the samples were placed in the furnace for 20 minutes. One pass of hot rolling was performed, and the rolled samples were again placed in the furnace for 3-5 minutes, and a second pass was performed. Similarly, 14 passes were applied in rolling operations. In stage one, the initial thickness of 10.6 mm was brought to 2.6 mm in 8 passes. Further, hot rolling was performed and another 6 passes were applied to reduce sheet thickness to 1.68 mm. The thickness reduction was kept at 1.0 mm per pass in stage-I and 0.18 mm per pass in stage-II of hot-rolling. The thickness of the samples was reduced to 75.5% of the initial thickness. After rolling in the 14th pass, the samples developed were normalized.

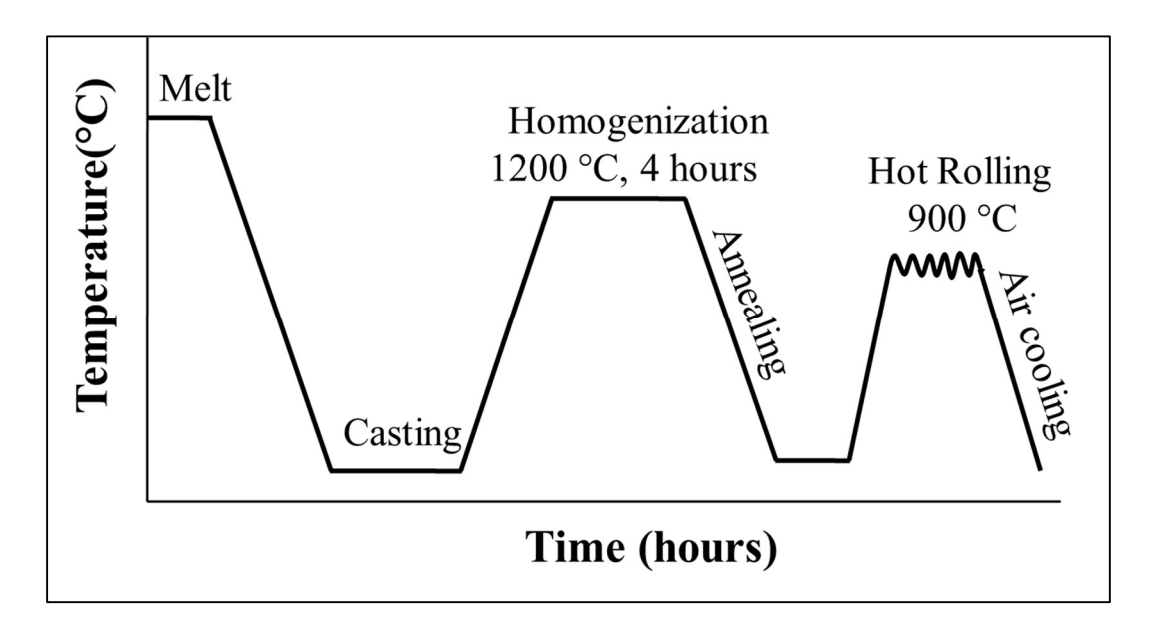


Figure 5.1 The schematic of the process flow chart.

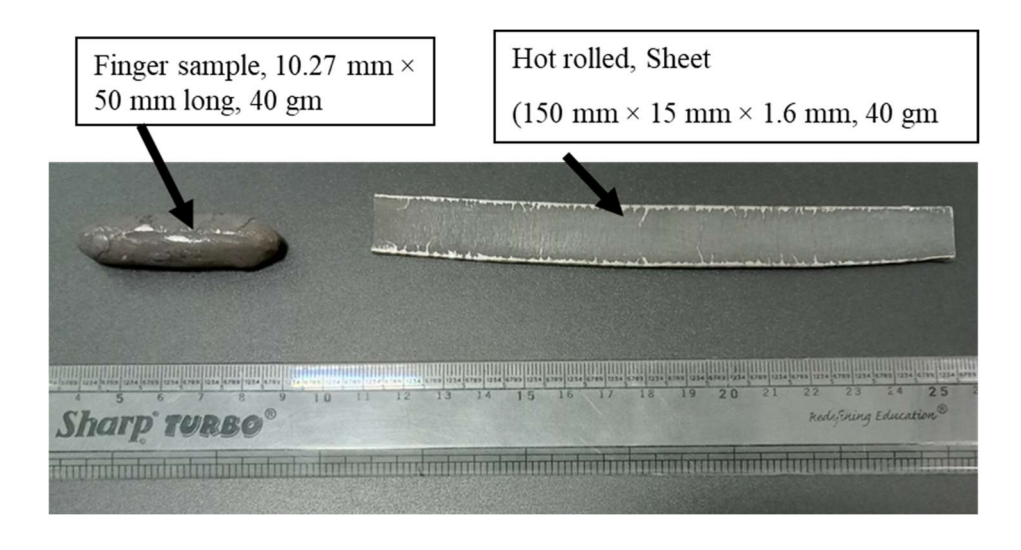


Figure 5.2 The finger-shaped sample, hot rolled to manufacture a sheet of (150 mm long, 15 mm width, 1.6 mm thickness) dimensions.

The homogenized ingot and hot-rolled sheet are shown in Figure 5.2. The strains applied during the rolling operations are shown in Table 5.1. In stage II, the 2.6 mm thickness was brought down to 1.68 mm in six passes, with a thickness reduction of 0.18 mm per pass.

Table 5.1 Strain applied in the rolling operations for Alloy 1, Alloy 2, Alloy 3, Alloy 4, and Alloy 5.

Rolling parameters							
Rolling stages	Pass number	Initial thickness (mm)	Final thickness (mm)	Strain applied (%)			
	1	10.27	9.27	9.74			
	2	9.27	8.27	10.79			
	3	8.27	7.27	12.09			
Stage I	4	7.27	6.27	13.76			
Stage-I	5	6.27	5.27	15.95			
	6	5.27	4.27	18.98			
	7	4.27	3.27	23.42			
	8	3.27	2.27	30.58			
	9	2.27	2.17	4.41			
	10	2.17	2.07	4.61			
Stage-II	11	2.07	1.97	4.83			
	12	1.97	1.88	4.57			
	13	1.88	1.78	5.32			
	14	1.78	1.68	5.62			

5.2.2 Characterization of hot rolled steels

The hot-rolled sheets were analysed under an optical microscope and field-emission scanning electron microscope (FE-SEM) to reveal the morphology. Further, X-ray diffraction was performed to identify the type and number of phases present in the novel alloys. The tensile strength was determined using data obtained from universal testing according to the ASTM E8 (ISO 6892) test standard. The microhardness was measured using a microhardness tester. The above-mentioned characterizations are described in sections 3.5.1 to 3.5.5.

5.3 Results

5.3.1 Optical micrographs of hot rolled at 900 °C

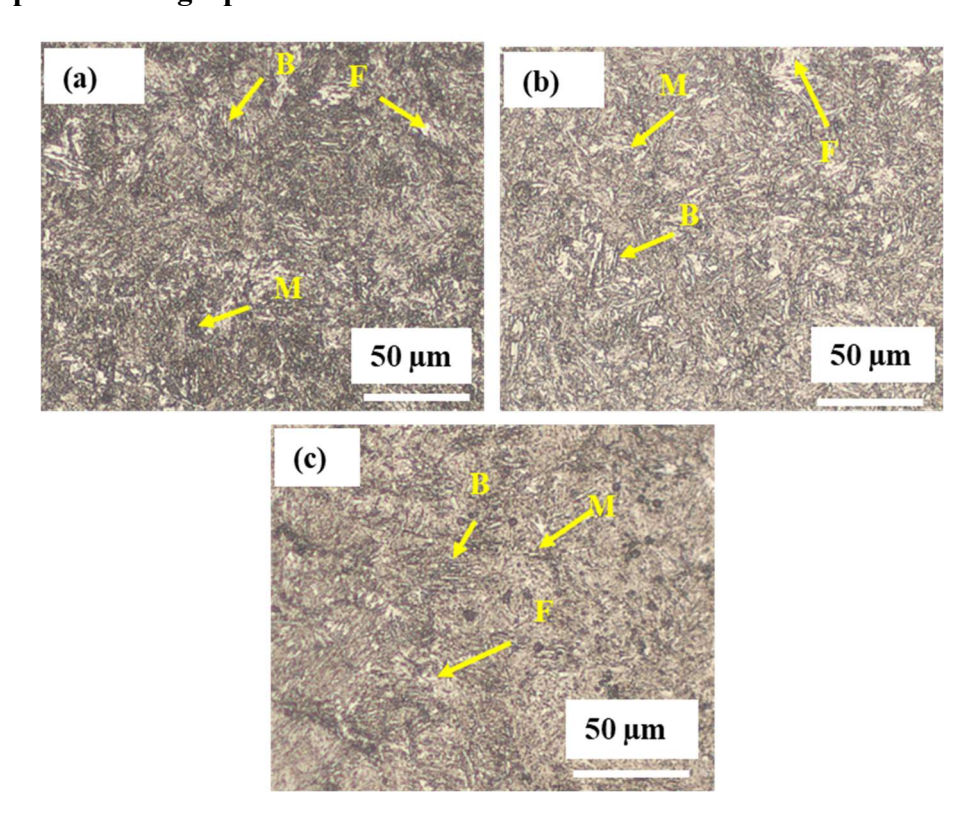


Figure 5.3 Optical micrographs of alloy steels hot rolled at 900 °C (a) Alloy 1 (Fe-4Mn-1.5Si), (b) Alloy 2 (Fe-6Mn-1.5Si), and (c) Alloy 3 (Fe-8Mn-1.5Si).

Figure 5.3 (a, b, c) shows the optical micrograph of the advanced high-strength steel hotrolled at 900 °C (initial soaking for 20 minutes) for Alloy 1, Alloy 2, and Alloy 3 respectively. Figure 5.3 (a) reveals ferrite (bright regions), bainite (bright parallel sheaves), and martensite (grey regions). The similar regions observed in Figure 5.3 (b, c) also correspond to the same types of phases. Figure 5.4 (a, b, c) represents the optical micrograph of the advanced high-strength steel hot rolled at 900 °C (initial soaking for 20 minutes) for Alloy 4, Alloy 2, and Alloy 5 respectively. The phases revealed from the micrographs of Figure 5.4 (a, b, c) are the same as those discussed in Figure 5.3 (a, b, c).

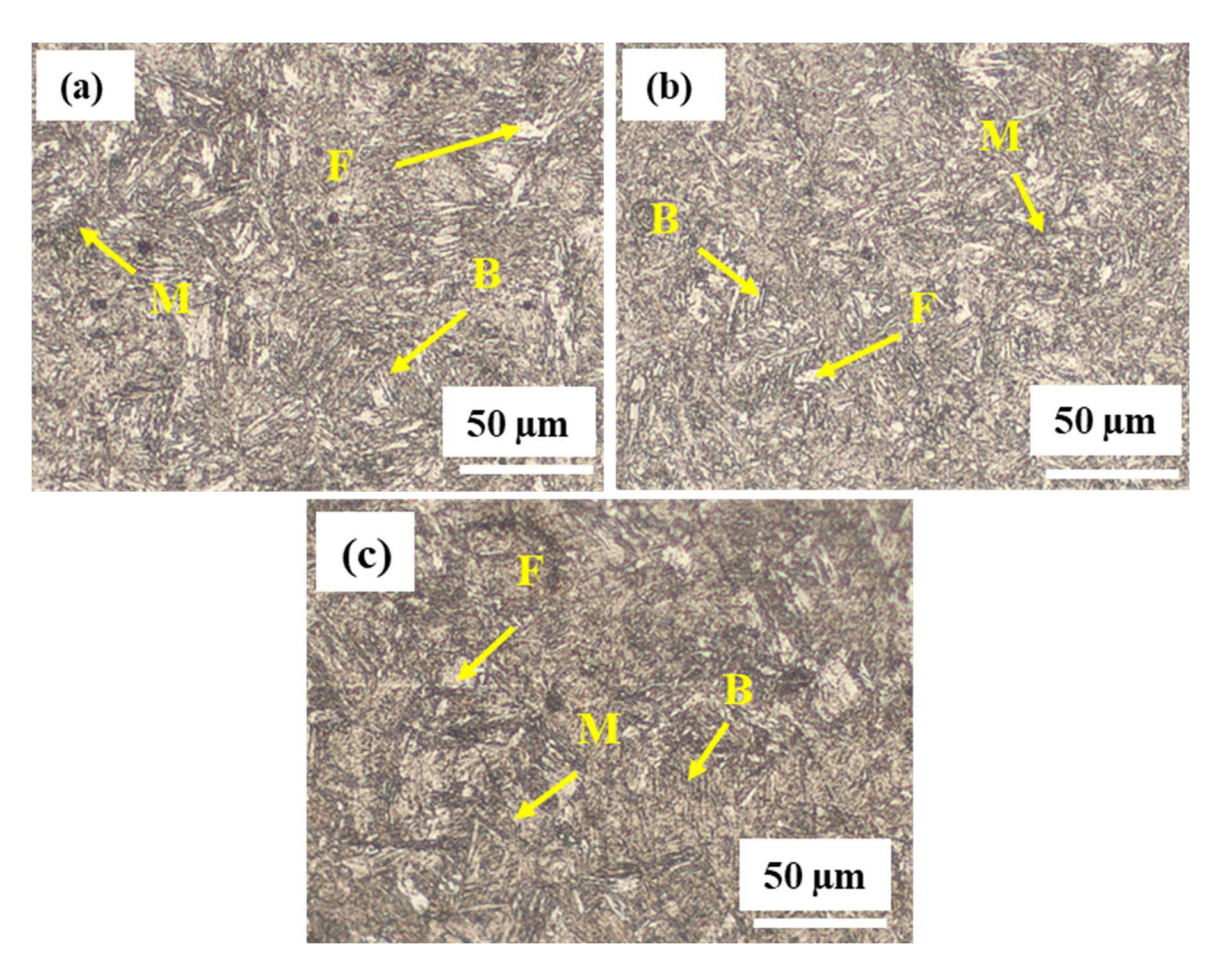


Figure 5.4 Optical micrographs of Fe-6Mn-ySi steels hot rolled at 900 °C, 20 min., (a) Alloy 4 (Fe-6Mn-1.0Si), (b) Alloy 2 (Fe-6Mn-1.5Si), (c) Alloy 5 (Fe-6Mn-2.0Si).

5.3.2 FESEM micrographs of hot rolled at 900 °C

5.3.2.1 Effect of manganese (Mn) alloying

The FE-SEM micrographs of alloy steel hot-rolled at 900 °C (initial soaking for 20 minutes) are shown in Figure 5.5. Figures 5.5 (a1, a2), Figures 5.5 (b1, b2), and Figures 5.5 (c1, c2) are the micrographs of Alloy 1, Alloy 2, and Alloy 3. The bright flat regions in the micrographs are ferrite, the embossed regions are bainite, and the grey flat regions are martensite, as shown in Figure 5.5 (a2) of Alloy 1. The same types of phases are observed in the micrographs of Alloy 2 and Alloy 3, as shown in Figure 5.5 (b2, c2). The volume fractions of bainite increases from 23 to 27 vol.% with increase in manganese content from 4 to 8 wt.%. Since Mn is known as austenite stabilizer, hence the volume fraction retained austenite increases from 8 to 12 vol.% with increase in Mn by 4 wt.%. similar microstructures with different processing routes are reported [70], [35],[71].

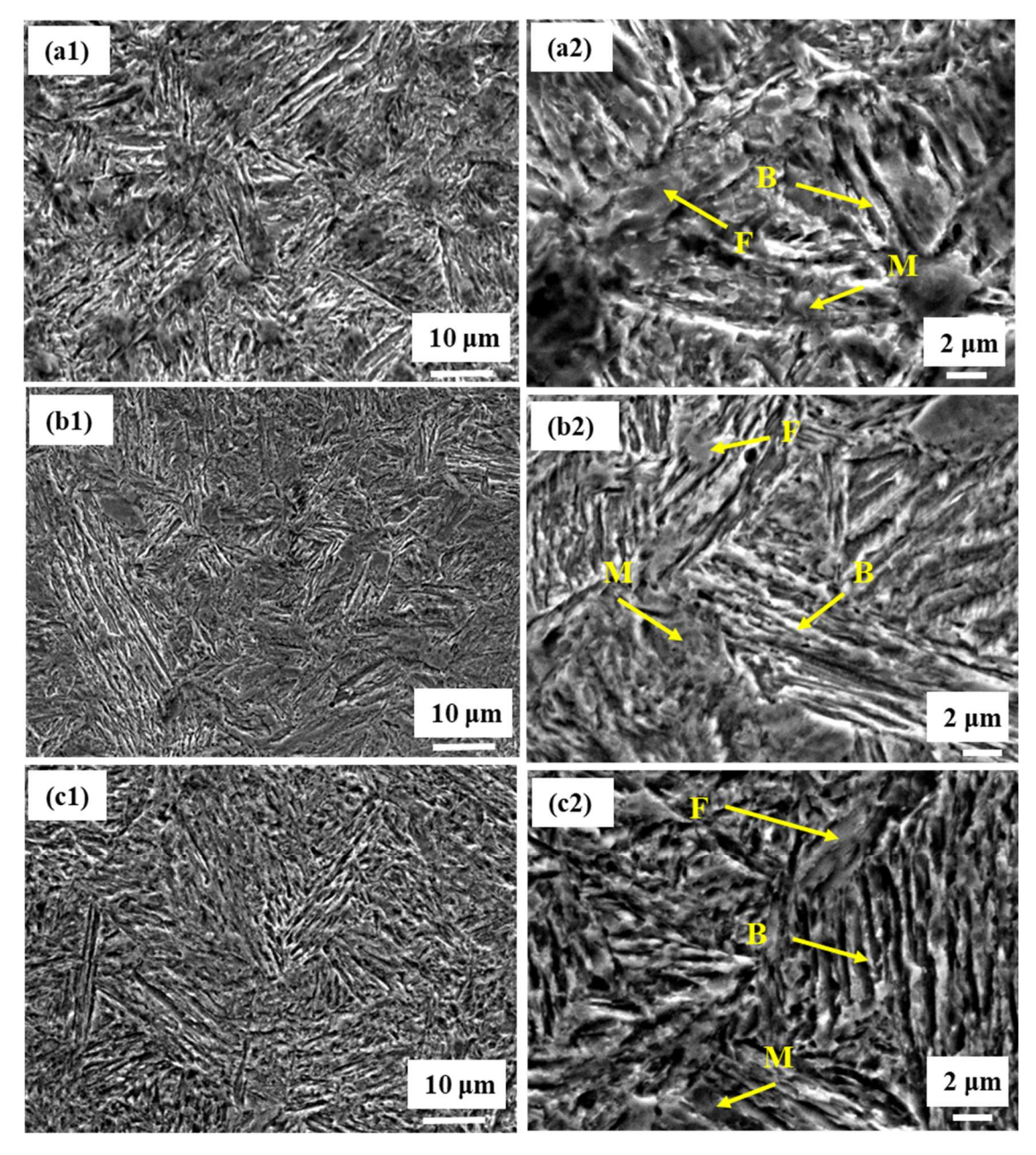


Figure 5.5 Field emission scanning electron micrographs of steels hot rolled at 900 °C, 20 min., (a1, a2) Alloy 1 (Fe-4Mn-1.5Si), (b1, b2) Alloy 2 (Fe-6Mn-1.5Si), (c1, c2) Alloy 3 (Fe-8Mn-1.5Si).

Table 5.2 Phase estimation of developed alloys with variation in Mn hot rolled at 900 °C.

Novel AHSS hot rolled at 900 °C							
Alloy/Phase Bainite Ferrite Martensite RA							
Alloy 1 (Fe-4Mn-1.5Si)	23	67	2.05	8			
Alloy 2 (Fe-6Mn-1.5Si)	25	65	1.6	10			
Alloy 3 (Fe-8Mn-1.5Si)	27	59.8	2	12			

5.3.2.2 Effect of silicon (Si) alloying

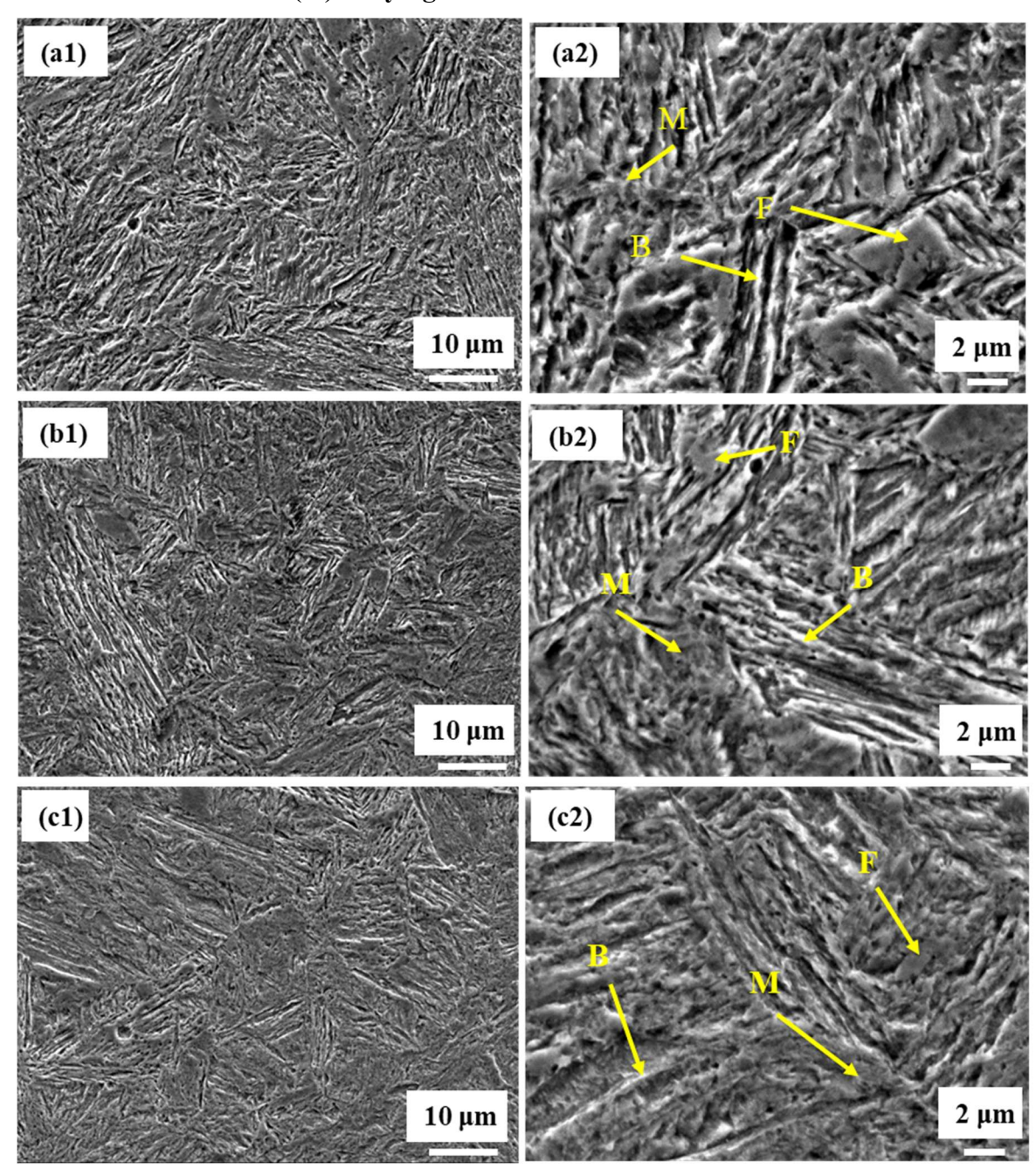


Figure 5.6 Field emission scanning electron micrographs of steels hot rolled at 900 °C, 20 min., at 2500X, (a1, a2) Alloy 4 (Fe-6Mn-1.0Si), (b1, b2) Alloy 2 (Fe-6Mn-1.5Si), (c1, c2) Alloy 5 (Fe-6Mn-2.0Si).

Table 5.3 Phase estimation of Alloys with variation in Si hot rolled at 900 °C.

Novel AHSS hot rolled at 900 °C							
Alloy/Phase Bainite Ferrite Martensite RA							
Alloy 4 (Fe-6Mn-1.0Si)	33	55.25	2.05	10			
Alloy 2 (Fe-6Mn-1.5Si)	25	65	1.6	10			
Alloy 5 (Fe-6Mn-2.0Si)	17	67.85	1.35	14			

The micrographs of Alloy 4, Alloy 2, and Alloy 5 are shown in Figure 5.6 (a2, b2, c2). The silicon is varied from 1 to 2 wt.% in the Alloy 4, Alloy 2 and Alloy 5. Similar phases, as described in Figure 5.5, were also observed in the micrographs of Alloy 4 and Alloy 5, as shown in Figure 5.6 (a2, c2). The volume fractions of bainite decreases from 33 vol.% to 17 vol.% with increase in Si from 1-2 wt.%. Since the silicon is a ferrite stabilizer, hence the volume fraction of ferrite increases from 55.25 vol.% to 67.85 vol.% with increase in silicon from 1 to 2 wt.%. The martensite is found between 1-2 wt.% in the developed in the Alloy 4, Alloy 2 and Alloy 5. The volume of retained austenite does not change significantly with variation of Si from 1 to 2 wt.%. The similar microstructures with different processing route are reported [72], [35][73], [74], [75], [76].

5.3.3 X-ray Diffraction of hot-rolled at 900 °C

The XRD patterns of hot-rolled alloys at 900 °C for Alloy 1, Alloy 2, and Alloy 3 are represented in Figure 5.7. The four peaks are matched to lattice planes (110), (200), (211), and (220) of α-ferrite; one low intense peak at 42.6 corresponds to retained austenite and matched with (111) lattice plane. Similar peaks were also obtained for Alloy 4, Alloy 2, and Alloy 5, with the difference that retained austenite peak is more prominent in the alloys in which the silicon was varied from 1 to 2 wt.%, as shown in Figure 5.8. The peak positions are listed in Tables 5.4 and 5.4 for Mn and Si variations. Mattia Franceschi et al. reported similar peaks in the case of Fe-0.430C-3.260Si-2.72Mn (wt.%) steel [35].

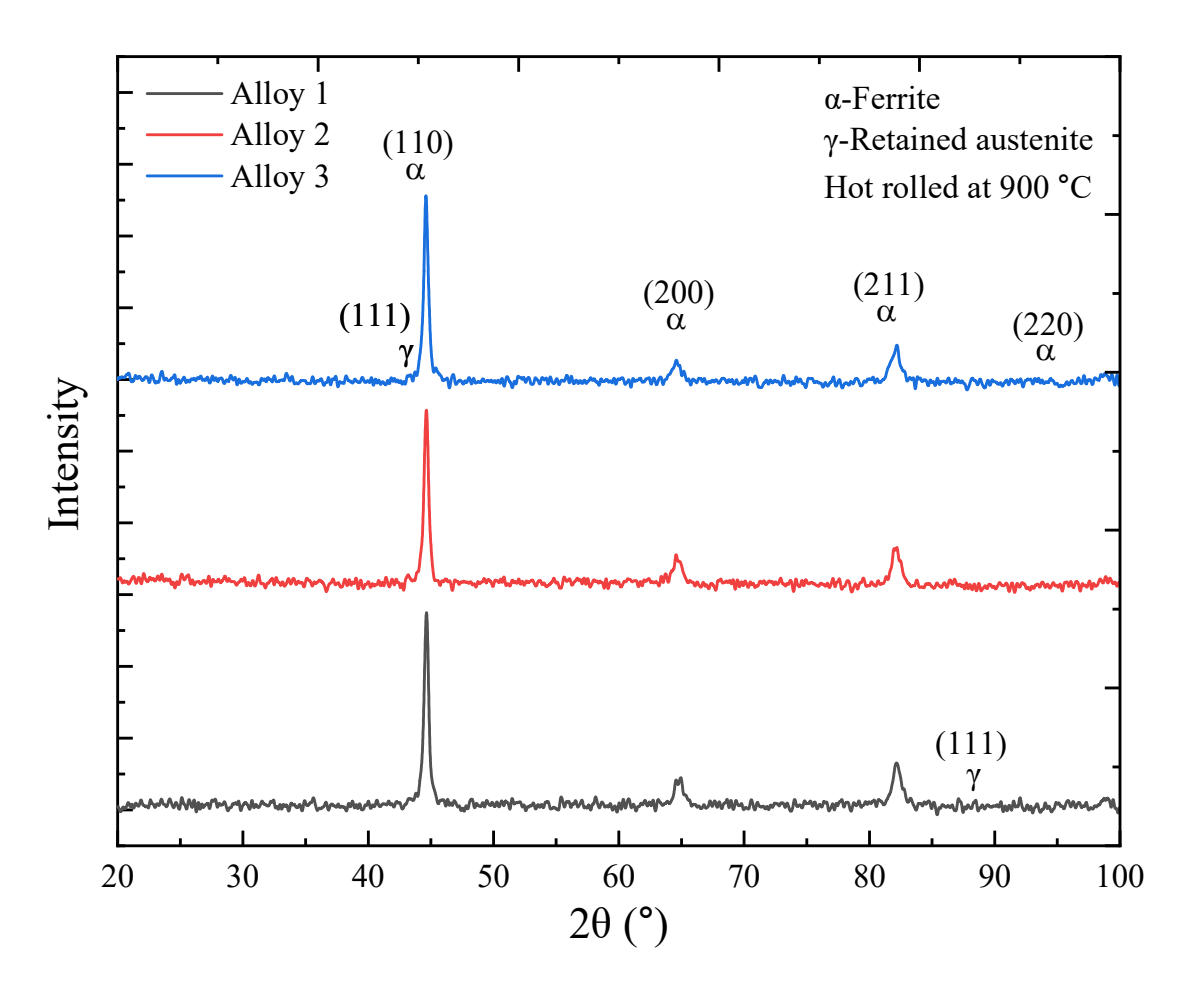


Figure 5.7 XRD spectra of AHSS hot-rolled at 900 °C, Alloy 1 (Fe-4Mn-1.5Si), Alloy 2 (Fe-6Mn-1.5Si), and Alloy 3 (Fe-8Mn-1.5Si).

Table 5.4 Peak positions of Alloy 1, Alloy 2, and Alloy 3 hot-rolled at 900 °C, (retained austenite, γ_A) with an increase in Mn contents.

Alloy/	α-ferrite,	α-ferrite,	α-ferrite,	α-ferrite,	(γΑ)
(hkl)	(110)	(200)	(211)	(220)	(111)
Alloy 1	44.66	64.92	82.16	98.91	43.40
Alloy 2	44.66	64.61	82.12	98.82	43.25
Alloy 3	44.66	64.52	82.16	98.68	43.15

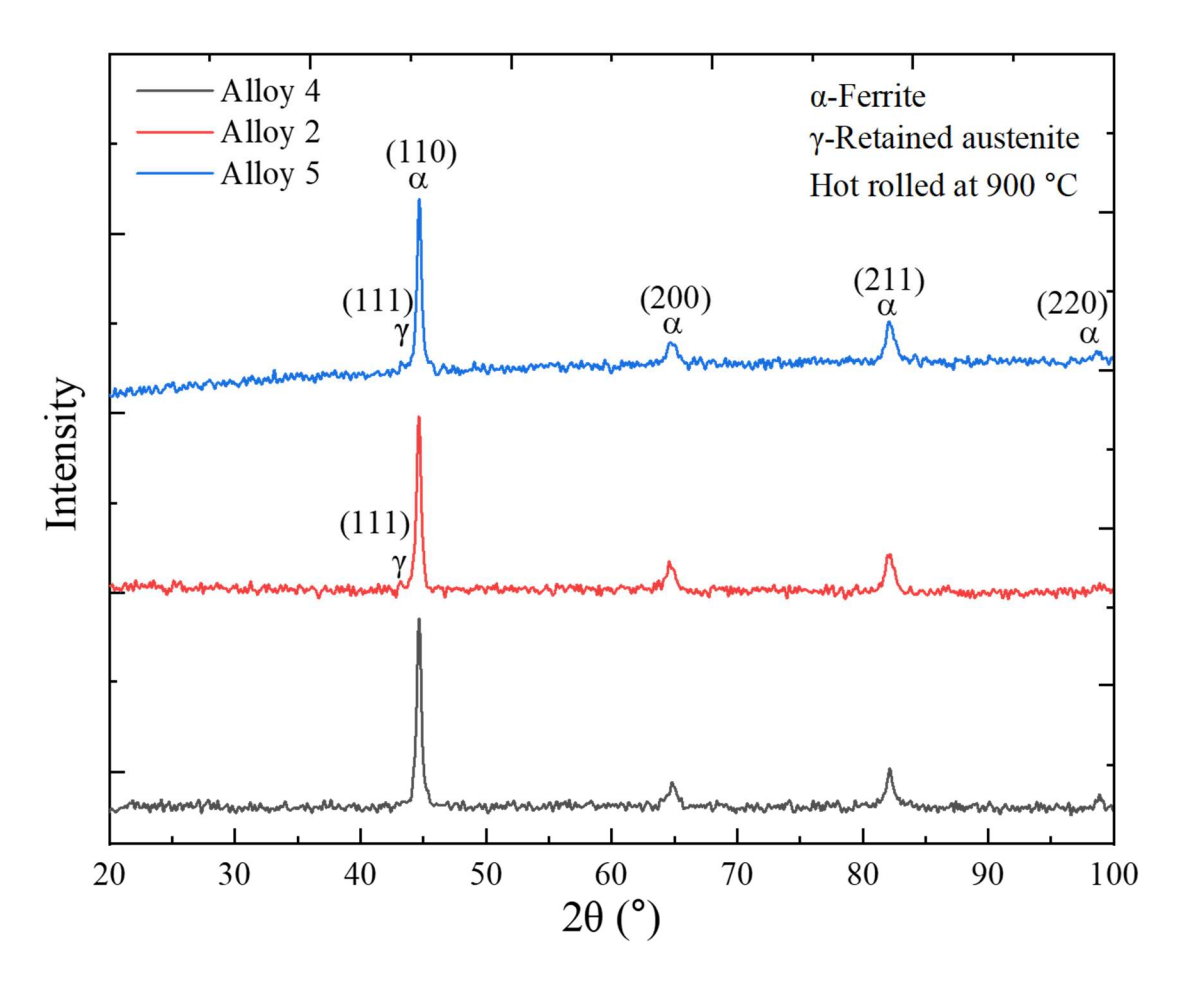


Figure 5.8 XRD spectra of AHSS hot-rolled at 900 °C, Alloy 4 (Fe-6Mn-1.0Si), Alloy 2 (Fe-6Mn-1.5Si), and Alloy 5 (Fe-6Mn-2.0Si).

Table 5.5 Peak positions of alloy 4, alloy 2, and alloy 5 homogenized at 1200 °C for 5 hours of soaking. (retained austenite, γ_A) with an increase in Si contents.

Alloy/	α-ferrite,	α-ferrite,	α-ferrite,	α-ferrite,	(γ _A),
(hkl)	(110)	(200)	(211)	(220)	(111)
Alloy 4	44.53	64.81	82.16	98.89	43.34
Alloy 2	44.66	64.61	82.12	98.82	43.25
Alloy 5	44.66	64.72	82.05	98.57	43.29

5.3.4 Mechanical Properties of hot-rolled at 900 °C

5.3.4.1 Microhardness measurements of hot-rolled at 900 °C

Table 5.6 Microhardness values of alloys hot-rolled at 900 °C.

Microhardness (VHN) Hot Rolled 900 °C, Load: 300 gf							
Sr No.	Alloy 1 Alloy 2 Alloy 3 Alloy 4 Alloy 5						
Average	517	546	565	540	596		
Stdev.	19	27	31	10	21		

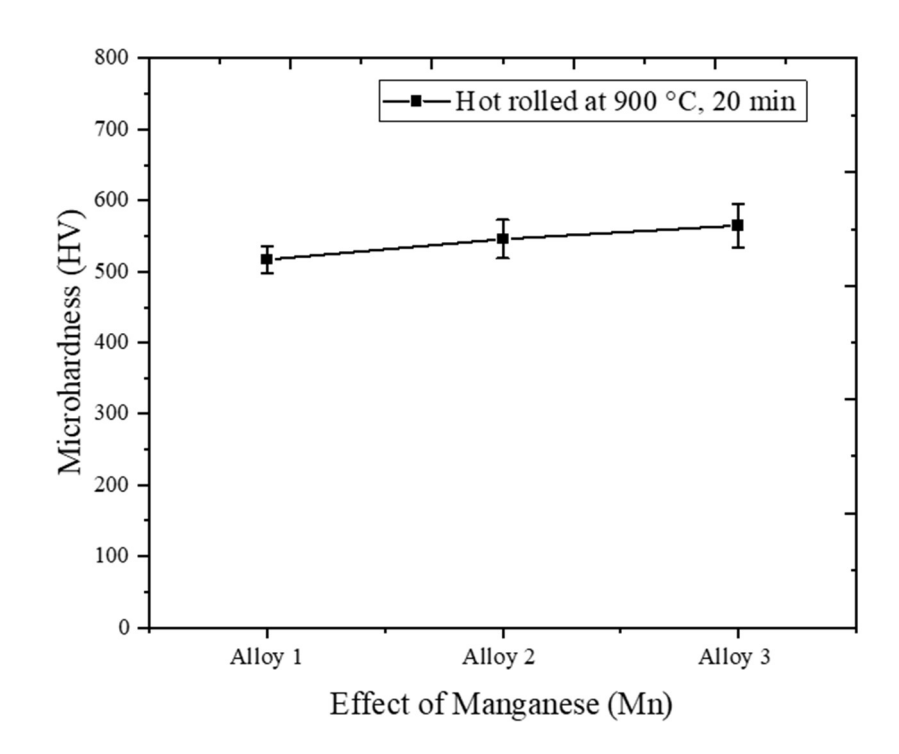


Figure 5.9 Microhardness of novel AHSS hot-rolled at 900 °C, Alloy 1 (Fe-4Mn-1.5Si), Alloy 2 (Fe-6Mn-1.5Si), and Alloy 3 (Fe-8Mn-1.5Si).

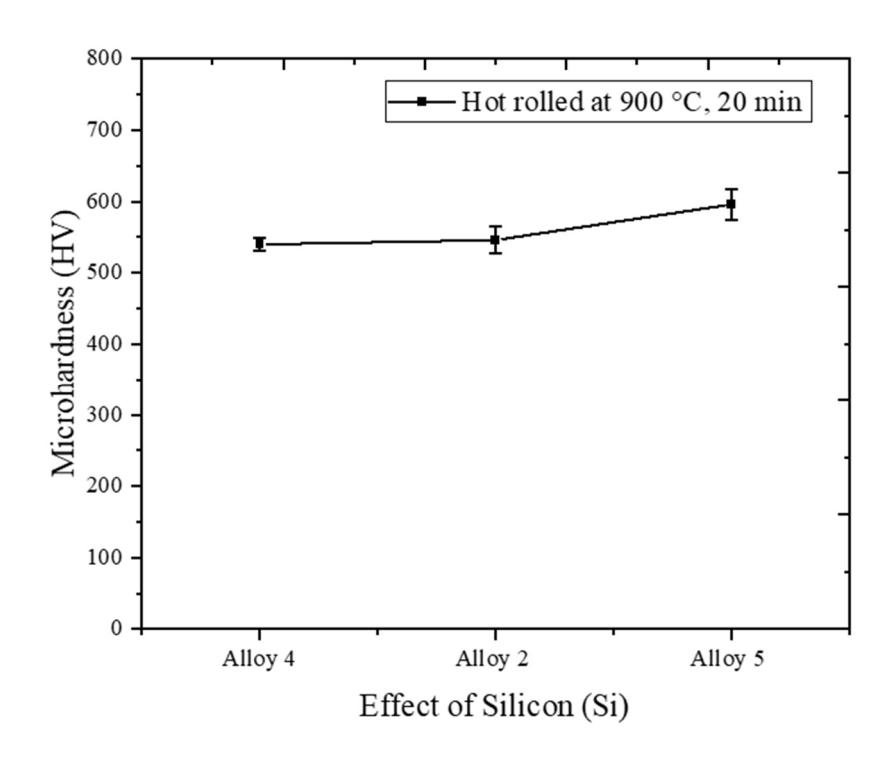


Figure 5.10 Microhardness of novel AHSS hot-rolled at 900 °C, Alloy 4 (Fe-6Mn-1.0Si), Alloy 2 (Fe-6Mn-1.5Si), and Alloy 5 (Fe-6Mn-2.0Si).

The microhardness values were measured by applying a load of 300 gf and selecting the dual time for 10 seconds. The microhardness measurements were repeated 10 times, and the average values are represented in Table 5.6. The microhardness values are measured in the range of 517 to 596 for all five alloys. The effect of Mn on the microhardness of hotrolled steel at 900 °C is presented in Figure 5.9, which shows the increasing trend from Alloy 1 to Alloy 3. The maximum microhardness among Alloy 1, Alloy 2, and Alloy 3 is 565 VHN for Alloy 3, while the lowest value is 517 VHN for Alloy 1. This indicates that the microhardness increases with increasing Mn contents in the novel AHSS which is probably due to an increase in bainite contents in the alloys. The effect of silicon (Si) additions on microhardness is also shown in Figure 5.10, which shows the same trend as discussed in Figure 5.9. The maximum value of microhardness of 596 VHN is obtained for Alloy 5. It is clear from Figure 5.10 that microhardness increases with the addition of silicon contents to the AHSS which makes steel hard and brittle by strengthening the microstructure.

The stress-strain curves are shown in Figure 5.11 for Alloy 1, Alloy 2, and Alloy 3. The ultimate tensile strengths are obtained at 1418 MPa, 1457 MPa, and 1625 MPa for Alloy 1, Alloy 2, and Alloy 3, respectively. The total elongation was measured at 17.28%, 16.27%, and 14.84% for Alloy 1, Alloy 2, and Alloy 3 respectively. The tensile strength increases with an increase in Mn content from 4 wt.% to 8 wt.%, while the total elongation decreases with an increase in Mn. The high tensile strength is attributed from TRIP effect.

5.3.4.2 Stress-Strain curves

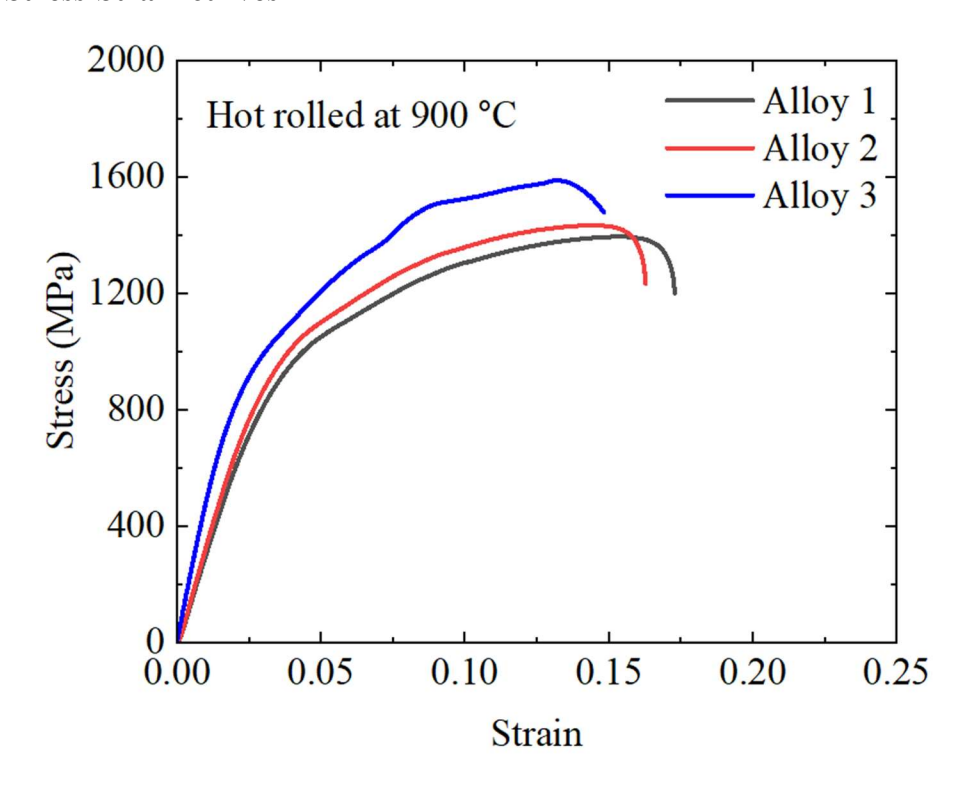


Figure 5.11 Stress-strain curves of novel AHSS hot-rolled at 900 °C, Alloy 1 (Fe-4Mn-1.5Si), Alloy 2 (Fe-6Mn-1.5Si), and Alloy 3 (Fe-8Mn-1.5Si).

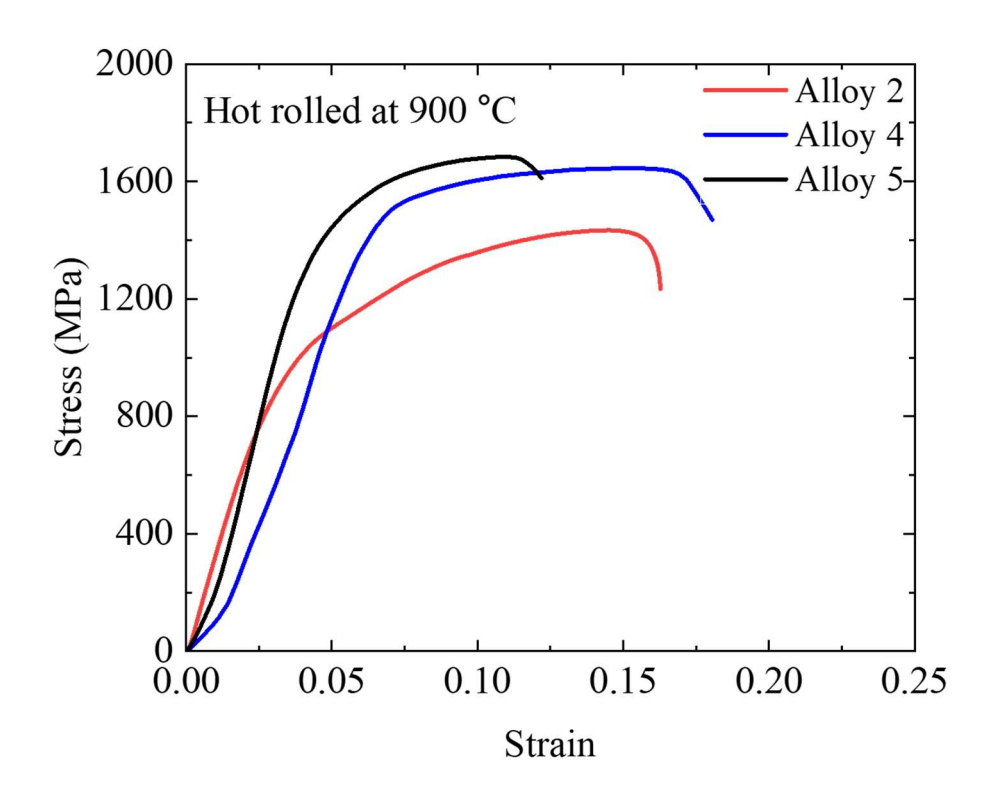


Figure 5.12 Stress-strain curves of novel AHSS hot-rolled at 900 °C, Alloy 4 (Fe-6Mn-1.0Si), Alloy 2 (Fe-6Mn-1.5Si), and Alloy 5 (Fe-6Mn-2.0Si).

The stress-strain curves for Alloy 4, Alloy 2, and Alloy 5 are presented in Figure 5.12. The ultimate tensile strengths are obtained at 1652 MPa, 1457 MPa, and 1690 MPa for Alloy 4, Alloy 2, and Alloy 5, respectively. The total elongation was measured at 18.1%, 16.3%, and 12.2% for Alloy 4, Alloy 2, and Alloy 5, respectively. It is observed from Figure 5.12 that a high strength of 1690 MPa is obtained for Alloy 5, which has 2 wt.% silicon. The addition of silicon decreases the elongation and makes steel hard and brittle. The mechanical properties evaluated from stress strain curves are shown in Table 5.7

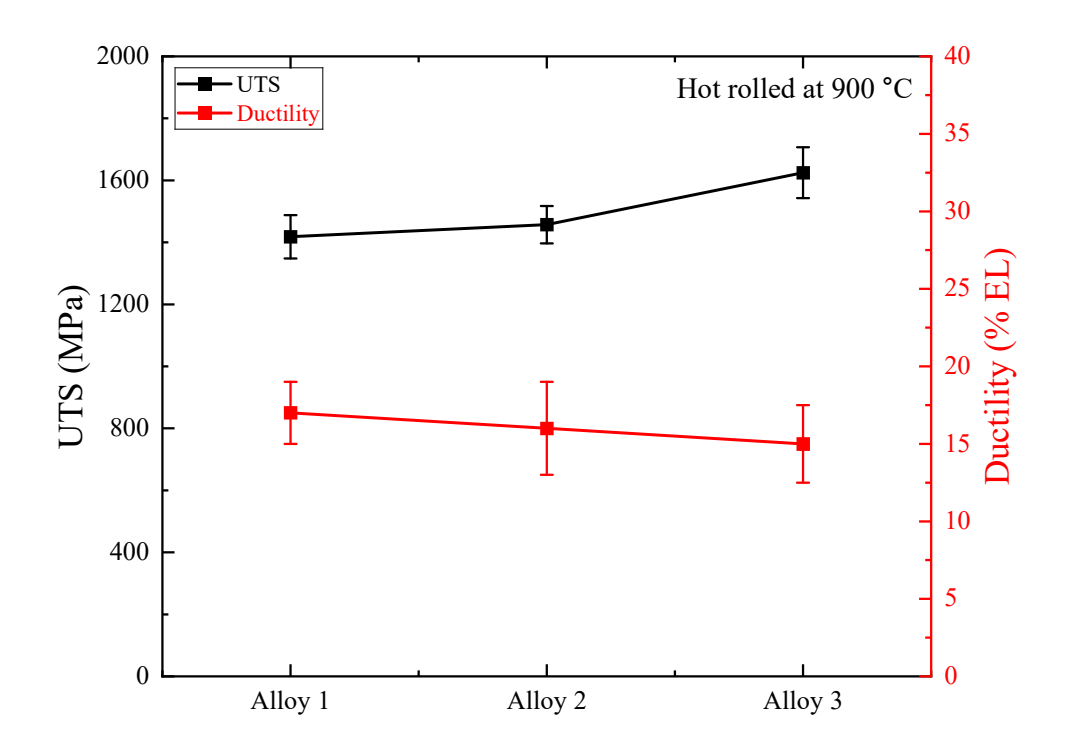


Figure 5.13 Effect of manganese (Mn) alloying in the novel AHSS hot-rolled at 900 °C, Alloy 1 (Fe-4Mn-1.5Si), Alloy 2 (Fe-6Mn-1.5Si), and Alloy 3 (Fe-8Mn-1.5Si).

The variation of the ultimate tensile strength and ductility with increasing Mn contents is shown in Figure 5.13. It is observed from Figure 5.13 that the ultimate tensile strength increases with an increase in Mn content, and the total elongation decreases with an increase in Mn content in the AHSS. The variation of the ultimate tensile strength and ductility with increasing Si contents is shown in Figure 5.14 which shows slight increase in UTS and decreasing elongations due to increase in hardness.

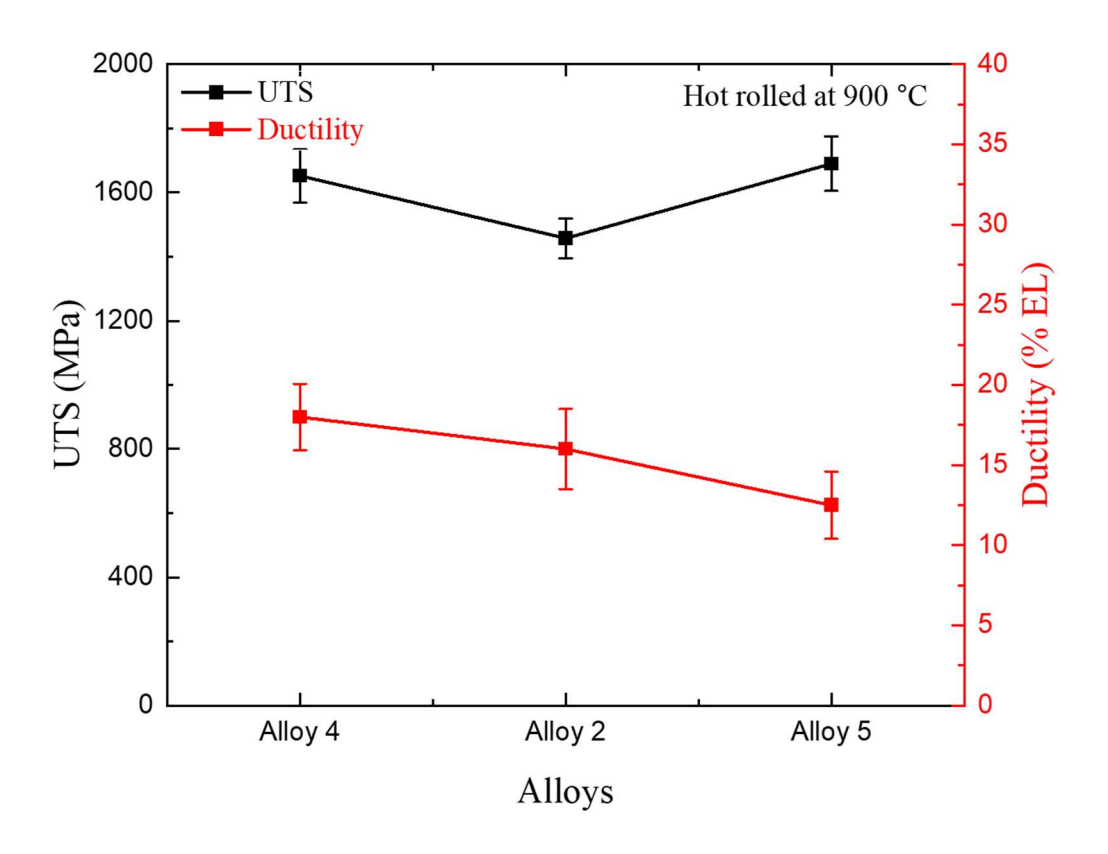


Figure 5.14 Effect of silicon (Si) alloying in the novel AHSS hot-rolled at 900 °C, Alloy 4 (Fe-6Mn-1.0Si), Alloy 2 (Fe-6Mn-1.5Si), and Alloy 5 (Fe-6Mn-2.0Si).

Table 5.7: Mechanical properties of novel AHSS hot-rolled at 900 °C.

Novel AHSS	Ultimate Tensile Strength σ _u (MPa)	Yield Strength σ _y (MPa)	Elongation El (%)
Alloy 1	1418 ± 42	840 ± 25	17.28 ± 0.5
Alloy 2	1457 ± 44	855 ± 26	16.27 ± 0.48
Alloy 3	1625 ± 49	871 ± 24	14.84 ± 0.45
Alloy 4	1652 ± 50	873 ± 27	18.1 ± 0.55
Alloy 2	1457 ± 44	855 ± 26	16.27 ± 0.48
Alloy 5	1690 ± 51	1390 ± 42	12.2 ± 0.35

5.3.5 Fracture Analysis

5.3.5.1 Effects of Mn alloying

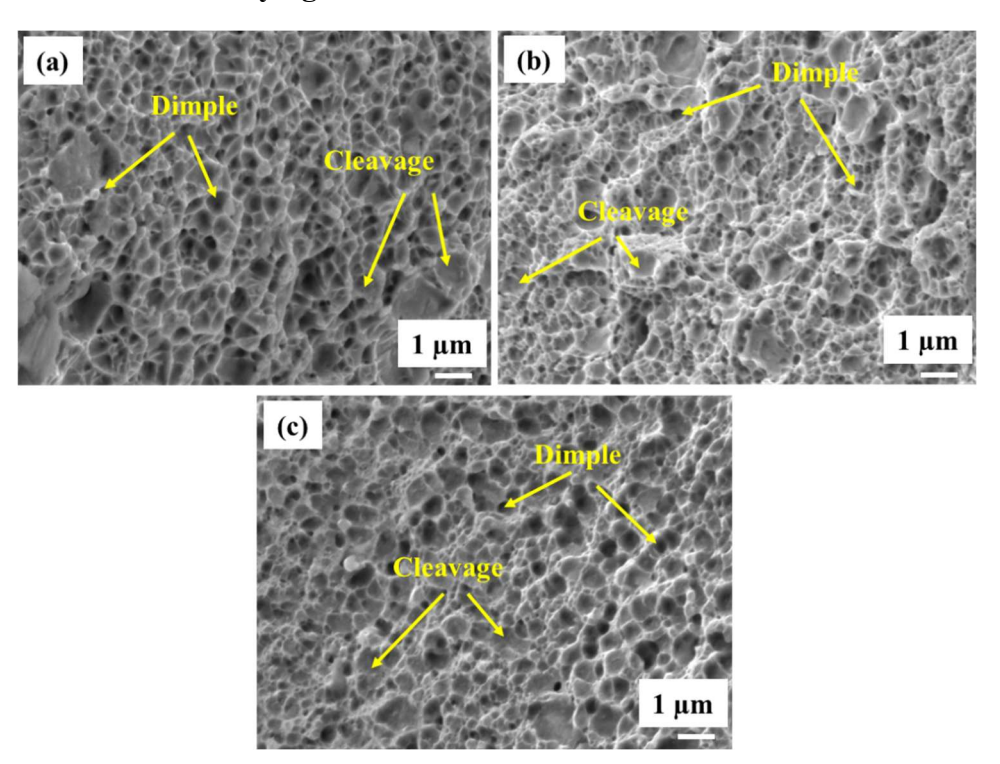


Figure 5.15 Fractographs of novel AHSS hot rolled at 900 °C at 4000X: (a) Alloy 1 (Fe-4Mn-1.5Si), (b) Alloy 2 (Fe-6Mn-1.5Si), and (c) Alloy 3 (Fe-8Mn-1.5Si).

FE-SEM analysis of fracture surfaces was carried out after tensile tests for the developed alloys, and the fractorgraphs are shown in Figure 5.15. The presence of dimples indicates a ductile fracture of Alloy 1. The dimples as well as facets are observed in the fractographs of Alloy 2. This mixture of dimples and facets indicates ductile fracture with less elongation than that of Alloy 1. Dimples and facets are also observed in the fractographs of Alloy 3, but relatively lower dimples as compared to Alloy 1 and Alloy 2; however, larger numbers of facets are observed in Alloy 3. These results confirm that Alloy 3 also follows ductile fracture with a lower elongation limited to around 15%. The number of dimples decreases with the addition of Mn contents to the alloys. The fewest dimples and more facets are seen in the fractographs of Alloy 3, which has an 8 wt.% manganese addition (as shown in Figure 5.15). More dimples and fewer facets are found in Alloy 1,

which has 4 wt.% manganese addition. Alloy 1 also exhibits higher ductility, up to 17.28%, which is more than Alloy 2 and Alloy 3. The moderate ductility is measured for Alloy 2, which has 6 wt.% manganese alloying. Overall, all three alloys, Alloy 1, Alloy 2, and Alloy 3, show a ductile failure mechanism with differences in ductility. Similar results were also reported [55] [71].

5.3.5.2 Effects of Si alloying

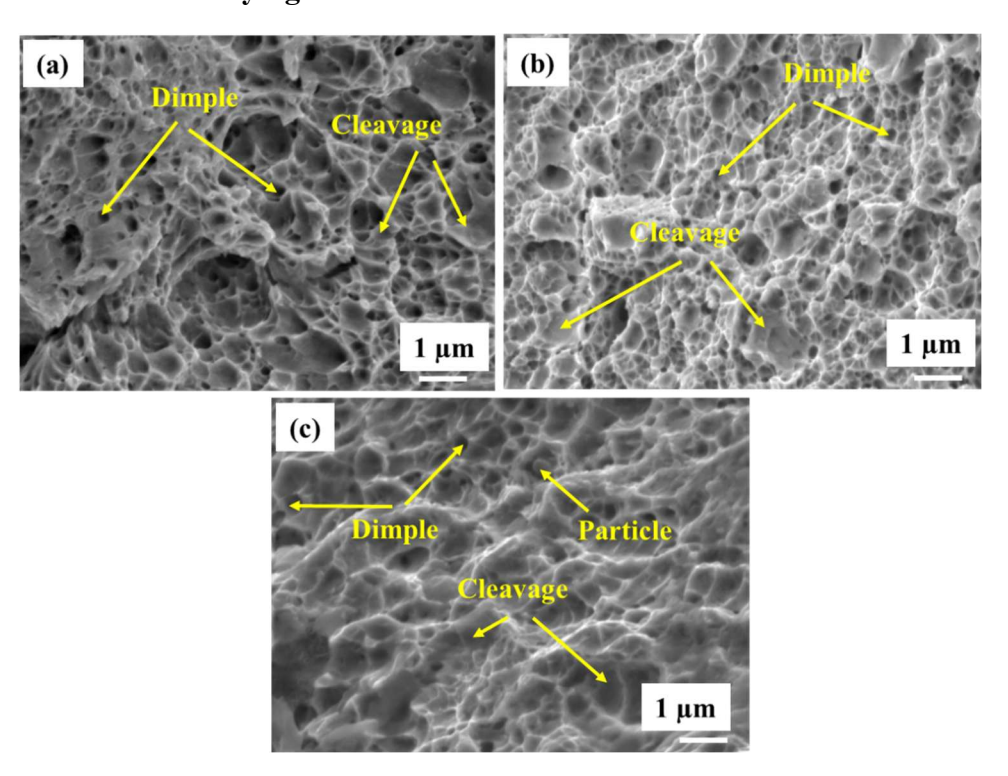


Figure 5.16 Fractographs of novel AHSS hot rolled at 900 °C, at 5000X (a) Alloy 4 (Fe-6Mn-1.0Si), (b) Alloy 2 (Fe-6Mn-1.5Si), and (c) Alloy 5 (Fe-6Mn-2.0Si).

The brittleness is found to increase with increasing silicon. FE-SEM analysis of fracture surfaces was performed after tensile tests for Alloy 4, Alloy 2, and Alloy 5, and the fractographs are presented in Figure 5.16. The material exhibits ductile regions, characterised by predominantly dimples, as well as brittle areas showing mainly cleavage and intergranular fracture. Within the ductile regions, certain areas display a cleavage-dominated behaviour with flat facets. The dimples and facets are observed in the fractographs of Alloy 4, with a higher number of dimples than facets, which indicates that the fracture is mostly ductile. The dimples as well as facets are also found in the

fractographs of Alloy 2, with a difference in the presence of more facets than facets observed in Alloy 4, which is attributed to increasing silicon from 1 to 2.0 wt.%. The failure of Alloy 2 is also ductile, with a moderate elongation that is lower than the elongation of Alloy 4. While fewer dimples and more facets are observed in Alloy 5, it depicts lower elongation than Alloy 4 and Alloy 2. Hence, the lowest ductility of 12.2 is achieved in Alloy 5 [77], [78], [79].

5.4 Discussion

5.4.1 Structure Property-corelation: Effect of Mn alloying

The phase diagrams are calculated with variation in Mn while keeping all other alloying additions constant. The types of phases and no of phases may be different as our process is not in equilibrium. The cooling rate in air is estimated 3.5 °C/s. The microstructure of AHSS developed after multi-pass hot-rolling followed by air cooling reveals ferrite, bainite laths martensite, and retained austenite. The phase fraction varies due to variations in manganese additions from 4 to 8 wt.%. The manganese promotes the formation of bainite. The fraction of bainite laths increases from 23 vol.% to 27 vol.% by increasing manganese from 4 to 8 wt.%. Insignificant effect of Mn addition has been observed in cases of martensitic transformation which is varying 1-2 vol.%. Since Mn is an austenite stabilizer, it enhances the vol.% of austenite from 8 to 12 vol.%. The segregation regions were not observed in the FE-SEM micrographs of all three alloy compositions with Mn variations. The microstructures are complex, hence, the AHSS developed in this work can be classified as CP-AHSS. Similar microstructures are reported in [16], [23], [35]. The stress-strain curves are plotted using the data obtained from uniaxial tension tests in rolling directions. The tensile tests were repeated three times in each condition. The ultimate tensile strength increases from 1418 to 1625 MPa with an increase in Mn contents from 4 to 8 wt.%, as shown in Figure 5.11. The microstructures contain martensite and bainite phases already existing in the matrix of alloys. The high tensile strength in the range of 1400 to 1600 MPa is observed due to presence of bainite up to 27 vol.%. The tensile strength was found to increase 200 MPa with increase in 6 vol.% bainite. The retained austenite transforms into

martensite during the deformation of the alloys. Consequently, there is an increase in the resistance offered on the path of dislocation movement, leading to high strength, as shown in Table 5.7. This effect is termed as TRIP effect. The estimated volume fractions of the phases are shown in Table 5.7. The total elongations are observed to decrease with an increase in Mn contents due to an increase in the vol.% of bainite and martensite phases in the microstructure as shown by Figure 5.11. The bainite and martensite are the hard phases. Hence, the elongation decreases with an increase in vol.% of these hard phases. In spite of bainite and martensite in the microstructure, the total elongations have not dropped significantly due to presence of retained austenite in the microstructure. Similar properties of medium manganese AHSS have been reported [9], [35], [48], [37].

The microhardness is found to be increasing from 517 to 565 VHN with an increase in bainite from 23 to 27 vol.% and martensite from 1.6 to 2.05 vol.%, as shown in Table 5.7. As bainite and martensite are hard phases, the hardness is observed to increase by 48 VHN with an increase in 4 vol.% bainite and 0.4 vol.% martensite. Similar hardness is reported in the work-[35], [80].

5.4.2 Structure Property-corelation: Effect of Mn alloying

The volume fractions of bainite decreases from 33 vol.% to 17 vol.% with increase in Si from 1-2 wt.%. Since the silicon is a ferrite stabilizer, hence the volume fraction of ferrite increases from 55.25 vol.% to 67.85 vol.% with increase in silicon from 1 to 2 wt.%. The martensite is found between 1-2 wt.% in the developed in the Alloy 4, Alloy 2 and Alloy 5. The volume of retained austenite does not change significantly with variation of Si from 1 to 2 wt.%. The tensile strength does not change significantly for alloys containing 1 wt.% and 2 wt.% silicon. The similar microstructures with different processing route are reported [72], [35]. The ultimate tensile strengths (UTS) of Alloy 4, Alloy 2, and Alloy 5 are found to increase by 1652 MPa, 1457 MPa, and 1690 MPa with elongation of 18.1%, 16.27%, and 12.2%, respectively. The addition of silicon does not increase UTS for Alloy 4 and Alloy 5. The increase of 1 wt.% Si addition decreases around 6 % the ductility of alloys and increase of 50 MPa UTS which is insignificant. Higher silicon makes the steel brittle and lowers the ductility of steel [34], [81], [82], [83].

5.5 Conclusion

- 1. An advanced high-strength steel has been successfully developed in a vacuum arc melting furnace using high-purity metals. The time-temperature transformation was developed using materials property software.
- 2. The microstructure revealed martensite, ferrite and bainite. The phase fractions are 1-2% martensite, 20-40% bainite, 10-12% retained austenite, and 46-69% ferrite. The presence of retained austenite was also verified by XRD analysis.
- 3. The ultimate tensile strengths (UTS) of Alloy 1, Alloy 2, and Alloy 3 are found to increase by 1418 MPa, 1457 MPa, and 1625 MPa with elongation of 17.28%, 16.27%, and 14.84%, respectively. The addition of manganese increases UTS and hardness while decreasing the ductility of alloys.
- 4. The ultimate tensile strengths (UTS) of Alloy 4, Alloy 2, and Alloy 5 are found to increase by 1652 MPa, 1457 MPa, and 1690 MPa with elongation of 18.1%, 16.27%, and 12.2%, respectively. The addition of silicon does not increase UTS and hardness significantly.
- 5. The fractographs of the five alloys are analyzed. The quantity of dimples is found to decrease by increasing the contents of manganese, which results in a drop in ductility. The fracture failure mechanism is a ductile failure with the formation of some extent of facets, which reduces elongations in the respective alloys. The elongation decreases with increase in silicon.
- 6. The alloys developed in this investigation are candidate materials that can replace existing materials used for automobile body in white (BIW) parts.

Chapter 6 Thermo-mechanical treatment at 1100 °C and mechanical properties

6.1 Introduction

In the present chapter, novel medium manganese steels with silicon additions have been explored and investigated for automotive application that provide tensile strength of more than 1 GPa with an elongation of 10 to 17 %. The nanoscale characterisation using Atom Probe Tomography (APT) has been performed to understand the nano-scale elemental distribution and its effect on the mechanical response of developed steels. It also involves establishing a simpler process to manufacture advanced high-strength steels for the automotive industries. The present investigation reports formation of bainite in hot rolled and air-cooled specimen and formation of complex-phase structure reaching a strength more than 1 GPa.

Over the last 13 years, a significant amount of research has been conducted on medium-Mn steels. According to Gibbs et al., a Fe-7.10Mn-0.10C steel that was annealed at 873 K for one week had tensile strength and total elongation of 876.0 MPa and 42.0%, Shi et al. studied four steels with Fe-5.0Mn-0.2-0.4C chemical respectively [50]. composition, revealing that they achieved 31.0-44.5 percent elongation and 950 to 1420 MPa tensile strength after six hours of annealing at 923 K [84]. Suh et al. proposed alloying Al element to medium Mn Fe-0.12 C-5.0 Mn-0.50 Si steels to elongation of 25% and reduce annealing time upto 3 min for continuous annealing process [32]. Hu et al. found that a vanadium-microalloyed Mn steel improved yield strength by allowing vanadium carbide particles to precipitate in delta-ferrite [85]. The Cu-containing medium Mn duplex lightweight of composition Fe-0.5C-12Mn-7Al-(0, 3)Cu (wt.%) steels were developed, and further research on this medium was conducted to develop quenching and partitioning steels [36], [86], [87]. H. J. Pan et al. attempted to enhance yield strength of medium manganese Fe-5.6Mn-0.19C-1.2Al-0.05Nb-0.22Mo steels by incorporating microalloying elements, Mo and Nb [88]. In addition, efforts have been made to enhance crashworthiness

while reducing fuel consumption and CO₂ emissions. Manganese enhances tensile strength and hardness in hot rolled steel sheets after intercritical annealing. Carbon increases austenite volume fraction but decreases due to cementite formation. Silicon enhances strength and elongation. Higher manganese content increases austenite volume fractions. Aluminum additions increase annealing temperatures [89].

HEXRD analysis of a Fe-0.150C-5.560Mn-1.10Si steel with 1.8 % aluminium revealed an increase in austenite fraction during isothermal holding, influenced by carbon partitioning and diffusion simulations [90]. Carbon clusters were found in martensitic ferrite matrix of various steels with different Si variants and partitioning temperatures, varying in content between 10-12 at.%, possibly indicating η-carbide precipitation in hot rolled followed by quenching and partitioning of Fe-0.4C-2.0 Mn-1.51Si-0.02Al-1.0Cr-0.5Ni steel [91]. A mean-field model connecting bulk material thermodynamics data to grain boundary thermodynamics, using Fe-Mn binary alloys, predicts spinodal segregation in the grain boundary, with segregation observed in compositions above a critical value and regular segregation in compositions below the critical composition that is observed by APT in low temperature tempered steel with composition of Fe-7Mn-0.1C-0.5Si [92]. The steel with composition Fe-0.064C-0.2Si-11.7Mn-0.006P-0.003S-2.9Al was cast and hot rolled followed by intercritical annealing. The air-cooled sample's abrupt carbon enrichment at phase boundaries is due to slow cooling rates, especially at low temperatures, allowing carbon to diffuse to interfaces, and low carbon diffusivity of austenite, preventing it from diffusing out of interface regions [79], [93].

A steel of composition Fe-12.20Mn-1.90Ni-0.60Mo-1.21Ti-0.30Al (at.%) after solution treatment and aging. A new austenite layer forms and grows on the residual austenite as a result of partitioning at the martensite/austenite interface, dramatically changing the composition of the austenite [63]. TEM and APT were used to observe the formation of nano-sized austenitic reversion layers at segregation containing martensite grain boundaries in Fe9Mn1.90Ni0.6Mo1.1Ti0.33Al0.1Si0.05C (at.%) steel [62]. The steel of composition Fe12Mn3Al0.05C (wt.%), after intercritical annealing at 585 °C, steel samples show changes in Mn and C composition across austenite grains. Austenite

reversion begins with face-centered cubic nuclei rich in Mn and C, followed by carbon partitioning observed by APT [94]. The study reveals that austenite stability should be adjusted to achieve optimal mechanical properties, while ferrite grain size should coordinate with austenite deformation. The study shows that total elongation increases with deformation temperature [95].

Huseyin Aydin et al. developed the third-generation Advanced High Strength Steels (AHSS) with manganese 5.0 to 10.0 wt.%, the process involves five stages, with the second quenching temperature and carbon partitioning conditions crucial for retaining austenite. The steels achieved a tensile strength up to 1650 MPa and a total elongation of around 20% [23]. Ma et al. investigated the medium manganese steels processed through austenitereverted-transformation (ART) annealing exhibit high strength (800-1600 MPa) and superior ductility 20-65 % [12]. Controlling austenite stability, enhances strain hardening rate, while the combination of transformation-induced plasticity and twinning-induced plasticity improves mechanical properties. Daniella M Pallsico et al. found that retained austenite morphology and composition significantly influence the mechanical properties of medium-Mn steels [96]. The ultimate tensile strength was obtained in the range of 1040 MPa to 1246 MPa with elongation up to 23 %. The formability index (UTS × TE) of Fe-0.15C-6Mn-1.5Al-1Si (wt.%) 3G AHSS medium-Mn is found from 24,000-40,000 MPa%. The tensile strength of Fe-6.150Mn-0.05-1.5Si (wt.%) and Fe-6.0Mn-0.08C-1.50Si-2.0Al-0.08V (wt.%) cold rolled steel annealed at 640 °C and 740 °C are found 1100 MPa and 1200 MPa respectively [46]. Seawoong Lee et al. reported a tensile strength of 1145 MPa with an elongation of 64% in Fe-10Mn-0.3C-3Al-2Si (wt.%) steel [47]. Medium-Mn TRIP steel (Fe-0.2C-6Mn-1.7Si-0.4Al-0.51Cr (wt. %) with cold rolled tempered martensite and martensitic starting microstructures was applied to continuous galvanizing line with heat treatments, tensile strength was obtained in the range of 1390 MPa to 1828 MPa [97]. Theoretical and kinetic simulations were used to describe the precipitation mechanism of carbides during different tempering stages of medium Mn martensite which were confirmed by atom probe tomography (APT) [64].

6.2 Methodology

6.2.1 Thermo-mechanical treatment

The finger-shaped steel samples were homogenised at 1200 °C for 4 hours, as shown in Figure 6.1. After homogenisation, steel samples were hot rolled in a laboratory-scale rolling mill, as described in Section 3.4. The rolling was performed in two stages and at 1100 °C. To perform rolling, the furnace was heated to the predefined temperature of 1100 °C with a heating rate of 6.6 °C per minute. When the furnace reached the target temperature, the samples were placed in the furnace for 20 minutes. One pass of hot rolling was performed, and the rolled samples were again placed in the furnace for 3-5 minutes, and a second pass was performed. Similarly, the 14 passes were applied in rolling operations. In stage one, the initial thickness of 10.6 mm was brought to 2.6 mm in 8 passes. The thickness reduction was kept at 1.0 mm per pass. The thickness of the samples was reduced to 76.5% of the initial thickness. After rolling in the 14th pass, the AHSS developed and were normalized.

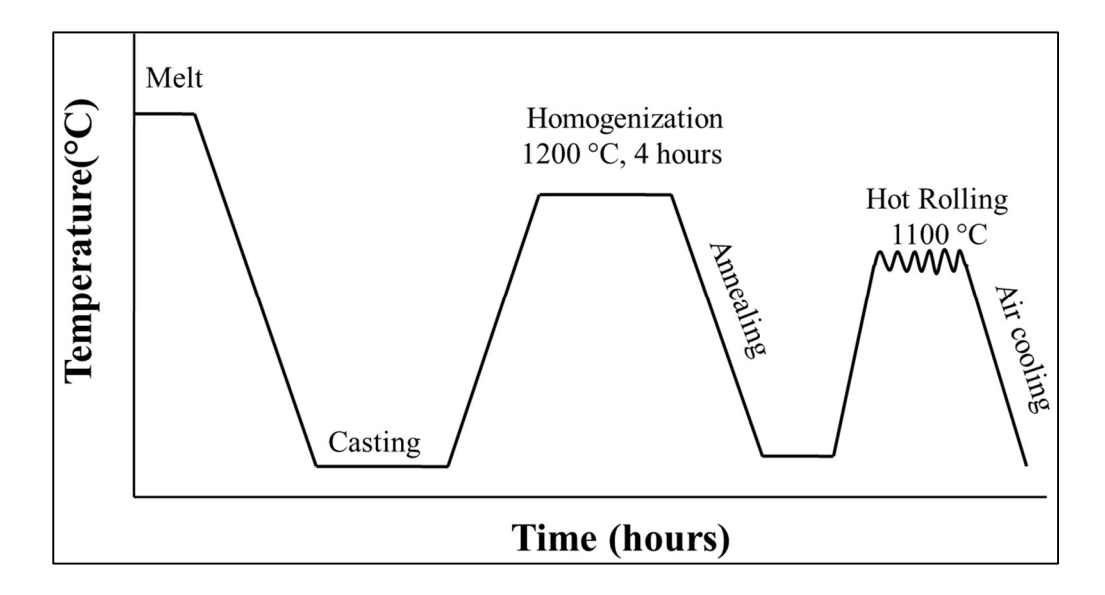


Figure 6.1 The process flow chart for manufacturing advanced high strength steels.



Figure 6.2 The finger-shaped sample is hot rolled to manufacture a sheet, 15 mm wide, and 1.6 mm thick.

The homogenised ingot and hot-rolled sheets are shown in figure 6.2. The strains applied during the rolling operations are shown in Table 6.1. In stage two of hot rolling, the 2.6 mm thickness was reduced to 1.68 mm in six passes, with a thickness reduction of 0.2 mm per pass.

Table 6.1 Strain applied in the rolling operations for the Alloy 1, Alloy 2, Alloy 3, Alloy 4 and alloy 5.

	Rolling parameters							
Rolling stages	Pass number	Initial thickness (mm)	Final thickness (mm)	Strain applied (%)				
	1	10.27	9.27	9.74				
	2	9.27	8.27	10.79				
	3	8.27	7.27	12.09				
Store I	4	7.27	6.27	13.76				
Stage-I	5	6.27	6.27	16.95				
	6	6.27	4.27	18.98				
	7	4.27	3.27	23.42				
	8	3.27	2.27	30.58				
	9	2.27	2.17	4.41				
	10	2.17	2.07	4.61				
Stage II	11	2.07	1.97	4.83				
Stage-II	12	1.97	1.88	4.57				
	13	1.88	1.78	6.32				
	14	1.78	1.68	6.62				

6.2.2 Characterization of hot-rolled steels

The hot-rolled sheets were analysed under an optical microscope and field-emission scanning electron microscope (FE-SEM) to identify the phases. Further, X-ray diffraction was performed to identify the type and number of phases present in the micrographs of novel alloys. The tensile strength was determined using universal testing machine according to the ASTM E8 (ISO 6892) test standard. The microhardness was measured using a microhardness tester. The above-mentioned characterizations are described in sections 3.6.1 to 3.6.6. The phase estimation of the developed alloys was carried out using the ASTM 562-point count method and retained austenite fraction was determined by XRD.

6.2.3 Three-dimensional atom probe tomography

Atom probe tomography (APT) was used to characterize the elemental distribution across phase barriers at nearly atomic scales. A Local Electrode Atom Probe 5000 HR apparatus with an ultraviolet laser (wavelength 355 nm) operating in laser-pulsing mode was used for the measurements. The analyzing chamber's base temperature was maintained steady at 60 K. The pulse frequency and energy of the laser were 200 kHz and 30 pJ, respectively. The dual-beam Helios G4 UX with a focused ion beam was utilized to prepare the APT samples. IVAS 6.3 was the software suite used for the analysis of the APT data.

6.3 Results and discussion

6.3.1 Optical micrographs of hot-rolled at 1100 °C

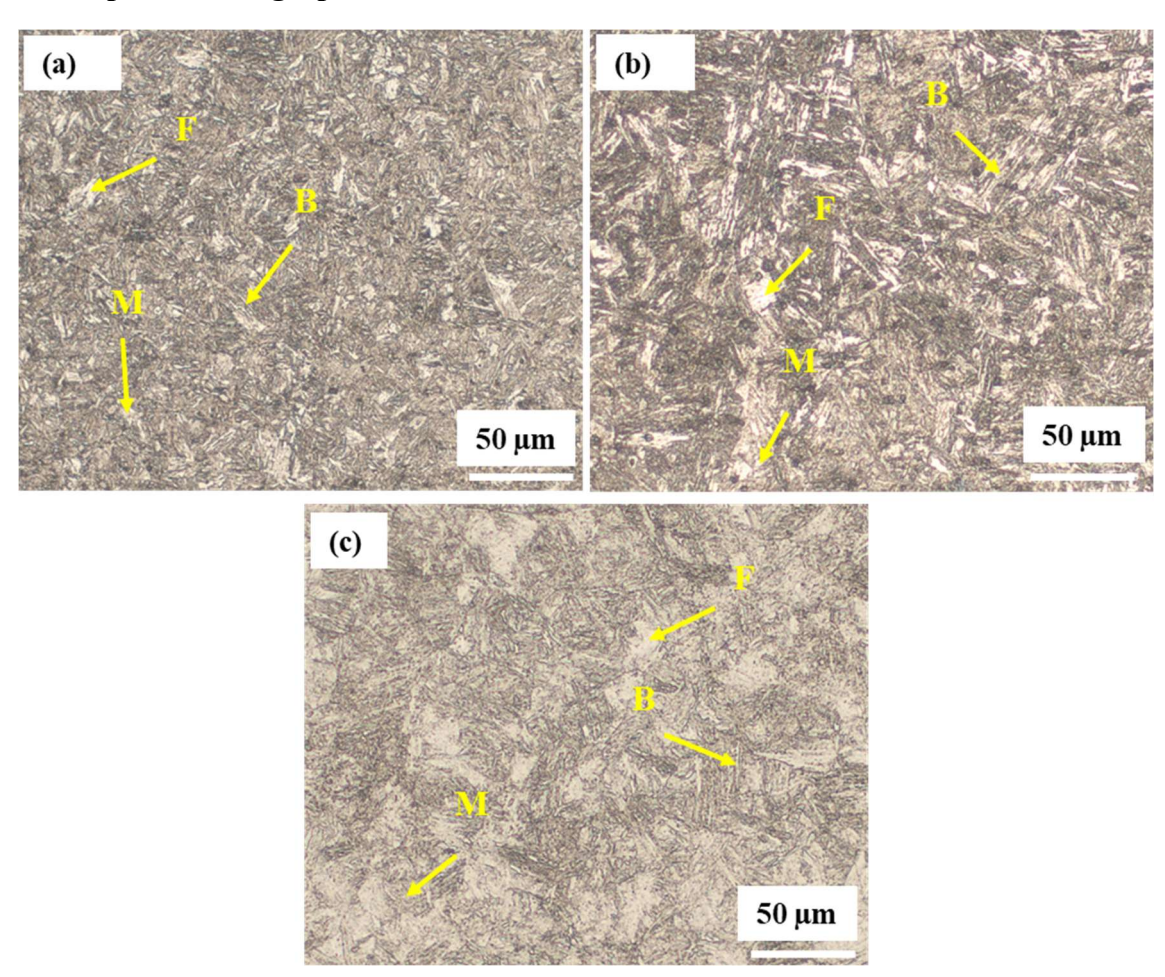


Figure 6.3 Optical micrographs of AHSS steels hot rolled at 1100 °C, (a) Alloy 1 (Fe-4Mn-1.5Si), (b) Alloy 2 (Fe-6Mn-1.5Si), and (c) Alloy 3 (Fe-8Mn-1.5Si).

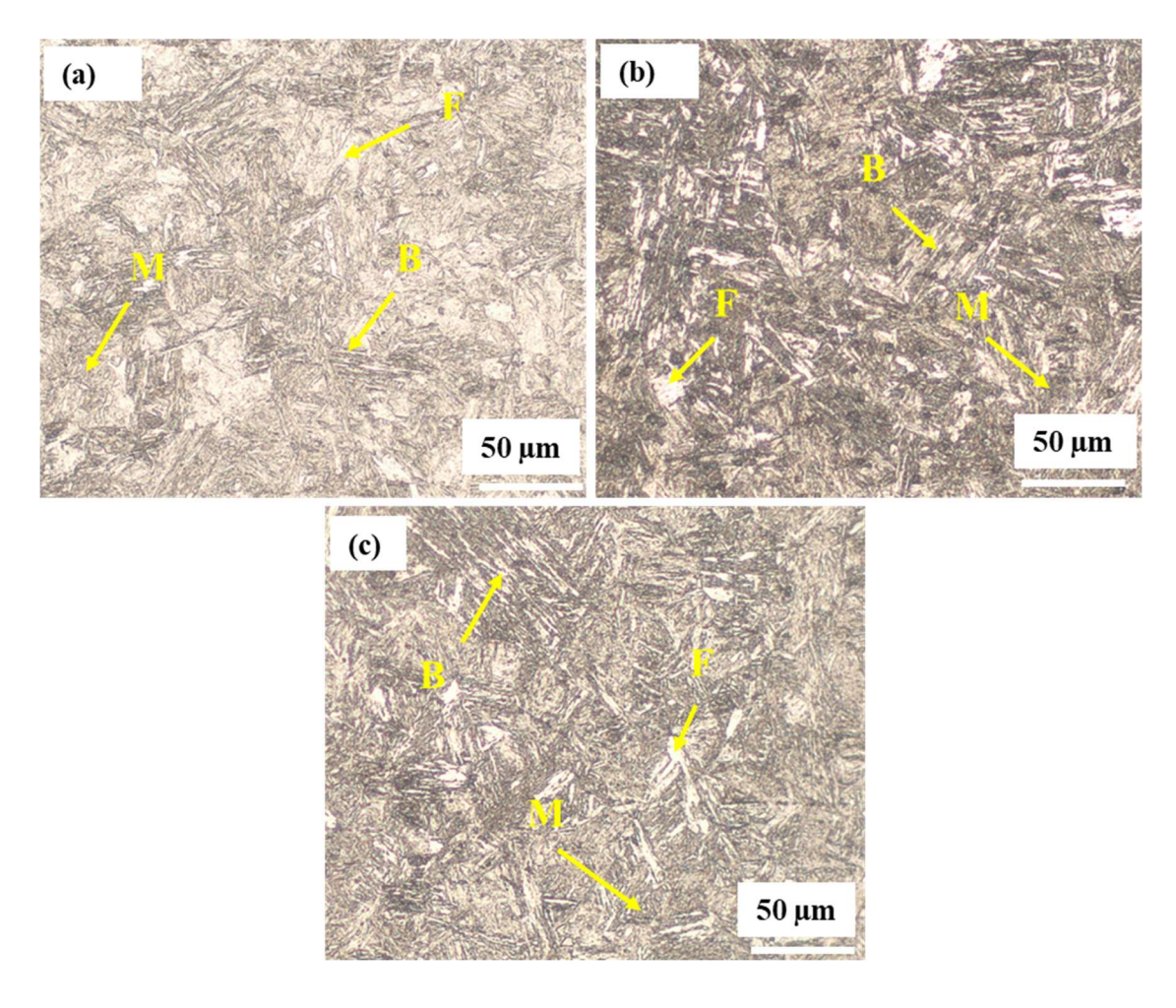


Figure 6.4 Optical micrographs of steels hot rolled at 1100 °C, (a) Alloy 4 (Fe-6Mn-1.0Si), (b) Alloy 2 (Fe-6Mn-1.5Si), and (c) Alloy 5 (Fe-6Mn-2.0Si).

Figure 6.3 (a, b, c) shows the optical micrograph of the advanced high-strength steel hotrolled at 1100 °C (initial soaking for 20 minutes) for Alloy 1, Alloy 2, and Alloy 3, respectively. Figure 6.3 (a) reveals ferrite (bright regions), bainite (bright parallel sheaves), and martensite (grey regions). The similar regions are observed in Figure 6.3 (b, c) also correspond to the same types of phases. Figure 6.4 (a, b, c) represents the optical micrograph of the advanced high-strength steel hot rolled at 1100 °C (initial soaking for 20 minutes) for Alloy 4, Alloy 2, and Alloy 5, respectively. The phases revealed from the micrographs of Figure 6.4 are the same as those discussed in Figure 6.3 (a, b, c).

6.3.2 Field-Emission micrographs of hot rolled at 1100 °C

6.3.2.1 Effect of manganese (Mn) alloying on micrographs

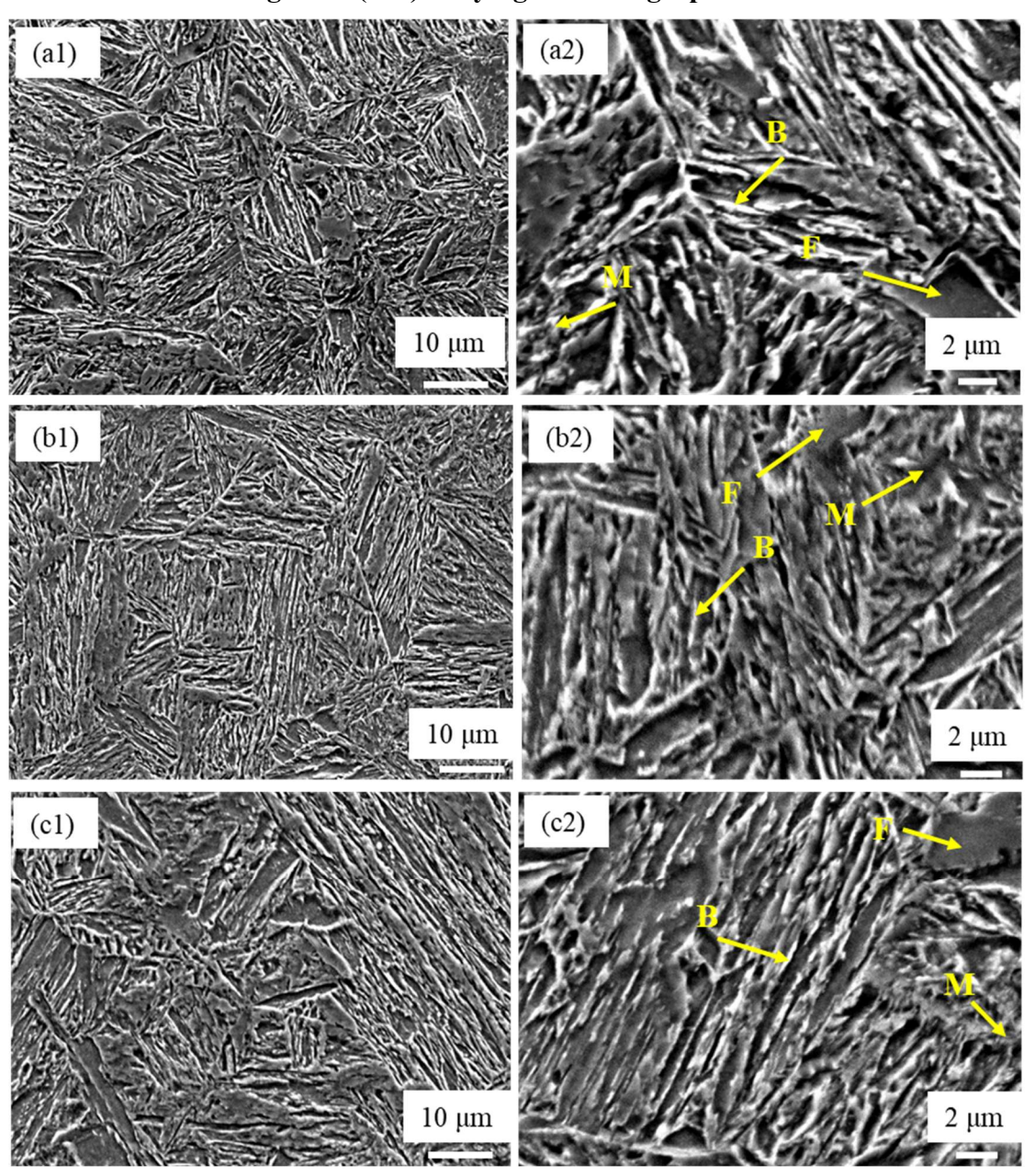


Figure 6.5 Field Emission Scanning Electron micrographs of steels hot rolled at 1100 °C, (a1, a2) Alloy 1 (Fe-4Mn-1.5Si), (b1, b2) Alloy 2 (Fe-6Mn-1.5Si), (c1, c2) Alloy 3 (Fe-8Mn-1.5Si).

Table 6.2: Phase estimation of Alloy 1 (Fe-4Mn-1.5Si), Alloy 2 (Fe-6Mn-1.5Si), and Alloy 3 (Fe-8Mn-1.5Si) hot rolled at 1100 °C.

Novel AHSS hot rolled at 1100 °C							
Alloy/Phase Bainite (vol.%) Ferrite (vol.%) Martensite (vol.%) RA (vol.%) Thickness of bainitic laths (nm)							
Alloy 1 (Fe-4Mn-1.5Si)	27	44.4	18.2	10.4	604		
Alloy 2 (Fe-6Mn-1.5Si)	24	46.6	21.4	9	563		
Alloy 3 (Fe-8Mn-1.5Si)	21	46.4	26.6	8	490		

The addition of manganese from 4 wt.% to 8 wt.% has lowered A1 and A3 temperatures, which were determined using JMatPro software (these transformation temperatures are given in Table 4.1). In addition to lowering A1 and A3 temperatures, the transformation temperatures for bainite, martensite, and ferrite are also lowered by increasing the addition of manganese. The increase in manganese contents in the alloys also increased the incubation time to start the transformation of bainite and other present phases in the microstructure. The FE-SEM micrographs of alloy steels hot-rolled at 1100 °C and soaked for 20 min are shown in Figure 6.5. The bright flat regions in the micrographs are ferrite, the embossed regions are bainite, and the grey flat regions are martensite. The volume fractions of phases revealed in the microstructure are estimated using ASTME 562, the point counting method and retained fraction is determined from XRD. The volume fractions of different phases are given in Tables 6.2 for Alloy 1, Alloy 2, and Alloy 3. The average volume fractions of phases present in the materials are 8 to 10.4 vol.% retained austenite, 21 to 27 vol.% bainite, and 18.2 to 25.6 vol.% martensite, and the balance is ferrite. The volume fraction of bainite increases from 21 to 27 vol.% by increasing the alloying contents of manganese from 4 wt.% to 8 wt.% in the novel AHSS. While the martensite in hot-rolled and air-cooled structures has increased from 18.2 to 25.6 vol.%, the retained austenite has lowered from 10.4 vol.% to 8 vol.%. As the silicon was also added and kept constant (≈ 1.4 wt.%) in Alloy 1, Alloy 2, and Alloy 3, which plays an important role in restricting carbide formation and hence makes available a larger amount of carbon to stabilise the austenite, It is observed that the volume of equiaxed ferrite is higher in Alloy 1, as shown in Figure 6.5 (a2), while the volume of this ferrite is lowest in

Alloy 3, as shown in Figure 6.5 (c2). This is also understood from the microstructure of 6.5 (a2, b2, c2): the volume of ferrite decreases with increasing contents of manganese in the developed AHSS. The microstructures confirm the presence of ferrite, bainite, martensite, and retained austenite. This investigation represents the formation of bainite during air cooling after rolling treatment. similar microstructures with different processing methods were reported in [72]-[35]. Kazi M. H. Bhadhon et al. reported carbide, ferrite, martensite, and retained austenite in intercritically annealed alloy [97].

6.3.2.2 Effect of silicon (Si) alloying on micrographs

The addition of silicon from 1.0 wt.% to 1.4 wt.% has lowered A1 and A3 temperatures while a further increase in silicon additions up to 2.0 wt.% raises A1 and A3 temperatures. In addition to changes in A1 and A3 temperatures, the transformation temperature for bainite and martensite also decreased up to 1.4 wt.% Si additions and further addition of silicon increase the bainitic and martensitic transformation temperatures. The FE-SEM micrographs of alloy steels in the hot rolled at 1100 °C soaked for 20 min are shown in Figure 6.6. The microstructure represents a complex phase. The bright flat regions in the micrographs are ferrite, the fringed regions are bainite, the grey flat regions are martensite in Figure 6.6 (a2, b2, c2). Bainite is identified as a needle-like structure, and ferrite is identified as light gray-equiaxed regions in the microstructure. Retained austenite is an interlayer structure [98]. The distribution of different phases observed in the microstructures is presented in Figure 6.6 (a1, b1, c1). The volume fractions of phases revealed in the microstructure are estimated using the ASTM E 562-point count method that are shown in Table 6.3. The volume fractions are measured for 10 images of each condition of the specimen. The average is presented as volume fractions. The volume fractions of retained austenite were measured using XRD. The average volume fraction of bainite has been reduced to 21.2 vol.% from 29.7 vol.% with increases in silicon contents from 1 wt.% to 2 wt.%. The martensitic volume fractions have increased from 19 vol.% to 24.5 vol.% due to an increase in silicon in the novel alloys. The average volume fraction of retained austenite was measured at 11.2 vol.%, 10 vol.%, and 8 vol.% for Alloy 4, Alloy 2, and Alloy 5. Higher addition of silicon up to 2.0 wt.% Si in the steel leads to the formation of ferrite, which was formed during solidification and inherited during hot

rolling. This investigation presents the special finding that the formation of bainite is observed during air cooling after rolling treatment. Similar microstructures were reported with different processing routes [72]-[35].

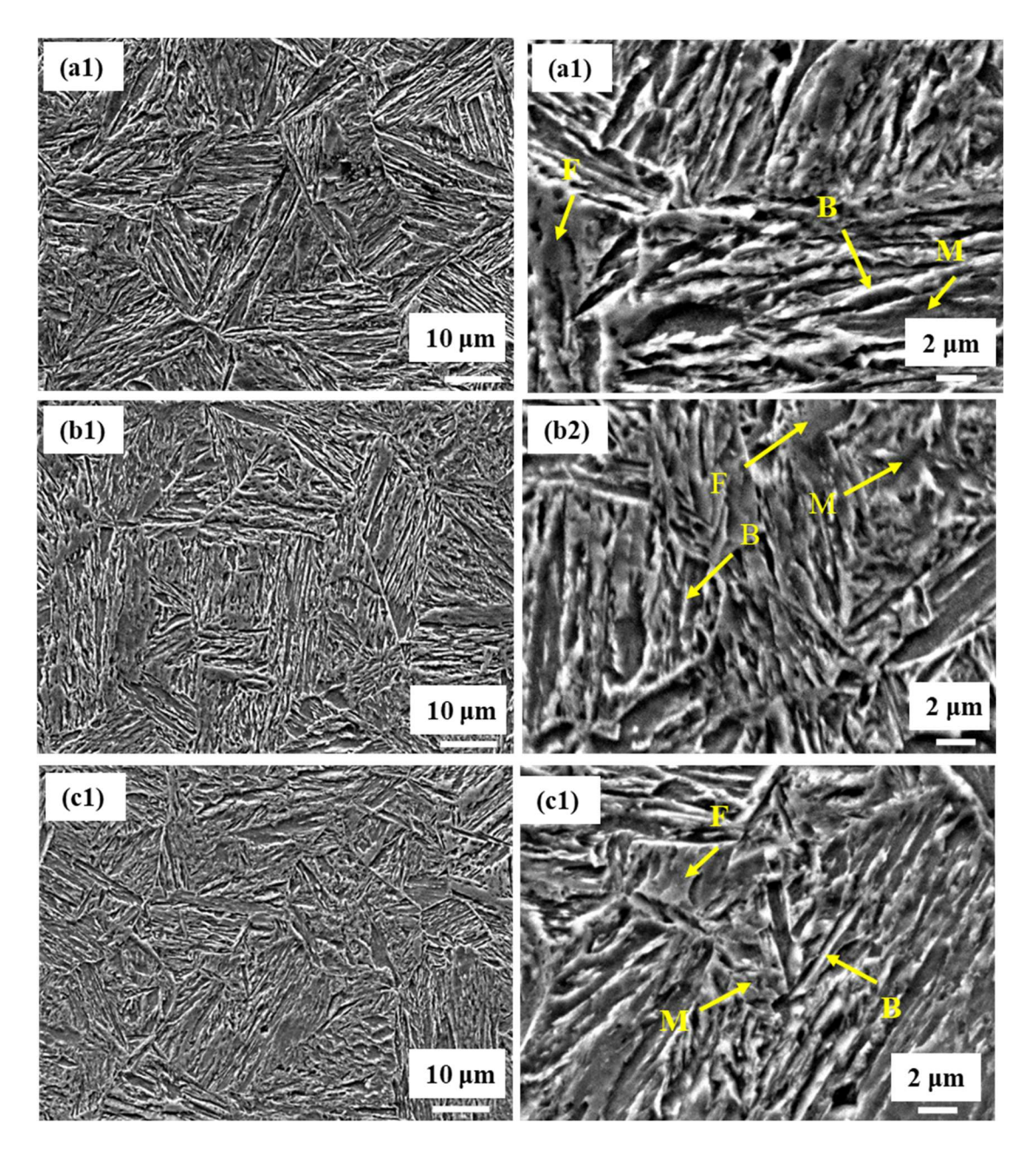


Figure 6.6 Field Emission Scanning Electron micrographs of steels hot rolled at 1100 °C, at 2500X, (a1, a2) Alloy 4 (Fe-6Mn-1.0Si), (b1, b2) Alloy 2 (Fe-6Mn-1.5Si), (c1, c2) Alloy 5 (Fe-6Mn-2.0Si).

Table 6.3 Phase estimation of Alloy 4 (Fe-6Mn-1.0Si), Alloy 2 (Fe-6Mn-1.5Si), and Alloy 5 (Fe-6Mn-2.0Si) hot rolled at 1100 °C.

Novel AHSS hot rolled at 1100 °C							
Alloy/Phase Bainite (vol.%) Ferrite (vol.%) Martensite (vol.%) RA (vol.%) Thickness of bainitic laths (nm)							
Alloy 4 (Fe-6Mn-1.0Si)	29.72	40.05	19	11.23	504		
Alloy 2 (Fe-6Mn-1.5Si) 24 46.6 21.4 9 563							
Alloy 5 (Fe-6Mn-2.0Si)	23.21	46.29	22.5	8	686		

6.3.3 X-ray Diffraction of hot rolled at 1100 °C

The XRD patterns of hot rolled alloy steels are represented in Figure 6.7. The four peak positions at 44.8° , 64.8° , 82.4° , and 98.8° are matched to lattice planes (110), (200), (211), and (220) of α -ferrite; one very low intense peak at 42.5° corresponds to retained austenite (111). Peaks other than α -ferrite and retained austenite are not found in the XRD patterns. The lattice parameters of Alloy 1, Alloy 2, and Alloy 3 are calculated at 3.8722 Å, 3.8708 Å, and 3.8705 Å respectively. It indicates that the lattice parameter decreases with an increase in manganese.

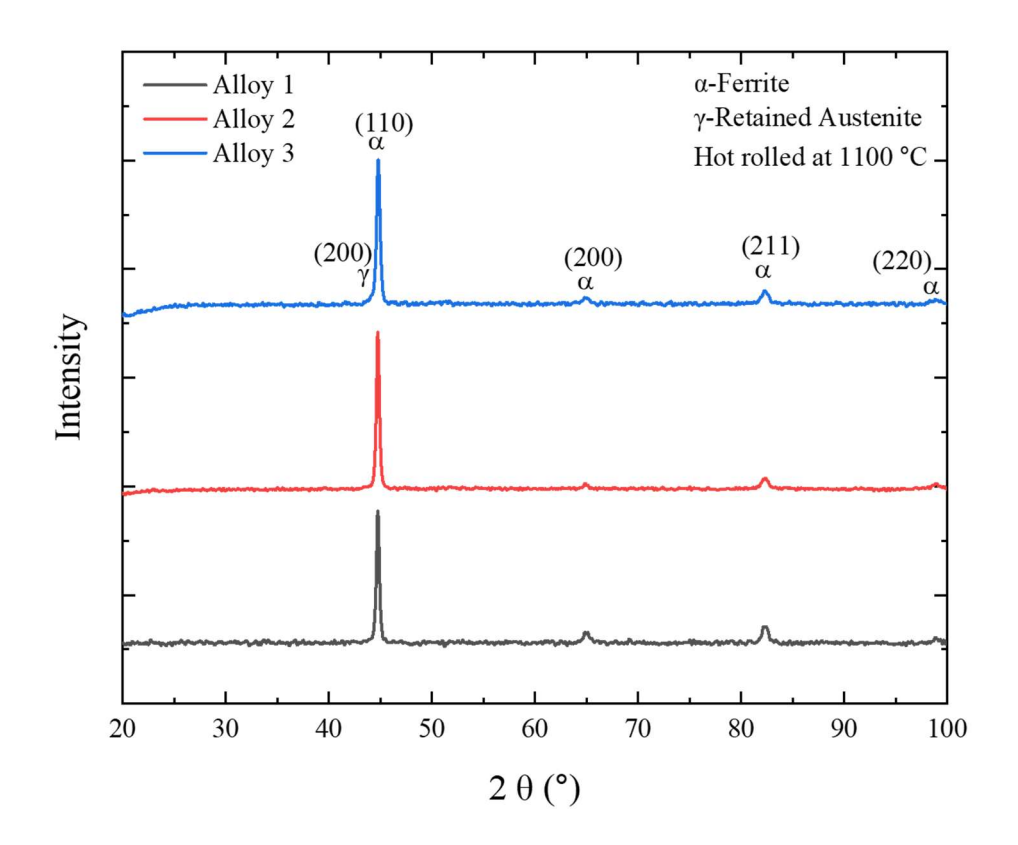


Figure 6.7 XRD-spectra of AHSS hot rolled at 1100 °C, Alloy 1 (Fe-4Mn-1.5Si), Alloy 2 (Fe-6Mn-1.5Si), and Alloy 3 (Fe-8Mn-1.5Si).

Table 6.4. Peak positions of Alloy 1, Alloy 2 and Alloy 3 hot rolled at 1100 $^{\circ}$ C, (retained austenite, γ_A) with an increase in Mn contents.

Alloy/	α-ferrite,	α-ferrite,	α-ferrite,	α-ferrite,	(γ _A),
(hkl)	(110)	(200)	(211)	(220)	(111)
Alloy 1	44.76	64.88	82.25	98.79	43.34
Alloy 2	44.65	64.81	82.36	98.99	43.25
Alloy 3	44.76	64.92	82.36	98.88	43.43

The X-ray diffraction spectra of hot rolled alloy steels are shown in Figure 6.8. The four peak positions at 44.66° , 64.82° , 82.16° , and 98.68° are matched to lattice planes (110), (200), (211), and (220) of α -ferrite; one very low intense peak at 43.6° corresponds to

retained austenite (111) for alloys. The carbide formation is not detected by the XRD spectra. It indicates that the addition of silicon is effective in stopping the formation of carbides in the alloy steels. Mattia Franceschi et al. reported similar peaks in the case of Fe-0.43C-3.26Si-2.72Mn (wt.%) steel [35].

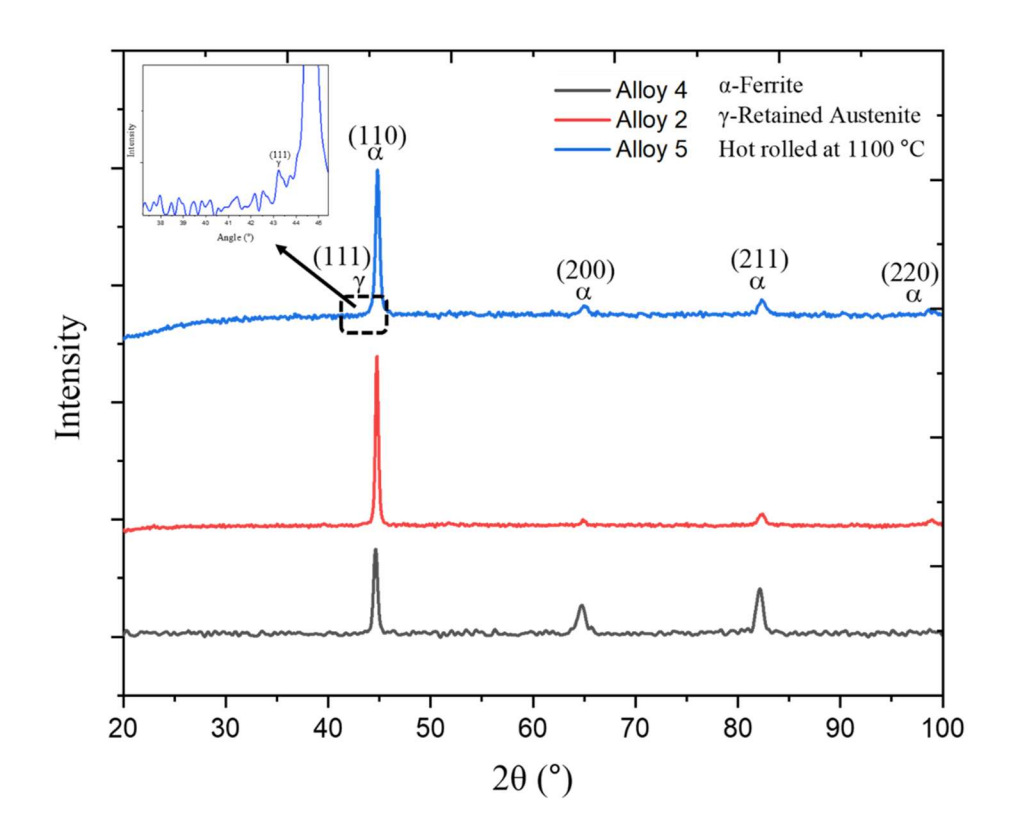


Figure 6.8 XRD-spectra of AHSS hot rolled at 1100 °C, Alloy 4 (Fe-6Mn-1.0Si), Alloy 2 (Fe-6Mn-1.5Si), and Alloy 5 (Fe-6Mn-2.0Si).

Table 6.5 Peak positions of alloy 4, alloy 2 and alloy 5 homogenized at 1200 $^{\circ}$ C, for 4 hrs. soaking. (retained austenite, γ_A) with an increase in Si contents.

Alloy/	α-ferrite,	α-ferrite,	α-ferrite,	α-ferrite,	(γ _A),
(hkl)	(110)	(200)	(211)	(220)	(111)
Alloy 4	44.66	64.82	82.16	98.68	43.60
Alloy 2	44.65	64.81	82.36	98.99	43.25
Alloy 5	44.76	66.01	82.36	98.57	43.05

6.3.4 Mechanical Properties of hot-rolled at 1100 °C

6.3.4.1 Microhardness measurements of hot-rolled at 1100 °C

Table 6.6 Microhardness values of AHSS hot-rolled at 1100 °C.

Micr	Microhardness (VHN)_Hot-Rolled 1100 °C, Load: 300 gf						
Sr No.	Alloy 1 Alloy 2 Alloy 3 Alloy 4 Alloy 5						
Average	395	432	502	423	475		
Stdev	16	12	9	9	12		

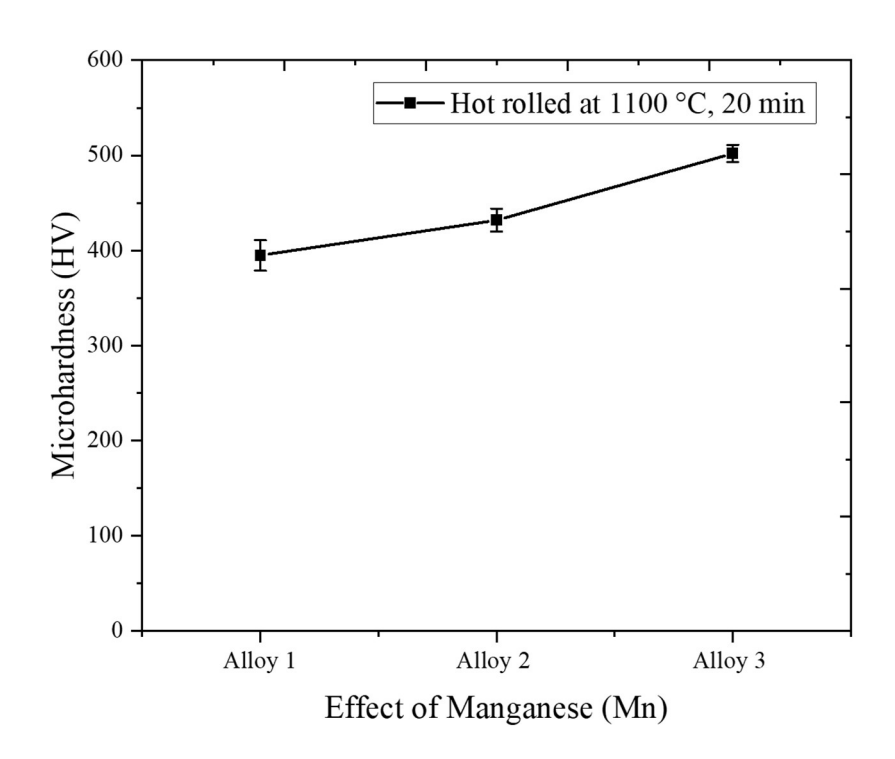


Figure 6.9 Microhardness of novel AHSS hot-rolled at 1100 °C, Alloy 1 (Fe-4Mn-1.5Si), Alloy 2 (Fe-6Mn-1.5Si), and Alloy 3 (Fe-8Mn-1.5Si).

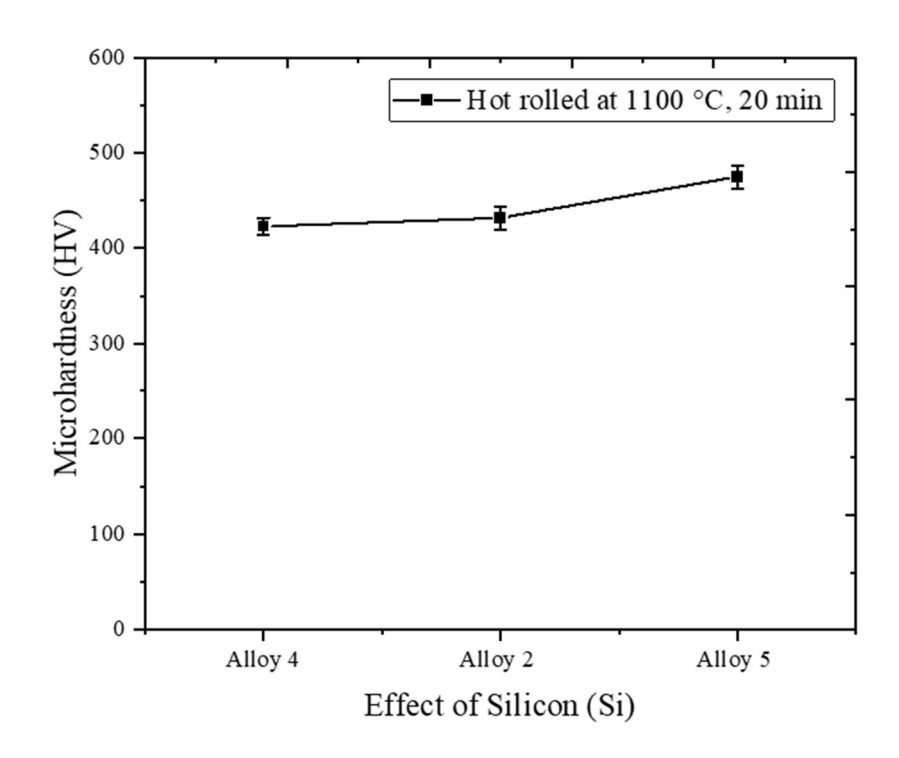


Figure 6.10 Microhardness of novel AHSS hot rolled at 1100 °C, Alloy 4 (Fe-6Mn-1.0Si), Alloy 2 (Fe-6Mn-1.5Si), and Alloy 5 (Fe-6Mn-2.0Si).

The measurements of microhardness values are presented in Table 6.6. Figure 6.9 shows the microhardness of developed alloys after hot rolled at 1100 °C (initial soaking for 20 minutes) microhardness of Alloy 1 is found lower than Alloy 2 and Alloy 3; Microhardness of Alloy 3 is found to be maximum 502 VHN among these three steels developed. The results indicate that microhardness increases by increase in manganese contents in the alloys. In addition to alloying elements, the formation of hard phases such as martensite and bainite in the alloys are responsible for higher microhardness and lower ductility. The microhardness values increase by increasing the silicon contents in the alloys from 1.0 wt.% to 2.0 wt.%. The hardness was repeated 10 times, and an average of harness values is presented on Vicker's hardness scale. Alloy 5 with 2 wt.% silicon exhibits 475 VHN (Vickers hardness number), and Alloy 4 with 1.0 wt.% silicon shows a harness of 423 VHN. The microhardness of 432 VHN was measured for Alloy 2, as shown in Figure 6.10. The increase of microhardness of alloys in with increase in Si is due to increase in volume fraction of martensite [99], [100], [101].

6.3.4.2 Effect of Mn on mechanical properties

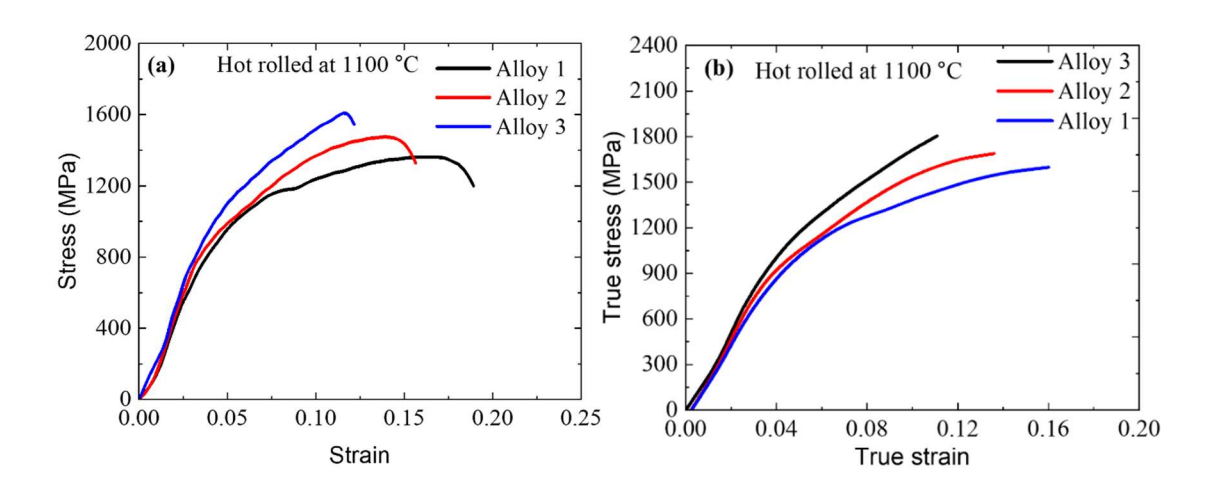


Figure 6.11 (a) Engineering stress-strain plots, (b) True stress-true strain plots, for AHSS hot rolled at 1100 °C and soaked for 20 min for Alloy 1 (Fe-4Mn-1.5Si), Alloy 2 (Fe-6Mn-1.5Si), and Alloy 3 (Fe-8Mn-1.5Si).

The tensile stress-strain plots are shown in Figure 6.11 (a). The mechanical properties calculated using stress-strain data are presented in Table 6.7. The ultimate tensile strength of Alloy 1, Alloy 2 and Alloy 3 are measured as 1412 MPa, 1476 MPa, and 1614 MPa, respectively. Elongations of the alloys are found to be 18.92%, 15.64% and 12.12% for Alloy 1, Alloy 2 and Alloy 3, respectively.

It is observed that the ultimate tensile strength increases by increasing the amount of manganese in the alloys. The tensile strength is found at 1418 MPa of Alloy 1 which contains 4 wt.% manganese and 1.4 wt.% Si with elongation of 18.92 %. When the content of manganese addition was increased from 4 wt.% to 6 wt.% the tensile strength increased 58 MPa with moderate elongation of 15.64%. The further increase in the alloying addition of manganese from 6 wt.% to 8 wt.% leads to an increase in tensile strength of 138 MPa. Overall, stress-strain curves indicate that the ultimate tensile strength (UTS) increases by an increase in the manganese contents from 4 wt% to 8 wt.% as shown in Figure 6.11 (a). The increase in UTS is due to formation of bainite while elongation is maintained with presence of retained austenite which provides TRIP effect. The further Kazi M. H. Bhadhon et al. reported tensile strength of 1410 to 1590 MPa and elongation of 13-21 %

after intercritical annealing at different temperatures from 675 -710 °C for 1 to 6 minutes [97]. Daniella M investigated a third-generation advanced high-strength steel (3G-AHSS) with a composition of 0.15C–6Mn–1.5Al–1Si (wt.%) and found tensile strength of 1040 MPa to 1246 MPa with 21 to 23 % elongation after intercritical annealing from 665 to 740 °C [96]. The present investigation represents a simplified process to achieve a high strength of more than 1400 MPa and elongation unlike to results found in the reported works [97], [96]. The true stress-true strain curves are shown in Figure 6.11 (b), these curves always go upwards. The increasing trend of strength was observed by increasing Mn contents in the novel alloys from 4 wt.% to 8 wt.%. The effect of manganese additions on UTS and ductility of the alloys are shown in Figure 6.12 (a). The ultimate tensile strength increases from 1412 MPa to 1614 MPa by addition of manganese contents 4 wt.%-8 wt.%. While the ductility decreases from 18.92% to 12.12% with the increase of manganese from 4 wt.% to 8 wt.%. the addition of manganese.

Table 6.7 Mechanical properties of Alloy 1, Alloy 2 and Alloy 3, hot rolled AHSS determined from tension tests.

Novel AHSS hot rolled at 1100 °C						
Novel AHSS	Ultimate Tensile Strenght, σu (MPa)	Yield Strength σ _y (MPa)	Elongation El (%)	Microhardness (VHN)		
Alloy 1	1412 ± 42	922 ± 27	18.92 ± 0.57	395 ± 12		
Alloy 2	1476 ± 45	955 ± 29	15.64 ± 0.46	432 ± 13		
Alloy 3	1614 ± 48	1127 ± 34	12.12 ± 0.36	502 ± 15		

The effect of manganese additions on UTS and the ductility of the alloys are shown in Figure 6.12. The ultimate tensile strength increases from 1412 MPa to 1612 MPa due to TRIP effect while the ductility decreases from 18.92% to 12.12% with the increase of manganese from 4 to 8 wt.% due to increase in volume fraction of martensite from 18 to 26 Vol.%. The yield strength increases with increase in Mn contents from 4 to 8 wt.% due to formation of bainite and TRIP aided effect.

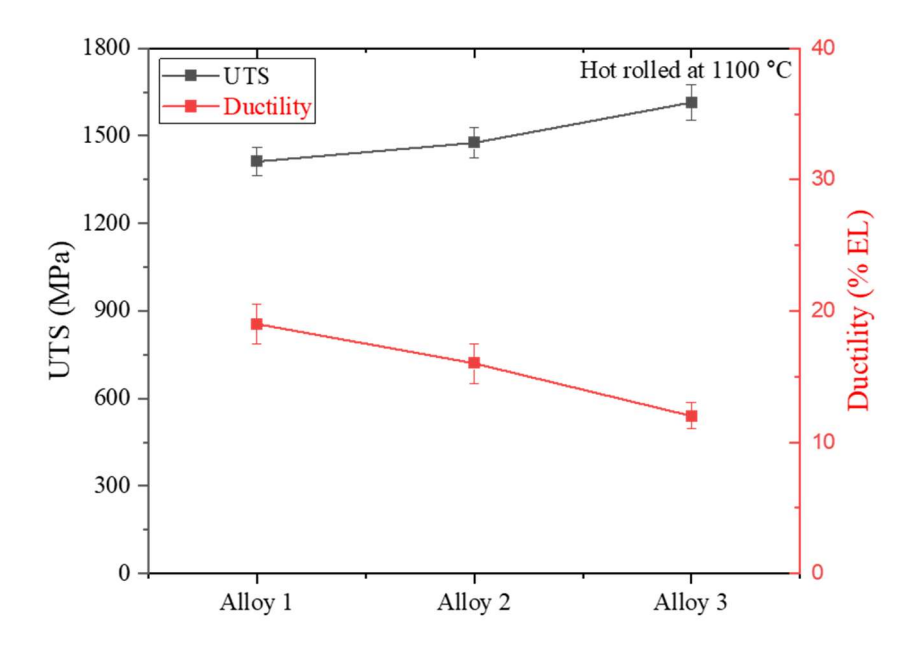


Figure 6.12 Effect of manganese (Mn) alloying in the novel AHSS hot rolled at 1100 °C, Alloy 1 (Fe-4Mn-1.5Si), Alloy 2 (Fe-6Mn-1.5Si), and Alloy 3 (Fe-8Mn-1.5Si).

6.3.4.3 Effect of silicon additions on mechanical properties of steel

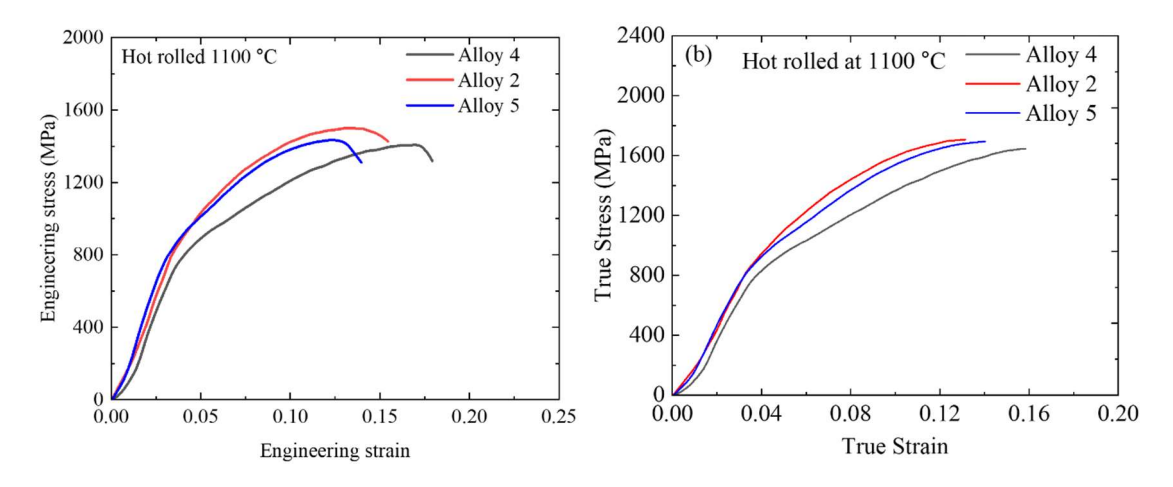


Figure 6.13 (a) Stress-strain curves of novel AHSS, (b) True stress-strain curve, hot rolled at 1100 °C, Alloy 4 (Fe-6Mn-1.0Si), Alloy 2 (Fe-6Mn-1.5Si), and Alloy 5 (Fe-6Mn-2.0Si).

The addition of silicon restricts the formation of carbides and stabilizes ferrite. Ultimate tensile strength increases due to silicon acting as a solid solution strengthener for the matrix. It is observed that matrix strengthening takes place with an increase in silicon up to 2.05 wt.%; however, further additions of silicon make steel brittle with a higher hardness (475 VHN), lowering strength and ductility [35]. The steels with a tailored composition with the addition of silicon (2.05 wt.%) and manganese (6 wt.%) produce high strength and limited ductility. The retained austenite is found in the steel as shown in XRD spectra. In addition to solid solution strengthening, the transformation-induced plasticity is also responsible for higher strength in such complex phase alloys due to the presence of retained austenite. The engineering stress-engineering strain curves are shown in Figure 6.13 (a). Results of Figure 6.13 (a) indicate that the ultimate tensile strengths (UTS) are similar to silicon variations from 1.0 wt.% to 2.0 wt.%. The ultimate tensile strengths of Alloy 4, Alloy 2, and Alloy 5 are measured as 1409 MPa, 1476 MPa, and 1438 MPa respectively. This high strength is attributed to the complex phase with retained austenite which exhibits transformation-induced plasticity (TRIP) effect. Elongations of the alloy steel are found at 18, 15, and 14 % for Alloy 4, Alloy 2, and Alloy 5 respectively. The elongation of Alloy 5 with 2.05 wt.% silicon lowered due to lowering in volume percent of retained austenite. Alloy 5 with 2.05 wt.% Si exhibits a hardness of 475 VHN, and it becomes brittle which is also observed in the fractograph given in Figure 6.16. The mechanical properties such as ultimate tensile strength (UTS), and yield strength are also determined that are listed in Table 6.8. The standard deviations of 56 MPa and 59 MPa are estimated for alloys 4 and 2, respectively, whatever change in UTS with an increase in the quantity of Si is observed that is close to the standard deviation. The total elongation decreases from 18 to 14 % with the increase of silicon from 1.0 to 2.05 wt.% [84], [102], [103], [104], [105], [106].

The yield strength increases with the alloying additions, from Table 6.8. The alloying additions act as solid solution strengthening. The yield strength increases from 742 MPa to 898 MPa with an increase in silicon from 1 to 2.05 wt.%. Silicon strengthens the matrix enhancing the yield strength of developed advanced high-strength steels. In addition, solid solution strengthening transformation-induced plasticity is also responsible for higher-yielding stress up to 898 MPa. The strain hardening increases slightly with an increase in silicon which also raise the yield strength [107]-[86]. It is intended to add key alloying

elements, like Mn, to the alloys. A few alloying elements, including Cr, Al, Ni, and Ti, could be among the small additions. By preventing the precipitation of carbide, the addition of certain alloying elements, such as silicon, has been crucial in stabilizing ferrite [38], [39]. The austenite transition temperature increases and the austenite two-phase zone expands with the addition of Si [11]. At room temperature, the fraction of retained austenite (RA) can be effectively increased by adding manganese (Mn). The increase in strength after plastic deformation until the stress-strain curve becomes flat is because of strain-hardening. Kazi M. H. Bhadhon et al. reported tensile strength of 1410 to 1590 MPa and elongation of 13-21 % [97]. Daniella M investigated a third-generation advanced high-strength steel (3Gen-AHSS) with a composition of 0.15C-6Mn-1.5Al-1Si (wt.%) and found tensile strength of 1040 MPa to 1246 MPa with 21 to 23 % elongation after intercritical annealing from 665 to 740 °C [96]. The effect of Si on UTS and ductility are shown in Figure 6.14 which shows drop in ductility due to increased volume fraction of martensite from 19 to 22.5 vol.%.

Table 6.8 Mechanical properties of novel AHSS hot-rolled at 1100 °C.

Novel AHSS	Ultimate Tensile Strength, σ _u (MPa)	Yield Strength σ _y (MPa)	Elongation El (%)	Microhardne ss (VHN)
Alloy 4	1409 ± 56	742 ± 29	18 ± 0.9	423 ± 9
Alloy 2	1476 ± 45	955 ± 29	15.64 ± 0.46	432 ± 13
Alloy 5	1438 ± 57	828 ± 26	14 ± 0.69	475 ± 12

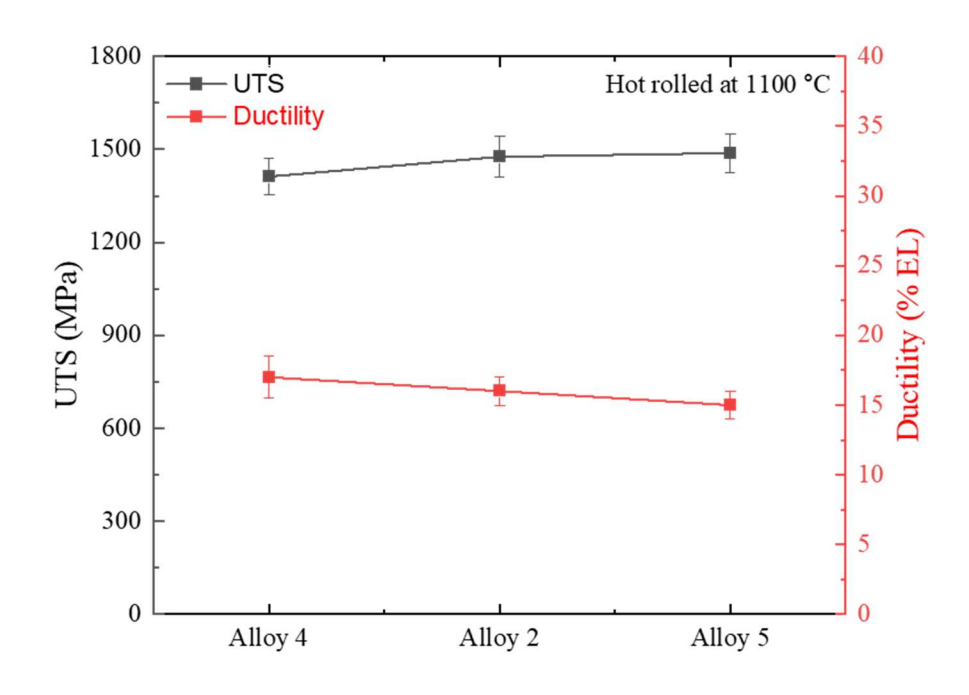


Figure 6.14 Effect of silicon (Si) alloying in the novel AHSS hot rolled at 1100 °C, Alloy 4 (Fe-6Mn-1.0Si), Alloy 2 (Fe-6Mn-1.5Si), and Alloy 5 (Fe-6Mn-2.0Si).

6.3.5 Fracture Analysis

6.3.5.1 Effect of Manganese on fracture behavior

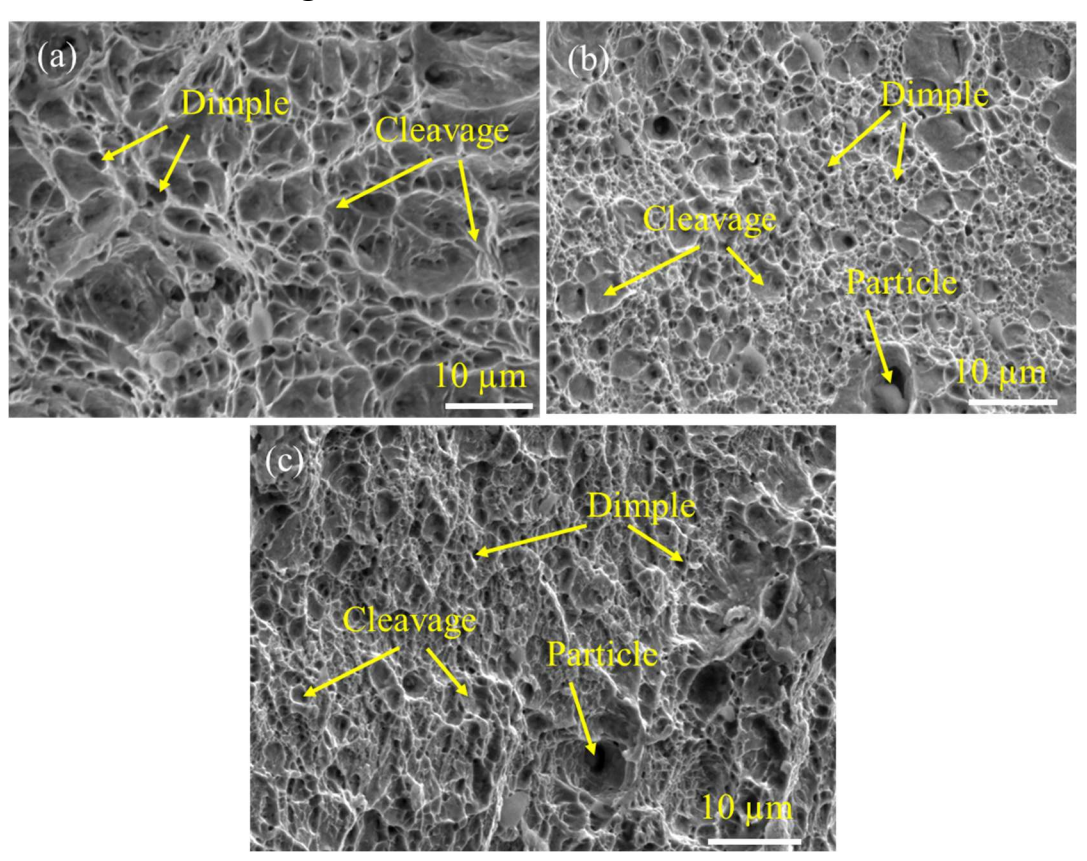


Figure 6.15 Fractographs of novel AHSS hot rolled at 1100 °C, 20 min., at 2000X, (a) Alloy 1 (Fe-4Mn-1.5Si), (b) Alloy 2 (Fe-6Mn-1.5Si), (c) Alloy 3 (Fe-8Mn-1.5Si).

FE-SEM analysis of fracture surfaces was carried out after tensile tests for the developed alloys and the fractographs are shown in Figure 6.15. The presence of dimples indicate ductile fracture of Alloy 1. The dimples as well as facets are observed in the fractographs of Alloy 2. This mixture of dimples and facets indicates ductile fracture with lower ductility than that of Alloy 1. Dimples and facets are also observed in the fractographs of Alloy 3 but relatively lower dimples as compared to Alloy 1 and Alloy 2; however, larger numbers of facets are observed in Alloy 3. These results confirm that Alloy 3 also follows ductile fracture with a lower ductility limited to 12.12%. The number of dimples decreases by increasing additions of Mn contents in the alloys. The least dimples and more facets are

seen in the fractographs of Alloy 3 which has 8 wt.% manganese addition. More dimples and fewer facets are found in Alloy 1 which has 4 wt.% manganese addition, Alloy 1 also exhibits higher ductility up to 18.92 % which is more than Alloy 2 and Alloy 3. The moderate ductility is measured for Alloy 2 which has 6 wt.% manganese alloying. Overall, all three alloys, Alloy 1, Alloy 2, and Alloy 3 show ductile failure mechanism with differences in ductility. Similar results were also reported [55], [71].

6.3.5.2 Effect of silicon on fracture behavior

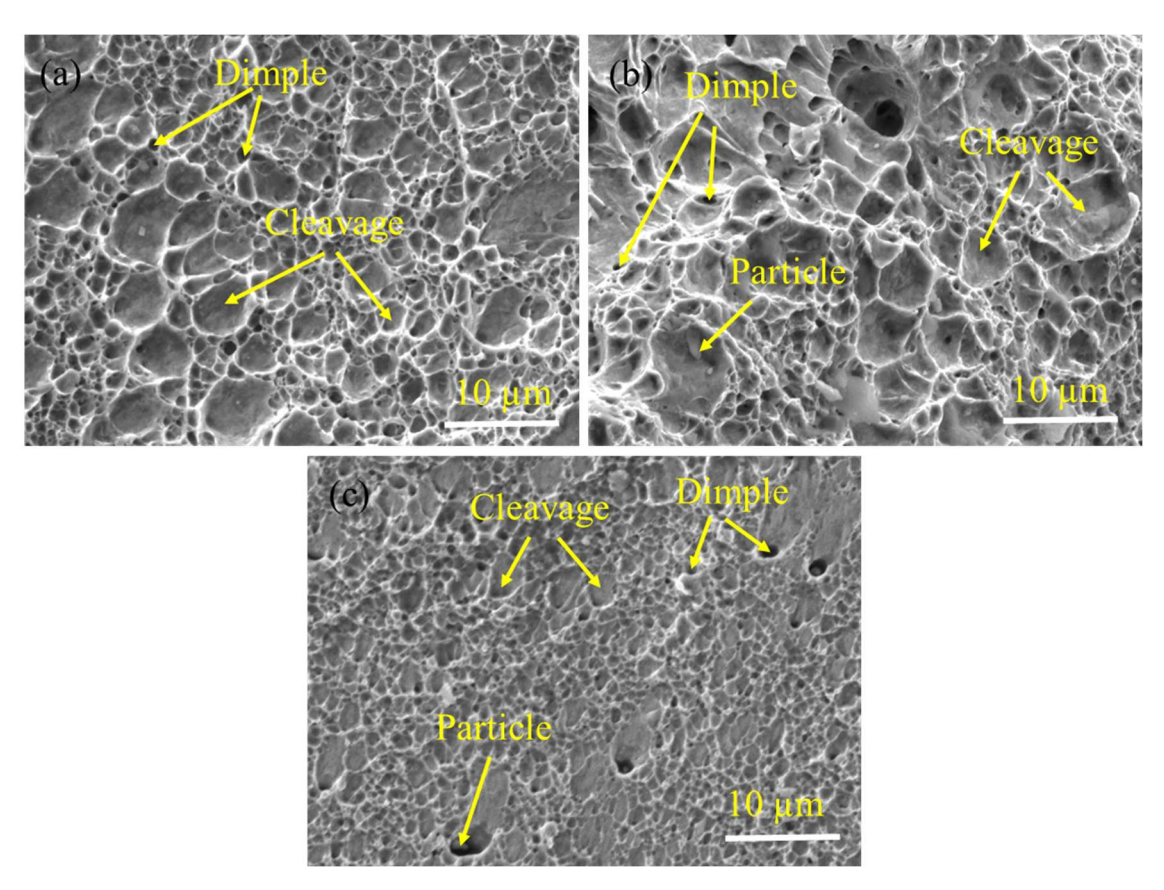


Figure 6.16 Fractographs of novel AHSS hot rolled at 1100 °C, at 2500X (a) Alloy 4 (Fe-6Mn-1.0Si), (b) Alloy 2 (Fe-6Mn-1.5Si), and (c) Alloy 5 (Fe-6Mn-2.0Si).

The brittleness is found to increase by increasing silicon. FE-SEM analysis of fracture surfaces was performed after tensile tests for Alloy 4, Alloy 2, and Alloy 5, and the fractographs are presented in Figure 6.16. The brittleness is found to increase by increasing silicon. FE-SEM analysis of fracture surfaces was performed after tensile tests for Alloy 4,

Alloy 2, and Alloy 5. The material exhibits ductile regions, characterized by predominantly dimples, as well as brittle areas showing mainly cleavage. Within the ductile regions, certain areas display a cleavage-dominated behavior with flat facets. The dimples and facets are observed in the fractographs of Alloy 4 with a higher number of dimples than facets which indicates that the fracture is mostly ductile. The dimples as well as facets are also found in the fractographs of Alloy 2 with a difference in the presence of more facets than facets observed in Alloy 4 which is attributed to increasing silicon from 1 to 1.41 wt.%. The fracture of Alloy 2 is also ductile, with a moderate elongation that is lower than the elongation of Alloy 4. While, fewer dimples and more facets are observed in Alloy 5, it depicts lower ductility than Alloy 4 and Alloy 2. Hence the lowest ductility of 14 % is achieved in Alloy 5. The regions with higher Mn concentrations show cleavage behaviour. The interfaces of ferrite and martensite exhibit intergranular fracture. This martensite is probably transformed from the austenite, causing an intergranular fracture [108], [109].

6.3.6 Atom probe tomography results

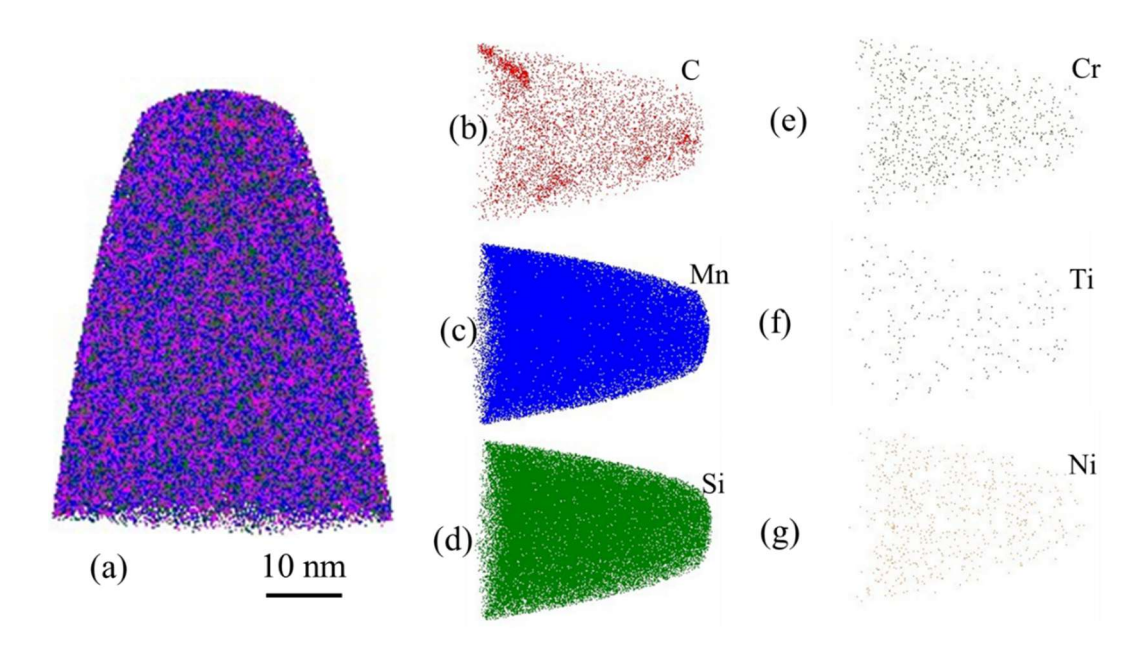


Figure 6.17 Three-dimensional Atom probe tomography of AHSS: (a) All elements, (b) Carbon (c) Manganese, (d) Silicon, (e) Chromium, (f) Titanium, and (g) Nickel.

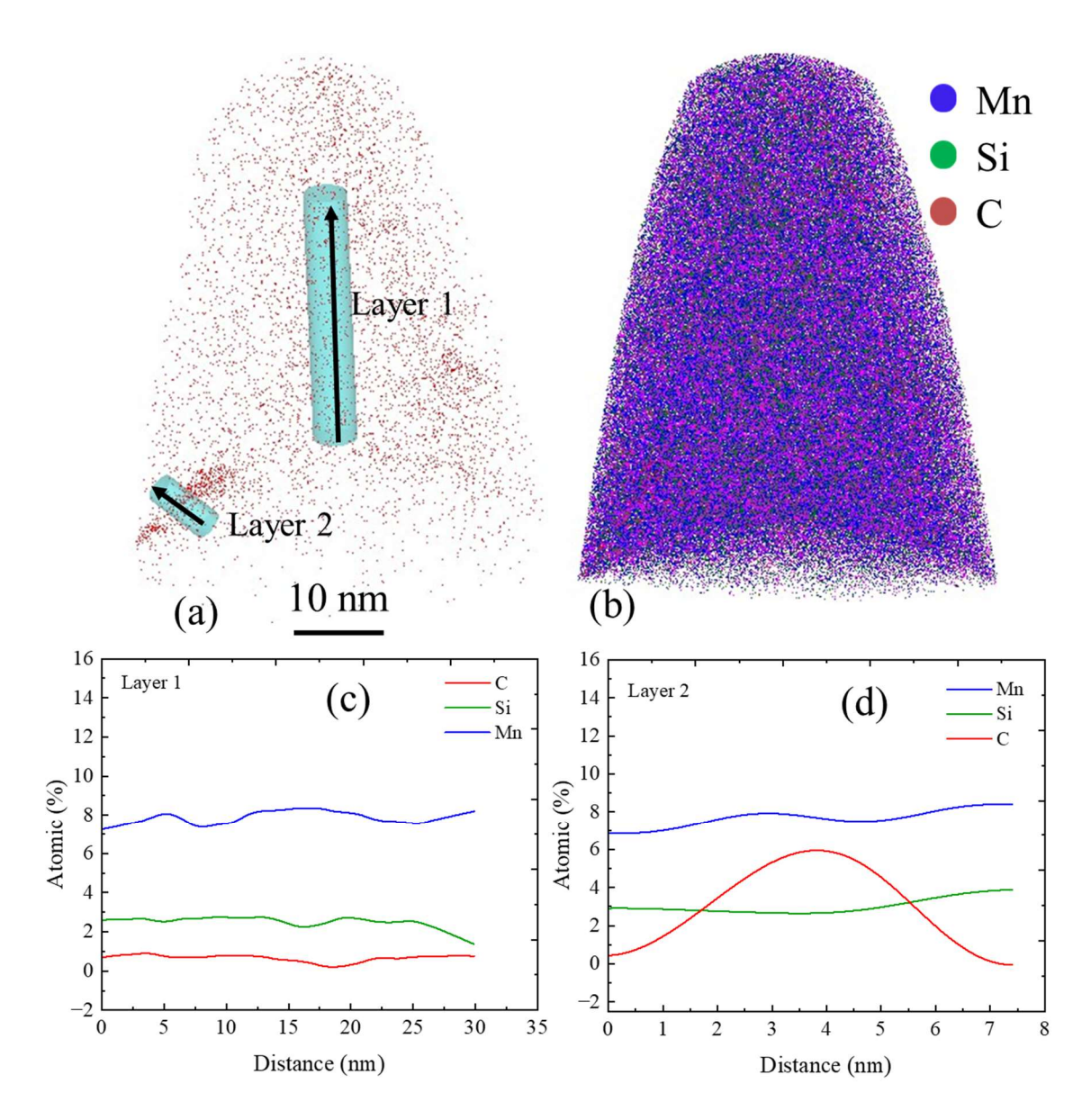


Figure 6.18 Three-dimensional Atom probe tomography of AHSS: (a) Carbon atoms, (b) Mn, Si, and C atoms (c) Proxigram developed from the data of iso surfaces displayed in, (d) Proxigram developed from the data of iso surfaces displayed in.. for Mn, Si, and C atoms.

Atom probe tomography (APT) was used to characterize the elemental distribution across phase barriers at nearly atomic scales. Three-dimensional atom probe tomography is represented for all elements in Figure 6.17 (a) which shows the uniform distribution of all elements present in the AHSS alloys. Figure 6.17 (b-g) shows 3 D atom probe tomography for C, Mn, Si, Cr, Ti, and Ni atoms that are uniformly distributed except carbon. The carbon segregation is observed in Figure 6.17 (b).

The distribution of Mn and Si are also uniform that represents good mechanical properties. Two layers are marked which are shown in Figure 6.18 (a). The variation of Mn, Si and C is our focus in present work which are shown in Figure 6.18 (b). The compositional profile obtained from layer 1 and layer 2 shown in Figure 6.18 (a) are represented in Figure 6.18 (c, d). The distribution of atoms of Mn, Si, and C are almost uniform on layer 1. The distribution of Mn in layer 2 indicates higher atomic percent (7.8 at.%) in the higher carbon region. The distribution of carbon in layer 2 is found non-uniform. Atomic percent of carbon was observed 5.98 at.% in the vicinity of layer 2 as shown in the composition profile of Figure 6.18 (d). The silicon is observed in less quantity (2.64 at.%) in the regions where carbon varies from 0.48 at.% to 5.98 at.%, this indicates that dissolution of silicon in this region is lowered as shown in Figure 6.18 (d) green curve. It is well known that Si is ferrite stabilizers and Mn is austenite stabilizer. Hence, the carbon rich region is retained austenite. So, the presence of retained austenite has been stablished by APT analysis.

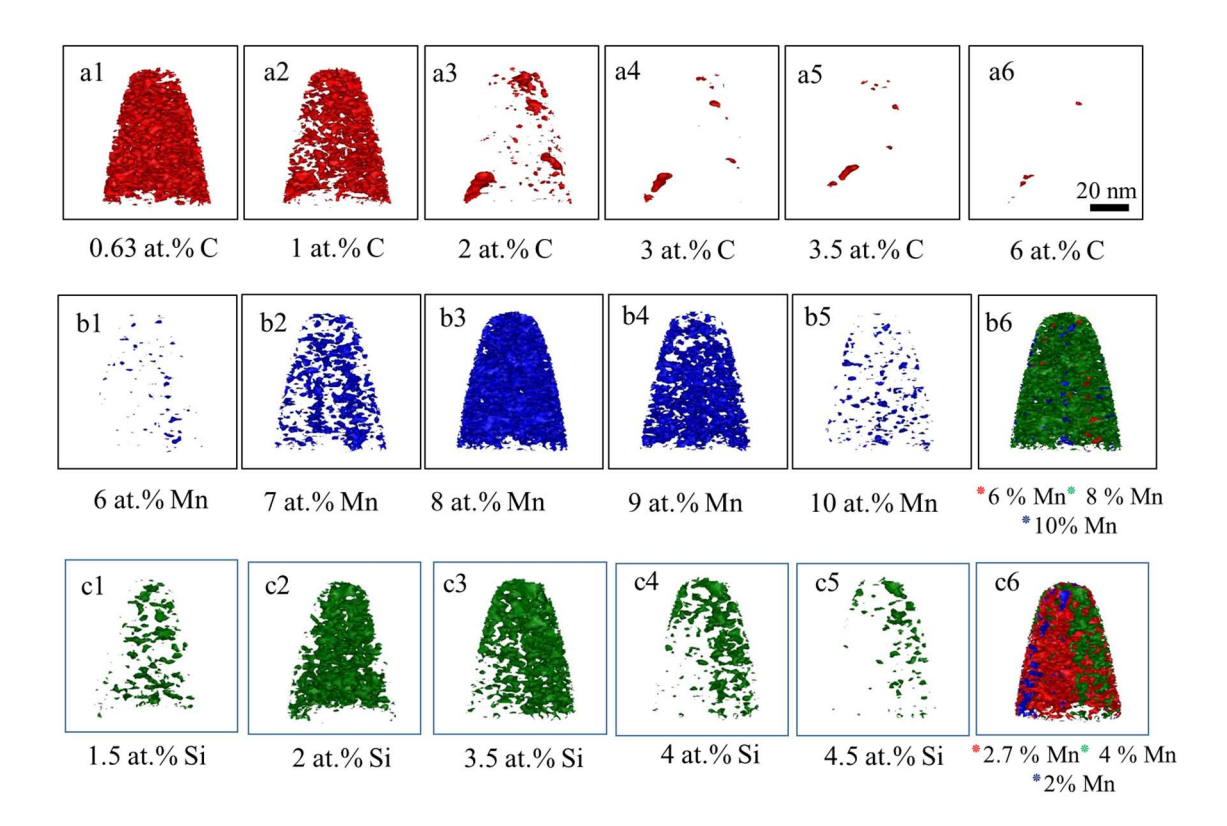


Figure 6.19 Three-dimensional Atom probe tomography of AHSS: (a1-a6) Carbon atoms, (b1-b6) Mn atoms (c1-c6) Si atom.

The presence of retained austenite is established by APT analysis, as shown in Figure 6.19 (a3). The microstructures contain martensite and bainite phases already existing in the matrix of alloys. The retained austenite transforms into martensite during the deformation of the alloys. Consequently, there is an increase in the resistance offered on the path of dislocation movement, leading to high strength and high toughness, as shown in Table 6.7. This effect is termed as TRIP effect.

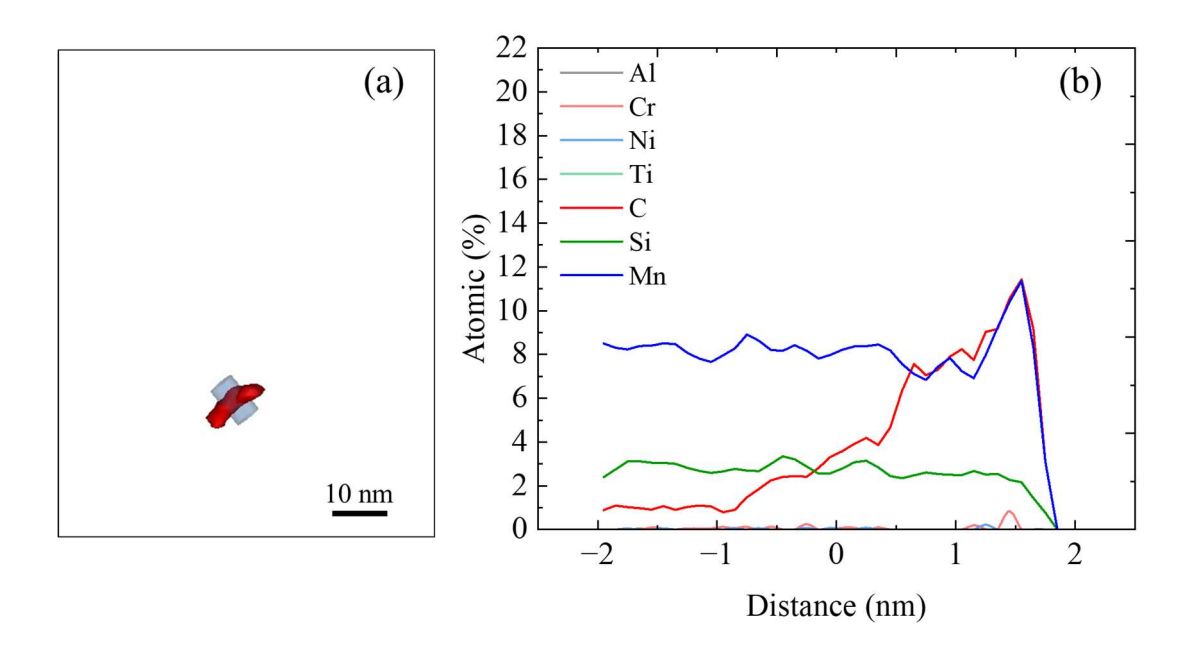


Figure 6.20 Three-dimensional Atom probe tomography of AHSS:(a) retained Austenite film (b) Proxigram developed from the data of iso-surfaces displayed in (a) at 3.5 at.%

The retained austenite have 8 at.% carbon and it has been observed in the film form of thickness 4.32 nm and 14.65 nm width as shown in Figure 6.20 (a). Similar results were achieved by Yan Ma et al. [79], they examined medium-Mn low-carbon steel and found carbon spike, while other microstructural features remained unchanged in air-cooled steel specimen.

6.3.6.1 Nanoscale distribution of elements and its effect on mechanical properties

The atom probe tomography is performed for Alloy 3 which contains 8 wt.% Mn. Figure 6.19 shows 3D APT of iso-surfaces of carbon (a1-a6), manganese (b1-b6), and silicon (c1-c6). The nominal carbon content is 0.63 at.% while 6 at.% carbon is observed in Figure 6.19 (a6). A film, rich in carbon is observed as shown in Figure 6.19 (a3-a6) in the bottom left corner of the images, similar to those observed in Figure 6.18. The silicon depleted regions are observed in Figure 6.19 (c1, c3-c5) in the bottom left corners of the images which indicates that this region exhibits a lower solubility of silicon. As silicon is ferrite stabilizer, it cannot be dissolved much in the austenite phase. Hence, the silicon depleted zones are found in the bottom left corner of the images shown in Figure 6.19 (c1, c3-c5).

It confirms the presence of retained austenite, same is discussed in Figure 6.18. The retained austenite provides better elongation. The retained austenite transforms into martensite during deformation, resulting in the transformation-induced plasticity (TRIP) effect. Due to the TRIP effect, high tensile strengths of 1412 to 1614 MPa is obtained for developed AHSS. The peak of retained austenite in XRD spectra is either not visible or very small due to the formation of nano-scale retained austenite. Nano-scale retained austenite provides the best response to mechanical properties. Figure 6.20 (a) represents the iso-surface of carbon atoms at 3.5 at.%, and Figure 6.20 (b) shows the proxigram of the iso-surface displayed in Figure 6.20 (a). The carbon and manganese concentrations in the film are 11 at.%. The silicon concentration varies from 2.7 to 2.99 at.% on the iso-surface in the thickness range of 0 –2 nm. Other alloying elements except Mn, Si and C are very low and their concentration profile is parallel to distance axis as shown in Figure 6.20 (b). Since, segregation or clustering of elements is not observed in Alloy 3, hence it is assumed that Alloy 1, Alloy 2, Alloy 4 and Alloy 5 will not possess segregation due to lower alloying additions. Similar results have been reported in earlier work [62], [64], [91].

6.3.7 Effect of hot rolling temperature on microstructure and Mechanical properties

The microstructures exhibit different amounts of phases hot rolled at higher temperature. The volume fraction of bainite is found to increase with the increase in temperature from 900 °C to 1100 °C for Alloy 1 while it was decreased for Alloy 2, Alloy 3, Alloy 4 and Alloy 5. The retained austenite was formed more in alloys hot rolled at 900 °C than 1100 °C. The martensite was formed 18 vol.% to 26 vol.% in alloys hot rolled at 1100 °C while this martensite was formed 1-2 vol.% in alloys hot rolled at 900 °C. The phase fraction of ferrite is higher hot rolled at 900 °C and lower in alloys hot rolled at 1100 °C.

The hardness values of alloys hot rolled at 900 °C are found higher than the hardness values for alloys obtained after hot rolling at 1100 °C. The highest hardness values of Alloy 5 are 596 and 475 hot rolled at 900 °C and 1100 °C respectively. The higher microhardness of Alloy 5 is possibly due to higher quantity of Si added in the alloy which makes steel hard

and brittle. The lowest hardness values of 395 VHN and 517 VHN for Alloy 1 are obtained due to less volume fractions of martensite and bainite after hot rolling at 1100 °C and 900 °C respectively. The ultimate tensile strength and ductility have not changed significantly with an increase in rolling temperature from 900 °C to 1100 °C. The UTS is between 1400-1700 MPa and elongation is between 12-19 % for both rolling temperatures as shown in Tables 5.7, 6.7 and 6.8.

6.4 Conclusion

- 1. An advanced high strength steel has been developed successfully in vacuum arc melting furnace using high-purity metals. The time temperature transformation was developed using materials property software and the results obtained are in good agreement with phase predicted by phase diagrams and solidification curves.
- 2. The most important novelty of this work is that the present investigation reports 21-27% bainitic laths formation through normalizing (air cooling) after rolling at 1100 °C. The alloys developed in this investigation are candidate materials that can replace existing materials used for Automobile Body in White (BIW) parts.
- 3. AHSS homogenized at 1200 °C for 4 hours and hot rolled at 1100 °C has produced remarkable mechanical properties. The FE-SEM microstructure after hot rolling and air cooling revealed martensite, ferrite, bainitic laths. The phase fractions are determined using the point counting method repeating 10 times. The phase fractions are 18.2-25.6 vol.% martensite, 21-27 vol.% bainitic laths, 8-10.4 % retained austenite and the 44.4- 45.4 vol.% is ferrite. The presence of retained austenite was also verified by XRD analysis.
- 4. The ultimate tensile strengths (UTS) of Alloy 1, Alloy 2 and Alloy 3 are found 1412 MPa, 1476 MPa and 1614 MPa with the elongation 18.92%, 15.64% and 12.12% respectively. The additions of manganese increase UTS and hardness while it decreases the ductility of alloys. The work hardening increases with increase in Mn contents.
- 5. The fractographs of alloy three alloys of Alloy 1, Alloy 2 and Alloy 3 are analyzed. The quantity of dimples is found to decrease by increasing the contents of manganese additions which results drop in ductility. The fracture failure

- mechanism is ductile failure with the formation of some extent of facets which reduces elongations in the respective alloys.
- 6. Retained austenite film of thickness 4.32 nm and length 14.65 nm has been observed using 3D atom probe tomography. The retained austenite provides transformation induced plasticity (TRIP) effects in the developed AHSS alloy resulting in high strengths and thus crash worthiness.
- 7. The average volume fraction of bainite has been reduced to 23.2 vol.% from 29.7 vol.% while increasing silicon additions from 1 wt.% to 2 wt.%. The martensite is found from 19 vol.% to 24 vol.% due to an increase in silicon additions. The average volume fraction of retained austenite was obtained at 11.2 vol.%, 10 vol.%, and 8 vol.% for Alloy 4, Alloy 2, and Alloy 5.
- 8. The ultimate tensile strengths of Alloy 4, Alloy 2, and Alloy 5 are found at 1409 MPa, 1438 MPa, and 1476 MPa, with elongations of 18, 15.6, and 14, respectively. The high tensile strength is observed due to the TRIP effect.
- 9. The fractographs of three alloys of Alloy 4, Alloy 2, and Alloy 5 with variations of silicon from 1-2 wt.% are analyzed. The quantity of dimples is found to decrease by increasing the contents of silicon additions from 1.0 wt.% to 2.0 wt.% which results in a drop in ductility from 18 to 14%. This is also confirmed by the increasing microhardness values by increasing silicon contents in the alloys. The fracture failure mechanism is ductile failure with the formation of some extent of facets, which reduces elongations in Alloy 2, and Alloy 5.
- 10. This research resulted in the development of a 3rd generation AHSS alloy that demonstrates a complex phase microstructure, including 21.2-29.7% bainite, through normalising (air cooling) after rolling. The alloys developed in this investigation, alloyed with 1.0 wt.% to 2.0 wt.% silicon and 6 wt.% manganese, are candidate materials that can replace currently utilised materials for automobile bodies and parts.

Chapter 7 Conclusion and Future Scope

The main aim of the present work was to achieve following objectives:

- 1. To study the effect of Mn concentration (4-8 wt.%) and Si (1-2 wt.%) on the microstructure and mechanical properties of thus formed steel,
- 2. To study the effect of Thermo-mechnical treatment at 900 °C and 1100 °C on microstructure and mechanical properties,
- 3. Nano-scale Characterization to study the carbon redistribution in the complex phase microstructure developed.

7.1 Conclusions

- 1. Advanced high-strength steels (AHSS) were developed using high-purity metals in a vacuum arc melting furnace. Time Temperature Transformation diagrams were developed using materials property software. AHSS's homogenization treatment was performed at 1200 °C for 4 hours. The four ferrite peaks were identified in homogenized steels. Field emission scanning electron micrographs revealed ferrite and pearlite in these alloys.
- 2. The homogenized AHSS were hot rolled at 900 °C for multiple passes followed by air cooling. The microstructure revealed 1-2% martensite, 20-40% bainite, 10-12% retained austenite, and 46-69% ferrite. The presence of retained austenite was also verified by XRD analysis.
- 3. The ultimate tensile strengths (UTS) of Alloy 1, Alloy 2, and Alloy 3 hot rolled at 900 °C were found to increase from 1418 MPa to 1625 MPa with elongation of 17.28%, to 14.84%. The addition of manganese increases UTS and hardness while decreasing the ductility of alloys. The ultimate tensile strengths (UTS) of Alloy 4, Alloy 2, and Alloy 5 did not change significantly and elongation was observed

- to decrease from 18.1% to 12.2%. The addition of silicon increases hardness while decreasing the ductility of alloys.
- 4. The fractographs of the five alloys hot rolled at 900 °C were analyzed. The quantity of dimples was found to decrease by increasing the contents of manganese, which resulted in a drop in ductility. The fracture failure mechanism is a ductile failure with the formation of some extent of facets, which reduced elongation in the respective alloys. The elongation decreases with increase in silicon. Similar features were observed in the fractographs of the five alloys hot rolled at 1100 °C.
- 5. The microstructure of AHSS developed after hot rolling at 1100 °C revealed ferrite, bainite, martensite and retained austenite. The phase fractions are 18.2-25.6 vol.% martensite, 21-27 vol.% bainitic laths, 8-10.4 % retained austenite and the 44.4-45.4 vol.% is ferrite for Alloy 1, Alloy 2 and Alloy 3.
- 6. After hot rolling at 1100 °C of alloys with increasing silicon additions from 1 wt.% to 2. The average volume fraction of bainite has been reduced to from 29.7 to 21.2 vol.% wt.%. The martensite is found at 19 vol.% to 24 vol.% due to an increase in silicon additions. The average volume fraction of retained austenite was obtained at 11.2 vol.%, 10 vol.%, and 8 vol.% for Alloy 4, Alloy 2, and Alloy 5.
- 7. The ultimate tensile strengths (UTS) of Alloy 1, Alloy 2, and Alloy 3 hot rolled at 1100 °C are found in the range of 1412 MPa to 1614 MPa with a drop in elongation from 18.92% to 12.12%. The additions of manganese increase UTS and hardness while it decreases the ductility of alloys. The work hardening also increases with an increase in Mn contents in the alloys. The ultimate tensile strengths of Alloy 4, Alloy 2, and Alloy 5 are found at 1409 MPa to 1476 MPa, with with drop in elongations from 17.62, to 15.1 %. The high tensile strength is observed due to the TRIP effect
- 8. Retained austenite film of thickness 4.32 nm and length 14.65 nm has been observed using 3D atom probe tomography. The retained austenite provides transformation-induced plasticity (TRIP) effects in the developed AHSS alloy resulting in high and thus crashworthiness.

- 9. The most important novelty of this work is that the present investigation reports 21-27% bainitic ferrite formation through normalizing (air cooling) after rolling. The alloys developed in this investigation are candidate materials that can replace existing materials used for Automobile Body in White (BIW) A-pillar and B-pillar parts.
- 10. This research resulted in the development of a 3rd generation AHSS alloy that demonstrates a complex phase microstructure, including 21.2-29.7% bainite, through normalising (air cooling) after rolling. The alloys developed in this investigation, alloyed with 1.0 wt.% to 2.0 wt.% silicon and 6 wt.% manganese, are candidate materials that can replace currently utilized materials for automobile bodies and parts.

7.2 Future Scope

- Translation of developed technology to develop advanced high strength steels for automotive application to commercial scale.
- Advanced characterization can be performed to understand the nano-level distribution of elements and its effects on the mechanical properties.
- The combination of hot rolling and cold rolling can be applied to novel alloys and the possibility of improvement of properties can also be explored.

References

- [1] R. Rana, "Low-Density Steels," *Jom*, vol. 66, no. 9, pp. 1730–1733, 2014, doi: 10.1007/s11837-014-1137-2.
- [2] R. Rana, "High modulus steels," *Can Metall Q*, vol. 53, no. 3, pp. 241–242, 2014, doi: 10.1179/0008443314Z.000000000178.
- [3] S. Chen, R. Rana, A. Haldar, and R. K. Ray, "Current state of Fe-Mn-Al-C low density steels," *Prog Mater Sci*, vol. 89, pp. 345–391, Aug. 2017, doi: 10.1016/J.PMATSCI.2017.05.002.
- [4] S. Zaefferer, J. Ohlert, and W. Bleck, "A study of microstructure, transformation mechanisms and correlation between microstructure and mechanical properties of a low alloyed TRIP steel," *Acta Mater*, vol. 52, no. 9, pp. 2765–2778, 2004.
- [5] J. H. Chung, J. B. Jeon, and Y. W. Chang, "Work-hardening and ductility enhancement mechanism of cold rolled multiphase TRIP steels," *Met Mater Int*, vol. 16, no. 4, pp. 533–541, 2010.
- [6] P. J. Jacques, "Transformation-induced plasticity for high strength formable steels," *Curr Opin Solid State Mater Sci*, vol. 8, no. 3–4, pp. 259–265, 2004.
- [7] J. G. Speer, D. V. Edmonds, F. C. Rizzo, and D. K. Matlock, "Partitioning of carbon from supersaturated plates of ferrite, with application to steel processing and fundamentals of the bainite transformation," *Curr Opin Solid State Mater Sci*, vol. 8, no. 3–4, pp. 219–237, Jun. 2004, doi: 10.1016/J.COSSMS.2004.09.003.
- [8] D. K. Matlock and J. G. Speer, "Third Generation of AHSS: Microstructure Design Concepts," *Microstruct Texture Steels*, pp. 185–205, 2009, doi: 10.1007/978-1-84882-454-6_11.
- [9] H. Qu, G. M. Michal, and A. H. Heuer, "Third generation 0.3c-4.0mn advanced high strength steels through a dual stabilization heat treatment: Austenite stabilization through paraequilibrium carbon partitioning," *Metall Mater Trans A Phys Metall Mater Sci*, vol. 45, no. 6, pp. 2741–2749, 2014, doi: 10.1007/s11661-014-2232-2.
- [10] C. D. Horvath, C. M. Enloe, J. P. Singh, and J. J. Coryell, "Persistent challenges to advanced high-strength steel implementation," *Iron Steel Technol*, vol. 14, no. 10, pp. 76–83, 2017.

- [11] B. Sun, F. Fazeli, C. Scott, N. Brodusch, R. Gauvin, and S. Yue, "The influence of silicon additions on the deformation behavior of austenite-ferrite duplex medium manganese steels," *Acta Mater*, vol. 148, pp. 249–262, 2018, doi: 10.1016/j.actamat.2018.02.005.
- [12] Y. Ma, "Medium-manganese steels processed by austenite-reverted-transformation annealing for automotive applications," *Mater Sci Technol (United Kingdom)*, vol. 33, no. 15, pp. 1713–1727, 2017, doi: 10.1080/02670836.2017.1312208.
- [13] Y.-K. Lee, "Microstructural evolution during plastic deformation of twinning-induced plasticity steels," *Scr Mater*, vol. 66, no. 12, pp. 1002–1006, 2012.
- [14] J.-E. Jin and Y.-K. Lee, "Effects of Al on microstructure and tensile properties of C-bearing high Mn TWIP steel," *Acta Mater*, vol. 60, no. 4, pp. 1680–1688, 2012.
- [15] O. Bouaziz, S. Allain, C. P. Scott, P. Cugy, and D. Barbier, "High manganese austenitic twinning induced plasticity steels: A review of the microstructure properties relationships," *Curr Opin solid state Mater Sci*, vol. 15, no. 4, pp. 141–168, 2011.
- [16] J. Han, S.-J. Lee, J.-G. Jung, and Y.-K. Lee, "The effects of the initial martensite microstructure on the microstructure and tensile properties of intercritically annealed Fe–9Mn–0.05 C steel," *Acta Mater*, vol. 78, pp. 369–377, 2014.
- [17] S. Lee and B. C. De Cooman, "On the selection of the optimal intercritical annealing temperature for medium Mn TRIP steel," *Metall Mater Trans A*, vol. 44, no. 11, pp. 5018–5024, 2013.
- [18] J. Rehrl, K. Mraczek, A. Pichler, and E. Werner, "The impact of Nb, Ti, Zr, B, V, and mo on the hydrogen diffusion in four different AHSS/UHSS microstructures," *Steel Res Int*, vol. 85, no. 3, pp. 336–346, 2014, doi: 10.1002/srin.201300087.
- [19] M. Dehghan, R. Miresmaeili, M. Askari-Paykani, and H. R. Shahverdi, "Effects of a Novel Severe Plastic Deformation Approach on Microstructural and Mechanical Characteristics of a Medium Manganese Advanced High Strength Steel," *Met Mater Int*, vol. 28, no. 5, pp. 1232–1245, 2022, doi: 10.1007/s12540-021-01007-5.
- [20] I. Mejía, A. E. Salas-Reyes, J. Calvo, and J. M. Cabrera, "Effect of Ti and B microadditions on the hot ductility behavior of a High-Mn austenitic Fe-23Mn-1.5Al-1.3Si-0.5C TWIP steel," *Mater Sci Eng A*, vol. 648, pp. 311–329, 2015, doi:

- 10.1016/j.msea.2015.09.079.
- [21] M. Gáspár, A. Balogh, and I. Sas, "Physical simulation aided process optimisation aimed sufficient HAZ toughness for quenched and tempered AHSS," *Proc IIW* 2015 Int Conf Pap IIW, vol. 1504, no. July, pp. 1–7, 2015.
- [22] D. K. Matlock and J. G. Speer, "Processing opportunities for new advanced high-strength sheet steels," *Mater Manuf Process*, vol. 25, no. 1–3, pp. 7–13, 2010, doi: 10.1080/10426910903158272.
- [23] H. Aydin, E. Essadiqi, I. H. Jung, and S. Yue, "Development of 3rd generation AHSS with medium Mn content alloying compositions," *Mater Sci Eng A*, vol. 564, pp. 501–508, 2013, doi: 10.1016/j.msea.2012.11.113.
- [24] T. Marin-Alvarado, "Modelling Scheil Cooling of a Metal Alloy Thermodynamic and Multiphysics Solidification," *Proc 2016 COMSOL Conf Bost*, no. October, 2016.
- [25] F. G. Caballero, H. K. D. H. Bhadeshia, K. J. A. Mawella, D. G. Jones, and P. Brown, "Design of novel high strength bainitic steels: Part 2," *Mater Sci Technol*, vol. 17, no. 5, pp. 517–522, 2001, doi: 10.1179/026708301101510357.
- [26] M. S. Kim and Y. B. Kang, "Development of thermodynamic database for high Mn-high Al steels: Phase equilibria in the Fe-Mn-Al-C system by experiment and thermodynamic modeling," *Calphad Comput Coupling Phase Diagrams Thermochem*, vol. 51, pp. 89–103, 2015, doi: 10.1016/j.calphad.2015.08.004.
- [27] K. K. Dhande, N. I. Jamadar, and S. Ghatge, "Design and analysis of composite brake pedal: an ergonomic approach," *Int J Mech Eng Robot Res*, vol. 3, no. 3, pp. 474–482, 2014.
- [28] S. L. Chen, Y. Yang, S. W. Chen, X. G. Lu, and Y. A. Chang, "Solidification simulation using scheil model in multicomponent systems," *J Phase Equilibria Diffus*, vol. 30, no. 5, pp. 429–434, 2009, doi: 10.1007/s11669-009-9568-0.
- [29] J. P. Schillé, Z. Guo, N. Saunders, and A. P. Miodownik, "Modeling phase transformations and material properties critical to processing simulation of steels," *Mater Manuf Process*, vol. 26, no. 1, pp. 137–143, 2011, doi: 10.1080/10426910903153059.
- [30] D. V. Edmonds and R. C. Cochrane, "Structure-property relationships in bainitic

- steels," *Metall Trans A*, vol. 21, no. 6, pp. 1527–1540, 1990, doi: 10.1007/BF02672567.
- [31] J. Speer, D. K. Matlock, B. C. De Cooman, and J. G. Schroth, "Carbon partitioning into austenite after martensite transformation," *Acta Mater*, vol. 51, no. 9, pp. 2611–2622, 2003, doi: 10.1016/S1359-6454(03)00059-4.
- [32] D. W. Suh, S. J. Park, T. H. Lee, C. S. Oh, and S. J. Kim, "Influence of Al on the microstructural evolution and mechanical behavior of low-carbon, manganese transformation-induced-plasticity steel," *Metall Mater Trans A Phys Metall Mater Sci*, vol. 41, no. 2, pp. 397–408, 2010, doi: 10.1007/s11661-009-0124-7.
- [33] S. J. Lee, S. Lee, and B. C. De Cooman, "Mn partitioning during the intercritical annealing of ultrafine-grained 6% Mn transformation-induced plasticity steel," *Scr Mater*, vol. 64, no. 7, pp. 649–652, 2011, doi: 10.1016/j.scriptamat.2010.12.012.
- [34] F. Huyan, J. Y. Yan, L. Höglund, J. Ågren, and A. Borgenstam, "Simulation of the Growth of Austenite from As-Quenched Martensite in Medium Mn Steels," *Metall Mater Trans A Phys Metall Mater Sci*, vol. 49, no. 4, pp. 1053–1060, 2018, doi: 10.1007/s11661-018-4497-3.
- [35] M. Franceschi *et al.*, "Effect of intercritical annealing and austempering on the microstructure and mechanical properties of a high silicon manganese steel," *Metals (Basel)*, vol. 10, no. 11, pp. 1–19, 2020, doi: 10.3390/met10111448.
- [36] S. Yan, T. Liang, J. Chen, T. Li, and X. Liu, "A novel Cu-Ni added medium Mn steel: Precipitation of Cu-rich particles and austenite reversed transformation occurring simultaneously during ART annealing," *Mater Sci Eng A*, vol. 746, pp. 73–81, Feb. 2019, doi: 10.1016/J.MSEA.2019.01.014.
- [37] C. Huang and M. Huang, "Effect of processing parameters on mechanical properties of deformed and partitioned (D&p) medium mn steels," *Metals (Basel)*, vol. 11, no. 2, pp. 1–19, 2021, doi: 10.3390/met11020356.
- [38] F. García Caballero, M. K. Miller, S. S. Babu, and C. García Mateo, "Atomic scale observations of bainite transformation in a high carbon high silicon steel," 2007.
- [39] E. Kozeschnik and H. Bhadeshia, "Influence of silicon on cementite precipitation in steels," *Mater Sci Technol*, vol. 24, no. 3, pp. 343–347, 2008.
- [40] M. Akram, M. Soliman, and H. Palkowski, "Nano-Bainitic Steels: Acceleration of

- Transformation by High Aluminum Addition and Its Effect on Their Mechanical Properties," *Metals (Basel)*, vol. 11, no. 8, p. 1210, 2021.
- [41] B. Sun *et al.*, "Microstructural characteristics and tensile behavior of medium manganese steels with different manganese additions," *Mater Sci Eng A*, vol. 729, pp. 496–507, 2018, doi: 10.1016/j.msea.2018.04.115.
- [42] I. Mejía, A. E. Salas-Reyes, J. Calvo, and J. M. Cabrera, "Effect of Ti and B microadditions on the hot ductility behavior of a High-Mn austenitic Fe–23Mn–1.5 Al–1.3 Si–0.5 C TWIP steel," *Mater Sci Eng A*, vol. 648, pp. 311–329, 2015.
- [43] Y. K. Lee and J. Han, "Current opinion in medium manganese steel," *Mater Sci Technol (United Kingdom)*, vol. 31, no. 7, pp. 843–856, 2015, doi: 10.1179/1743284714Y.0000000722.
- [44] G. Aggyen, ASM Handbook Properties and Selection Irons Steels and High Performance Alloys 1990, vol. 1. 1990. doi: 10.3390/met9050560.
- [45] H. Qu, G. M. Michal, and A. H. Heuer, "A 3rd generation advanced high-strength steel (AHSS) produced by dual stabilization heat treatment (DSHT)," *Metall Mater Trans A Phys Metall Mater Sci*, vol. 44, no. 10, pp. 4450–4453, 2013, doi: 10.1007/s11661-013-1871-z.
- [46] S. Lee, Y. Estrin, and B. C. De Cooman, "Constitutive modeling of the mechanical properties of V-added medium manganese TRIP steel," *Metall Mater Trans A*, vol. 44, no. 7, pp. 3136–3146, 2013.
- [47] S. Lee and B. C. De Cooman, "Tensile behavior of intercritically annealed 10 pct Mn multi-phase steel," *Metall Mater Trans A*, vol. 45, no. 2, pp. 709–716, 2014.
- [48] D. W. Suh, J. H. Ryu, M. S. Joo, H. S. Yang, K. Lee, and H. Bhadeshia, "Medium-alloy manganese-rich transformation-induced plasticity steels," *Metall Mater Trans A*, vol. 44, no. 1, pp. 286–293, 2013.
- [49] R. Sun, W. Xu, C. Wang, J. Shi, H. Dong, and W. Cao, "Work Hardening Behavior of Ultrafine Grained Duplex Medium-Mn Steels Processed by ART-Annealing," *steel Res Int*, vol. 83, no. 4, pp. 316–321, 2012.
- [50] P. J. Gibbs, E. De Moor, M. J. Merwin, B. Clausen, J. G. Speer, and D. K. Matlock, "Austenite stability effects on tensile behavior of manganese-enriched-austenite transformation-induced plasticity steel," *Metall Mater Trans A*, vol. 42,

- no. 12, pp. 3691–3702, 2011.
- [51] D. V. Edmonds, K. He, F. C. Rizzo, B. C. De Cooman, D. K. Matlock, and J. G. Speer, "Quenching and partitioning martensite-A novel steel heat treatment," *Mater Sci Eng A*, vol. 438–440, no. SPEC. ISS., pp. 25–34, 2006, doi: 10.1016/j.msea.2006.02.133.
- [52] B. Wolfgang and P. Kriangyut, "Grain Refinement and Mechanical Properties in Advanced High Strength Grain Refinement and Mechanical Properties in Advanced High Strength Sheet Steels," no. January, 2016.
- [53] R. F. Meknassi and M. Tisza, "Recent third generation of advanced high strength sheet steels: Processing routes and properties," *EJONS XI Int Conf Math Eng Nat Med Sci*, pp. 148–158, 2021.
- [54] Z. J. Xie, G. Han, W. H. Zhou, X. L. Wang, C. J. Shang, and R. D. K. Misra, "A novel multi-step intercritical heat treatment induces multi-phase microstructure with ultra-low yield ratio and high ductility in advanced high-strength steel," *Scr Mater*, vol. 155, pp. 164–168, 2018, doi: 10.1016/j.scriptamat.2018.06.042.
- [55] R. Han, G. Yang, Z. Fu, D. Xu, Y. Xu, and G. Zhao, "Effect of low-temperature hot rolling on the microstructure and mechanical properties of air-cooling medium manganese martensitic wear-resistant steel," *Mater Charact*, vol. 203, no. 947, p. 113139, 2023, doi: 10.1016/j.matchar.2023.113139.
- [56] S. Ghosh, K. Rakha, S. Reza, M. Somani, and J. Kömi, "Atomic scale characterization of carbon partitioning and transition carbide precipitation in a medium carbon steel during quenching and partitioning process," *Mater Today Proc*, vol. 62, no. P14, pp. 7570–7573, 2022, doi: 10.1016/j.matpr.2022.04.649.
- [57] M. Shah, S. K. Das, and S. G. Chowdhury, "Effect of Alloying Elements on Microstructure and Mechanical Properties of Air-Cooled Bainitic Steel," *Metall Mater Trans A Phys Metall Mater Sci*, 2019, doi: 10.1007/s11661-019-05177-1.
- [58] H. K. D. H. Bhadeshia, Bainite in Steels Theory and Practice Third Edition. 2015.
 [Online]. Available:
 https://books.google.ca/books?id=kzjyrQEACAAJ%0Ahttps://www.crcpress.com/
 Bainite-in-Steels-Theory-and-Practice-ThirdEdition/Bhadeshia/p/book/9781909662742

- [59] M. Emami, M. Askari-Paykani, E. Farabi, H. Beladi, and H. R. Shahverdi, "Development of New Third-Generation Medium Manganese Advanced High-Strength Steels Elaborating Hot-Rolling and Intercritical Annealing," *Metall Mater Trans A Phys Metall Mater Sci*, vol. 50, no. 9, pp. 4261–4274, 2019, doi: 10.1007/s11661-019-05352-4.
- [60] H. E. Boyer and A. G. Gray, "Atlas of Isothermal and Cooling Transformation Diagrams," *Met Park OH Am Soc Met*, 1977.
- [61] A. Ito, A. Shibata, and N. Tsuji, "Thermomechanical processing of medium manganese steels," *Mater Sci Forum*, vol. 879, pp. 90–94, 2017, doi: 10.4028/www.scientific.net/MSF.879.90.
- [62] D. Raabe *et al.*, "Segregation engineering enables nanoscale martensite to austenite phase transformation at grain boundaries: A pathway to ductile martensite," *Acta Mater*, vol. 61, no. 16, pp. 6132–6152, 2013, doi: 10.1016/j.actamat.2013.06.055.
- [63] O. Dmitrieva *et al.*, "Chemical gradients across phase boundaries between martensite and austenite in steel studied by atom probe tomography and simulation," *Acta Mater*, vol. 59, no. 1, pp. 364–374, 2011, doi: 10.1016/j.actamat.2010.09.042.
- [64] A. Kwiatkowski da Silva, G. Inden, A. Kumar, D. Ponge, B. Gault, and D. Raabe, "Competition between formation of carbides and reversed austenite during tempering of a medium-manganese steel studied by thermodynamic-kinetic simulations and atom probe tomography," *Acta Mater*, vol. 147, pp. 165–175, 2018, doi: 10.1016/j.actamat.2018.01.022.
- [65] M. Askari-Paykani, H. R. Shahverdi, and R. Miresmaeili, "First and third generations of advanced high-strength steels in a FeCrNiBSi system," *J Mater Process Technol*, vol. 238, pp. 383–394, 2016, doi: 10.1016/j.jmatprotec.2016.07.043.
- [66] D. Raabe *et al.*, "Current Challenges and Opportunities in Microstructure-Related Properties of Advanced High-Strength Steels," *Metall Mater Trans A Phys Metall Mater Sci*, vol. 51, no. 11, pp. 5517–5586, 2020, doi: 10.1007/s11661-020-05947-2.

- [67] E. Asghari, R. Hayati, A. Momeni, N. Setoudeh, and A. Mohassel, "Using JMatPro Simulation to Study the Effect of Heat Treatment Temperature on the Dissolution of Gamma-Prime Phase in Inconel 617 Nickel-Based Superalloy," *Iran J Mater Form*, vol. 10, no. 2, pp. 44–54, 2023, [Online]. Available: https://ijmf.shirazu.ac.ir/article 7125.html
- [68] Z. Fan, "A microstructural approach to the effective transport properties of multiphase composites," *Philos Mag A*, vol. 73, no. 6, pp. 1663–1684, 1996.
- [69] Z. Fan, P. Tsakiropoulos, and A. P. Miodownik, "A generalized law of mixtures," *J Mater Sci*, vol. 29, pp. 141–150, 1994.
- [70] A. Joseph and A. V. A. L. From, "The Effect of Initial Job Experiences."
- [71] H. Zhang *et al.*, "Ultrafine-grained dual-phase maraging steel with high strength and excellent cryogenic toughness," *Acta Mater*, vol. 211, p. 116878, 2021, doi: 10.1016/j.actamat.2021.116878.
- [72] S. Yan, T. Li, T. Liang, and X. Liu, "Adjusting the microstructure evolution, mechanical properties and deformation behaviors of Fe-5.95Mn-1.55Si-1.03Al-0.055C medium Mn steel by cold-rolling reduction ratio," *J Mater Res Technol*, vol. 9, no. 2, pp. 1314–1324, 2020, doi: 10.1016/j.jmrt.2019.11.058.
- [73] N. Zhong, X. D. Wang, L. Wang, and Y. H. Rong, "Enhancement of the mechanical properties of a Nb-microalloyed advanced high-strength steel treated by quenching-partitioning-tempering process," *Mater Sci Eng A*, vol. 506, no. 1–2, pp. 111–116, 2009, doi: 10.1016/j.msea.2008.11.014.
- [74] D. V Edmonds, "Tensile deformation of two experimental steels containing silicon," *Mater Sci Technol*, vol. 3, no. June, pp. 432–440, 1987.
- [75] C. Y. Wang, J. Shi, W. Q. Cao, and H. Dong, "Characterization of microstructure obtained by quenching and partitioning process in low alloy martensitic steel," *Mater Sci Eng A*, vol. 527, no. 15, pp. 3442–3449, 2010, doi: 10.1016/j.msea.2010.02.020.
- [76] A. Taub, E. De Moor, A. Luo, D. K. Matlock, J. G. Speer, and U. Vaidya, "Materials for Automotive Lightweighting," *Annu Rev Mater Res*, vol. 49, pp. 327–359, 2019, doi: 10.1146/annurev-matsci-070218-010134.
- [77] P. G. B. de Oliveira, F. E. Mariani, L. C. Casteletti, A. Itman Filho, A. L. Neto,

- and G. E. Totten, "Boro-Austempering Treatment of High-Strength Bainitic Steels," *J Mater Eng Perform*, vol. 29, no. 6, pp. 3486–3493, 2020, doi: 10.1007/s11665-020-04590-7.
- [78] Ö. N. Cora and M. Koç, "Promises and Problems of Ultra/Advanced High Strength Steel (U/AHSS) Utilization in Automotive Industry," *7th Automot Technol Congr* (OTEKON 2014), no. May, pp. 1–8, 2014, doi: 10.13140/2.1.4725.0883.
- [79] Y. Ma *et al.*, "Phase boundary segregation-induced strengthening and discontinuous yielding in ultrafine-grained duplex medium-Mn steels," *Acta Mater*, vol. 200, pp. 389–403, 2020, doi: 10.1016/j.actamat.2020.09.007.
- [80] M. Bohuslav, J. Hana, H. Daniela, K. Ludmila, and K. Danuše, "The Effect of Mn and Si on the properties of advanced high strength steels processed by quenching and partitioning," *Mater Sci Forum*, vol. 654–656, pp. 94–97, 2010, doi: 10.4028/www.scientific.net/MSF.654-656.94.
- [81] S. Chenna Krishna, N. K. Karthick, A. K. Jha, B. Pant, and R. M. Cherian, "Effect of Hot Rolling on the Microstructure and Mechanical Properties of Nitrogen Alloyed Austenitic Stainless Steel," *J Mater Eng Perform*, vol. 27, no. 5, pp. 2388–2393, 2018, doi: 10.1007/s11665-018-3317-7.
- [82] R. Kumar, R. K. Dwivedi, and S. Ahmed, "Stability of Retained Austenite in Carbide Free Bainite during the Austempering Temperature and its Influence on Sliding Wear of High Silicon Steel," *Silicon*, vol. 13, no. 4, pp. 1249–1259, 2021, doi: 10.1007/s12633-020-00513-2.
- [83] P. C. Chakraborti and M. K. Mitra, "Microstructure and tensile properties of high strength duplex ferrite-martensite (DFM) steels," *Mater Sci Eng A*, vol. 466, no. 1–2, pp. 123–133, 2007, doi: 10.1016/j.msea.2007.02.042.
- [84] J. Shi, X. Sun, M. Wang, W. Hui, H. Dong, and W. Cao, "Enhanced work-hardening behavior and mechanical properties in ultrafine-grained steels with large-fractioned metastable austenite," *Scr Mater*, vol. 63, no. 8, pp. 815–818, Oct. 2010, doi: 10.1016/J.SCRIPTAMAT.2010.06.023.
- [85] Z. P. Hu *et al.*, "Effect of intercritical rolling temperature on microstructure-mechanical property relationship in a medium Mn-TRIP steel containing δ ferrite," *Mater Sci Eng A*, vol. 720, pp. 1–10, Mar. 2018, doi:

- 10.1016/J.MSEA.2018.02.052.
- [86] Y. Li *et al.*, "The austenite reversion and co-precipitation behavior of an ultra-low carbon medium manganese quenching-partitioning-tempering steel," *Acta Mater*, vol. 146, pp. 126–141, Mar. 2018, doi: 10.1016/J.ACTAMAT.2017.12.035.
- [87] H. Song *et al.*, "Novel ultra-high-strength Cu-containing medium-Mn duplex lightweight steels," *Acta Mater*, vol. 135, pp. 215–225, Aug. 2017, doi: 10.1016/J.ACTAMAT.2017.06.035.
- [88] H. J. Pan *et al.*, "Microstructure evolution and enhanced performance of a novel Nb-Mo microalloyed medium Mn alloy fabricated by low-temperature rolling and warm stamping," *Mater Des*, vol. 134, pp. 352–360, Nov. 2017, doi: 10.1016/J.MATDES.2017.08.047.
- [89] Y.-K. Lee and J. Han, "Current opinion in medium manganese steel," *Mater Sci Technol*, vol. 31, no. 7, pp. 843–856, 2015.
- [90] A. Mehrabi, H. Zurob, I. E. Benrabah, J. R. McDermid, "Austenite formation in a medium-Mn steel during intercritical annealing via in situ high-energy X-ray diffraction," *J Mater Res Technol*, vol. 30, no. April, pp. 2158–2167, 2024, doi: 10.1016/j.jmrt.2024.03.241.
- [91] S. Ghosh *et al.*, "A combined 3D-atomic/nanoscale comprehension and ab initio computation of iron carbide structures tailored in Q&P steels via Si alloying," *Nanoscale*, vol. 15, no. 23, pp. 10004–10016, 2023, doi: 10.1039/d3nr00816a.
- [92] A. Kwiatkowski da Silva, R. D. Kamachali, D. Ponge, B. Gault, J. Neugebauer, and D. Raabe, "Thermodynamics of grain boundary segregation, interfacial spinodal and their relevance for nucleation during solid-solid phase transitions," *Acta Mater*, vol. 168, pp. 109–120, 2019, doi: 10.1016/j.actamat.2019.02.005.
- [93] Y. Ma, W. Song, S. Zhou, A. Schwedt, and W. Bleck, "Influence of intercritical annealing temperature on microstructure and mechanical properties of a coldrolled medium-mn steel," *Metals (Basel)*, vol. 8, no. 5, 2018, doi: 10.3390/met8050357.
- [94] J. T. Benzing *et al.*, "Multi-scale characterization of austenite reversion and martensite recovery in a cold-rolled medium-Mn steel," *Acta Mater*, vol. 166, pp. 512–530, 2019, doi: 10.1016/j.actamat.2019.01.003.

- [95] L. Luo, W. Li, L. Wang, S. Zhou, and X. Jin, "Tensile behaviors and deformation mechanism of a medium Mn-TRIP steel at different temperatures," *Mater Sci Eng A*, vol. 682, pp. 698–703, 2017.
- [96] D. M. Pallisco and J. R. McDermid, "Mechanical property development of a 0.15C–6Mn–2Al–1Si third-generation advanced high strength steel using continuous galvanizing heat treatments," *Mater Sci Eng A*, vol. 778, no. February, p. 139111, 2020, doi: 10.1016/j.msea.2020.139111.
- [97] K. M. H. Bhadhon, X. Wang, and J. R. McDermid, "Effects of CGL-compatible thermal processing, starting microstructure, and Sn micro-alloying on the mechanical properties of a medium-Mn third generation advanced high strength steel," *Mater Sci Eng A*, vol. 833, 2022, doi: 10.1016/j.msea.2021.142563.
- [98] L. Zhao, L. Qian, J. Meng, Q. Zhou, and F. Zhang, "Below-Ms austempering to obtain refined bainitic structure and enhanced mechanical properties in low-C high-Si/Al steels," *Scr Mater*, vol. 112, pp. 96–100, 2016, doi: 10.1016/j.scriptamat.2015.09.022.
- [99] R. Kuziak, R. Kawalla, and S. Waengler, "Advanced high strength steels for automotive industry: A review," *Arch Civ Mech Eng*, vol. 8, no. 2, pp. 103–117, 2008, doi: 10.1016/s1644-9665(12)60197-6.
- [100] A. A. Popoff, "Simplified hot rolling load calculations incorporating material strain rates," *Int J Mech Sci*, vol. 18, no. 11–12, pp. 529–532, 1976, doi: 10.1016/0020-7403(76)90078-3.
- [101] Q. Zhu *et al.*, "Heterostructure mediated high strength and large ductility in novel medium-Mn steels with low Mn content," *Acta Mater*, vol. 276, no. May, p. 120092, 2024, doi: 10.1016/j.actamat.2024.120092.
- [102] Z. H. Li, J. K. Ren, C. Wang, X. Wang, R. D. K. Misra, and G. D. Wang, "Design of a cold-rolled novel advanced high-strength steel: An analysis of microstructural evolution and mechanical properties," *Mater Charact*, vol. 163, no. August 2019, 2020, doi: 10.1016/j.matchar.2020.110265.
- [103] Z. Cai, S. Wang, Y. Zhou, J. Dong, L. Ma, and S. Liu, "Influence of aging treatment on mechanical properties and wear resistance of medium manganese steel reinforced with Ti(C,N) particles," *Friction*, vol. 11, no. 11, pp. 2059–2072,

- 2023, doi: 10.1007/s40544-022-0712-8.
- [104] A. Arlazarov, M. Gouné, O. Bouaziz, A. Hazotte, G. Petitgand, and P. Barges, "Evolution of microstructure and mechanical properties of medium Mn steels during double annealing," *Mater Sci Eng A*, vol. 542, pp. 31–39, 2012.
- [105] Y. Dong *et al.*, "Analysis of phase transformation thermodynamics and kinetics and its relationship to structure-mechanical properties in a medium-Mn high strength steel," *J Mater Res Technol*, vol. 27, no. November, pp. 5411–5423, 2023, doi: 10.1016/j.jmrt.2023.10.231.
- [106] R. Ding, Z. Dai, M. Huang, Z. Yang, C. Zhang, and H. Chen, "Effect of pre-existed austenite on austenite reversion and mechanical behavior of an Fe-0.2C-8Mn-2Al medium Mn steel," *Acta Mater*, vol. 147, pp. 59–69, 2018, doi: 10.1016/j.actamat.2018.01.009.
- [107] H. K. D. H. Bhadeshia and D. V. Edmonds, "Bainite in silicon steels: New composition-property approach," *Met Sci*, vol. 17, no. 9, pp. 420–425, 1983, doi: 10.1179/030634583790420646.
- [108] Q. Lai *et al.*, "Damage and fracture of dual-phase steels: Influence of martensite volume fraction," *Mater Sci Eng A*, vol. 646, pp. 322–331, 2015.
- [109] M. Calcagnotto, Y. Adachi, D. Ponge, and D. Raabe, "Deformation and fracture mechanisms in fine-and ultrafine-grained ferrite/martensite dual-phase steels and the effect of aging," *Acta Mater*, vol. 59, no. 2, pp. 658–670, 2011.